Advances in Industrial Control

Martin Kozek
Alexander Schirrer *Editors*

Modeling and Control for a Blended Wing Body Aircraft

A Case Study

AIC

Springer

Advances in Industrial Control

More information about this series at http://www.springer.com/series/1412

Martin Kozek · Alexander Schirrer
Editors

Modeling and Control for a Blended Wing Body Aircraft

A Case Study

Springer

Editors
Martin Kozek
Alexander Schirrer
Vienna University of Technology
Vienna
Austria

ISSN 1430-9491 ISSN 2193-1577 (electronic)
ISBN 978-3-319-10791-2 ISBN 978-3-319-10792-9 (eBook)
DOI 10.1007/978-3-319-10792-9

Library of Congress Control Number: 2014950649

Springer Cham Heidelberg New York Dordrecht London

Printed on acid-free paper

Springer is part of Springer Science+Business Media (www.springer.com)

Series Editors' Foreword

The series *Advances in Industrial Control* aims to report and encourage technology transfer in control engineering. The rapid development of control technology has an impact on all areas of the control discipline (new theory, new controllers, actuators, sensors, new industrial processes, computer methods, new applications, new philosophies,…—new challenges). Much of this development work resides in industrial reports, feasibility study papers, and the reports of advanced collaborative projects. The series offers an opportunity for researchers to present an extended exposition of such new work in all aspects of industrial control for wider and rapid dissemination.

Aerospace has always been a fertile field for testing the techniques of advanced modern control. New control methods that have a multivariable framework and promise ways of computing controllers able to withstand quantifiable levels of uncertainty are always going to be of interest in applications where the models are large-scale, high-order, resonant, and conceptually complex. When the methods of H_∞ and robust control first appeared in the literature, the *Advances in Industrial Control* series saw several entries applying these techniques to airframe dynamics, including:

- *Robust Multivariable Flight Control* by Richard J. Adams, James M. Buffington, Andrew G. Sparks, and Siva S. Banda (ISBN 978-3-540-19906-9, 1994);
- H_∞ *Aerospace Control Design* by Richard A. Hyde (ISBN 978-3-540-19960-1, 1995); and
- *Robust Aeroservoelastic Stability Analysis* by Rick Lind and Marty Brenner (ISBN 978-1-85233-096-5, 1999).

The trend of new control methods finding application in the aerospace field continues and we can cite the recent *Advances in Industrial Control* monograph *Fault Detection and Fault-Tolerant Control Using Sliding Modes* by Halim Alwi, Christopher Edwards and Chee Pin Tan (ISBN 978-1-85729-649-8, 2011) as one example where the control scheme was tested on a professional civil aircraft flight simulator. And then there is the *Advanced Textbooks in Control and Signal Processing* volume: *Robust and Adaptive Control with Aerospace Applications* written

by two highly respected aerospace control engineers, Eugene Lavretsky and Kevin Wise (ISBN 978-1-4471-4395-6, 2013).

A development of the last few years is a spate of monographs in the series reporting control developments for autonomous mini-aircraft, commonly called "drones". This is a development driven by the emergence of a new technological aerospace vehicle. With the theme of emerging technologies for the aerospace field, there have been several European research programs funding some projects to investigate the interface between such technologies and the capabilities of advanced control techniques. One example was the recent *Advances in Industrial Control* monograph: *Fault Diagnosis and Fault-Tolerant Control and Guidance for Aerospace Vehicles*: *From Theory to Application* by Ali Zolghadri, David Henry, Jérôme Cieslak, Denis Efimov and Philippe Goupil (ISBN 978-1-4471-5312-2, 2013).

The present monograph *Modeling and Control for a Blended Wing Body Aircraft*: *A Case Study* with Editors Martin Kozek and Alexander Schirrer is another example of the outcomes of recent European aerospace research. This time the objective was to investigate the "greening" of air travel through the use of a "blended wing body" (BWB) aircraft to reduce fuel consumption and CO_2 production and the capabilities of today's advanced control methodologies. Thus, the monograph reports a modeling and design study with several advanced robust control methods applied to a conceptual BWB aircraft. The research project was titled "Active Control for Flexible 2020 Aircraft" and the craft itself was dubbed the "ACFA 2020"; an interesting artist's impression of the futuristic-looking aircraft appears on page 12 of the monograph. The proposed aircraft was designed for civil applications with control design performance requirements of robust stabilization of the aircraft and structural design goals of aero-structural dynamic shaping, vibration and load alleviation. These design goals are also linked to passenger ride comfort.

The monograph's content comprises eight chapters divided into an opening overview chapter, followed by Part I (three chapters) reporting the aircraft modeling, the technical and conceptual design and the models necessary for the control studies (namely, the application of model reduction techniques). Part II (three chapters) focuses on the control design starting with a review of control techniques, followed by feedback control and finishing with feed-forward control designs. The eighth chapter (Part III) concludes the monograph with a discussion of the results and presents ideas for future research directions.

Far from being purely academic research, the work reported in this monograph was guided by leading aerospace companies, including EADS Innovation Works, Airbus France, Hellenic Aerospace Industry (HAI) S.A., and the Israel Aerospace Industries (IAI). Interested readers will include the aerospace and control academic communities and engineers from a wide range of aerospace, modeling, and control disciplines.

Glasgow, Scotland, UK

Michael J. Grimble
Michael A. Johnson

Foreword

The need for improved performance, reduced operating costs, and reduced effect of aircraft emissions on climate change is driving aircraft designers to adopt lightweight, high-aspect ratio flexible wings. Reducing weight decreases aerodynamic drag, leading to less fuel consumption. High-aspect ratio wings minimize drag over lift, improving the aircraft performance on aspects such as long range and endurance. These modifications are being applied to modern commercial airplanes, mainly by using composite materials for both fuselage and wings. On the other hand, lightweight, high-altitude vehicles with large wing span exhibit high flexibility and significant deformation in flight increasing the interaction between the rigid body and structural dynamics modes.

The Active Control of Flexible 2020 Aircraft program (ACFA 2020) concentrated on reductions in fuel consumption, CO_2 and NOx emissions reduction and reduction in external noise by 50 %. A blended wing body (BWB) aircraft configuration was selected as an innovative approach to future commercial aircraft. The ACFA 2020 project embraced the two challenges (emissions and noise), and the following main deliverables were formulated:

- Design of multi-objective active multi-input/multi-output (MIMO) control concepts for BWB-type aircraft.
- Predesign of an ultra-efficient ACFA 2020 aircraft configuration.

This book describes the modeling and design of the BWB aircraft, the application of several MIMO flight control techniques for rigid body and aeroelastic control of the BWB aircraft, and validation of the model combined with the flight control techniques.

This book is perfectly timed to provide insight to researchers and engineers working on future aircraft systems. I had the pleasure of following the ACFA 2020 progress during the program. It is exciting to see this manuscript documenting ACFA 2020 come to fruition.

Minnesota, USA, July 2014

Gary Balas
Distinguished McKnight University Professor
Aerospace Engineering and Mechanics
University of Minnesota

Preface

This book is based on the outcome of the European Commission (EC)-funded research project "Active Control of a Flexible 2020 Aircraft" (ACFA 2020), which was conducted from 2008 to 2011. It succeeded the EC-funded research projects "Very Efficient Large Aircraft" (VELA) and "New Aircraft Concepts Research" (NACRE), which investigated concepts for a large blended wing body (BWB) commercial aircraft. The ACFA 2020 project worked out multi-objective control concepts as well as an ultra-efficient BWB predesign aircraft model for 450 passengers.

This book collects several major results from the ACFA 2020 project covering key developments in structural and dynamic modeling as well as multi-variable, multi-objective control design methods. The scope of the book covers the conceptual design as well as the modeling process to obtain a numerical simulation model and model reduction methods to obtain the basis for controller design. The second part is dedicated to control design, covering various advanced feedback and feed-forward design methods to address the multitude of arising control goals: stabilization, load alleviation, flight dynamics, and comfort. The last part comprises validation results of the proposed control concepts, especially the achieved loads alleviation and comfort aspects, and a discussion of further work and open issues.

The purpose of this book is two-fold: (i) promote the results obtained in the research project, illustrated at the considered BWB aircraft pre-design model and (ii) present the methods for modeling, control design, and optimization that have been developed. We believe that this book is a valuable source of information to both scientists and engineers active in the aerospace and control communities. It contains specific information about the problems and solutions found in the predesign of a BWB concept and also demonstrates advanced control design methods on a complex application example.

The ACFA 2020 project answered several fundamental questions, such as the general load alleviation potential, but it was out of scope to produce a complete BWB control architecture or to conduct in-depth optimization of actuators. Therefore, several open issues remained and are addressed in the discussion and outlook.

We are grateful for the dedication, enthusiasm, and continuing support of the ACFA 2020 consortium and the involved individual work groups. Rudolf Maier and Andreas Wildschek from Airbus Group Innovations (formerly EADS Innovation Works) have initiated and led the research project in a cooperative and stimulating way. The members of the project's Scientific Advisory Group contributed invaluable inputs during the project's progress: Gary Balas (University of Minnesota, USA), Dagfinn Gangsaas (Aerospace Control Dynamics LLC, USA), Mark Lowenberg (University of Bristol, UK), and Ilkay Yavrucuk (Middle East Technical University, Turkey). We thank our Scientific Officer at the European Commission, Pablo Perez-Illana, for his understanding of a research project's needs and support during the project. Finally, our personal thanks go to Springer Verlag, where Oliver Jackson and Charlotte Cross proved to be our reliable signposts for guiding us through the long process of publication.

The results presented in this book have been developed within the ACFA 2020 research project. This project has been financially supported by the European Union Framework Programme 7 under the FP7 project number 213321. Many thanks also go to the NACRE consortium, especially to ONERA, DLR, and the NACRE-task 2.2 team, for providing aerodynamic and structure data of a large BWB aircraft configuration which strongly supported the development of methods and tools early in the ACFA 2020 project.

Vienna, July 2014

Martin Kozek
Alexander Schirrer

Contents

Acronyms

BC	Business Class
BFGS	Broyden–Fletcher–Goldfarb–Shanno
BWB	Blended Wing Body
CACSD	Computer-Aided Control Systems Design
CAS	Control Augmentation System
CFD	Computational Fluid Dynamics
CFRP	Carbon-Fiber-Reinforced Polymer
CG	Center of Gravity
CWB	Carry-through Wing Box
DC gain	Static Gain
DLM	Doublet Lattice Aerodynamic Model
DR mode	Dutch Roll Mode
EC	European Commission
EMA	Electro-Mechanical Actuator
FBC	Feedback Control
FCS	Flight Control System
FE	Finite Element
FEM	Finite Element Method
FFCC	Feed-Forward Command Control
FFDC	Feed-Forward Disturbance Control
FIR	Finite-Impulse Response
GAF	Generalized Aerodynamic Forces
GLAS	Gust Load Alleviation System
HIFOO	$\mathscr{H}_\infty$ Fixed-Order Optimization
I/O	Input/Output
ICAO	International Civil Aviation Organization
L/D-ratio	Lift/Drag-ratio
LAS	Load Alleviation System
LFR	Linear Fractional Representation
LFT	Linear Fractional Transformation

LMI	Linear Matrix Inequality
LP	Linear Programing
LPV	Linear Parameter-Varying
LQ	Linear-Quadratic
LQG	Linear-Quadratic Gaussian
LTH	Luftfahrttechnisches Handbuch (engl. Aviation Technology Handbook)
LTI	Linear Time-Invariant
MAC	Mean Aerodynamic Chord
MDO	Multidisciplinary Design Optimization
MIMO	Multi-Input Multi-Output
MISO	Multi-Input Single-Output
OWE	Operating Empty Weight
PAX	Passengers
PM	Phugoid Mode
QP	Quadratic Programming
RANS	Reynolds-Averaged Navier–Stokes
RB	Rigid-Body
RBF	Radial Basis Functions
ROM	Reduced-Order Model
RP	Robust Performance
RS	Robust Stability
SAS	Stability Augmentation System
SISO	Single-Input Single-Output
SPA	Singular Perturbation Approximation
SPM	Short-Period Mode
ST	State Truncation
T/W-ratio	Thrust/Weight-ratio
YC	Economy Class

Chapter 1
Overview and Motivation

M. Kozek, A. Schirrer, B. Mohr, D. Paulus, T. Salmon, M. Hornung, C. Rößler, F. Stroscher and A. Seitz

1.1 Greening Air Transport

M. Kozek and A. Schirrer

The greening of air transport is one major issue in reducing the impact of mobility to climate change and environmental impact in general. Due to the close interdependence between legislative bodies, aircraft manufacturers, air transport operators, economy, and consumers, the need for a technological contribution to mitigate the adverse effects of air transport exists worldwide. With 2.2 billion passengers yearly and an estimated 2 % contribution to man-made CO_2 emissions today's air transport seems to have a well-balanced benefit to cost relation [17]. However, this is expected to increase to 3 % by 2050 with the ever increasing growth in traffic.

Governments and aircraft industry have thus established coordinated action which comprises new goals of future aircraft on the one hand and funding of research on the other hand. The European Commission is, therefore, actively supporting research programs where research and development for green air transport is funded [17, 26, 85]. One of the driving forces in setting new goals for technology in air transport is the Advisory Council for Aeronautics Research in Europe (ACARE) [1]. This board develops and defines visions and goals which usually constitute benchmarks for both industry and research.

M. Kozek (✉) · A. Schirrer
Vienna University of Technology, Vienna, Austria
e-mail: martin.kozek@tuwien.ac.at

B. Mohr · D. Paulus · M. Hornung · C. Rößler · F. Stroscher
Technische Universität München, Munich, Germany

T. Salmon
Airbus Operations S.A.S., Toulouse, France

A. Seitz
German Aerospace Center, Cologne, Germany

M. Kozek and A. Schirrer (eds.), *Modeling and Control for a Blended Wing Body Aircraft*,
Advances in Industrial Control, DOI 10.1007/978-3-319-10792-9_1

1.2 The ACARE 2020 Vision

M. Kozek and A. Schirrer

A Strategic Research Agenda (SRA) had been published by the ACARE in November 2002, and in March 2005 an update was delivered. Main objective of the SRA is to stimulate and promote research for the "ACARE vision 2020" which focuses on the following main topics:

- 50 % reduction in both fuel consumption and related CO_2 emissions and 80 % reduction in NO_x.
- Reduction of perceived external noise by 50 %.

These goals were the main drivers for formulating the ACFA 2020 project proposal. Note that the current updated "ACARE vision 2050" already aims for a 75 % reduction in CO_2, 65 % reduction in noise, and 90 % NO_x reduction (all per passenger-kilometer) [2].

Conventional aircraft design could only achieve these goals by improvements in lightweight materials and engine characteristics. However, fundamental changes in aircraft configuration promise a much larger margin for improvement. One of the most promising concepts is the so-called blended wing body (BWB) configuration. A blended wing body (BWB) design minimally distinguishes between wing-fuselage and fuselage-tail and consequently exhibits a much more centered volume than the stretched cylindrical shape of a conventional aircraft. This is especially favorable for transporting a large number of passengers, and several theoretical advantages of traditional aircraft can be expected:

- greater internal volume
- aerodynamics and structural efficiency
- noise reduction
- reduced cost-per-seat-mile.

A reduction in fuel consumption can not only be expected from reduced structural weight but also from a minimal wetted area in relation to load capacity. A reduction in perceived external noise can be expected from adapted high-lift devices and the possibility to place the engines on top of the aircraft in front of the trailing edge or even integrated in the airframe. Fundamental design problems of such BWB concepts have been solved in earlier projects by Boeing [52] and the European Union (EU). In the EU funded projects VELA [42] and NACRE [25] large passenger aircraft concepts have been studied. The results for the 750 passenger NACRE flying wing configuration was therefore one of the starting points for the ACFA 2020 project. However, most of today's long-distance flights are served by aircraft with around 450 passenger capacity. This is one of the reasons why Boeing initiated research for a 450-passenger BWB aircraft, see [52]. Since the predicted efficiency of that design is significantly higher than for the NACRE flying wing, a more advanced BWB design for 450 passengers was sought for.

It is interesting to note that some criticism on the ACARE vision has been expressed lately. In [33] the authors claim that based on a number of studies from other authors the expected technological potential for the next 20–40 years is unrealistically optimistic. Furthermore, it is stated that behavioral change can be combined with technological advances to yield even more substantial benefits.

1.3 The ACFA 2020 Project

M. Kozek and A. Schirrer

1.3.1 Overview and Deliverables

The before mentioned challenges constituted the core of the framework 7 Area "Green Aircraft—Flight Physics" in 2007, and a consortium was formed which set up a collaborative project aiming at solutions to those challenges [55]. The project was named "ACFA 2020—Active Control for Flexible 2020 Aircraft" and lasted from 2008 to 2011.

Note that the design of a BWB aircraft is an integrated task, where strongly interacting fields like aerodynamics, structural analysis, flight mechanic design, actuators, and control design have to be considered simultaneously. Since currently, there exist no comprehensive integrated methods to tackle such a complex problem, it is necessary to iterate through the individual design tasks in order to come up with an optimal solution. Due to limited time and resources, the ACFA 2020 project could only establish that iteration loop and exemplarily complete the first iteration. The results presented in this book, therefore, constitute a good starting point for optimization but are not the final result of such a procedure.

The studies conducted in the European projects VELA and NACRE had clearly identified the need for a specific control system for such aircraft concepts. However, no such investigation had taken place in the mentioned research projects. Aside from the control system issue, the next step to a predesign of a fuel-efficient European BWB aircraft was in order. The ACFA 2020 project embraced these two challenges, and the following main deliverables were formulated:

1. Design of multi-objective active multi-input multi-output (MIMO) control concepts for BWB-type aircraft
2. Predesign of an ultra-efficient ACFA 2020 aircraft configuration.

1.3.2 Main Deliverable 1: Solutions for Active MIMO Control for BWB-Type Aircraft

For conventional aircraft configurations active load alleviation systems had already been developed in the European AWIATOR project [41] as well as in the German

national project MODYAS [47]. A short review on the history of such active control systems can be found in Sect. 1.7. In the past, these control systems have been employed to reduce critical loads and to improve handling qualities. Also an improvement in ride comfort had been achieved. An important feature of load reduction is the increase in aircraft efficiency by reduction of structural weight. All of these features are also important assets for the integrated design of a BWB aircraft.

It must be emphasized here that the control design for a BWB configuration is considerably more challenging than for a conventional aircraft. First of all this is caused by the different flight mechanics of the BWB aircraft. Instead of improving the generic dynamic behavior of a conventional aircraft, the BWB control design must imprint the desired closed-loop dynamics in order to provide handling qualities for the pilot. The open-loop behavior may be even unstable due to the missing empennage and the center of gravity location. This task therefore calls for a MIMO control design which explicitly considers strong coupling between the individual controls and outputs. The controller must also be capable to guarantee performance over the flight envelope, either by scheduling, adaptive algorithms or by robust design. Last but not least, the integration of the controller design in the overall system optimization must already be considered in the aircraft design.

Main goals of the ACFA 2020 main deliverable 1 therefore were:

1. Aerodynamic loads: minimization to reduce structural weight of BWB-type aircraft (improved fuel efficiency)
2. Handling qualities: meet requirements for response to pilot inputs, desired gust response, pitch, and Dutch Roll mode (DR mode) damping
3. Ride comfort: reduction of 50 % with respect to baseline BWB aircraft concepts (stabilizing controller only).

Some of the goals defined above can be achieved by separate control design methods (for example, feed-forward control for handling qualities, feedback control for load alleviation and comfort), but in general an integrated control design approach is necessary to meet all required criteria.

1.3.3 Main Deliverable 2: ACFA 2020 Aircraft Configuration (Predesign of an Ultra-Efficient 450 Passenger BWB-Type Aircraft)

The ACFA 2020 aircraft configuration is an ultra-efficient 450 passenger tailless composite aircraft with aerodynamic wing/fuselage blending. The engines are mounted over the rear fuselage such that minimum exterior noise signature can be expected. For load reduction as well as for improved ride comfort and handling qualities the active MIMO control architecture developed in ACFA 2020 main deliverable 1 is applied.

Half of the projected 50 % reduction in fuel consumption should be provided by the savings of structural weight of the airframe. The other half is expected to come from

the reduced fuel consumption of future engine technologies. This would allow an overall 50 % reduction of CO_2 can be achieved by the proposed BWB design. A verification of the reduction in fuel consumption was performed using Breguet's formula.

1.3.4 Consortium and Figures

A wide range of partners from industry and academia constituted the ACFA 2020 consortium. The respective core competence of the partners formed a background of knowledge specifically tailored to meet the project objectives. Another important aspect for selection was to transfer knowledge from the European projects VELA and NACRE by integrating partners from DLR, ONERA, FOI, TUM, and AIRBUS. This choice ensured maximum efficiency in providing both expert knowledge on the key challenges of the ACFA 2020 project and access to already existing knowledge on nonconventional aircraft configurations. As a matter of fact, model, and aerodynamic data from NACRE project were used for development of design tools and the associated workflow. Twelve partners from eight European nations together with IAI from Israel constitute the ACFA 2020 consortium:

- Airbus France
- Alenia Aeronautica S.p.A.
- BTU, Bialystok Technical University
- CTU, Czech Technical University
- DLR, Deutsches Zentrum fr Luft- und Raumfahrt e.V.
- EADS-IW, EADS Innovation Works (today Airbus Group Innovations)
- FOI, Swedish Defence Research Agency
- HAI, Hellenic Aerospace Industry S.A.
- IAI, Israel Aerospace Industries
- NTUA, National Technical University Athens
- ONERA
- TUM, Technical University Munich
- TUV, Vienna University of Technology, Institute of Mechanics and Mechatronics.

Coordinator of the project was Dr. Rudolf Maier from Airbus Group Innovations (formerly EADS Innovation Works). The work was conducted under Grant-Agreement number ACP7-GA-2008-213321, starting at March 1st, 2008 and lasting for 48 months. Total budget of the project was 4.588 million Euros, and the EU contribution was 3.125 million Euros.

1.4 Recent Developments in New Aircraft Configurations

B. Mohr, D. Paulus and T. Salmon

The commercial aviation market is projected to have steady growth up to the year 2030 [12]. The world's fleet of aircraft is forecast to more than double in the next 20 years [3]. However, the commercial aviation industry will face changes in the near

Table 1.1 ACARE target values

	Vision 2020 (%)	Flightpath 2050 (%)
CO_2	−50	−75
NO_x	−80	−90
Noise	−50	−65

future. One of them is the shortage of fossil fuels and its impact on operating cost and airline business models. Furthermore, the awareness regarding emissions, that is, noise and pollutants, is growing among civilians and politicians. As a result, future aircraft will need to be more cost and fuel efficient. In addition, noise levels, especially during take-off and landing, will have to be lowered significantly to facilitate more movement at airports. The target values[1] for improvements have been established by the European Commission (EC), see [27, 28] and Table 1.1.

The majority of current civil transport aircraft uses the typical wing-cylindrical-fuselage-tail configurations powered by turbofan engines. The most obvious and straightforward efficiency gain could be achieved by further improving the airframe and engines, while continuing to use this conventional layout as it has been done for the past 60 years. This could be achieved by applying a combination of the following options:

- Improved aerodynamics, for example, laminar flow, new airfoils and winglets, etc.
- Next-generation engines, for example, geared turbofan (GTF), unducted fans (UDF), etc.
- Lightweight structures, for example, material usage, new structural concepts, etc.
- Innovative systems, for example, more electric system architecture, active and adaptive control, etc.

However, the conventional layout has been progressed so far over the past decades that it is gradually reaching an asymptotic limit in terms of efficiency, especially from an airframe point of view. If the current trend is held, Flightpath 2050 targets are not likely to be reached. This is why several sources postulate the investigation of completely new aircraft configurations for the long term [15]. Many options for innovative aircraft configurations exist and are targeted at providing breakthroughs in terms of aerodynamics, engine and material technology. Some configurations are given as an example that have recently been studied and in some cases even made their way into the sky, such as the Piaggio Avanti:

- Lockheed Martin and Stanford University box-wing concept
- University of Pisa Prandtl-Plane concept
- Piaggio P180 three-surface aircraft (TSA)
- Bauhaus Luftfahrt Claire Liner concept
- Boeing Sugar Volt concept

[1] Relative to year-2000 aircraft.

- Airbus concept plane
- Oblique flying wing (OFW)
- Blended wing body (BWB).

The goal of most unconventional configurations envisaged for civil air transport use is to improve efficiency and reduce fuel burn. The most common ground among these new configurations is improved aerodynamic behavior by means of an innovative layout.

The intent of some of these configurations is to take advantage of nonplanar wings, such as bi-plane, tri-plane, box wing, or Prandtl-plane configurations, by reducing the production of lift dependent drag. One big challenge with these configurations is finding the optimal balance between improved aerodynamics of nonplanar wings and inherently higher wing structural weights. With the same total wing area and the same wing span, the wing box chord, and depth become very small for sustaining ground and flight loads. Another challenge with these configurations can be the aircraft operations on the ground and airport compatibility. Also, cargo and cabin doors might not be very easily accessible for boarding/deplaning, catering, and servicing.

The oblique flying wing is an interesting concept, since it can theoretically achieve good performance at high speed (limited wave drag) while still having good low-speed capabilities for take-off and landing (high-lift production and low-induced drag). This is achieved by adapting the wing sweep angle in flight. However, weight and technical complexity of the wing pivoting system, in particular for civil applications where certification regulations require a very high level of safety, would be a significant challenge. Hence, this type of configuration is probably more suitable for military applications, in particular for high-speed aircraft (Mach number >1).

Another trend is to look toward wings with a very high-aspect ratio. This is in fact more a stretch of the classical layout to its limit in terms of reduction of induced drag rather than an entirely novel configuration. The wing aspect ratio is a highly efficient lever to improve the aerodynamic efficiency of an aircraft. This has long been used for gliders and now is also being used on long-endurance UAVs. For civil transport applications, however, the optimum in span and aspect ratio for fuel burn is quickly reached because of the effect on the wing weight. For this reason some specific structural features, such as wing struts, can be used to counteract the detrimental effect of increasing wing span. One example is the strut-bracing used on the high-aspect ratio wing of the Boeing Sugar Volt concept. This concept combines an aerodynamically efficient wing with a hybrid propulsion system, in order to significantly reduce the fuel burn of the aircraft.

In fact, the very aggressive targets in terms of fuel burn or CO_2 reduction, like the ones set by ACARE, will only be reached in the long term if aircraft configurations can combine disruptive designs in many domains, especially in aerodynamics and propulsion. Such designs will be enabled by progress made in materials, such as composites and advanced systems. Examples of disruptive propulsion systems are:

- Open-rotors (propulsive efficiency increase by means of an increased by-pass ratio), for example, GE36 UDF

- Boundary layer ingestion (improves aircraft fuel efficiency by re-energizing the aircraft wake)
- Hybrid propulsion/electrical propulsion (reduce fuel burn by using partially or totally alternative energy, such as electricity, to power the aircraft), for example, Boeing Sugar Volt concept
- Distributed/multifan concepts (improved fuel efficiency and better flexibility for propulsion integration), for example, Bauhaus Luftfahrt Claire-Liner.

Finally, another design which is of great interest (in particular for capacity aircraft) is the flying wing. The basic principle of the flying wing is to have everything embedded in a single wing volume, in particular the payload (passenger and cargo in case of civil transport application), which is normally located in a cylindrical fuselage. This leads to minimizing wetted areas and thus to maximizing lift/drag ratio (L/D ratio). On the flying wing even the control and trim surfaces are part of the wing movables. The term "blended wing body" is used very often to account for configurations that may deviate from the pure flying wing shape in order to accommodate the payload (several flattened shapes of different sweep angles blended together, bulge on the surface, etc.), the control surfaces (winglets, fins, etc.), and the engines (podded engines). In the US, the term "hybrid wing body" is often used. With blended or hybrid wing bodies, lift is produced both by the central body and by lateral wings. This contributes to a much better L/D ratio compared to the classical configuration.

Furthermore, the BWB concept offers noise reduction potential if the engines are mounted on top of the aircraft, enabled through the noise shielding effect produced by the central body.

One of the big challenges of the BWB configuration is linked to the integration of the payload (cargo and passengers for civil aircraft) into the center section volume. Given that the size of human body (especially the height) is more or less constant across the world, the smaller the aircraft the bigger the challenge, since it requires aerodynamic profiles of bigger relative thickness when the aircraft is shorter. Typical relative thicknesses of 16–18 % are commonly used for the aerodynamic profiles of the BWB center section. For this reason, as will be explained in Chap. 2, an aircraft capacity of 450 passengers was considered for the ACFA project in order to stay within reasonable limit in terms of integration for the cabin and cargo compartment.

1.5 Recent European Research Activity on the BWB

D. Paulus and T. Salmon

In aerospace history, since Lilienthal's bird flight experiments, many unconventional aircraft have been studied, developed, and sometimes flown, often as an answer to contradictory or extreme requirements [81]. Flying wing configurations can be traced

back to Hugo Junkers' J1000. A comprehensive overview, from the 1930s and the Horten brothers to the current experimental configurations, is given in [90].

Recent progress in design methods and especially computational power has enabled the development of unconventional aircraft with greater precision than ever before. To achieve sustainable growth in the future, for example, coping with an increasing demand while lowering the energy and ecological footprint, the flying wing configuration seems to be a very interesting option that is very fuel efficient and particularly suited for large capacity.

In Europe growing attention from the aerospace industry and academia has been focused on dedicated aspects of the development of civil commercial blended wing body configurations. The aircraft configuration models used for such activity have changed and evolved over several research programs as shown later in this chapter.

This aim of this research activity has primarily been to:

- Improve the understanding of such unconventional configurations and identify their potential, in particular in the context of civil air transport
- Identify risks and challenges of the BWB concept and propose ways to overcome them
- Improve the design method and tools necessary to design and develop such configurations.

The challenges are numerous and research programs have tried to tackle most of them. A non-exhaustive list of topics to address are:

- Evacuation scenarios
- Ground handling
- Aerodynamic load distribution to cope with highly loaded outer wing, desired pitching moment characteristics and very thick central profiles
- Potentially higher approach speeds (due to the absence of a high-lift leading edge device and to the compromise to be made on the wing trailing edge movables between control, trim, high-lift, and load alleviation functions)
- Rotation at take-off
- Short moment arm for movables and control surfaces that represent a challenge for stability and control, both longitudinal and laterally
- Structural arrangement for non-cylindrical cabin compartment and innovative ways to deal with large composite elements
- Passenger comfort
- Passenger acceptance
- Compliance with certification requirements (for instance, relaxed stability criteria in regards to advance control and actuator technology may be an option to realize the full aerodynamic potential of such configuration)
- Flutter behavior (especially if large winglets are used for lateral control)
- Scarce data either from testing or flight tests
- Current design methods widely based on conventional tube-and-wing aircraft configurations and only partially transferable to BWB aircraft.

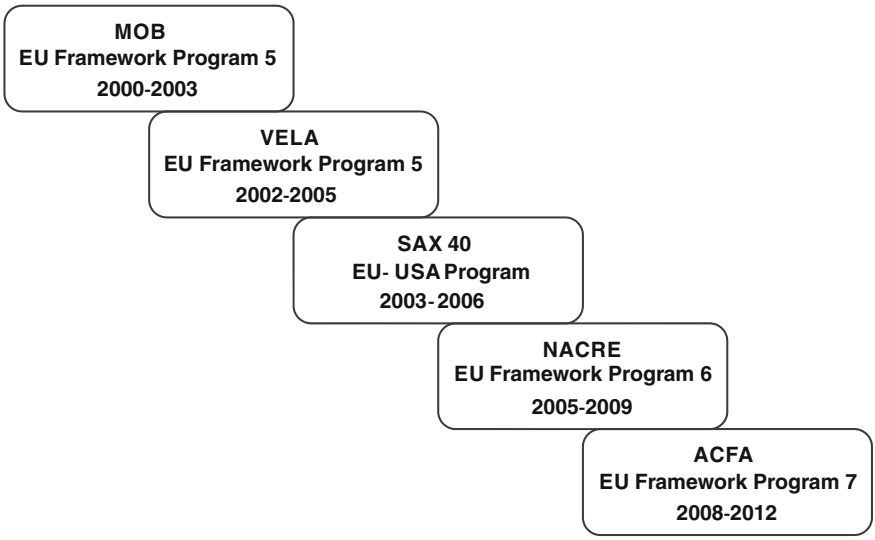

Fig. 1.1 European research programs 2000–2012

Hence, the last decade saw five BWB-related research programs in Europe as shown in Fig. 1.1:

- Multidisciplinary Optimization of a Blended Wing Body (MOB)
- Very Efficient Large Aircraft (VELA)
- New Aircraft Concepts Research (NACRE)
- Active Control for Flexible Aircraft (ACFA 2020)
- Silent Aircraft Initiative with the latest SAX-40 design (University of Cambridge and Massachusetts Institute of Technology collaboration).

Every research project in Fig. 1.1 is dedicated to the concept of BWB aircraft. In the MOB project, the goal was to build a preliminary design model with a multidisciplinary approach. The methods applied were considered best practice at the time and comprised in-house as well as commercially available solutions. The result is the Computational Design Engine (CDE) which was applied to BWB configuration [59].

The VELA (Fig. 1.2) project was focused on a very high capacity aircraft. The findings showed few problems in stability and control. It estimated a saving potential of nearly 10 % in mass and 4–8 % in aerodynamics. The identification of the limited availability of computation and simulation methods was another key finding. The aerodynamic optimization was conducted mainly for the cruise phase [21].

The NACRE configuration (Fig. 1.3) followed VELA from 2005 to 2010. The focus was placed on environmental friendliness and passenger comfort. Among the topics addressed were the propulsion integration aft of the center of gravity, the laminar wing, and the demonstration of passenger evacuation.

Fig. 1.2 VELA BWB configuration (© VELA consortium)

The Silent aircraft initiative, a joint European and American cooperation launched in 2003, has been undertaken to finds ways to dramatically reduce aircraft noise. Several technologies were studied, including BWB configurations with buried top-mounted engines. The SAX-40 (Silent Aircraft eXperimental, Fig. 1.4), was one of aircraft designs that came out of this program [38].

The latest European Commission funded project was Active Control for Flexible Aircraft (ACFA) 2020 from 2008 to 2012 which mainly focused on the BWB configuration. The configuration carries 450 passengers with a highly swept back center

Fig. 1.3 NACRE configuration (© NACRE consortium)

Fig. 1.4 The SAX-40 BWB configuration (© Silent aircraft consortium)

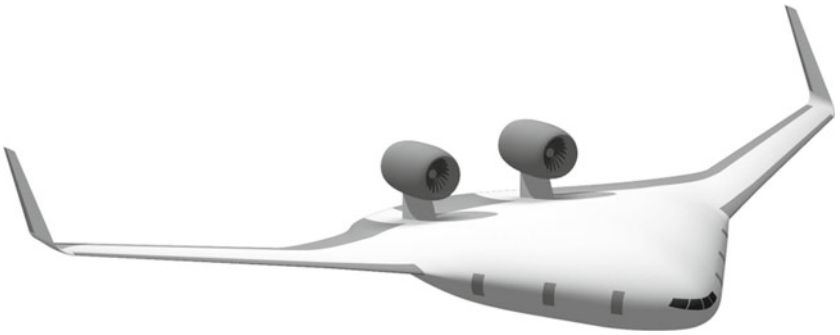

Fig. 1.5 The ACFA BWB configuration (© ACFA consortium)

part wing and two podded turbofan engines (Fig. 1.5). The engines are positioned aft on the center part of the wing. It targeted the reduction of structural loads and the improvement of ride comfort by actively controlling the aircraft throughout the mission with effective control algorithms [55].

1.6 Recent Developments in Aircraft Conceptual Design Modeling and Simulation Methods

M. Hornung, D. Paulus, C. Rößler, F. Stroscher, T. Salmon and A. Seitz

This section introduces the state of the art in aircraft design modeling techniques which is not necessarily limited to BWB aircraft and thus can be applied to any new design.

1.6.1 Overall Design

Aircraft conceptual design is the first step in designing a new aircraft. Starting from a set of requirements, different configurations are studied, including the sizing of major

components, such as fuselage, wings, tails, and power plant up to performance and cost analyses. The goal is to determine if an aircraft can in principle be built that meets the requirements and, if so, what the most suitable configuration is. After the conceptual design, the selected configuration is matured during the preliminary design phase, followed by the development and detailed design, resulting in all necessary data to start the production of the new aircraft.

Simple and time efficient methods must be used in the conceptual design phase where many configurations are investigated. The classical, academic approach is a combination of empirical and simple analytical equations summarized in aircraft design books (for example [78, 82, 89, 96]). Aircraft design is an iterative process, going through the different disciplines, such as propulsion, aerodynamics, structure and weights, and optimizing parameters until a feasible configuration is found and all requirements are met. Hence, the described handbook methods are automated with the help of computer programs. To name one, Advanced Aircraft Analysis (AAA) [18] is such tool to size or re-engineer existing airplanes. Its methods are based on Jan Roskam's eight-volume work "Airplane design" [82] and on one of his publications on flight mechanics [80]. Another example is Raymer Design Software (RDS) [79]. This aircraft design program is based on the book "Aircraft Design: A Conceptual Approach" [78]. As is the case in AAA, the engineer can change the design parameters after each iteration in RDS. Additionally, RDS includes an optimization algorithm to optimize up to six parameters (thrust/weight ratio (T/W ratio), wing loading, aspect ratio, taper ratio, sweep, and wing airfoil thickness). The result can be graphically illustrated as a Pareto frontier.

The challenge is to find the global optimum because there are many contradicting disciplines in aircraft design. A small sacrifice in one area could gain huge advantages in another area, leading to an overall improved solution. Furthermore, increasing complexity and technologies interacting in a way that prevent each of them from being handled separately requires an integrated design and optimization approach which handles the various disciplines simultaneously. This enables finding a globally optimal design, which may not be obtained when the disciplines are handled sequentially. To overcome these challenges, new aircraft design methods must be applied. A recent field is multidisciplinary design optimization (MDO). A brief overview of MDO methods can be found in literature [4, 92]. This approach is, for example, used in a design method developed by ONERA [19].

While classical configurations can be handled well with the empirics-based handbook methods, more universal methods are necessary for new configurations due to the lack of an empirical database. With increasing computational power, methods based on underlying fundamental physics can be used, allowing more accurate performance predictions for new technologies and new aircraft configurations. One example is PrADO (Preliminary Aircraft Design Optimization), which has been developed at Technical University of Braunschweig [37]. It features over 50 analysis modules with different methods, depending on the required level of detail and aircraft configuration. Another example is a conceptual design method for small electric UAV developed at Technical University of Munich [83] which again requires a different

approach in weight estimation and aerodynamics compared to larger aircraft at higher speeds.

The increasing complexity of aircraft design projects and the globalization of the industry led to a distribution of system design among various research centers located in different countries. Hence the data exchange between the teams becomes a crucial point in the design process. Therefore, the German Aerospace Center (DLR) has developed a new data exchange file format called Common Parametric Aircraft Configuration Schema (CPACS) [53]. CPACS is XML-based and contains data of aircraft, rotorcraft, engines, climate impact, fleets, and missions. Process information is also stored in CPACS. It is, therefore, a common language between the disciplinary analysis tools and a driver for multidisciplinary and multi-fidelity design in distributed environments. In the same context, DLR developed an integrated framework called RCE which allows the user to couple the individual tools to multidisciplinary process chains for analysis and optimization tasks [53]. Using the combination of CPACS and RCE, individual process chains can be created and used to evaluate the impact of new technologies. Similar to the CPACS/RCE approach, Bauhaus Luftfahrt is developing OpenCDT (Conceptual Design Tool). It includes integrated data management, as well as organizational aspects of an MDO process. The vision of OpenCDT is to provide a framework for conceptual aircraft design that enables the integration of design data and functionality from existing software tools, that it supports the collaboration between discipline teams, and that it is flexible enough to be adapted for designing unconventional aircraft concepts [64].

1.6.2 Propulsion

Propulsion modeling is carried out to optimize engine performance and its integration into the airframe. The ACFA project applied a non-disclosable generic engine model and used the Gasturb Software [30]. Reference [84, pp. 11–13] has combined the Gasturb software with an aircraft design framework and in his thesis has summarized the state of the art in propulsion modeling: In the United States of America, "the methodological contributions published, mainly employed shared solutions for the disciplinary analyses, such as the FLight OPtimization System (FLOPS) [56], the Weight Analysis of Turbine Engines (WATE) code [63], and the NASA Engine Performance Program (NEPP) [74]. Connecting these codes, the Integrated Propulsion/Airframe Analysis System (IPAS) [50] was introduced in 1992. IPAS allows for a concurrent optimization of engine and airframe design parameters and was demonstrated for the high-speed aircraft design case [50]. […] The design code integration framework COMETSBOARD [34] was introduced as an optimization engine for multidisciplinary aircraft and propulsion system design tasks [69–73]." Also [Geiselhardt] created an "engine cycle and aircraft configuration optimization […] for supersonic civil transport application [31]. […] A survey of distinguished propulsion system simulation software may be found in [91]. The overview includes proprietary ("in-house") as well as commercially available software solutions" [84, pp. 11–13].

In Europe, the German Aerospace Center (DLR) not only works on an integrated aircraft design framework but also on "the integration of engine preliminary design into the overall aircraft design process […with the] Technology Integration for the Virtual Aircraft (TIVA) [54]. […] Initiated as part of the VITAL project and further developed within the NEWAC project [99], the tool TERA (Techno-economic and Environmental Risk Assessment) targets a multidisciplinary engine assessment of environmental impact and cost of ownership [62]. […] TERA includes modules for aircraft and engine performance, engine weights, economics, environment, noise, and emissions. For engine performance considerations, Cranfield University's in-house code TURBOMATCH [67] is used. Aircraft performance is simulated using the HERMES code, which computes typical performance characteristics for given aircraft geometry, weight information, and mission profile ownership [62]. Here, calculations are based upon handbook methods according to Jenkinson [43]. Engine operational characteristics are provided by TURBOMATCH [22]. A corresponding flow chart is given in [22]. The modules of the TERA framework are embedded in an ISight [86] workflow scheme [13]. (Further reading is recommended in [68, 76] and [22].) […] A most recent overview of TERA capabilities is given in [49, 51]" [84, pp. 11–13].

1.6.3 Aerodynamics

The principal goal of any aerodynamic modeling effort is the determination of the forces and moments in this case generated by the airframe, that is, its wings, control surfaces, and components. Generally, the modeling approaches are of different accuracy in that they make use of permissible simplifications to reduce complexity or to shorten computation time. The highest complexity does not necessarily produce the most accurate results. A large existing database can produce equally satisfying results depending on the configuration. Further reading is recommended in [7] or [45]. The most dominant effects reflected in the different methods comprise the flow characterization (that is, laminar (potential) or turbulent), the consideration of the boundary layer (inviscid or viscous calculations) and the flow speed (subsonic, transonic, hypersonic), also divided into compressible, or incompressible flow. Only methods of highest accuracy will be capable of dealing with all effects of flow. Since high-accuracy methods often demand high computational resources and substantial preparation effort, the conceptual design relies on simplified approaches to obtain results rapidly and to enable iterations. The following listing provides an introduction of commonly used computational methods for aerodynamic forces and moments of an aircraft.

1.6.3.1 Approximation Methods

The wing is one of the most important components to evaluate lift, drag, and moment characteristics. It is usually divided into section cuts for which the pressure

distribution (c_p) is solved, either by mathematical functions based on the geometry or by existing computation programs requiring only the most crucial parameters as input. This enables the deduction of 2D forces and moments of the airfoil and is then integrated over the y-axis (lateral direction) over the entire span for a 3D solution. For conventional tube-and-wing aircraft configuration and some selected unconventional (for example, delta) configurations, preliminary estimates for the entire aircraft can be drawn from handbook approaches such as [78] or [29]. Software tools for the 2D airfoil to the isolated, yet dominating wing of the aircraft are XFoil [24] for 2D airfoils and XFLR5 which is an extended version incorporating solutions for 3D wing layouts. Panel methods are frequently used in aircraft design. They divide the geometric shape into trapezoidal elements with differing length and width from which an averaged pressure is calculated and transferred (for example, as downwash) at reference points to the next panel until the pressure distribution over the entire span is integrated. The differences within the panel methods exist based on whether the pressure is averaged or concentrated on the 25 % line. Potential (irrotational) and incompressible flows are the prerequisites for these approaches. A combination of sources, sinks, doublets, and a vortex line, is added and combined to represent the flow field [7]. This is also known as the vortex lattice method. Panel division and calculation of the forces and moments for thin airfoils and small angles of attack are satisfactory for most applications. Viscous or inviscid calculation approaches may be selected by the user. Prominent software examples are [9, 93] or [94]. The former two are (extended) vortex lattice methods for linear aerodynamic wing design applications and the latter offers the choice of using the lifting line theory, the vortex lattice method, or a 3D panel method. The PAWAT software implements an extension to the lifting line theory to account for the effects of integrating a propeller propulsion system and the influence of multiple wings' interaction [87]. The following section illustrates the theory behind the software [87]: "The lifting-line method in this is based on [40] […which] enables the method to be used for systems of lifting surfaces with arbitrary camber, sweep, and dihedral. Further the method is able to account for nonlinear airfoil data by solving a nonlinear system of equations. The aerodynamics of a lifting surface is synthesized using a composite of horseshoe-shaped vortices, which model the distribution of bound vorticity over the surface of the wing and the distribution of free vorticity in the trailing vortex sheet in a discrete way. The bound portion of each horseshoe vortex is placed coincident with the wing quarter chord line. The trailing vortices are aligned either to the free stream velocity or to the local flow velocity. The trailing vortices may be modeled to follow the wing surface (including a flap deflection) and leave the wing at the trailing edge […]." A propeller and slipstream model is used to superimpose the wing aerodynamics. "The propeller model is based on a blade element approach, i.e., the propeller blades are radially divided into blade elements. Additionally, the propeller is modeled by a number of azimuthal blade positions to account for non-axial flow conditions and periodical geometry changes like blade flapping and blade pitching. […] Different models have been implemented to calculate the self-induced velocity at the propeller blades: (i) simple momentum theory as in [23] with no radial variation of self-induced velocity, (ii) blade element momentum theory as in [44], (iii) [39] to compute axial and

tangential induced velocities. […] The lifting surface and propeller aerodynamics are coupled by calculating the system in an iterative way […] based on the resulting induced velocities" [87].

1.6.3.2 Higher Accuracy Methods

Methods of higher accuracy are usually of numerical origin. They very accurately solve the flow field around an aircraft at discrete points because the modeling approach theoretically reflects all complex flow effects, such as turbulence, friction, or compressibility. They require mesh generation, which is often coupled to a CAD system, preprocessing where the flow conditions are set up and solving and post-processing to extract the forces and moments from the modeling of the flow problem. The effort required for the modeling process is large despite the fact that research has greatly progressed over the last decade. It is possible to couple structural and aerodynamic effects. The aerodynamic theory is the computational fluid dynamics (CFD) approach as described in many textbooks, such as in [6]. Different levels of accuracy dominate. The highest accuracy is reached by solving the Navier-Stokes equations; however the frictionless Euler equations or the Reynolds-averaged Navier-Stokes (RANS) equations are often employed. The latter equations consider friction in the boundary layer and are solved in combination with one or more models of the turbulence. Although the mathematical formulation with the Navier-Stokes equations is physically comprehensive, the simplified RANS equations are more often used, since the computation time for direct numerical simulation (DNS) can easily take months. Structured or unstructured meshes are mostly built manually to solve the discretized flow control volume, and the flow physics are then solved at each of the points (knots) in that mesh with an appropriate solver. This requires strong computational resources, especially in three-dimensional analysis. The latest research applications make use of automatic mesh generation and dynamic mesh adaption for which many publications exist, for example, [100]. CFD used to be employed in the later, more detailed phases of the development. However, for complex flow phenomena, or in the absence of test facilities, its use in predesign becomes more frequent. A topic of growing importance for preliminary design is finding the optimal trade-off between fast, lightweight methods on one side and strong, time-consuming, and expectedly highly accurate CFD simulation on the other side. The results of the analysis process, if conducted by skilled experts, are often excellent for lift and momentum predictions and agree well with test data. Drag predictions rely on the boundary layer and turbulence modeling and often remain less accurate with fully turbulent RANS computations. Prominent software in the research and development environment are VS Aero, Ansys, elsA, and the TAU code. VS Aero [97] is reduced in modeling complexity to enable rapid result generation. Comprehensive CFD software packages, including structural and thermal interaction on the commercial side are Ansys with its modules, CFX and Fluent [8], and the academic software TAU [10] by the German Aerospace Center (DLR) and elsA [5] by the French Aerospace Center ONERA.

1.7 Flight Control Design

M. Kozek and A. Schirrer

The general development of ever more lightweight structures in aircraft and the availability of first analog and then powerful digital computers led to an increased prevalence of active flight control system (FCS). It is important to note that active FCS cannot be simply added to existing aircraft concepts—instead, an integrated approach becomes necessary: The whole loop with sensors, on-board computers, pilot controls, electromechanic or electrohydraulic actuators, and aerodynamic controls needs to be optimized together with the aeroelastic (and possibly flexible) structure of the aircraft. A beneficial, deep integration of active FCS therefore requires its consideration already during early design stages.

1.7.1 General Goals

One main focus of most active FCS is to provide an automatic system aimed at reducing structural loads. This so-called load alleviation system (LAS) typically incorporates systems for gust and/or maneuver load control. In high-performance aircraft (such as fighter planes or unmanned air vehicles) ride comfort is not a concern and maneuver load is usually the only design criterion. In passenger aircraft, however, mainly gust-alleviation is the critical sizing load, but active suppression of wing bending modes and maneuver load alleviation may additionally be considered. One of the main features of such systems is the reduction of the bending moment augmentation near the wing root during steady and unsteady maneuvers. This reduction can be utilized to allow for more lightweight structures and consequently be mapped into benefits such as improved payload, extended structural life, and higher fuel efficiency. Note that certification requirements pose a considerable challenge for active FCS in general and LAS more specifically. In principle, the in-flight availability of the LAS system must be sufficient to assure the same level of safety as in conventional aircraft. This is especially true for civil aircraft; in military aircraft these requirements may be considerably relaxed. Total cost (including design cost, indirect, and direct operating costs) may be increased to a point where utilization of such a system becomes economically unattractive.

The other main focus of an active FCS is to imprint predefined flight dynamics to a new aircraft. Here, mainly the existing flight dynamics of classical passenger aircraft without active FCS are considered as desirable closed-loop characteristics for a modern civil aircraft equipped with active FCS. It is therefore possible to guarantee similar flight behavior of different aircraft (size, payload, propulsion) within certain margins. This is especially important for aircraft with unconventional open-loop flight dynamics or even unstable behavior. The result of a well-designed active FCS is in all these cases to provide a familiar flight behavior and good handling qualities for the pilot.

1.7.2 Loads Alleviation

Beginning in the 1970s publications on the implementation of active FCS in both military and civil aircraft have emerged. Most of them focus on conventional passenger aircraft, fighter planes, or unmanned air vehicles; only a few publications deal with BWB configurations.

One of the early works on LAS was conducted at NASA under the SST Program [75] where a considerable weight reduction was reported for the NASA SCAT-15F concept based on a reduction of the wing root bending moment by 5–9 %. As early as 1978, this LAS allowed for more lightweight structures, leading to a reduced fuel consumption and extended fatigue life [48]. A saving of 2–3 % in operational costs was estimated from a 15 % weight reduction. For the Lockheed C-5A, a specific LAS was designed to reduce both maneuver and gust-induced wing bending moments [20]. The fully automatic LAS was developed, tested in-flight, and finally incorporated in the aircraft. This so-called active lift distribution control system achieved a reduction in relevant wing stresses by 20–30 % resulting in a life improvement factor of 1.25.

NASA conducted a project from 1977 to 1979 [60] which reported that a weight reduction of 2.5 % of the wing structural box is possible from adding an LAS for bending moment alleviation. Also beginning at the end of the 1970s was the development of an LAS for the long-range version of Lockheed's L-1011 Tristar. It became possible to increase the wing span length without increasing weight due to structural savings. With increased wing span and the resulting higher wing aspect ratio (meaning less induced drag), fuel consumption was reduced. The details of this project can be found in [11, 61, 77].

Another project by NASA early in the 1990s focused on the F-111A fighter-bomber aircraft [95]. An automated LAS was implemented and tested where flap deflections were controlled according to flap position, true air speed, Mach number, dynamic pressure, normal acceleration, and wing sweep position. An increase of more than 1 g in load factor was reported without the need for structural re-enforcements due to constant wing bending moments.

An interesting extension has been presented in [16]: The authors present a method for a robust damage-mitigating control. They add a fatigue crack model to the aeroservoelastic model of the aircraft to come up with an integrated control scheme. This approach targets the fatigue problem most specifically, and an early consideration during the design process is advised by the authors.

More recent publications focus on the active damping of wing bending modes, thus alleviating structural fatigue loads but also lowering pitch attitude variation and vertical accelerations in the cabin [35, 58, 98]. These are important results because the single goal of comfort enhancement for gust load alleviation may lead to an undesired increase of structural loads [36]. For an unmanned air vehicle with joined-wing configuration, an LAS is presented in [66]. The load reduction is achieved by rearranging the aerodynamic loads (symmetrical actuation of the ailerons), but the vertical load factor is kept constant. In [65], the application of a similar LAS for an

EASA CS-25 business aircraft is given. The author reports an increase in fatigue life of up to 67.5 % at the wing root.

1.7.3 Handling Qualities

As mentioned before, the active FCS should also provide a desirable flight behavior and good handling qualities for the pilot. Historically, these design goals have already been achieved with analog equipment several decades ago (for example, [32, 46]). Since the 1970s, textbooks covering the state of the art of their respective times have been available [57, 80]. Excellent sources for today's rich material on that topic are the textbooks [14, 88]. Any active FCS must explicitly consider both the actual open-loop flight dynamics, the desired closed-loop dynamics, as well as the existing control surface configuration. While the desired closed-loop characteristics are always similar (and represent a well-behaved classical aircraft of the respective type), both, open-loop dynamics and control surfaces heavily depend on the specific aircraft configuration. Especially for the BWB configuration the latter characteristics are quite unconventional and challenging. The actual level of improvement achieved by active control concepts applied to BWB-type configurations is a hardly investigated research topic so far. Consequently, in the ACFA 2020 project the system's aeroelastic properties with respect to modern control design methodologies have been investigated. Thereby, the potential in structural load reduction, improvement of ride comfort, and attainable handling qualities were main drivers.

1.7.4 ACFA 2020 Control Design Challenges

It is important to note that modern conventional aircraft designs could in many cases still be operated by a pilot without an active FCS since the dynamic behavior of such a design is quite generic. Although individual gains of the pilot controls and the related time constants may differ considerably, typical modes can be expected. In the case of the ACFA BWB design, this is no longer true. The open-loop aircraft dynamics are unstable in usually stable modes, and most dynamic characteristics are completely different from conventional designs. A suitable active FCS is therefore an integral part of the aircraft design and faces entirely new challenges in terms of the unconventional open-loop system dynamics.

A general control structure is presented in Fig. 1.6 where the overall active control concept is schematically decomposed into three parts:

Feedback control (*FBC*). Relevant flight mechanic data and measurements reflecting aeroelastic dynamical behavior are utilized to improve and unify the aircraft dynamics with respect to pilot needs over the flight envelope and to reduce the effect of unmeasurable disturbances.

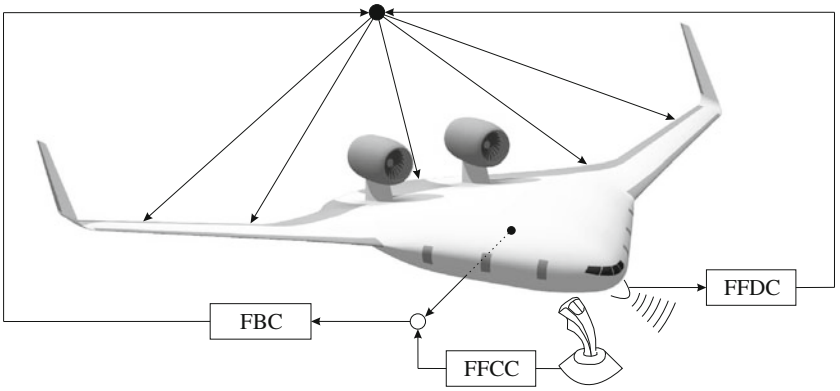

Fig. 1.6 BWB aircraft configuration and schematic of an active control concept [55]

Feed-forward command control (*FFCC*). The desired pilot command is transformed into control surface commands in an optimized manner with respect to handling qualities, limited control effort, and reduced maneuver-induced structural loads.
Feed-forward disturbance control (*FFDC*). A priori knowledge of disturbances provided by adequate measurements is utilized to act early on the control surfaces, again in an optimized way to reduce disturbance-induced structural loads and vibration‘s as well as to improve ride comfort.

For all three control tasks, a variety of control concepts can be utilized, including robust design, parameter-dependent and scheduled control, adaptive control, or a mixture of these.

References

1. Aerospace and Defence Industries Association of Europe ASD (2014) About ACARE. http://www.acare4europe.com/about-acare
2. Aerospace and Defence Industries Association of Europe ASD (2014) Latest ACARE documents. http://www.acare4europe.com/documents/latest-acare-documents
3. AIRBUS (2012) Global market forecast 2012–2031. http://www.airbus.com/company/market/forecast/
4. Alexandrov V, Hussaini M (2000) Multidisciplinary design optimization: state of the art. In: 8th AIAA/UASAF/NASA/ISSMO symposium on multidisciplinary analysis and optimization, Long Beach
5. An overview of the multi-purpose elsA flow solver (2013) http://www.aerospacelab-journal.org/fr/panorama-general-logiciel-elsA
6. Anderson JD (1995) Computational fluid dynamic. McGraw-Hill, New York
7. Anderson JD (2007) Fundamentals of aerodynamics. McGraw-Hill, New York
8. ANSYS Inc. (2013) Ansys CFX and fluent software. http://www.ansys.com/Products/Simulation+Technology/Fluid+Dynamics

9. ANSYS Inc. (2013) The AVL software. http://web.mit.edu/drela/Public/web/avl/
10. ANSYS Inc. (2013) The TAU code. http://tau.dlr.de/startseite/
11. Bendixen GE, O'Connell RF, Siegert CD (1981) Digital active control system for load alleviation for the lockheed L-1011. Aeronaut J 86(849):430–436
12. BOEING (2012) Current market outlook 2012–2031. http://www.boeing.com/boeing/commercial/cmo/
13. Bretschneider S, Arago O, Staudacher S (2007) Architecture of a techno and environmental risk assessment tool using a multi-modular build approach. In: 18th international symposium on air-breathing engines, Beijing. ISABE-2007-1103
14. Brockhaus R (2001) Flugregelung (Flight Control). Springer, Heidelberg
15. Buttazzo G, Frediani A (2012) Variational analysis and aerospace engineering: mathematical challenges for aerospace design. Springer, Germany
16. Caplin J, Ray A, Joshi S (2001) Damage-mitigating control of aircraft for enhanced structural durability. IEEE Trans Aerosp Electron Syst 37(3):849–862
17. Clean sky JU (2014) Clean sky 2. http://www.cleansky.eu/. Accessed 8 July 2014
18. DARcorporation (2013) Advanced aircraft analysis. http://www.darcorp.com/Software/AAA/
19. Defoort S, Balesdent M, Klotz P, Schmollgruber P, Morio J, Hermetz J, Blondeau C, Carrier G, Bérend N (2012) Multidisciplinary aerospace system design: principles, issues and onera experience. J Aerosp Lab AL04-12(4)
20. Disney TE (1977) C5-A active load alleviation system. J Spacecr 14(2):81–86
21. DLR (2011) Das VELA-Projekt (the vela project). http://www.dlr.de/as/Portaldata/5/Resources/dokumente/projekte/vela/The_VELA_Project.pdf
22. Doulgeris G (2008) Modelling & integration of advanced propulsion systems. PhD thesis, School of Engineering, Cranfield University
23. Dreier ME (2007) Introduction to helicopter and tiltrotor flight simulation. American Institute of Aeronautics and Astronautics, Reston
24. Drela M (2007) The XFOIL program. http://web.mit.edu/drela/Public/web/xfoil/
25. European Commission (2014) Flying high with innovative aircraft concepts. http://ec.europa.eu/research/research-for-europe/transport-nacre_en.html
26. European Commission (2014) Horizon 2020—the EU framework programme for research and innovation. http://ec.europa.eu/programmes/horizon2020/
27. European Commission and Directorate-General for Research and Innovation (2001) European aeronautics: a vision for 2020. Office for official publications of the European communities, Luxembourg
28. European Commission, Directorate-General for Research and Innovation, and Directorate-General for Mobility and Transport (2011) Flightpath 2050: Europe's vision for aviation: maintaining global leadership and serving society's needs. Publications office of the European union, Luxembourg
29. Finck RD, Hoak DE (1978) USAF stability and control Datcom. Technical report, flight control division, air force dynamics laboratory, wright-patterson air force base
30. GasTurb GmbH (2013) GasTurb 12. http://www.gasturb.de/. Accessed 8 July 2014
31. Geiselhart K (1994) A technique for integration engine cycle and aircraft configuration optimization. Technical report, lockheed engineering & sciences company, Hampton, Virginia, NASA-CR-191602
32. Goldsmith HA (1964) Stability and control of supersonic aircraft at low speeds. In: 4th ICAS congress, Paris, France
33. Graham WR, Hall CA, Vear Morales M (2014) The potential of future aircraft technology for noise and pollutant emissions reduction. Transport Policy (in press)
34. Guptill J, Coroneos R, Patnaik S, Hopkins D, Berke L (1996) Cometboards users manual, release 1.0. Technical report, Lewis Research Center, Cleveland, Ohio. NASA Technical Memorandum, NASA-TM-4537
35. Hahn K-U, Koenig R (1992) ATTAS flight test and simulation results of the advanced gust management system LARS. In: AIAA atmospheric flight mechanics conference, Hilton Head Island

36. Hecker S, Hahn K-U (2007) Advanced gust load alleviation system for large flexible aircraft. In: 1st CEAS European air & space conference, Berlin
37. Heinze W, Österheld CM, Horst P (2001) Multidisziplinäres Flugzeugentwurfsverfahren PrADO—Programmentwurf und Anwendung im Rahmen von Flugzeug-Konzeptstudien (Multidisciplinary aircraft design method PrADO—program design and application in aircraft concept studies). In: Jahrbuch der DGLR-Jahrestagung 2001, Hamburg
38. Hileman J, Spakovszky Z, Drela M, Sargeant M (2007) Airframe design for "Silent Aircraft". In: 45th AIAA aerospace sciences meeting and exhibit, Reno, Nevada
39. Hunsaker DF (2007) A numerical blade element approach to estimating propeller flowfields. In: Proceedings of the AIAA aerospace sciences meeting and exhibit, Reno, Nevada
40. Hunsaker DF, Snyder D (2006) A lifting-line approach to estimating propeller/wing interactions. In: Proceedings of the 24th applied aerodynamics conference, San Francisco
41. IST World (2014) Aircraft wing advanced technology operations (AWIATOR). http://www.ist-world.org/ProjectDetails.aspx?ProjectId=db962e43efb743e6968bc0430a00b4c1&SourceDatabaseId=9cd97ac2e51045e39c2ad6b86dce1ac2
42. IST World (2014) Very efficient large aircraft (VELA). http://www.ist-world.org/ProjectDetails.aspx?ProjectId=bc5fe779da034fe4926c266e1c644b66&SourceDatabaseId=9cd97ac2e51045e39c2ad6b86dce1ac2
43. Jenkinson L, Simpkin P, Rhodes D (1999) Civil jet aircraft design. AIAA Education Series. Elsevier, Amsterdam
44. Johnson W (1980) Helicopter theory. Dover, New York
45. Katz J, Plotkin A (2001) Low-speed aerodynamics. Cambridge University, Cambridge
46. Kehrer WT (1964) Longitudinal stability and control of large supersonic aircraft at low speeds. In: 4th ICAS congress, Paris, France
47. Kordt M (2008) Multi objective dynamic aircraft synthesis—MODYAS. Airbus deutschland GmbH
48. Kurzhals PR (1978) Active controls in aircraft design. Executive summary. In: FMP symposium on stability and control, Ottawa
49. Kyprianidis K, Lehmayr B, Alexiou A, Xu L (2010) TERA2020—rationale, objectives and design algorithm. In: European workshop on new aero engine concepts, Munich
50. Lavelle T, Plencner R, Seidel J (1992) Concurrent optimization of airframe and engine design parameters. In: 4th symposium on multidisciplinary analysis and optimization cosponsored by the AIAA, USAF, NASA, and OAI, Cleveland, Ohio, Sept 1992. AIAA-92-4713
51. Lehmayr B, Kyprianidis K, Alexiou A, Xu L (2010) TERA2020 optimization of new AC configurations. In: European workshop on new aero engine concepts, Munich
52. Liebeck RH (2002) Design of the blended-wing-body subsonic transport. In: 40th AIAA aerospace sciences meeting and exhibit, Reno, Nevada
53. Liersch CM, Hepperle M (2011) A distributed toolbox for multidisciplinary preliminary aircraft design. In: 60th Deutscher Luft- und Raumfahrtkongress 2011, Bremen, Germany, Sept 2011
54. Liersch C, Hepperle M (2009) A unified approach for multidisciplinary preliminary aircraft design. In: 2nd CEAS European air and space conference, Manchester, Oct 2009
55. Maier R (2014) ACFA 2020 project. http://www.acfa2020.eu/index.html. Accessed 8 July 2014
56. McCullers L (1984) Aircraft configuration optimization including optimized flight profiles. In: Recent experiences in multidisciplinary analysis and optimization, proceedings of a symposium held at NASA langley research center, Hampton, Virginia, April 1984. NASA Conference Publication 2327, Part 1, pp 395–412
57. McRuer D, Ashkenas I, Graham D (1973) Aircraft dynamics and automatic control. Princeton University, Princeton
58. Merat R (2008) Study of a direct lift control system based on the A380 aircraft. In: 46th AIAA aerospace sciences meeting and exhibit, Reno, Nevada, 2008
59. Morris A, Arendsen P, Larocca G, Laban M, Voss R, Hönlinger H (2004) MOB—a European project on multidisciplinary design optimization. In: 24th international congress of the aeronautical sciences, Yokohama

60. NASA contractor report 3164 (1980) Selected advanced aerodynamics and active control technology concepts development on a derivative B-747 aircraft, 1980. NASA langley research center under contract NAS1-14741 with the Boeing commercial airplan company
61. O'Connell RF (1980) Design, development, and implementation of an active control system for load alleviation for a commercial transport airplane. AGARD-R-683
62. Ogaji S, Pilidis P, Hales R (2007) TERA—a tool for aero-engine modelling and management. In: 2nd world congress on engineering asset management and the 4th international conference on condition monitoring, Harrogate
63. Onat E, Klees G (1979) A method to estimate weight and dimensions of large and small gas turbine engines. Technical report, Boeing military airplane development, Seattle, Washington. Technical report, NASA-CR-199481
64. OpenCDT website (2014) www.opencdt.org. Accessed 30 June 2014
65. Paletta N (2011) Maneuver load controls, analysis and design for flexible aircraft. PhD thesis, University of Napoli, Italy
66. Paletta N, Belardo M, Pecora M (2010) Load alleviation on a joined-wing unmanned aircraft. J Aircr 47(6):2005–2016
67. Palmer P (1990) The turbomatch scheme for aero/industrial gas turbine engine design point/off design performance calculation. SME, thermal power group, technical report, Cranfield University
68. Pascovici D (2008) Thermo economic and risk analysis for advanced long range aero engines. PhD thesis, School of Engineering, Cranfield University
69. Patnaik S, Lavelle T, Hopkins D, Coronets R (1997) Cascade optimization strategy for aircraft and air-breathing propulsion system concepts. J Aircr 34(1):136–139
70. Patnaik S, Guptill J, Hopkins D, Lavelle T (1998) Neural network and regression approximations in high-speed civil aircraft design optimization. J Aircr 35(6):839–850
71. Patnaik S, Guptill J, Hopkins D, Lavelle T (1998) Neural network and regression approximations in high speed civil transport aircraft design optimization. Technical report, Lewis research center, Cleveland, Ohio. NASA Technical Memorandum, NASA/TM-1998-206316
72. Patnaik S, Hopkins D, Berke L (1996) A general-purpose optimization engine for multidisciplinary design applications. In: 6th symposium on multidisciplinary analysis and optimization cosponsored by AIAA, USAS, NASA, ISSO, and USAF, Bellevue, Washington, Sept 1996. AIAA-96-4163
73. Patnaik S, Lavelle T, Hopkins D, Coronets R (1996) Cascade optimization strategy for aircraft air-breathing propulsion system concepts. In: 6th symposium on multidisciplinary analysis and optimization cosponsored by AIAA, USAS, NASA, ISSO, and USAF, Bellevue, Washington, Sept 1996. AIAA-96-4145
74. Plencner R, Snyder C (1991) The navy/nasa engine program (NEPP)—a user's manual. Technical report, Lewis Research Center, Cleveland, Ohio, 1991. NASA Technical Memorandum, NASA-TM-105186
75. Pratt KG (1974) A survey of active controls benefits to supersonic transport. In: Symposium on advanced control technology, Los Angeles, California
76. Quintero V (2009) Techno-economic and environmental risk assessment of innovative propulsion systems for short-range civil aircraft. PhD thesis, School of Engineering, Cranfield University
77. Ramsey HD, Lewolt JG (1979) Design maneuver loads for an airplane with an active control system. In: AIAA 20th structures, structural dynamics, and materials conference, St. Lois, Missouri
78. Raymer DP (2006) Aircraft design: a conceptual approach, 4th edn. American Institute of Aeronautics and Astronautics, Reston
79. Raymer DP (2013) Dan raymer's aircraft design & RDS website. http://www.aircraftdesign.com/
80. Roskam J (1995) Airplane flight dynamics and automatic flight controls. DARcorporation
81. Roskam J (1998) What drives unique configurations. In: Advanced aerospace aerodynamics; proceedings of the aerospace technology conference and exposition, Anaheim, pp 1–17

82. Roskam J (2002) Airplane design. DARcorporation, Lawrence, Canada
83. Rößler C (2012) Conceptual design of unmanned aircraft with fuel cell propulsion system, 1st edn. Verlag Dr. Hut, Munich, Germany
84. Seitz A (2011) Advanced methods for propulsion system integration in aircraft conceptual design. PhD thesis, Technische Universität München, pp 11–13
85. Sesar JU (2014) SESAR from innovation to solution. http://www.sesarju.eu/
86. Simulia website (2010) http://www.simulia.com/
87. Steiner H-J, Hornung M, Baur S, Holzapfel F (2010) Modeling of propeller-wing aerodynamics for aircraft featuring large number of control devices. In: Deutscher Luft- und Raumfahrtkongress 2010, Hamburg
88. Stevens BL, Lewis FL (2003) Aircraft control and simulation. Wiley, Jersey
89. Stinton D (2001) The design of the aeroplane, 2nd edn. Blackwell Science, Malden
90. Storck R (2002) Die historische Entwicklung der Nurflügelflugzeuge der Welt (The historic development of flying wing aircraft in the World). Bernard & Graefe, Bonn
91. Technology Panel (AVT) Task Group AVT-036 (2007) Performance prediction and simulation of gas turbine engine operation for aircraft, marine, vehicular, and power generation. Technical report, NATO (North Atlantic Treaty Organisation), 2007. Final report of the RTO applied vehicle technology panel (AVT) task group TR-AVT-036
92. Tedford NP, Martins JRRA (2010) Benchmarking multidisciplinary design optimization algorithms. Optim Eng 11:159–183
93. The Tornado software (2013) http://www.redhammer.se/tornado/
94. The XFLR5 program (2013) http://www.xflr5.com/xflr5.htm
95. Thornton SV (1993) Reduction of structural loads using maneuver load control on the advanced fighter technology integration (AFTI)/F111 mission adaptive wing. In: NASA technical memorandum 4526, NASA Dryden Research Facility
96. Torenbeek E (1982) Synthesis of subsonic airplane design. Delft University, The Netherlands
97. VSAERO software (2013) http://www.ami.aero/software-computing/amis-computational-fluid-dynamics-tools/vsaero/
98. Wildschek A, Maier R, Hromčík M, Haniš T, Schirrer A, Kozek M, Westermayer C, Hemedi M (2009) Hybrid controller for gust load alleviation and ride comfort improvement using direct lift control flaps. In: 3rd European conference for aerospace sciences (EUCASS), Paris
99. Wilfert G, Sieber J, Rolt A, Baker N, Touyeras A, Colantouni S (2007) New environmental friendly aero engine core concepts. In: 18th international symposium on air-breathing engines, Bejing. ISABE-2007-1120
100. Yoo I, Lee S (2012) Reynolds-averaged Navier-Stokes computations of synthetic jet flows using deforming meshes. AIAA J 50(9):1943–1955

Part I
Aircraft Design and Modeling

Chapter 2
Conceptual Design

H. Baier, M. Hornung, B. Mohr, D. Paulus, Ö. Petersson, C. Rößler, F. Stroscher and T. Salmon

2.1 Introduction

Highly efficient future aircraft configurations are needed in order to cope with ever-growing air traffic and to sustain and improve passenger comfort and freight requirements. The configurations within the project ACFA 2020 are designed for the growing mid-range and long-haul market segments of 400 passengers and beyond. Airbus considers the biggest market share with 42 % order value from 2010 to 2029 to be taken by mid-size twin aisle aircraft. If long-range large aircraft are included, new order value rises to 60 % [4].

Two aircraft configurations were investigated in AFCA 2020. The superior design was chosen to be further analyzed. Active control was investigated as a means to increase aerodynamic efficiency and to improve ride comfort. Since active control not only directly influences the control surfaces, the conventional aircraft design process had to be adapted at an early stage of development. Tailless aircraft configurations with wing-fuselage blending potentially offer low fuel consumption, mainly achieved by drag reduction, reduced structural weight, and by the significantly lower wetted area ratio [5, 7]. Exterior noise can be minimized by an advanced high-lift system or by shielding of the engines [1]. Airframe development for a blended wing body (BWB) and a wide body configuration with carry-through wing box (CWB), as the basis for further control studies, was conducted within the first year of the project.

This chapter discusses the conceptual aircraft design and selection process of a highly efficient BWB and CWB configuration on a specified design mission. The challenges and development methods are described beginning with the requirements definition. The main body will present the results of the design process with a special

H. Baier (✉) · M. Hornung · B. Mohr · D. Paulus · Ö. Petersson · C. Rößler · F. Stroscher
Technische Universität München, Munich, Germany
e-mail: baier@tum.de

T. Salmon
Airbus Operations S.A.S., Toulouse, France

M. Kozek and A. Schirrer (eds.), *Modeling and Control for a Blended Wing Body Aircraft*,
Advances in Industrial Control, DOI 10.1007/978-3-319-10792-9_2

focus on the multidisciplinary design optimization (MDO) of the fuselage and wing box. Systematically comparing the developed configurations led to the selection of an aircraft that is most suitable for the proposed mission and further development. This chapter is adapted with slight modifications from [10].

2.2 Requirements and Mission Definition

A set of requirements for operational performance, fuel and passenger capacities was established with project partners [8]. The most relevant requirements are given in the following.

2.2.1 Operational Performance

Global requirements begin with the mission definition as shown in Table 2.1. The development focuses on a carrier design for at least 460 passengers (Pax) on a 7,200 nautical mile mission in a two-class layout. Flight altitude is 33,000 ft and higher, with a cruise Mach number of 0.85. The aircraft must be able to fly at its optimum altitude during the entire cruise phase, for which climb and buffet ceilings were defined. For slow approaches, a speed of less than 150 knots is considered to be optimal [1].

2.2.2 Passenger Cabin and Landing Gear Definition

For the BWB, the baseline layout is a two-class arrangement with a total of 470 passengers in a business class (BC)/economy class (YC) class splitting of 56/414. On the other hand, the CWB has a two-class arrangement with 464 passengers in BC/YC splitting of 60/404. For the landing gear, a wheel track of less than 16 m (International Civil Aviation Organization (ICAO) Code F) and a rotation clearance angle of greater than 11° shall be achieved.

Table 2.1 ACFA mission definition

ACFA global requirements	
Approach speed	$<$150 kt
Range	$\geq$7,200 nm
Cruise Mach number	0.85
Initial cruise altitude	$\geq$33,000 ft
Pax	$\geq$460 in two-class layout

2.2.3 Lifting Surface Requirements

New aircraft wing span is restricted to 80 m under the International Civil Aviation Organization (ICAO) Code F. Winglets for yaw control, in the event that one engine is inoperative, are an option. The leading-edge sweep angle shall be 55° for the BWB center body.

The BWB outer wing and CWB wing sweep and relative thickness need to be designed to optimize the fuel burn of the overall aircraft in an aerodynamic performance/weight trade-off. Hence, the BWB center body's maximum relative thickness should not exceed 17 %. The spanwise load distribution target in the early phase is elliptic as it has been identified as a potential optimum, since a large part of the flying wing structure is not sized by aerodynamic loading but by pressurization.

2.2.4 Fuel Capacity

Fuel capacity is set to be greater than the maximum take-off weight (MTOW) minus operating empty weight (OWE) plus 0.7 times the two-class payload. For 464 passengers and an assumed 105 kg per passenger, the payload sums up to 48,720 kg. This results in the basic fuel capacity formula (2.1):

$$m_{\text{Fuel}} > \text{MTOW} - \text{OWE} - 34{,}104\,\text{kg} \tag{2.1}$$

2.3 Design Process

This section describes the design methods and processes applied to the CWB and BWB configurations based on the preceding definition of global requirements.

2.3.1 Structural Weight

2.3.1.1 Fuselage Design

The fuselage was sized according to cabin and passenger requirements. For unconventional fuselage shapes, the methods applied for current commercial aircraft with an aft empennage are not applicable. Foregoing parametric studies of cross section with different radii and structural thickness were optimized in close cooperation with the Institute of Lightweight Structures (see Chap. 3). The cabin integration for unconventional aircraft designs revealed the necessity of using finite element (FE) models to obtain mass and center of gravity estimates for the fuselage, since

conventional statistical equations cannot be applied for the unconventional cross section. Both layouts were optimized for cross-sectional and wetted area. In addition, the provision of six exits at each side and an easy loading and unloading of the unit load devices 3 (LD) and pallets is foreseen. A cruise angle of attack of less than 3° at 1.7° can be considered as comfortable.

2.3.1.2 Wing

The Luftfahrttechnisches Handbuch (engl. Aviation Technology Handbook) (LTH), a German aerospace publication for civil and military aircraft applications [2], was used for BWB and CWB wing weight calculations and also applied for the slats, flaps, and ailerons including paint. After the establishment of the FE model, wing weight calculations were compared with the analytical model and FE results were used for a more detailed concept development.

2.3.1.3 Conventional Structural Elements

The weights of the structural elements which do not significantly differ from conventional design were computed from the LTH [2]. The results were either directly calculated or validated with published data. As mentioned above, the fuselage primary structure was designed with a FE model. Secondary structure elements, such as cabin and cargo floors, doors, landing gear (main/front), cockpit and cabin windows, horizontal and vertical stabilizers, engines including the controls, subsystems, oxygen, and deicing systems, were also calculated according to the LTH [2]. Further systems in this calculation included communication, electric wiring, furnishing, water installation, and operator items.

2.3.2 Aerodynamics and Control

2.3.2.1 Subsonic Regime

To ensure the comparability of the CWB to the BWB configuration, the same methods and approach for both configurations were used. The core is a combination of empirical equations to calculate the aerodynamic efficiency at trimmed conditions. With these equations, variable parameters have been optimized to attain maximum aerodynamic efficiency at different angles of attack and flight altitudes. In addition, a vortex lattice method with 3D panels was used to develop the profiles and to calculate pressure and lift distributions. The BWB requires specially designed airfoils as stability has to be achieved through sweep and twist adjustments. The center section has to accommodate the cabin box which decreases aerodynamic performance in the transonic speed region. The three-dimensional target lift distribution was achieved

by iterating the local twist and spanwise twist with specially adapted airfoils with a half-span partition into five wing panels. Hence, low lift coefficients are required in the middle section and higher lift coefficients at the outer parts of the wing. A twist distribution for near elliptic lift was identified as best concerning aerodynamic performance measured by the glide ratio or total drag at the design cruise condition.

2.3.2.2 Transonic Regime

Aerodynamics are especially challenging in conceptual design for the transonic regime. As with many aspects for unconventional aircraft, analytical methods inaccurately describe the physical effects of shock and wave drag effects. The Lock formula described and adapted by [6] for the estimation of wave drag effects is sufficient for preliminary estimates [7]. For validation, a comparison was performed with already available aerodynamic computations conducted within AIRBUS.

2.3.2.3 Stability and Control

The flight control surfaces of the ACFA BWB at this stage are ailerons, elevators, winglet rudders, slats, and flaps, in addition to spoilers and airbrakes. Unlike the CWB, no horizontal tail for trim can be used to trim the BWB. Instead, sweeping the wing and twisting the outer wing section is necessary. The influencing factors for flight control analysis in the preliminary design phase are weight in terms of MTOW and total wing span. Stability was analyzed with software, combining lifting line with vortex lattice and a 3D panel method. Additional analyses were conducted with calculations and available test data [14] based on [13].

2.3.3 Engine

The generic and scalable engine model used was provided by AIRBUS. It comprises a 115 klb take-off thrust engine and its characteristics during take-off, climb and cruise in regard to available thrust and fuel consumption. The model provided data for all relevant flight altitudes and temperature offsets from the International Standard Atmosphere (ISA), see Fig. 2.1.

Since two pylon-mounted engines are located over the center body of each configuration, scaling rules for the adaption of weight, specific fuel consumption (SFC), and dimensions were also implemented in agreement with AIRBUS. The take-off and initial climb is the decisive regime for the sizing of the engines and highly depend on the aerodynamic efficiency during acceleration and rotation. As in the conceptual development stage, the assessment of low-speed aerodynamics and take-off speeds is preliminary; a fixed thrust/weight ratio (T/W ratio) of 0.27 for both BWB and CWB was assumed. The engine size was computed according to (2.2):

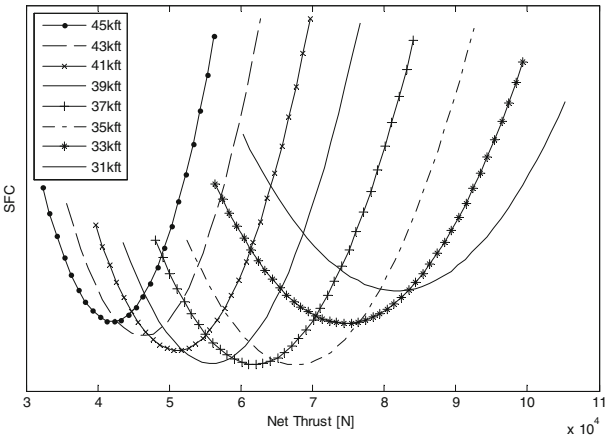

Fig. 2.1 Cruise specific fuel consumption (SFC) curves for BWB at different altitudes

$$F_{\text{engine}}\,(\text{lbf}) = 0.27 \times \text{MTOW}\,(\text{kg}) \times 9.81\,(\text{m/s}^2)/(4.448222\,(\text{lbf/N}) \times n_{\text{engines}}[-]) \tag{2.2}$$

2.4 Multidisciplinary Design Optimization in the Structural Design Process

Details of the structural design of both ACFA 2020 aircraft concepts are given in the corresponding reports [9, 15]. Both concepts considered in the ACFA project are unconventional in nature, particularly with respect to the fuselage designs. Therefore, the applicability of traditional statistics-based mass estimation routines must be examined critically. In the case of the BWB configuration, the ACFA project was able to build upon experience from previous European framework programs, such as Very Efficient Large Aircraft (VELA) and New Aircraft Concepts Research (NACRE). For the CWB configuration, however, few data points were available. The design and mass estimate of the CWB fuselage was therefore performed in a closely coupled MDO process iterating between conceptual and structural designs.

Given the width of the cabin, a conventional circular cross-section pressure vessel is intangible for the CWB fuselage design, as this would lead to too much wasted space. Initial studies including, for example, elliptical cross sections quickly led to a so-called double-bubble design as a good trade-off between cross-sectional area and resistance to internal pressure loads. This design consists of two side-by-side pressure vessels supported by frames with a double-spherical section pressure bulkhead at the rear of the cabin. In the center, vertical struts connect the frames at the top and bottom surfaces and the floor beam. To determine the cross-sectional shape, an FE half-model of a section through the fuselage consisting of two frames, the outer skin, floor, and central supports was created and used as a basis of a multi-objective

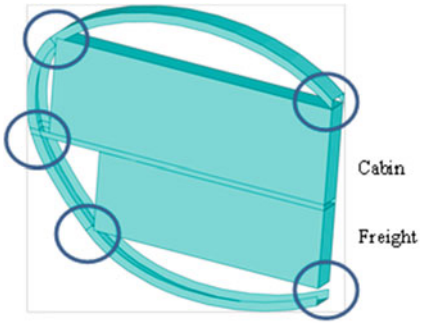

Fig. 2.2 Design of the cross section: *Circled points* indicate design points of the spline; *boxes* are the prescribed dimensions for cabin and freight volume

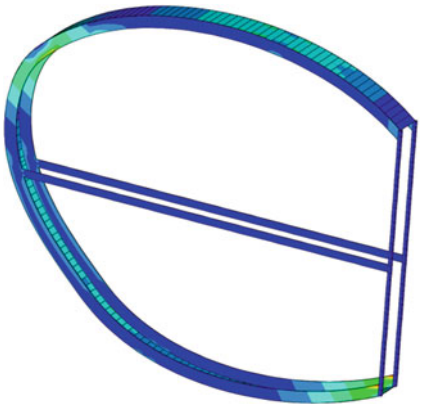

Fig. 2.3 Major principal strain in the fuselage cross section due to an internal pressure of 1 bar. Maximum strain (*green/yellow*) of 4.6‰

optimization of the structure (see Figs. 2.2 and 2.3). The shape of the cross section is given by four splines with support points at the corners of the boxes defining the payload volume provided by AIRBUS. The optimizer varies the distance of each control point from the payload circled in Fig. 2.2 and the slope of the spline, as well as the height of the frames at each point. An internal pressure of 1 bar is applied to the skin and symmetrical boundary conditions applied at the center line. The thickness of the skin and frames was kept constant. In addition to geometric constraints, the major principal strain in the structure was not allowed to exceed 5‰. The material was quasi-isotropic carbon fiber. The objective of the optimization was the minimization of a weighted sum of the normalized mass and the total cross-sectional and wetted area of the section.

After running the optimization with varying weighting of the two objectives, the resulting shapes and sectional masses were discussed with the conceptual design team. This resulted in the selection of the cross section shown in Fig. 2.3, with the mass of the section serving as the basis for the fuselage mass estimate.

In the case of the CWB wing box, the outer geometry was determined during the conceptual design stage, as well as the positions of front and rear spars. Position and length of a center spar were free to change during the structural design. The CWB

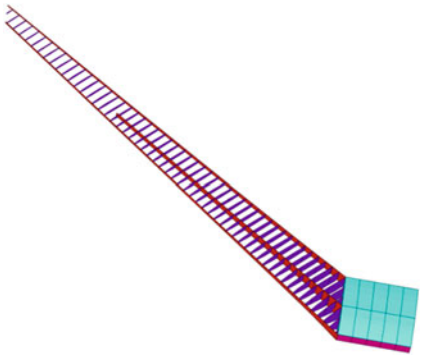

Fig. 2.4 Parameterized model of the internal structure of the CWB wing box with variable rib spacing and angle, as well as center spar position and length

wing is thin and highly swept, but is generally of a conventional configuration and thus expected to correspond well with statistical mass estimations.

To obtain a good configuration for the positioning of the wing box ribs, a parameterized FE model of the wing box was created as shown in Fig. 2.4, where the outer skin has been removed in the figure to expose the ribs and center spar. In this model, the position and length of the front and rear spars are constant, along with the wing profile, twist, and dihedral. Spacing of the ribs in the wing box can be varied, as can the angle between the ribs and the front spar. The chordwise position of the center spar and its sweep and length can also be varied in the model. The model has symmetric boundary conditions on the center plane. Elliptical pressure loads simulating lift of a 2.5 g pull-up maneuver and of a −1.0 g push-over maneuver are applied in two separate load cases with the weight of the fuselage included as distributed forces on the center part of the wing box in each case. Spar webs and ribs are constructed of quasi-isotropic carbon-fiber-reinforced polymer (CFRP), wing skin, and spar caps are highly orthotropic to take advantage of the well-defined load paths. Stringers in the outer skin are modeled using layered shell elements; the top layer modeled corresponding to the wing skin itself and subsequent layers are modeled to the stringer webs and caps. These subsequent layers, therefore, have near-zero stiffness orthogonal to the stringers, as well as a near-zero shear stiffness.

A parameter study of the internal structure of the wing box was performed using a genetic algorithm [3]. Apart from the geometric variables described above, the thickness of the wing skin and spar webs was also varied by the algorithm. In the model, constraints are placed on the displacement at the tip and the major and minor principal strains in the structure. However, since the primary failure mode of the wing skin is expected to be skin buckling, a separate model was used to assess the stability of the skin as shown in Fig. 2.5. During each evaluation, a skin panel between two ribs near the wing root is automatically exported, re-meshed with a finer element size, and the section forces from the global model are applied for each of the two load cases. Finally, a linear buckling analysis is performed and the resulting load factor is returned to the genetic algorithm.

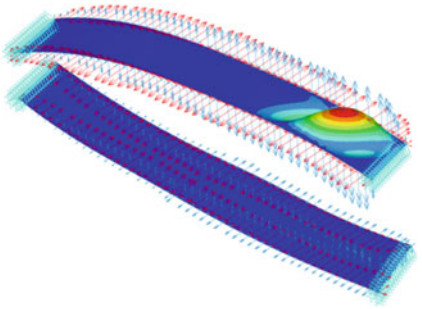

Fig. 2.5 Buckling field between two ribs in the wing box

The objective function of the genetic algorithm was the mass of the wing box. After about 15 generations with a population size of 60, the algorithm had converged to a solution with a rib spacing of about 800 mm and an angle between ribs and front spar of about 95°. Buckling strength in both load cases was the limiting constraint.

With the finalized topology of the wing box structure, a structural sizing optimization of the FE half-model, including the fuselage, tail and simplified engine mountings, was performed. Mass modeling was performed in cooperation with the conceptual design, distributing nonstructural masses representing landing gears, and other equipment in the fuselage according to the conceptual mass estimate. Likewise, a mass point representing the engine is positioned at the center of gravity of the engine and connected by rigid beams to the fuselage. Fuel masses are distributed in the wing and connected via rigid-body elements to the wing box. Symmetric boundary conditions are applied at the center plane. An elliptical pressure distribution representing the lift in both the positive 2.5 g maneuver as well as the −1.0 g maneuver was applied to the wing (see Fig. 2.6), a constant pressure was applied to the tail surfaces (see Fig. 2.7), and an internal pressure of 1.4 bar was applied to the fuselage between the pressure bulkheads at the rear and the nose.

In order to further improve the model, stringers in the wing skin were modeled as beam elements with the skin as a single-layer orthotropic shell. Stringers in the fuselage, tail and stabilizers were modeled in the same manner.

The sizing optimization of the half-model comprised 54 design variables consisting of the thickness of the wing skin separated into several design zones, the thickness of the fuselage skin similarly divided into zones and thickness of the stabilizer skin,

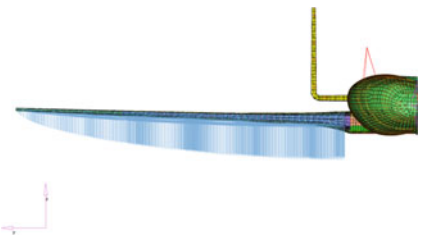

Fig. 2.6 Elliptical lift distribution applied to the wing distribution for structural sizing

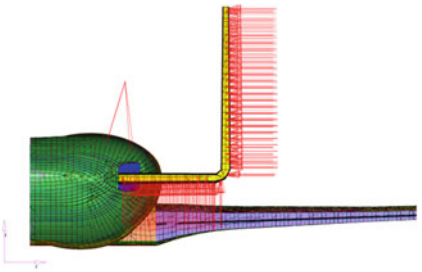

Fig. 2.7 Static load on the tail

shear webs of the fuselage frames, as well as spars and ribs in the wing and stabilizer. Dimensions of the stringers in the wing, stabilizers, and pressure hull were also variable, as well as the dimensions of the caps of spars and ribs in the wing and stabilizer, in addition to the caps of the frames in the fuselage. Elastic strain in the structure was constrained to remain within $\pm 5‰$. The objective of the optimization was minimum structural mass.

Convergence was generally rapid with a candidate optimal solution usually delivered in less than 35 iterations with stringent convergence criteria. Starting the optimization from several starting points resulted in the selection of an optimum design on which to base the final structural design.

The design resulting from the sizing optimization is intuitive: strength-limited components (that is, those close to the strain limit) are the wing skin near the wing root, the fuselage skin where the wing box passes through the hull and the stringers in the wing to around 2/3 of the span. Also following intuition, the thickness of the wing skin decreases when going from root to tip and thicknesses of shear webs in spars and frames tend to their minimum values, since no constraints on the stability of these components were included. Sizing variables of the stabilizers all tend to their minimum values indicating that the loads applied to them might need to be reviewed.

Comparing the mass of the final structural design with the initial mass estimates of the conceptual design results in a difference of about 5 % for the wing with the structural model mass being greater. This rather small difference is consistent with the conventional design of the wing. In the fuselage, the structural model mass is almost 15 % lighter than the conceptual design, despite the latter being based on the original FE section model. Similarly, the mass of the stabilizers in the structural model is 20 % less than the initial estimate. The most likely explanation for these discrepancies is lack of dimensioning load cases, such as impact at landing or the loss of an engine at take-off, as well as nonconservative sizing rules for the shear webs and skins in the hull considering only static strength and not stability.

Finally, a more detailed aeroelastic tailoring was performed of the wing box in isolation [11]. Mass and inertia properties of the rest of the structure were concentrated at a mass point located at the center of gravity and this was connected to the wing box using rigid elements as shown in Fig. 2.8. Modeling of the tail was greatly simplified. It was connected to the mass point at the center of gravity using beam elements whose mechanical properties were determined from the detailed FE

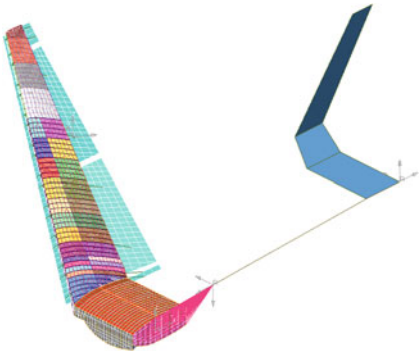

Fig. 2.8 FE model of wing with simplified tail surfaces for aeroelastic tailoring

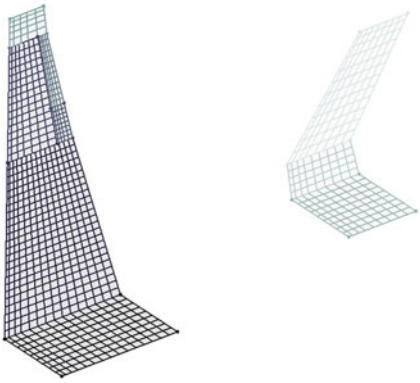

Fig. 2.9 DLM mesh of wing and tail including split aileron vertical stabilizer and trim surface

model of the fuselage. Flaps and slats were included as plates with approximated mass and stiffness properties and fastened to the wing box without stiffening it in bending. Boundary conditions were applied at the center of gravity; both symmetric and anti-symmetric cases were included.

In addition to the structural model, a DLM was created as shown in Fig. 2.9. The aerodynamic model includes the wing and tail surfaces, as well as the split aileron.

The 2.5 and -1.0 g static load cases were simulated by trimming the aircraft with the corresponding constant vertical acceleration using the horizontal tail surface (excluding the part of the tail contained within the fuselage). In addition, positive and negative roll maneuvers due to deflection of each of the ailerons or both of them together were included. The response to discrete $1 - \cos$ gusts of various lengths was also assessed.

For aeroelastic tailoring, the wing skins were modeled as four-layer shells with one layer for each fiber orientation, 0°, 90°, and ±45° with properties smeared across the thickness of the shell. The optimizer was free to vary the thickness of each layer separately. Constraints, as before, were placed on the elastic strain in the material. Additionally, a constraint was placed on the minimum steady-state roll rate to ensure control effectiveness and on the difference between first bending and torsional

eigenfrequencies to avoid flutter problems. As previously, the objective was to minimize mass.

The tailored design does not differ significantly from the previous sizing of the wing box, except at the outer third of the span where additional stiffness, and therefore material, must be added to the wing to ensure compliance with the roll effectiveness constraint. The critical gust loads (both positive and negative) also lead to excessive strains in this region requiring reinforcement, whereas the strength at the wing root after sizing for the static maneuver cases is adequate. The main reason for the critical loads at this location is because the center spar ends here which modifies the shear flow for torsional loads.

2.5 Configuration Selection

The one-year conceptual design process demonstrated the feasibility of both aircraft concepts. Selected results will be presented in this section leading to a comparison and thus selection of the BWB concept over the CWB design.

2.5.1 Results

Selecting a future aircraft layout within the ACFA framework was conducted based on a detailed trade-off analysis comprising the categories geometry, aerodynamics, weights, and mission performance. The work in this section represents first year-end collaborative research results [8, 12]. Figure 2.10 depicts the two basis configurations with their main dimensions.

2.5.1.1 Geometry

The CWB in its final configuration has a wing aspect ratio of 10.83, whereas the BWB has a ratio of only 4.82 due to its unconventional form. One reason is the 80 m wing span limitation. The all-lifting BWB airframe results in a low required C_L in cruise and low induced drag.

The increased lifting surface and reference area of the BWB potentially increases low-speed lift. The detailed trade-off for cruise drawbacks for flying in higher altitudes can be significant. Although the reference area of the BWB is much larger, the overall wetted area is 3.6 % less leading to lower zero lift friction drag. Taper ratios are 0.09 for the BWB and 0.29 for the CWB.

The CWB fuselage accommodating the passenger cabin is 14.77 m longer. The reason for this is the widening of the cabin box along the y-axis in the BWB. Effects on ride comfort were evaluated later in the project. The current CWB and BWB configuration can house at least 30 LD3 containers. Both concepts position the

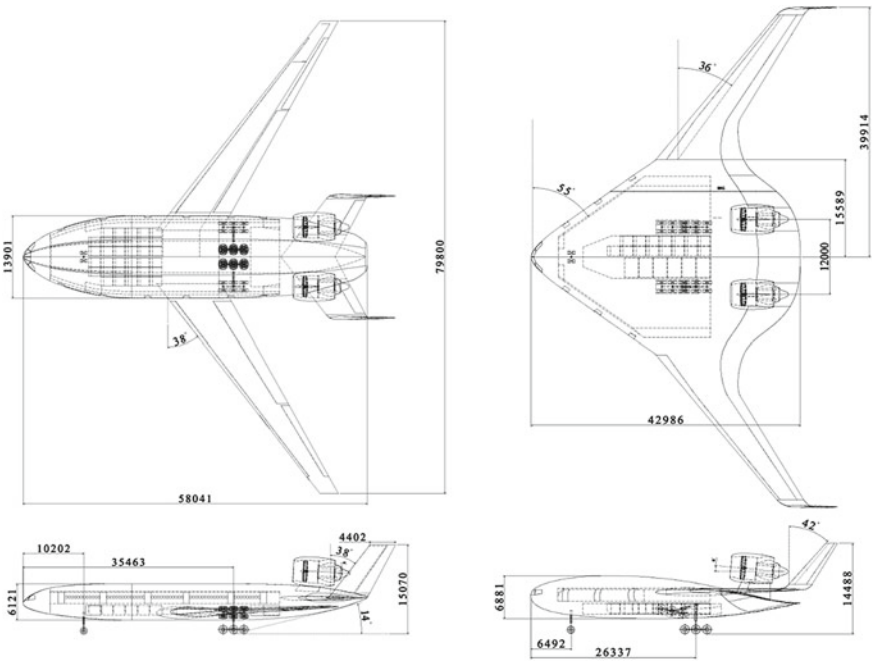

Fig. 2.10 Overview of CWB (*left*) and BWB (*right*)

engines on top of the fuselage with possible shielding effects expected to be larger for the BWB. However, no significant structural advantages are expected, since the structural reinforcements of conventional under-wing engine mounting are also required for the envisaged central aft mounting.

For yaw control, the CWB configuration uses double fins with rudders, whereas the BWB uses winglets with a rudder chord of 30 % of the winglet.

Trim is also challenging. Neglecting trim drag on the BWB seems a reasonable approach as it can be assumed that fuel transfer between the different central and outboard fuel tanks could be used to have the aircraft center of gravity (CG) aligned with the center of pressure in cruise without having to deflect the elevators, so without creating trim drag. This is a target approach assuming that it is possible to design the fuel system in such way that it could cope with the CG variation due to different payload level (baggage and passengers) and variation of fuel volume on-board along the flight. The approach seems reasonable given the significant internal volume in the wing and in the center body of the BWB that gives enough flexibility to install the fuel tanks appropriately. A study on the ACFA 2020 BWB configuration has been done in [16]. The same kind of approach has been used within Airbus for internal projects on BWB in the recent years.

All trailing edge movables are needed on the BWB. In comparison, the CWB has a heavy movable H-tail, which counteracts center of gravity shifts during flight

more easily and with fewer flight dynamics interactions. Damping capabilities for flight stability are generally lower on the BWB due to smaller lever arms and higher coupling effects. However, more sophisticated approaches are necessary to perform a detailed stability and performance assessment.

2.5.1.2 Aerodynamic Performance and Stability

The BWB has a better lift/drag ratio (L/D ratio) at the reference Reynolds number and a very low C_{D0}, since the ratio of wetted area to S_{ref} is lower. As the BWB aspect ratio is also low, induced drag increases rapidly with C_L and leads to very low optimum C_L of 0.25 for the BWB. Opposite effects lead to a higher optimum C_L of 0.47 on the CWB [12]. Hence for the total lift force in cruise, the lower C_L for the BWB requires a larger wing area. Figures 2.11 and 2.12 depict the lift distribution along the span for CWB and BWB. CWB distribution is close to an elliptic lift distribution which results in low induced drag. Figure 2.12 shows the lift distribution of the BWB at the due date of the configuration selection and indicates the need for further modification of the lifting body geometry. The final configuration and lift distribution is presented in [7].

Stability analysis revealed a slightly stable (1 % static margin) configuration and the need for more detailed models since the margin range is small and the accurate determination in preliminary design with conventional methods is challenging.

2.5.1.3 Weights

Comprehensive data for all system and structure weights was computed. Especially for highly complex elements of the overall aircraft, the methods from conventional

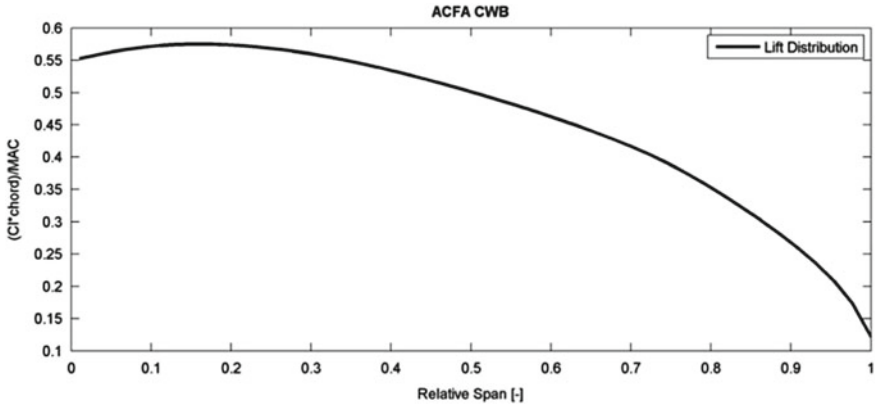

Fig. 2.11 ACFA CWB lift distribution

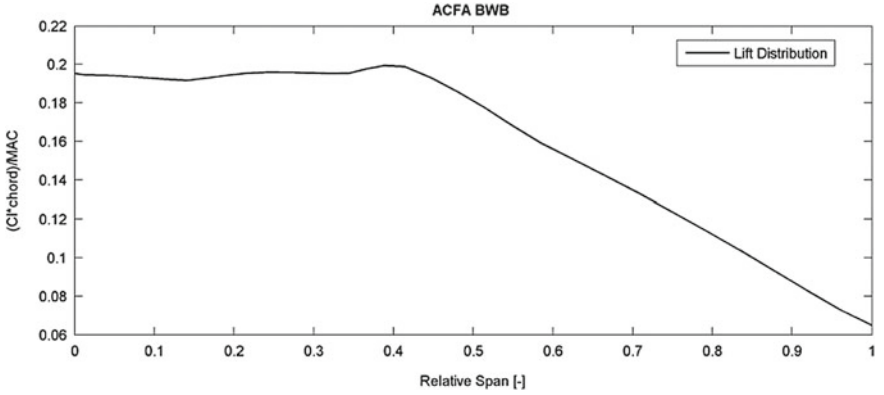

Fig. 2.12 ACFA BWB lift distribution

aircraft design need refinement. The BWB aircraft realizes a weight advantage of 14.10 t. The horizontal and vertical stabilizers on the CWB add a 25.6 % weight penalty, since conventional tail horizontal stabilizers on the BWB do not exist. Because operator items are assumed to be equal for both configurations, the BWB achieves an OWE advantage of 9.7 t over the CWB. Both configurations are separated by a 23.79 t MTOW advantage for the BWB.

2.5.1.4 Engine

Based on the calculations in preliminary design and the CWB's lower optimum altitude, CWB thrust per engine is 126.7 klb sized for the minimum T/W ratio of 0.27. BWB cruise and stepped altitude requirements lead to thrust of 119.6 klb per engine.

2.5.2 Aircraft Selection

As the conceptual aircraft design has revealed, both configurations offer promising advantages for future air transport (see Table 2.2). The BWB's weight benefit is significant and the inferior cruise and resulting fuel burn performance of the CWB, whose cruise L/D is 21.7 compared to 24.2 of the BWB, is a further disadvantage of the CWB. The higher flight altitudes for the BWB and thus the required engine thrust does not exceed what current engines available on the market can deliver.

For its superior mission performance in fuel consumption on a 7,200 nm (4,000 nm) mission, the BWB beats the CWB by more than 13 %. No development obstacles have been identified; hence the BWB was studied and optimized in the detailed development phase of the ACFA 2020 project.

Table 2.2 Mission performance comparison for BWB and CWB [12]

	BWB	CWB	Δ (%)
TOW	401.6 t	428.4 t	−6.7
OWE	255.0 t	234.7 t	8.0
2-Class Pax capacity	470	464	1.3
Engine size	119.6 klb	126.7 klb	−5.9
CL of L/Dmax	0.25	0.47	
L/Dmax	24.2	21.7	10.3
Block fuel 4,000 nm	62.03 t	68.16 t	
	131.8 kg/Pax	146.9 kg/Pax	−11.5
Block fuel 7,200 nm	116.47 t	130.25 t	
	247.8 kg/Pax	280.7 kg/Pax	−13.3
Initial cruising altitude (ICAC)	36,000 ft	33,100 ft	8
TTC at 31,000 ft	25.6 min	25.6 min	0

2.5.3 Conclusion and Outlook

Within the project time frame of one year, two conceptual commercial aircraft designs for a long-haul mission were developed and compared based on a comprehensive set of requirements. The selection process was driven by the mission performance calculations based on geometric, aerodynamic, and weight analysis. Furthermore, a comprehensive MDO was performed to optimize fuselage cross section and wing box design.

The selection of the BWB is a result of its superior efficiency. Compared to an improved wide body design such as the CWB, the mission performance results in 15.46 t less fuel burn with corresponding CO_2 savings.

Ongoing research in the field of aircraft design addresses the preliminary design process adoptions and the design for active control technologies [7]. Especially in the areas of stability analysis, transonic aerodynamics and structure, conventional methods need adjustments in order to efficiently apply them in conceptual design. Ride comfort and passenger acceptance, as well as the inclusion of these radical configurations in the controlled airspace, are issues necessitating further research.

Additional improvements to reach the ACARE goals and to lower fuel consumptions beyond what can be achieved by new airframe designs are expected from innovative engine technologies and more efficient air traffic management.

Acknowledgments The authors are very much indebted to all ACFA 2020 partners for their contributions. The authors are especially grateful to R. Maier and A. Wildschek from Airbus Group Innovations (formerly EADS Innovation Works) and J.-J. Mirat from AIRBUS for their continuing support. The authors would also like to thank participating colleagues K. Ploetner and B. Brueckner from Technische Universität München. Finally, we would like to thank W. Staudacher for his valuable contributions concerning the overall aircraft configuration.

References

1. Hileman J, Spakovszky Z, Drela M, Sargeant M (2007) Airframe design for "Silent Aircraft". In: 45th AIAA aerospace sciences meeting and exhibit, Reno, Nevada, USA
2. IABGmbH. Luftfahrttechnisches Handbuch (LTH) (2008) (English: Aviation Technology Handbook). Ottobrunn, Germany. http://www.lth-online.de. Accessed 8 July 2014
3. Langer H (2005) Extended evolutionary algorithms for multiobjective and discrete design optimization of structures. PhD thesis, Technische Universität München, Munich, Germany
4. Leahy J (2010) Airbus global market forecast 2010–2029. Toulouse, France
5. Liebeck RH (2004) Design of the blended wing body subsonic transport. J Aircr 41(1):10–25
6. Malone B, Mason WH (1995) Multidisciplinary optimization in aircraft design using analytic technology models. J Aircr 32(2):431–438
7. Mohr B, Paulus D, Baier H, Hornung M (2012) Design of a 450 passenger blended wing body aircraft for active control investigations. J Aerosp Eng 226(12):1513–1522
8. Mohr B, Plötner K, Rößler C (2010) ACFA 2020 WP 1. Final report. Munich, Germany
9. Paluch B, Joly D (2010) D1.2 Part 1: design steps of the BWB finite element model. Lille: ONERA, France
10. Paulus D, Salmon T, Mohr B, Rößler C, Petersson Ö, Stroscher F, Baier H, Hornung M (2013) Configuration selection for a 450-passenger ultraefficient 2020 aircraft. Prog Flight Dyn GNC Avionics 6:601–618
11. Petersson Ö, Stroscher F, Baier H (2010) Multidisciplinary optimisation of aircraft wings including gust loads. In: 2nd aircraft structural design conference, London. Royal Aeronautical Society
12. Salmon T (2009) Comparison dossier of the two 450 passenger aircraft configurations for ACFA 2020, ACFA 2020 D1.5. Chatillon, France
13. Schemensky RT (1973) Development of an empirically based computer program to predict the aerodynamic characteristics of aircraft. Technical report, Air Force Flight Dynamics Laboratory. AFFDL-TR-73-144
14. Staudacher W (2011) ACFA BWB conceptual design calculations. Munich, Germany
15. Stroscher F, Petersson Ö, Baier H (2009) D1.3 Part 2: structural design of the ACFA 2020 CWB configuration, Munich, Germany
16. Wildschek A, Stroscher F, Haniš T, Belschner T (2013) Fuel management system for cruise performance optimization on a large blended wing body airliner. In: Progress in flight dynamics, guidance, navigation, control, fault detection, and avionics, vol 6. EDP Sciences, pp 651–670

Chapter 3
Numerical Simulation Model

F. Stroscher, A. Schirrer, M. Valášek, Z. Šika, T. Vampola, B. Paluch, D. Joly, C. Breitsamter, M. Meyer, D. Paulus, T. Klimmek and H. Baier

3.1 Introduction

F. Stroscher and A. Schirrer

The active control design activities in ACFA 2020 are based on a numerical flight simulation model of the BWB aircraft configuration which shall predict its flight dynamics, as well as structural dynamic response. The classical approach of aircraft flight simulation is a 6 degrees of freedom flight dynamic model, not considering the dynamic response (that is, vibrations) of the airframe, as well as its impact on the flow field around the wetted surface. Aircraft structural dynamics are classically considered in structural loads analysis (for example, landing loads) and aeroelastic stability (for example, flutter) or response analysis (for example, transient gust response). This separated approach is well suited for flight simulation of classical wing-fuselage aircraft whose aeroelastic response does not remarkably interact with its flight dynamics.

However, for larger aircraft with high wing spans, aerodynamic coupling between flight dynamic and aeroelastic motion becomes more significant because wing vibration frequencies are lower and closer to those of the flight dynamic modes

F. Stroscher (✉) · C. Breitsamter · M. Meyer · D. Paulus · H. Baier
Technische Universität München, Munich, Germany
e-mail: stroscher@llb.mw.tum.de

A. Schirrer
Vienna University of Technology, Vienna, Austria

M. Valášek · Z. Šika · T. Vampola
Czech Technical University in Prague, Prague, Czech Republic

B. Paluch · D. Joly
ONERA, Châtillon, France

T. Klimmek
German Aerospace Center, Cologne, Germany

M. Kozek and A. Schirrer (eds.), *Modeling and Control for a Blended Wing Body Aircraft*,
Advances in Industrial Control, DOI 10.1007/978-3-319-10792-9_3

(for example, the short-period mode). This holds true for the ACFA 2020 BWB aircraft, which is even more prone to such interactions due to the following properties: First, its airframe is highly flexible compared to wing-fuselage aircraft. The low wing loading, achieved by the fuselage acting as lifting surface, allows for a lightweight, thin and thus flexible wing design. Second, a significant aerodynamic coupling of flight dynamic and aeroelastic motion is present because the wide wing-like fuselage is involved in structural deformations. This behavior is well observable at the first bending mode, which clearly shows wing deflection, but also pitch rotation of the fuselage. Consequently, the aerodynamic coupling of aeroelastic and flight dynamic degrees of freedom will be considered in the BWB aircraft flight simulation model.

For control design, a linearized simulation model in the time domain is required. It shall be parametric with respect to multiple mass configurations of the aircraft, as well as flight conditions. Its numerical order has to be relatively low in order to efficiently perform parametric control studies. The state-space formulation is applied for the formulation of the aircraft equations of motion. The state vector $\mathbf{x}$ is comprised of the plant degrees of freedom and their first time derivatives. The input Eq. (3.1) is a first-order differential equation, relating the state vector time derivative to the state vector by the system matrix $\mathbf{A}$ and the input vector $\mathbf{u}$ by the input matrix $\mathbf{B}$. The output Eq. (3.2) relates plant outputs to the state variables and inputs by the output matrix $\mathbf{C}$ and the feed-through matrix $\mathbf{D}$.

$$\dot{\mathbf{x}} = \mathbf{A}\mathbf{x} + \mathbf{B}\mathbf{u} \tag{3.1}$$

$$\mathbf{y} = \mathbf{C}\mathbf{x} + \mathbf{D}\mathbf{u} \tag{3.2}$$

This chapter outlines two approaches to obtaining a numerical simulation model suitable for dynamic simulation studies and for control design (after performing further order-reduction, see Chap. 4):

- In the initial phase of the ACFA 2020 project, a predesign model of a large 750-passenger BWB aircraft configuration has been made available by the NACRE project consortium [2] to the ACFA 2020 consortium. This way, the development of the necessary methods and tools for modeling, order-reduction, and control design could be started early in the project during the conceptual design phase leading to the ACFA 2020 flying wing design. Section 3.2 reports on the necessary adaptation tasks to the NACRE BWB configuration to enable control-related dynamic simulation, see also [8].
- The actual modeling tasks of the selected ACFA BWB configuration are presented in Sects. 3.3–3.5. Section 3.3 reports on the structural modeling via the finite element method (FEM). An FE model of the airframe is utilized for the computation of its natural modes, which are used as a reduced set of degrees of freedom for the aeroelastic equations of motion. Section 3.4 outlines aerodynamic modeling and analysis tasks. High-fidelity as well as standard aerodynamic tools are applied for the computation of the aerodynamic database. On the one hand, steady aerodynamic derivatives of the rigid aircraft are required for flight dynamic modeling. On the other hand, unsteady aerodynamic forces on modal coordinates,

so-called generalized aerodynamic forces (GAF) will be derived. The reduction of structural and aerodynamic degrees of freedom to a limited number of common modal coordinates is a highly effective model order reduction principle, which is common practice in aeroelastic simulation. Finally, the coupled flight dynamic and aeroelastic equations of motion will be derived from structural dynamic and aerodynamic data in Sect. 3.5. The nonlinear flight dynamic equations of motion are coupled to the aeroelastic equations of motion. The linear state-space model is derived by numerical linearization of the coupled equations.

3.2 Preliminary Structural Modeling

M. Valášek, Z. Šika and T. Vampola

This section describes the adaptations on the finite element (FE) model of the flying wing configuration of the starting structure, a BWB aircraft configuration laid out for 750 passengers that has been made available by the NACRE project [2]. This model was utilized in the initial phase of the ACFA 2020 project for developing, testing, and tuning the modeling and control design methods that were later applied to the ACFA 2020 BWB configuration (designed for 450 passengers).

An overview on the performed model modifications is given in [8]. The structural modifications detailed in the following were necessary to achieve a structural model applicable for structural dynamic analysis for different mass configurations. Starting point of the adaptation was the FE model of the primary structure of the flying wing configuration. The model was examined regarding structural dynamic and structural stability (buckling) characteristics. To eliminate the detected and unwanted local modes, additional structural elements in the form of beams were integrated. Furthermore, some missing parts in primary structure like tail, engines, pylons, and cockpit were modeled. In addition, masses were incorporated for the consideration of the fuel and other nonstructural components. Finally, a structural dynamic analysis was performed for various mass configurations.

3.2.1 Testing FEM Structure

All designed methods and concepts used for the optimal design of the flying wing were tested and tuned on the simplified flexible structure. Due to the size of the flexible model was used for only so-called primary structure and the missing parts (tail, fuel masses, engines, nonstructural masses) have been modeled as a discrete mass in the primary structure (Figs. 3.1 and 3.2).

The FE model of the primary structure was scrutinized in order to detect causes for the poor structural dynamic characteristics. The model was examined regarding structural dynamic and structural stability (buckling) characteristics. To eliminate

Fig. 3.1 Primary structure (made available by the NACRE project [2])

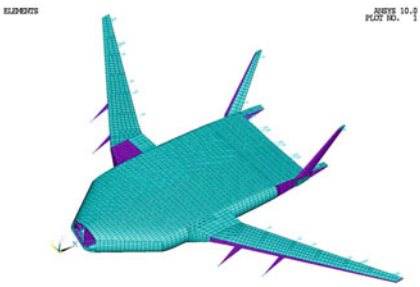

Fig. 3.2 Modified testing structure of the flying wing

the detected and unwanted local modes, additional structural elements in the form of beams were integrated to the primary structure to reinforce the fuselage of the testing structure of the flying wing. The geometric configurations of the added beams were derived from the buckling analysis. The calculated allowable stresses gave hints for the designer to adapt the thickness of various shell elements of the structure. The reinforcement of the fuselage on the contrary increases the total mass of the flying wing. The additional beams were used in the fuselage and transition areas (Fig. 3.3).

The original primary structure contained not all structural parts of the aircraft. The biggest missing part was the tail. Therefore, the tail structure was connected to the primary structure. In order to reduce the size of the model, only the load carrying parts were used. The leading and trailing edges for the vertical tails were left out. The structure of the rudder was replaced by a simple plate structure. This allowed for the consideration of control surface modes (Fig. 3.4).

As for the fuselage, beam elements were integrated to stiffen the structure in order to avoid parasitic modes. In contrary to the stiffening structure for the fuselage, the additional beam elements have no mass. This was done to simplify the process to balance the center of gravity (CG) position of the overall structure including nonstructural components. Otherwise, a more extensive dimensioning process would have been necessary.

The engines were modeled as one mass point at the CG of the engine. For the pylons, a simple beam structure was applied to achieve a distributed connection of the pylon to the wing box. By varying the structural properties of the beams, realistic structural dynamic characteristics of the engine/pylon structure were achieved (Fig. 3.5).

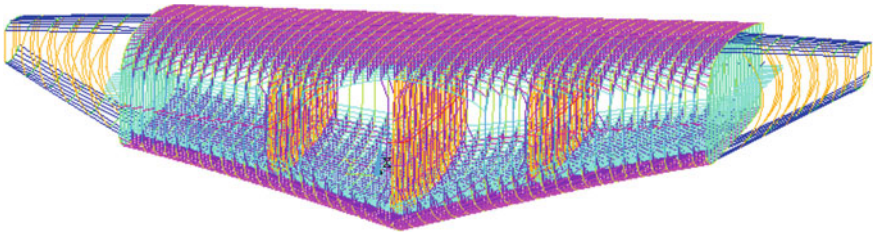

Fig. 3.3 Additional stiffening elements in the fuselage and transition areas of the testing structure

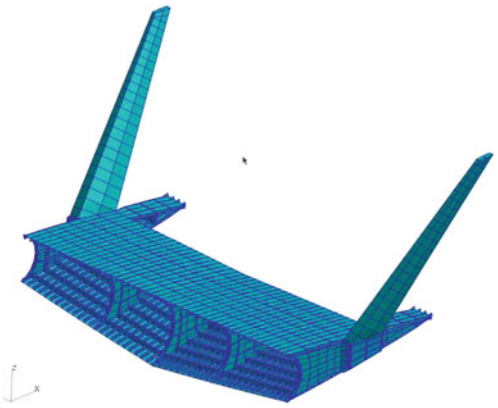

Fig. 3.4 FE model of tail structure

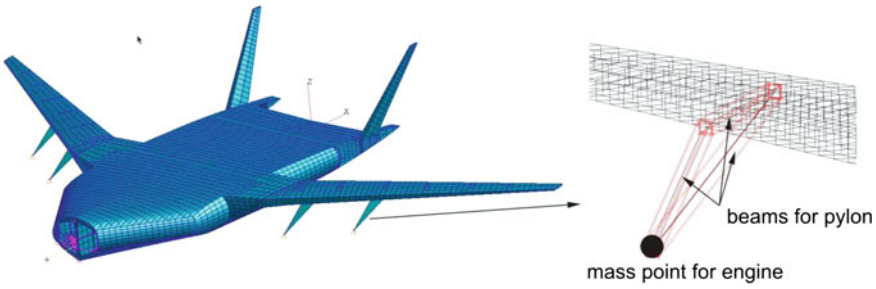

Fig. 3.5 Model of engines and pylons

A single mass point was used for representing the cockpit. The mass and the location were taken from the mass value and the CG position of the detailed structural model of the previous project modeling complete aircraft model (Fig. 3.6).

The fuel tank masses were modeled as concentrated masses distributed in the wing. For the tanks 1 and 2, the fuel is represented by only one mass point. For tanks 3 and 4, mass points per sections between two ribs are designated. The breakdown of the masses for tanks 3 and 4 for full fuel tanks is proportional to the volumes

Fig. 3.6 Cockpit structure

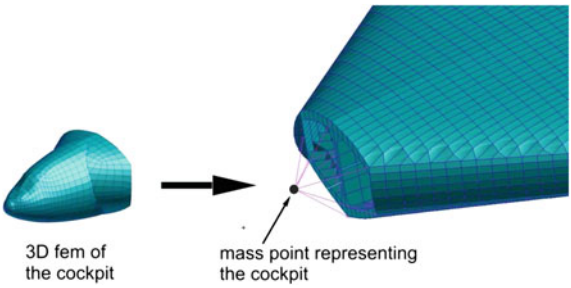

of each section. For the state-space models, different fuel configurations have to be taken into account. Therefore, a widespread applied strategy was used by emptying the tanks from inside of the wing to outside. This approach brings out a relief of the root bending moment of the wing due to fuel masses (Figs. 3.7, 3.8 and 3.9).

The additional nonstructural masses were redistributed in the fuselage modeling the loads. The mass points were connected to the structure by using a connection element (RBE3 element) that defines a constraint relation in which the motion at a "reference" grid point is the least square weighted average of the motions at other grid points. The element is useful for "beaming" loads and masses from a "reference" grid point to a set of grid points. The overview of the distribution of the nonstructural masses in the plane is introduced in Fig. 3.10.

For testing purpose of assembled flexible structural model were suggested the loading cases for that were computed the mean aerodynamic chord (MAC) to prove the quality of the model and compare the assembled structure with previous concepts of the flying wing. The loading cases were realized according to Fig. 3.11.

For the different load cases were computed positions of the CGs. The CG position is crucial for the stability of the structure. It was tuned according to similar structures to obtain reasonable values (Fig. 3.12).

Due to the needs of the driving algorithms, the validity of the structural model was tested by the conditions of the symmetry too (Fig. 3.13).

The eigenfrequencies for the right half and left half of the model were compared for chosen mass configuration. The boundary condition was applied in the plane of symmetry. The differences between eigenfrequencies of the left and right half of the structural model were computed. For the first 30 structural eigenmodes was the maximal frequency difference between left and right half of the model for all mass variants is below 0.3 Hz. It means that the symmetry of the structural model was very good and assembled model could be used for testing of the derived methods and concepts for the optimal design of the ACFA flying wing. The total frequency densities of the assembled flexible structure were in a good accordance with the previous concepts of the flying wings structure without parasitic modes in the frequency range 0–30 Hz (Figs. 3.14, 3.15 and 3.16).

In the next step, the shear and normal forces and bending torques in the wings root were computed.

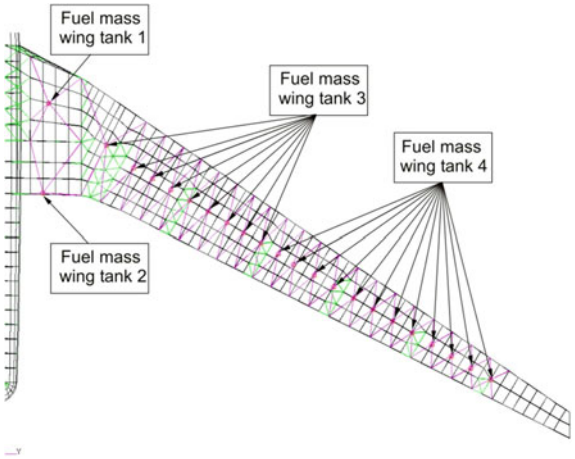

Fig. 3.7 Fuel masses in the wing tanks

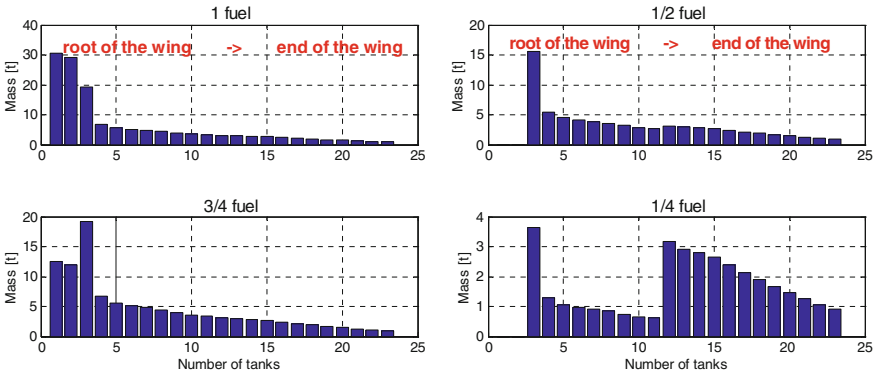

Fig. 3.8 Emptying strategy of the fuel tanks

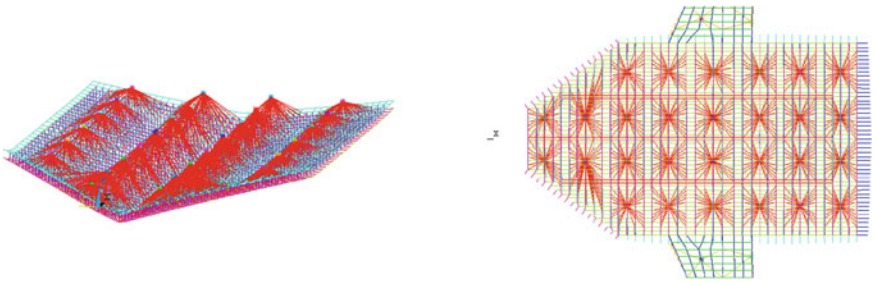

Fig. 3.9 Lumped masses in the testing structure of the flying wing

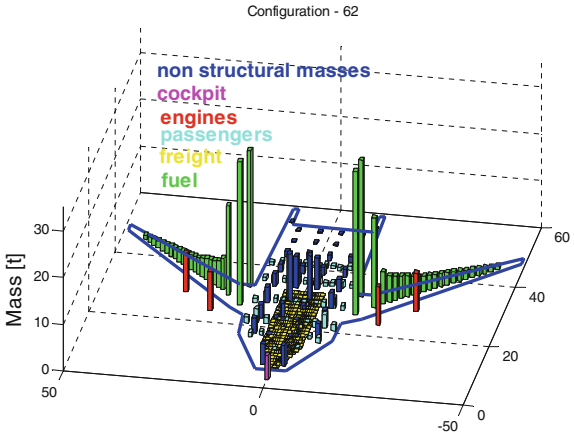

Fig. 3.10 Distribution of the nonstructural masses in the plane

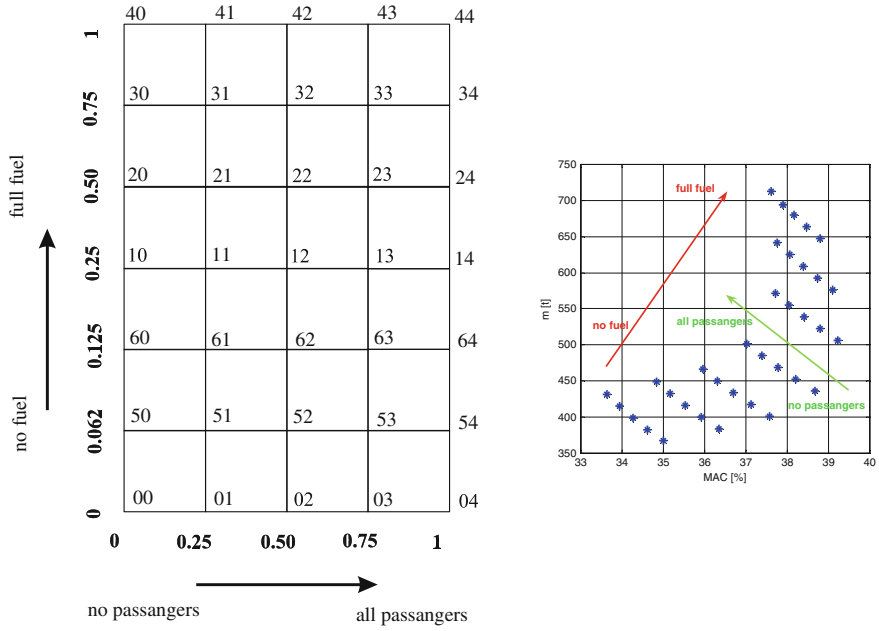

Fig. 3.11 Definition of load cases

Finally for the proved flexible structure of the flying wing, the result mass and stiffness matrixes for the all load case configurations were generated and a first hundred eigenmodes were computed. These information were used for deriving the reduced-order model (ROM) (Fig. 3.17).

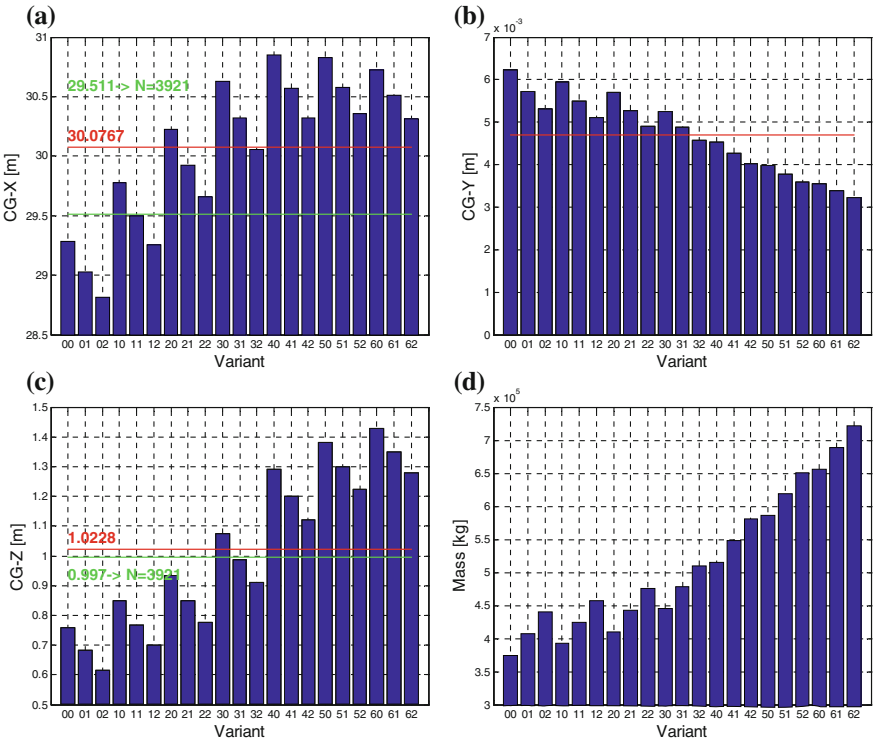

Fig. 3.12 Center of gravity positions of load cases. **a** CG x. **b** CG y. **c** CG z. **d** Mass variants

3.3 ACFA BWB Structural Modeling

B. Paluch and D. Joly

3.3.1 Overview on Structural Modeling

This section describes the step adopted for the construction of the BWB FE model within the framework of the ACFA program. After a brief description of the aircraft geometry and the configuration as well as the material properties, more realistic loading cases were determined in agreement with AIRBUS. The single shell concept used for the fuselage was validated through a detailed calculation which led to reinforce the initial structure to improve its buckling behavior. After having taken into account the distributions of the nonstructural masses, finite element calculations showed that the maximum strain criterion is satisfied. The aircraft mass breakdown and inertia parameters could then be determined from this model (Figs. 3.13, 3.14 and 3.15).

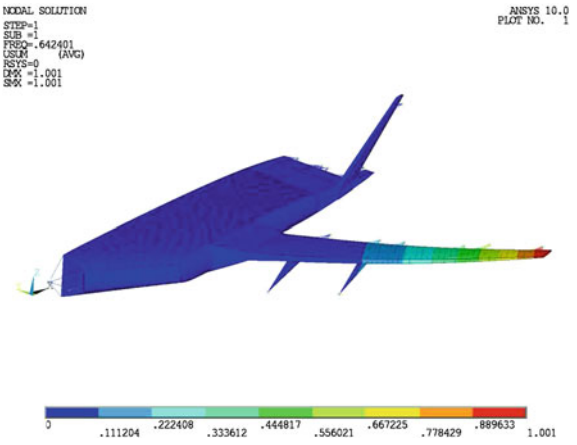

Fig. 3.13 Structural model—*left half*

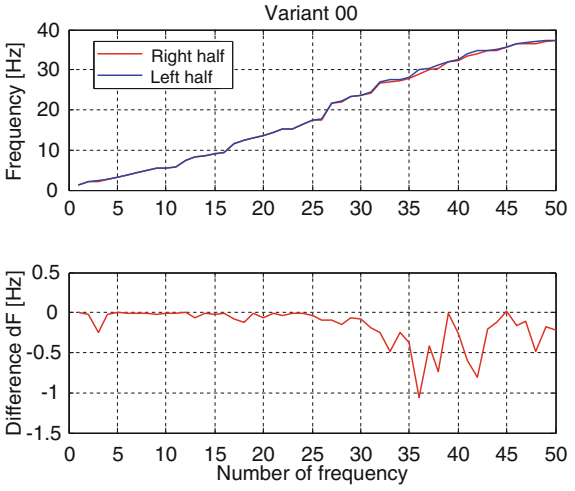

Fig. 3.14 Variant 00—frequency differences

Because of the shape and the structural complexity of the BWB, the usual assumptions related to strength could become too restrictive. Consequently, an FE has been built to calculate the thickness of the various components. The evaluation of a new configuration is generally carried out on three levels:

Conceptual: starting from the aircraft mission specifications global results concerning the most adapted aircraft geometry and performances are obtained. Simple calculation procedures and expert knowledge are employed and the internal structure of the aircraft is not considered.
Preliminary: starting from more detailed specifications, a more precise weight estimation of the primary and secondary structures is done, requiring more refined computer codes, such as the FEM.

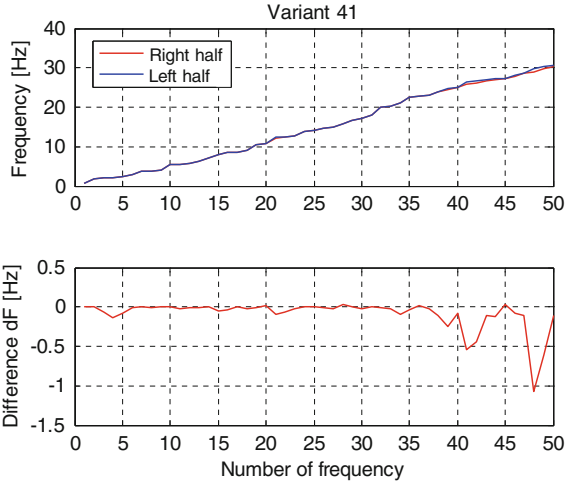

Fig. 3.15 Variant 41—frequency differences

Detailed: details (for example, technological constraints due to manufacturing) of most of the aircraft parts or components are considered, leading to a precise evaluation of the performances and costs of the project.

In this project, the design dedicated to the aeroelastic evaluation of this BWB concept is more relevant on a preliminary level than on a conceptual one. The main problem in the design step is to know the size of the smallest structural component that one should take into account in the FE model. For the BWB, this size has been limited to the frames and the stiffeners. Smaller components such as stringers, which play an important role for elastic stability of fuselage and wing skins, for example, were not meshed but included in the skin properties. In this manner, an FE model could be built with a reasonable but sufficiently large number of nodes and elements, allowing to perform an accurate analysis concerning flutter, weight estimation, and design evaluation.

3.3.2 ACFA Geometry

3.3.2.1 Overall Configuration

The geometry of the BWB configuration was defined in the reference document published in July 2008 by Technical University of Munich (TUM). The plane form of the aircraft is shown in Fig. 3.18: the overall length and span are equal to about 43 and 80 m, respectively.

In this document, the following zones are distinguished in the structural concept and in the FE model, respectively (Fig. 3.19):

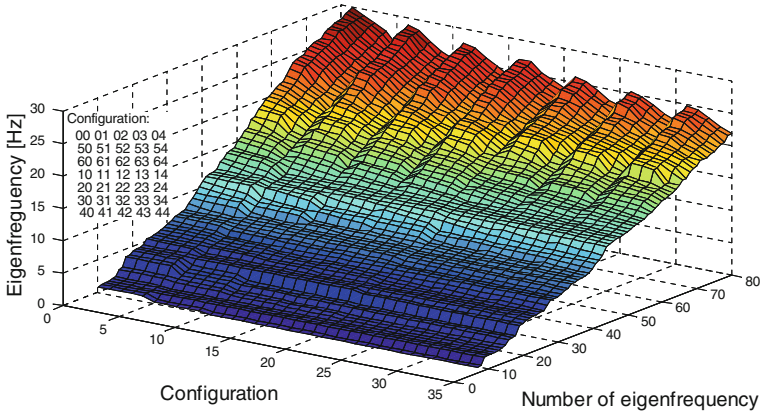

Fig. 3.16 Eigenfrequencies over load cases

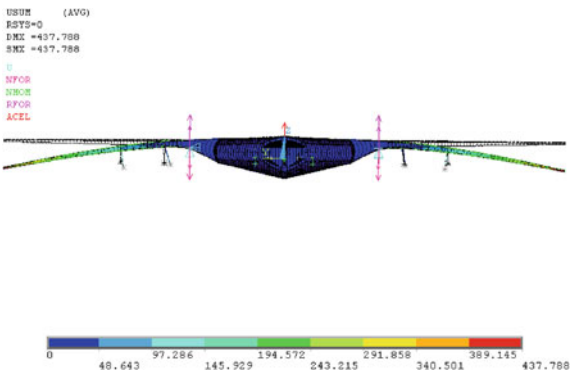

Fig. 3.17 Testing structure—static deformation 2 g

- the passengers cabin (pressurized),
- the cockpit (pressurized),
- the rear fuselage,
- the transition area (located between the cabin and the wing),
- the wing box,
- and the winglet box located at the wing tip.

Schematically, an aircraft structure can be split into two parts:

- the *primary* structure, designed to support the main loads such as aerodynamics, cabin pressurization, and so on. The different zones defined previously are included in this category,
- and the *secondary* structures which do not support the main loads, grouped in the following devices:
  - the aerodynamic devices like flaps (colored in blue in Fig. 3.19) and slats (green in Fig. 3.19),

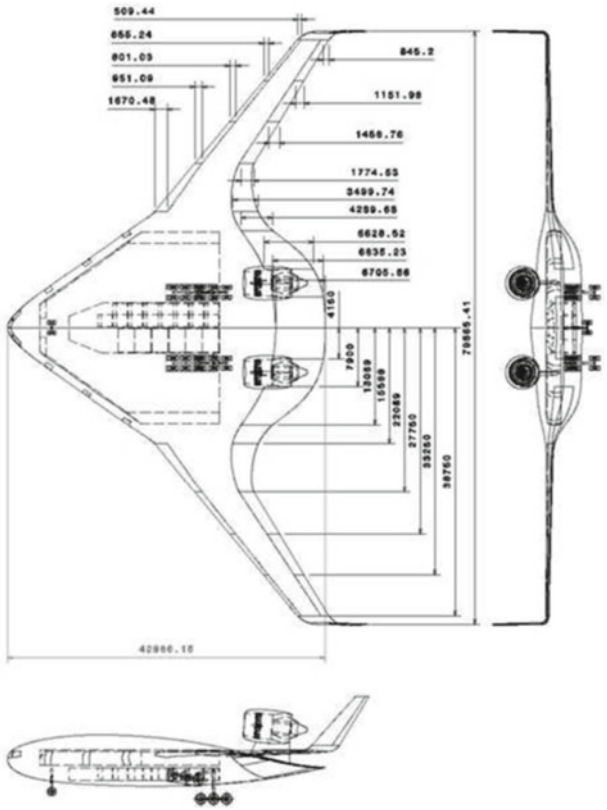

Fig. 3.18 ACFA BWB overall dimensions

– the tanks,
– the engines,
– the "active" components (actuators, …),
– the "passive" components (seats, …).

All the devices attached to the primary structure do not affect the resistance of the primary structure.

3.3.2.2 External Geometry

The external geometry of the aircraft was defined by a set of airfoils whose coordinates were communicated to ONERA by TUM. The global aircraft geometry reference frame (Fig. 3.20) is defined by:

- the frame origin O located at the aircraft nose,
- the X axis directed backward (from the cockpit to the rear),

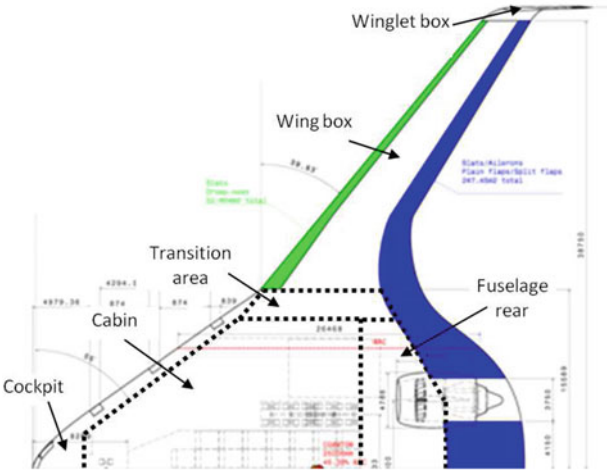

Fig. 3.19 BWB main structural parts

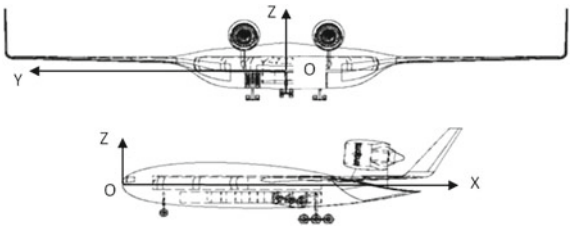

Fig. 3.20 BWB reference frame

- the *Y* axis directed from the fuselage center to the wing tip,
- and the *Z* axis defining a direct reference frame with the previous axis (and directed upward).

Except for the winglets (whose airfoil are defined in planes parallel to the *XOY* plane), the aircraft was defined by a series of airfoils whose coordinates are expressed in planes parallel to the *XOZ* plane, and for several positions in span (along the *Y* axis). The external shape can be defined by ruled surfaces between two consecutive airfoils.

3.3.2.3 Internal Geometry

Cabin volume was designed to obtain a capacity of 470 passengers divided into two classes (business class (BC) and economy class (YC)) on one deck. The cargo bay is designed to have a capacity of 30 LD3s (that is, 12 pallets). The rear landing gear boxes are located on both sides of the cargo bay as indicated in Fig. 3.21. The

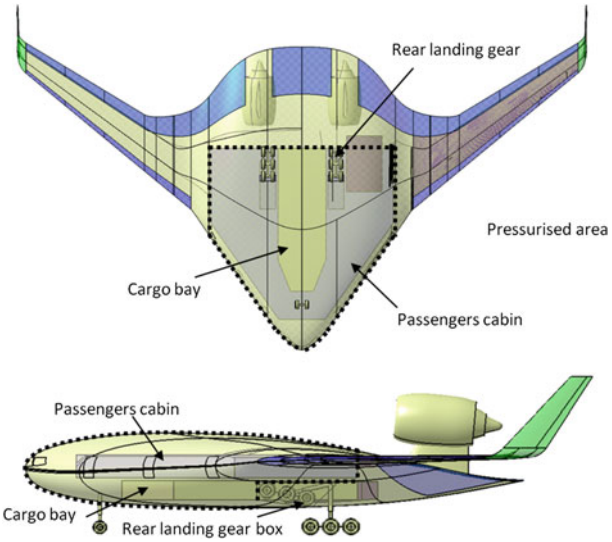

Fig. 3.21 CAD view of cabin and cargo bay locations in the BWB fuselage

pressurized volume of the cabin is thus defined (Fig. 3.21) by the external surface of the fuselage, the cabin bulkheads, and the lateral walls between the cabin and the transition area. Since the landing gear bays are not included in this pressurized volume, they will not be modeled as structural elements.

The pressurized area will be the subject of a specific structural concept developed in preceding European programs (VELA and NACRE). The rear part of the fuselage (non-pressurized) is delimited by the rear cabin bulkhead and the wall which will have to support the flaps. In the same way, the wing box is delimited by the leading and trailing edge spars which respectively support the four slats and the flaps (Fig. 3.22).

3.3.3 Material Properties

3.3.3.1 Composite Materials

The major part of the structure will be manufactured with carbon fiber/epoxy matrix laminates. C. Dienel from DLR-FA listed the advantages and the disadvantages (Table 3.1) of the various processes which could be used to manufacture the structure: hand lay-up, prepregs, or liquid composite molding (LCM).

According to Table 3.1, DLR deduced that it would be preferable, in terms of mechanical properties to production cost ratio, to use composites worked out by LCM. If the mass of the aircraft obtained with LCM composites would be too high, DLR-FA then recommends to choose prepregs, in order to save mass.

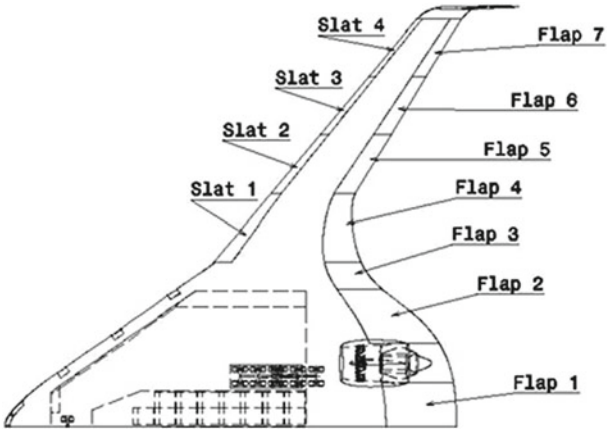

Fig. 3.22 Positions of flaps and slats

Another important material property is volumetric mass. TUM decided to take a volumetric mass of $1{,}800\,\mathrm{kg/m^3}$ for all composite materials due to the local reinforcements. Since this work concerns a preliminary design, the mass will be evaluated without considering the structure details. Some parts of the structure will be made up of a combination of structural elements, such as the wing and cabin skins. In both cases, the composite panels are stiffened by stringers.

To size the structure, a yielding stress criterion is required, and AIRBUS Hamburg suggested to use the following allowable strains for all considered composite materials:

Ultimate loads:

$$|\varepsilon| \leq \varepsilon_{\mathrm{ult}} = 0.5\,\% \tag{3.3}$$

Table 3.1 Qualitative evaluation of current composite manufacturing processes (from C. Dienel, DLR-FA)

	Hand lay-up	Prepreg technology	Liquid composite molding (LCM)
Initial cost	Low	High	Medium
Tooling costs	Low	High	High
Labor costs	High	Medium	Medium
Material costs	Low	High	Low
Series volume	<1,000 p.a.	<3,000 p.a.	<50,000 p.a.
Cycle time	3–24 h	5–24 h	15 min–24 h
Mechanical properties	Modest	Very good	Good
Quality	Modest	Very good	Good

Limit loads:

$$|\varepsilon| \leq \varepsilon_{\text{lim}} = \frac{1}{1.5}\varepsilon_{\text{ult}} = 0.35\,\% \tag{3.4}$$

This value has been obtained by dividing the ultimate load by a factor of 1.5. The allowable value for limit loads takes into account the margins due to fatigue and damage tolerance. The criterion which will be used contains the maximum absolute value of the principal strain, such as:

$$\varepsilon = \max\left(\varepsilon_{\text{I}}, \varepsilon_{\text{II}}\right) \tag{3.5}$$

This value is compared with one of the two values (3.3) and (3.4), depending on the studied load case, assuming that the allowable strains are identical in tension and compression.

3.3.3.2 Other Materials

Other materials which could be used in the structure design are essentially aluminum alloys with the following characteristics (recommended by TUM for a current alloy):

- Young's modulus $E = 70\,\text{GPa}$
- Poisson's coefficient $\nu = 0.3$
- yield strength $\sigma_{\text{e}} = 300\,\text{MPa}$ which leads to a yield strain of about $0.4\,\%$
- volumetric mass $\rho = 2{,}750\,\text{kg/m}^3$.

3.3.3.3 Technological Constraints

A major technological constraint is the minimal thickness of a laminate. For the skins, this thickness could be relatively small. However, composite materials being not ductile, possible impacts can cause more serious damage to composites than to metals. For the skins, AIRBUS recommends to use a minimal thickness of 2 mm in order to preserve a sufficient level of laminate damage tolerance.

3.3.4 Load Cases

3.3.4.1 Cabin Pressurization

The maximum pressure difference in the passenger cabin and the cockpit, at the highest flight altitude, is $\Delta p = 0.7\,\text{bar}$. This value corresponds to the difference between the cabin and the atmospheric pressure, multiplied by a safety factor. Two cases have to be considered:

- limit pressure with $\Delta p = 0.7\,\text{bar}$
- ultimate pressure with $\Delta p = 0.7\,\text{bar} \times 2 = 1.4\,\text{bar}$

The second case corresponds to the cabin pressure test. During the sizing step, this case will be considered apart from the other load cases.

3.3.4.2 Aerodynamic Loads

The total lifting force L acting on the half-BWB is given by the relationship:

$$L = \int_0^{Y_T} l(y)\,\mathrm{d}y = \frac{1}{2} M g f_\mathrm{L} \tag{3.6}$$

where M is the mass of the aircraft (MTOW, MZFW, …) depending on the considered flight configuration, g the acceleration of gravity ($9.81\,\text{m/s}^2$), and f_L the load factor. Let be:

$$\Delta Y_\mathrm{t} = \frac{1}{3}\left(Y_\mathrm{E} - Y_\mathrm{F}\right) \quad \text{and} \quad \Delta Y_\mathrm{w} = \frac{2}{3}\left(Y_\mathrm{E} - Y_\mathrm{F}\right) \tag{3.7}$$

the lengths of the second zone, where the subscripts t and w are related to the second and last third of the wing span, respectively. The lifting force is then equal to:

$$L = \left(\frac{1}{2}\Delta Y + \Delta Y_\mathrm{w} + Y_\mathrm{F}\right) l_\mathrm{max} \tag{3.8}$$

from where one can easily deduce l_max and consequently the aerodynamic pressures exerted on the fuselage (p_f) and the wing (p_w), given by:

$$p_\mathrm{w} = \frac{l_\mathrm{max}\Delta Y_\mathrm{w}}{A_\mathrm{w}} \quad \text{and} \quad p_\mathrm{f} = \frac{l_\mathrm{max} Y_\mathrm{F}}{A_\mathrm{f}} \tag{3.9}$$

where A_f and A_w are the projected areas of the fuselage and the 2/3 wing, respectively. For the fuselage, as for the wing, one considers the total projected area (from the leading edge toward the trailing edge), that is, the area including slats and flaps.

The calculation of the pressure distribution to be taken into account in the FE model will be based on an elliptic distribution. The two values of mass (for the half-BWB) to consider for the calculation of this new pressure distributions are MTOW = 200 t and MZFW = 151 t. The calculation has been performed considering the following law for the kinetic lifting force l:

$$l = l_\mathrm{max}\sqrt{1 - \left(\frac{Y}{Y_\mathrm{E}}\right)^2}. \tag{3.10}$$

Together with (3.9), the following relationship results:

$$L = \sum_{i=1}^{N} l_i(Y)\Delta Y_i = l_{\max} \sum_{i=1}^{N} \sqrt{1 - \left(\frac{Y_i}{Y_E}\right)^2}\,\Delta Y_i = \frac{1}{2} M g f_L \tag{3.11}$$

Equation (3.11) allows to calculate $l_{\max}$ by carrying out the summation on a number N of slices along the span Y. For the three loading cases considered hereafter, the following values have been calculated:

- Case A: $l_{\max} = 161{,}228\,\mathrm{N/m}$ for $M = 200\,\mathrm{t}$ (MTOW of the half-BWB) with $k = 2.5$
- Case B: $l_{\max} = 121{,}727\,\mathrm{N/m}$ for $M = 151\,\mathrm{t}$ (MTOW of the half-BWB) with $k = 2.5$
- Case C: $l_{\max} = 64{,}491\,\mathrm{N/m}$ for $M = 200\,\mathrm{t}$ (MTOW of the half-BWB) with $k = 1$

To calculate the pressure field, it is necessary to take into account the chord variation law according to Y. The chord is interpolated linearly between two reference airfoils. For each section located at a Y_i position, the pressure p_i is given by:

$$p_i = \frac{l_{\max}}{c_i} \sqrt{1 - \left(\frac{Y_i}{Y_E}\right)^2}\,, \tag{3.12}$$

where c_i is the local chord at position Y_i. The pressure distribution calculated according to (3.12) gives, a priori, a load case more unfavorable than that initially proposed by TUM. In Fig. 3.23 the strong differences due to the various Cases A–C are shown.

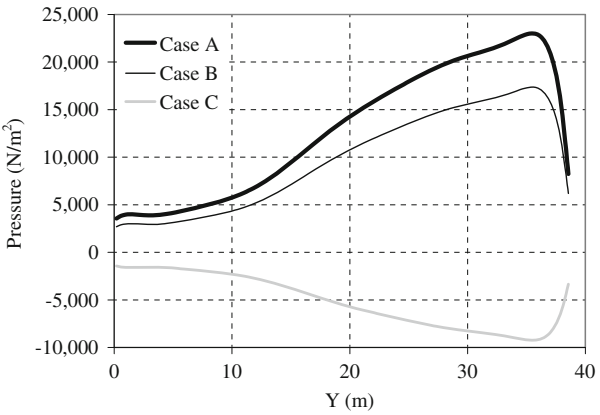

Fig. 3.23 Pressure distributions calculated for the load Cases A, B, and C

Table 3.2 Load cases considered for the BWB sizing

Load			Maximum	Mass		Load factor		Cabin pressure
Case	Subcase	Type	strain (%)	Type	Value (t)	Aero. (g)	Inertia (g)	(bar)
A	1	Limit	0.34	MTOW	200.0	2.5	−2.5	–
	2	Limit	0.34	MTOW	200.0	2.5	−2.5	0.7
B	1	Limit	0.34	MTOW	151.0	2.5	−2.5	–
	2	Limit	0.34	MTOW	151.0	2.5	−2.5	0.7
C	1	Limit	0.34	MTOW	200.0	−1.0	1.0	–
	2	Limit	0.34	MTOW	200.0	−1.0	1.0	0.7
D	1	Ultimate	0.50	–	–	–	–	1.4

3.3.4.3 Load Cases Summary

The various loading cases, which have to be considered to size the primary structure, are summarized in Table 3.2. The positive sign means that the loads are applied upward (that is, on the lower side for the aerodynamic loads), while the negative sign means that the loads are directed downward. For the first three Cases A, B, and C, the inertia loads are always applied in the opposite direction to the aerodynamic loads. In the Case D, one considers only the ultimate cabin pressure without any other load.

3.3.5 Structural Concepts

3.3.5.1 Passengers Cabin

The structural concept adopted by ONERA for the pressurized part of the fuselage is that which had already been proposed in the previous European programs VELA [4] and NACRE [2], totally or partially dedicated to flying wings. The pressurized part of a flying wing, made up of a volume which upper (suction face) and lower sides (under-surface) are relatively flat, constitutes the most unfavorable configuration in terms of structure behavior with respect to the compressive forces. In this area, the fuselage does not have a circular cross section, and the pressure cannot be only balanced by tensile stresses in the skins. In the absence of frames, the upper and lower skins will be subjected to bending moments, and thus to very important stress gradients through the thickness. The main issue of this configuration is that it is necessary to stiffen the skin in order to limit, as much as possible, the flexural strains (and consequently the stresses) to minimize the mass. By order of decreasing importance, the three types of loading which induce bending moments on the fuselage skins are:

- the cabin pressurization,
- the transmission of a part of the bending moment from one wing to the other (along the *Y* axis), the other part being transmitted by nonpressurized rear part of the fuselage,

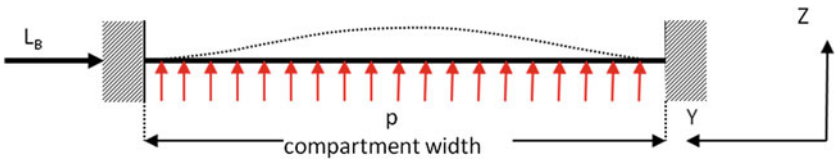

Fig. 3.24 Loads acting on the fuselage upper skin

- and the transmission, along the fuselage (according to direction X), of the bending moment induced by the weight of the aircraft structure as well as freight and passengers.

The first and the third load cases all concern the cabin, while the second concerns, approximately, the part of the fuselage located between the wing roots.

If one considers the cabin separation walls as nondeformable (in fact there are slightly extended in traction), the upper side and lower side can be modeled (Fig. 3.24) as flat panels clamped at their two ends. One of the two supports is fixed (on the level of the symmetry plane XOZ of the fuselage), the other is movable.

The inner side of the skin is subjected to the cabin pressure p, since on one of the embeddings one has a tensile force L_B or a compression force, induced by the bending moment M_B passing through the central part of the fuselage and due to the aerodynamic lifting force acting on the wings.

3.3.5.2 Configuration

In this configuration, it is obvious that a skin of a few millimeters thickness will be unable to support these loads. The proposed single shell concept should support the skin with transverse frames (I cross-section beams) lying in the direction Y. These frames are in theory sufficient to support compression and tensile stresses induced by the cabin pressurization acting on the skins. They support also the tensile (or compression) stresses due to the side forces L_B.

The bending moment supported by the transverse frames being very important, the frame pitch is considerable smaller (about half) in X direction than in Y direction. However, these frames are not able to support the bending moment along the X axis, due to the weight of the aircraft. For this reason, it is also necessary to put frames in the X direction. To avoid skin buckling, it would then be necessary to put stringers on the inner skin side in the X direction.

The transverse and longitudinal frames constitute a kind of grid of the fuselage structure which is able to support at the same time the cabin pressure as well as the bending moments due to the lifting loads and the aircraft weight. The skins, lying on a frame network, can then be locally considered as plates embedded on their circumference. Since the frames support the bending moments as well as the lateral compression load, the skin can then have a small thickness. However, in order to avoid a too large deflection of the skin panels located between each frame under the

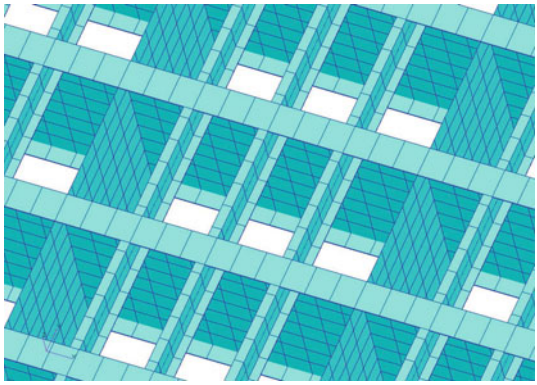

Fig. 3.25 Skin stringers layout within the supporting grid

action cabin pressurization, it is also necessary to put stringers on the inner skin side. Three stringers were laid out according to Fig. 3.25.

3.3.5.3 Finite Element Modeling of a Fuselage Portion

After having described the basic fuselage structure as well as the principles which guided the technological choices, it is necessary to check, in detail, if the design solutions are relevant from a mechanical point of view, and if they lead to a light-weight concept. For this purpose, the single shell structure has been modeled by finite elements to check the structural behavior under cabin pressurization and buckling.

A representative flat portion of the fuselage has been considered. It contains 13 transverse frames along the X axis and 8 longitudinal frames along the Y axis. The skins and the frames were meshed with 4 node quadratic elements (Q4 linear interpolation), while the frame flanges as well as the stringers were meshed with beam elements. This mesh is sufficiently refined to calculate the local displacements and deflections to show the stress concentrations and to perform buckling calculation with confident results. The boundary conditions consist of clamping (blocking of Y displacements) on one side, a blocking of vertical displacements (according to Z) on the longitudinal frames. In this area, the frames can be considered as embedded on one side, but free to move in the transverse direction on the opposite side, due to the lateral load L_B, a blocking of displacements along X on both the transverse frame ends.

The materials used to manufacture the different components are:

- for the skins: quasi-isotropic carbon-fiber-reinforced polymer (CFRP) laminate
- for the longitudinal and transverse frames: orthotropic CFRP laminate
- and for the stringers: orthotropic CFRP laminate.

The cabin pressurization $p = 0.7$ bar (see Sect. 3.3.4.1) and the lateral load L_B have been taken into account. This load depends on the bending moment due to the

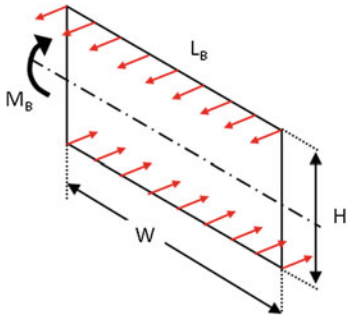

Fig. 3.26 Membrane loads acting on fuselage skin

aerodynamic pressure distribution discussed in Sect. 2.4. The most adverse loading Case A has been applied by integrating the respective pressure distribution.

According to the diagram of Fig. 3.26, one can estimate the lineic compression load L_B in the following way. If we assume that only the lower and upper skins of the fuselage support the bending moment, one can then write that:

$$L_B = \frac{M_B}{HW} \tag{3.13}$$

where W and H respectively represent the equivalent width of the fuselage involved in the transmission of the bending moment and the distance between the two skins. A mean value of L_B equal to approximately 500 kN/m was calculated.

The first calculation checked the stresses induced by the cabin pressurization only. Figure 3.27 shows the map of the displacement field calculated by FEM, where it is clearly visible that displacements result from the superposition of a global displacement due to the transverse frame deflection, and a local skin deflection, limited to small values because of the stringer stiffness. The mean skin waviness amplitude does not exceed 20 mm, which should not deteriorate the air flow around the fuselage, and thus the aerodynamic performances. Strain distributions in the skins and the frames have been checked. It can be noted that the maximum strain does not exceed 0.2 %, which largely satisfies the allowable strain criterion in Sect. 3.3.3.1. The longitudinal frames are strained at a very low level.

In the overall weight estimation, the transverse frames have the most significant weight contribution, because they mainly support the bending moments. Overall, a total specific weight of 21 kg/m^2 was estimated for the design.

In addition to the pressure cabin loading case, we added a lateral compression load $L_B = 500$ kN/m to check the buckling behavior of this fuselage portion. We chose a nonlinear elastic calculation method, giving results closer to reality. This calculation consists of application of load increments and to evaluate the tangent stiffness matrix at each iteration. For the initial concept, the buckling load is equal to approximately 25 % of the ultimate load. This small value was mainly due to the local buckling of the transverse and longitudinal frame flanges. It has been decided to put stiffeners on the longitudinal frames, and to reinforce the lower parts of the transverse frames with

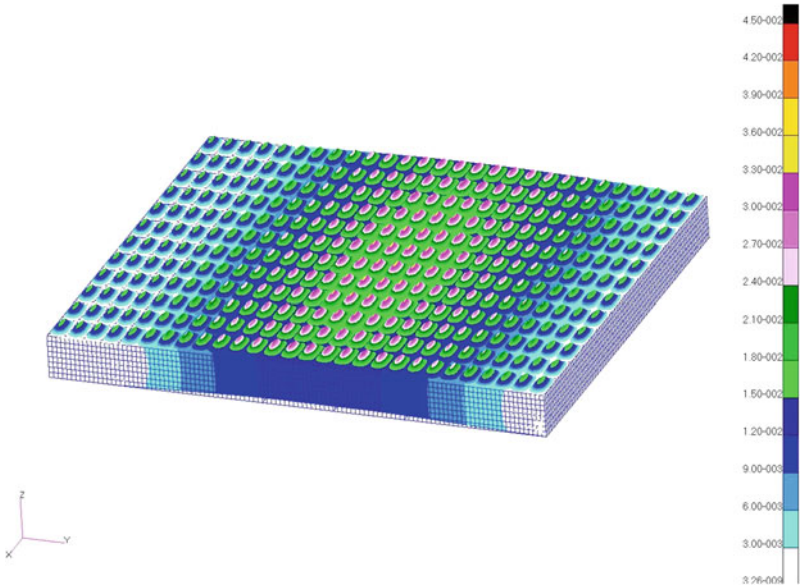

Fig. 3.27 Displacement field (*left scale* in m) calculated for cabin pressure only

cross-section beams. The frames were also reinforced by using a sandwich structure to increase the flexural inertia in the transverse direction. Since the transverse flexural stiffness of the frames plays a central role, it is preferable to reinforce them by a kind of stringer, rather than to increase the web thickness. For this reason, the thickness of the transverse frames was not modified.

The thickness of the skin was changed, and this modified structure supports the combined effect of the cabin pressurization and the lateral compression load. In fact, L_B has a stiffening effect on the frames, and the global displacement is smaller than that obtained for the cabin pressurization only. The mass per unit area increases from 21 to 23 kg/m^2. The cabin will thus be reinforced in this way to resist at the same time to the internal pressurization, to the compression load induced by the bending moment due to the wings, but also to the bending moment due to aircraft own weight and payload (along axis X). As for the wing, we will use an equivalent material with specific properties for membrane/flexion coupling.

3.3.5.4 Cabin Lateral Bulkheads

Around the cabin, the forces induced by cabin pressurization are supported by three convex walls located:

- at the fuselage leading edge (CB1),
- between the cabin and the transition area (CB2),
- at the rear cabin bulkhead (CB3).

In the optimal case, these walls should have a semi-cylindrical shape, in order to balance the cabin pressure by tensile stresses, to minimize the wall deformation as well as its thickness and mass. This constitutes the ideal case which, in fact, is only satisfied for CB3 since it is not possible to design a semicircular wall when:

- the external shape is imposed, as for the leading edge of cabin (CB1), by the aerodynamic shape of the airfoil,
- there is a strong variation of the external shape, as in the transition area.

In those cases, the wall can have only an elliptic shape which main dimensions ($b/h < 1$) are imposed by the tangency conditions with the other surfaces. Indeed, when the b/h ratio decreases, it is necessary to increase the wall thickness to maintain the strains below the allowable level, which leads to an increase in the mass. The addition of stiffeners on the wall skin (I cross-section shape) makes it possible to reduce the strains, by limiting the deflection, and thus to minimize the mass. This is the solution adopted in the fuselage concept to stiffen the bulkheads CB1 and CB2, but also CB3. Although in the rear bulkhead CB3, the shape is already semicircular, stiffeners were added to improve the elastic stability of the bulkhead regarding to local buckling.

3.3.5.5 Passengers Floor

The passengers floor (Fig. 3.28) is manufactured with composite material transverse beams (along Y axis) connected by some longitudinal beams of the same size. These beams confer floor flexural stiffness, and support another set of beams of smaller section along the X axis, with a small pitch to be able to fix the passenger seat rails. The largest beams are connected to the cabin separation walls as well as the cabin bulkheads by lattices made up of circular cross-section rods connected to the X and Y frames. There are two kinds of lattices: those laid out in vertical plane to attach

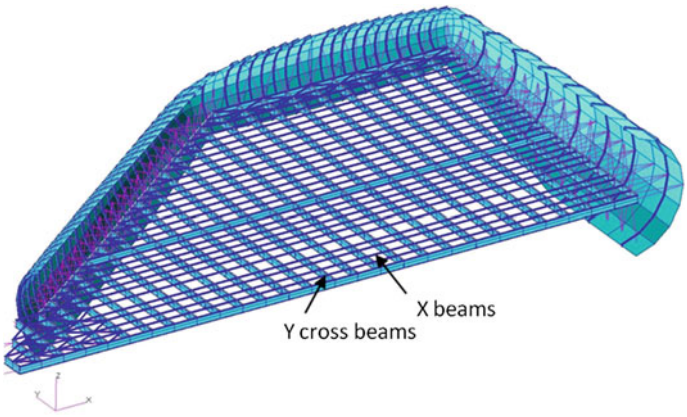

Fig. 3.28 Passengers floor mesh and construction

the cabin floor to the cabin structure, and those arranged on a horizontal plane to attach the passenger floor to the bulkheads to avoid large lateral displacements. This lattice consists of parallel rods connected to each other by rods laid out in diagonal (Fig. 3.28) to support the shear forces.

3.3.5.6 Transition Area

The transition area is a more complex structure subjected to high loads, since the bending moment is transmitted from the wing to the fuselage, as well as the shear forces. Figure 3.29 shows two views of the FE mesh to distinguish the main components:

- the skins (on top left of Fig. 3.29),
- the four spars: the first (S1) connecting the cabin leading edge spar, and the third one (S3) connecting the trailing edge spar to the rear fuselage spar,
- stiffeners laid out between the spars on the skin sides and connecting the wing box to the fuselage *Y* frames.

The four spars are reinforced by flanges (not shown in Fig. 3.29) extended to the wing.

3.3.5.7 Rear Fuselage

The rear fuselage part, although not pressurized, has to support the engines, the aerodynamic pressure loads, and the forces at the flap hinges. It also transmits a fraction of the wing bending moment, because the last spar of the transition area is attached to one of the two transverse frames. The structure is conventional in the sense that it consists of two spars connected with ribs, on which lie the skins. In this manner, the structure is designed as a nondeformable box. However, spars,

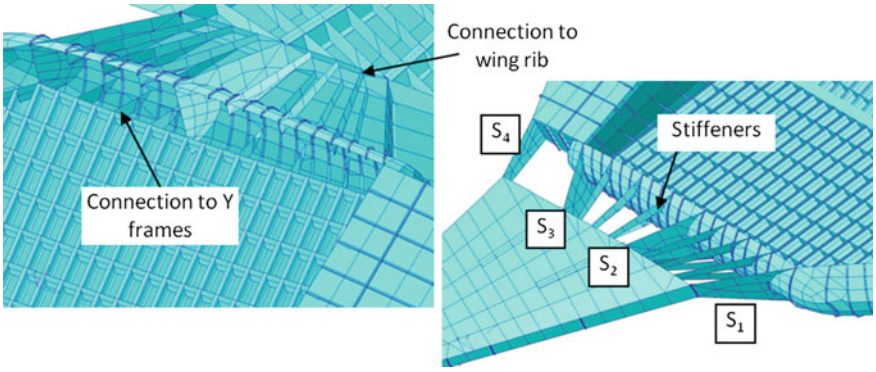

Fig. 3.29 Transition area structure

ribs, and skins are thin, and the risk of buckling is avoided by laying stiffeners on these components. To simplify the FE model, the engine mast is modeled with beam elements connected to one of the spars, and the engine is represented by a mass point.

3.3.5.8 Wing

The wing can be divided in three zones (Fig. 3.30) called W_1, W_2, and W_a. The two first are related to the wing itself, while the last one is related to the reinforcement of the wing tip in the vicinity of the winglet. The structure contains four spars in W_1 part and three in W_2, ribs as well as skins (not shown in Fig. 3.30). The skins and the spars are subjected to compression and tensile stresses due to the bending moment, while the ribs ensure the elastic stability of the skins with respect to global buckling. Between two consecutive ribs, the skins are reinforced by stringers to avoid local buckling.

The rib pitch p_R has been determined by the following empirical rule:

$$p_R = 0.8\sqrt{t_A} \tag{3.14}$$

where t_A is the airfoil thickness. Since the airfoil chord (and consequently the thickness) decreases from the wing root toward the wing tip, p_R decreases also along the span Y_L. In order to build the wing mesh in a simple way, the rib pitch is varied by steps of decreasing values.

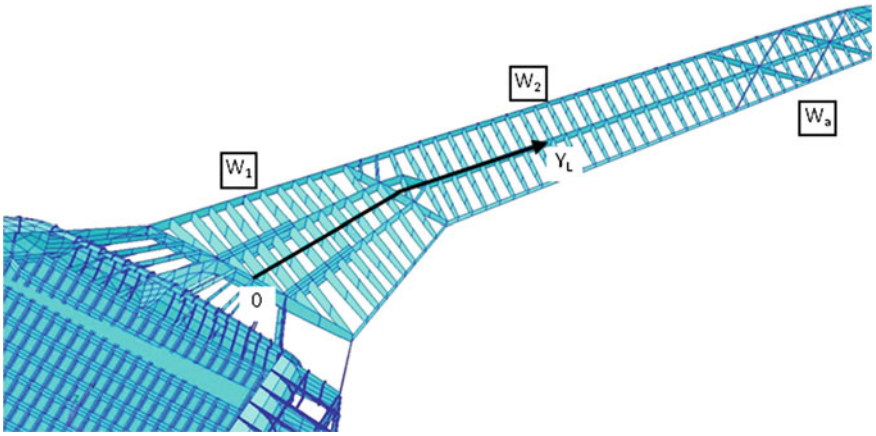

Fig. 3.30 Wing structure

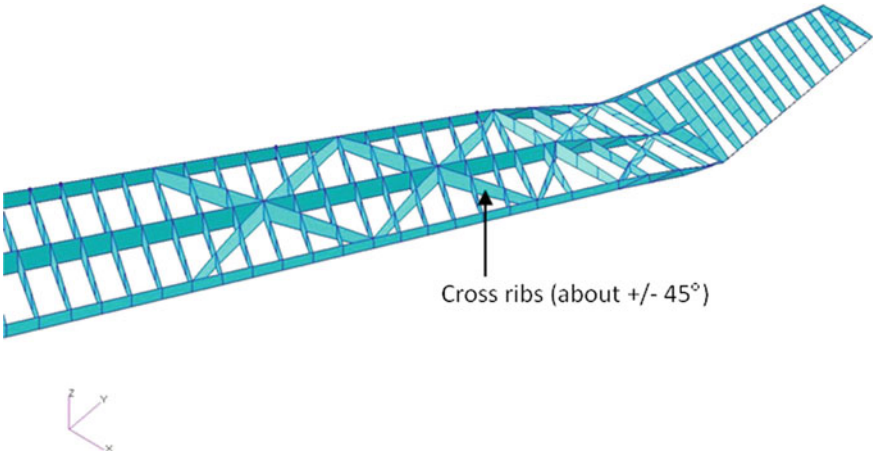

Fig. 3.31 Winglet structure

3.3.5.9 Winglet

The winglet has the same structure as the wing, except that there are two spars instead of three (Fig. 3.31). Preliminary flutter analyses revealed a too great flexibility in torsion of the wing area W_a. Consequently, this area was reinforced by cross ribs laid out at angles equal to more or less 45° to the spar direction. The flutter calculations moreover showed that the mass of the winglet was also important, and that its size had to be reduced.

3.3.5.10 Flaps and Slats

In order to simplify the FE model, which has to be sufficiently representative of the real structure behavior (in particular for flap modes), the slats and the flaps were modeled with plate elements (Fig. 3.32), in accordance with the geometrical data of Chap. 2, namely:

- 4 slats (1–4) attached on the wing box,
- 4 flaps (4–7) attached to the wing box, and
- 3 flaps (1–3) attached to the rear fuselage.

The structure of each flap consists of two skins assembled on spars and ribs. A flap is articulated on the wing trailing edge with several hinges and is actuated by jacks. The jacks (2 per flap) and the hinges (3 per flap) were modeled with beam elements on which stiffness and mass were allocated. The hinge and jack masses were determined by analytical formulations and were distributed on the flaps. Figure 3.51 shows a flap cross section and one can consider, at first approximation, that the two skins constitute an isosceles triangle. From the trailing edge spar heights h_1 and h_2 corresponding to the flap span beginning and end positions, we determined the

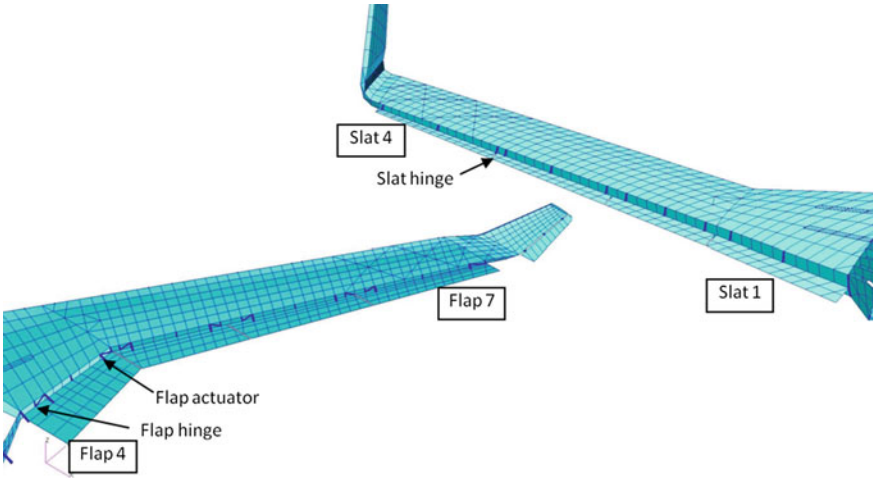

Fig. 3.32 Slats and flaps FE modeling

average height h of this flap as well as the average heights H_{m} (Fig. 3.33), such that:

$$h = \frac{h_1 + h_2}{2}; \quad H_{\mathrm{m1}} = \frac{5}{6}h; \quad H_{\mathrm{m2}} = \frac{1}{2}h; \quad H_{\mathrm{m3}} = \frac{1}{3}h \tag{3.15}$$

In order to take into account a decreasing flexural stiffness, the flaps were divided into three elements along the chord c. Each element consists of two skins of same thickness e, parallels between them with a distance H_{m1}, H_{m2}, and H_{m3} according to their position in chord. In the FE model, a plate element is thus affected with a thickness $2e$, and its inertia I_1 per unit of width has a value:

$$I_1 = \frac{(2e)^3}{12} \tag{3.16}$$

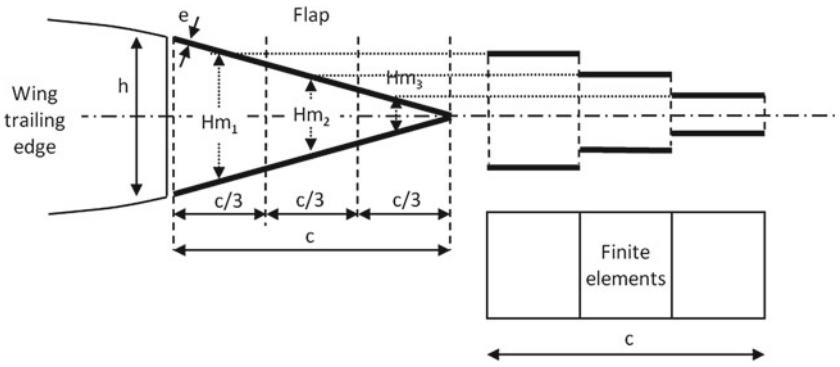

Fig. 3.33 Equivalent flap stiffness scheme

In fact, the real inertia I_2 of the plate element is:

$$I_2 = 2e\left(\frac{H_\mathrm{m}}{2}\right)^2 \tag{3.17}$$

In the Nastran plate element properties card we affected a multiplying coefficient R for the inertia of each element, in function of its position in chord such as:

$$R = \frac{I_2}{I_1} = \frac{2H_\mathrm{m}^2}{e^3} \tag{3.18}$$

The material considered is a quasi-isotropic composite laminate. Since inertia depends primarily on the skins, only the skins were taken into account in the calculation of R.

3.3.6 Nonstructural Masses

The FE model automatically takes into account the mass of each element, through the dimensions and the density of the material (see Sect. 3.3.3.1). However, it is also necessary to incorporate the nonstructural masses.

3.3.6.1 Fuel Tanks

Among all these masses, the fuel ($\rho = 803\,\mathrm{kg/m^3}$) represents the most important part, and is distributed as follows (Fig. 3.34):

- Wing tank 1: 13,500 kg
- Wing tank 2: 5,150 kg
- Wing tank 3: 4,750 kg
- Center tank: 35,300 kg.

For each tank, the masses were assigned uniformly on the tank projected area, connected to the eight nodes located at the corners of each subtank (the displacement of each node of the structure is related to the displacement of the mass node).

In this model, we considered a full fuel center tank located in the fuselage area indicated in Fig. 3.35, that is, below the passengers floor and over the X and Y frames of the fuselage primary structure.

As proposed by Airbus, this tank will be probably used to adjust the aircraft CG and will not be uniformly filled over its entire length. This procedure allows to adjust the CG position X_g (compared to origin 0 of Fig. 3.35) by variation of the filling length X_m.

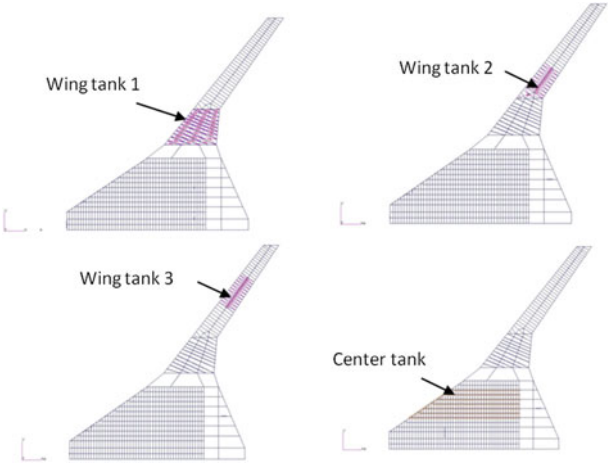

Fig. 3.34 Fuel tanks mass distribution on the BWB FE model

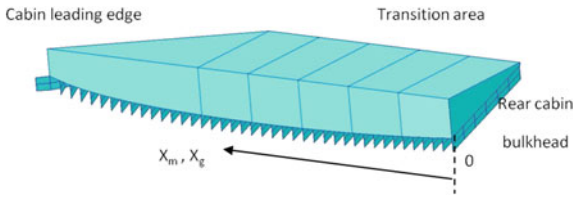

Fig. 3.35 Center fuel tank geometry

3.3.6.2 Flaps, Slats and Landing Gears

Due to the size of the flaps located at the rear fuselage and the loads they have to support, their mass per unit area is higher than those of the flaps located on the wing trailing edge. Within the framework of the previous European Commission (EC) program NACRE task 3.2, concerning the engine integration at the rear of a flying wing, these flaps have been suitably meshed. From this work, a realistic value has been estimated for this unconventional flap.

The mass of the landing gear was assigned in the same way as for the fuel tanks. The masses were distributed uniformly over the projected area of the bays and on the lower side skin of the fuselage. To preserve the simplicity of the model, the landing gear boxes were not meshed, although they probably represent a certain mass penalty (Fig. 3.36).

3.3.6.3 Equipments

The masses of the equipments have been grouped into three categories:

- navigation and communication: 900 kg
- electric systems and furnishings: 9,685 kg
- operating items: 17,710 kg.

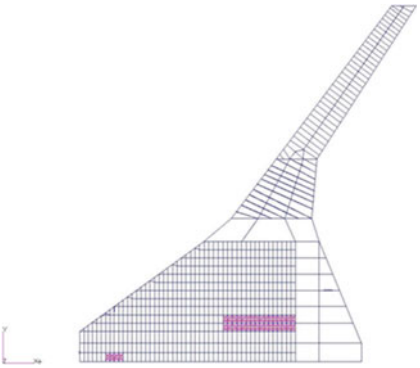

Fig. 3.36 Landing gears mass distribution on the BWB FE model

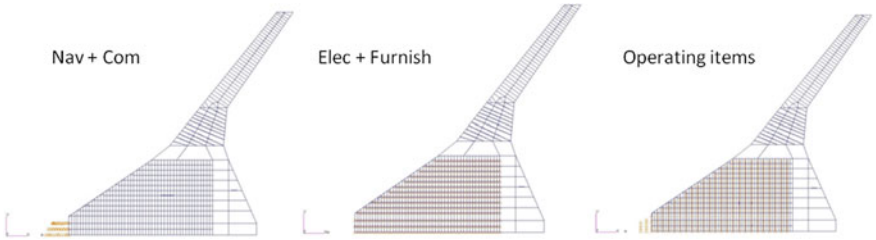

Fig. 3.37 Equipment mass distribution on the BWB FE model

These values were obtained by gathering the various mass items provided by TUM. Their assignment has been done in the same way as explained before (Fig. 3.37).

3.3.6.4 Freight and Passengers

The mass assignment is shown in Fig. 3.38. Freight as well as passengers masses were evaluated as 7,200 and 19,100 kg, respectively.

3.3.7 Finite Element Calculation

3.3.7.1 Mesh

Only one half of the aircraft has been meshed (Fig. 3.39), and the mesh is composed of the following elements (with linear displacement interpolation):

- CQUAD4: quadrangular plate elements
- TRIA3: triangular plate elements

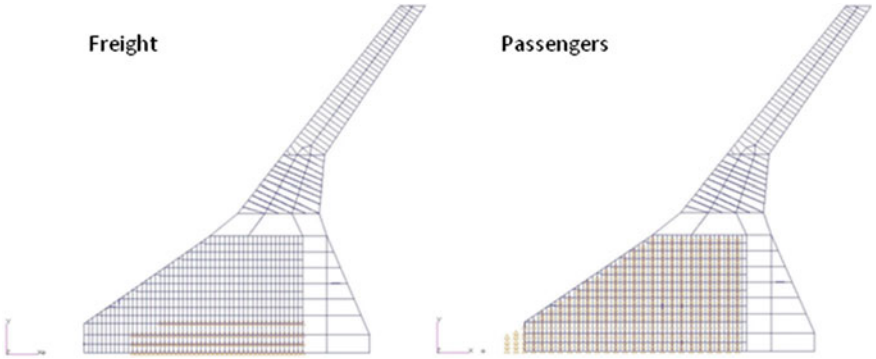

Fig. 3.38 Freight and passengers mass distribution on the BWB FE model

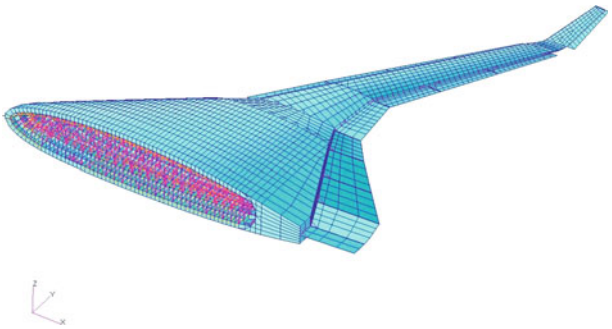

Fig. 3.39 Complete FE model of the half-BWB

- CBAR: beam element
- CROD: rod elements (tensile/compression force along rod axis only).

The total number of nodes and elements are equal to about 11,800 and 23,000 respectively. The structure has been meshed with PATRAN software and the FE calculations were performed with NASTRAN (MSC Software).

3.3.7.2 Loads and Boundary Conditions

For the static calculations, the loading cases of Table 3.2 were applied to the model. The boundary conditions consisted in blocking in the mid plane ($Y = 0$):

- all the displacements in the Y direction for the nodes located in this plane (loading symmetry condition),
- displacements in the Z direction for the nodes located at the two ends of the fuselage,

- and some displacements in the X directions for the nodes located in the vicinity of the cockpit.

3.3.7.3 Strain Analysis Procedure

For each loading case, it was evaluated that the strains supported by the different structural components did not exceed the allowable values of Table 3.2. Consider loading Case D, for which the allowable strain should not exceed 0.5 %. Let the principal strains calculated at the center of each element number i ($i = 1, \ldots, N$) of a given structural component (for example, the lower fuselage skin), N being the number of elements of this component. For each element i, one takes only into account the maximum value of the principal strain, such as:

$$\varepsilon^i = \max\left(\varepsilon_{\mathrm{I}}^i, \varepsilon_{\mathrm{II}}^i\right), \tag{3.19}$$

$\varepsilon_{\mathrm{I}}^i, \varepsilon_{\mathrm{II}}^i$ being the principal strains.

For each element having an area S_i, the couples (S^i, ε^i) are ranked by increasing strain values, such as:

$$\varepsilon^i < \varepsilon^{i+1} \tag{3.20}$$

The associated probability is then evaluated with the following relationship:

$$P^i = \frac{\sum_{j=1}^{i} S^j}{\sum_{j=1}^{N} S^j}, \tag{3.21}$$

the denominator representing the area of the component. In this way, one obtains the fraction of the component area for which the strain is smaller than a given value ε^i. The graph of Fig. 3.40 shows the strain distribution function for the lower fuselage skin calculated for the loading Case D of Table 3.2.

From Fig. 3.40, it is obvious that 60 % of the skin area is subjected to a strain lower than about 0.2 %, and that the whole component is not subjected to strains higher than 0.5 %. The strain criterion (1) is thus satisfied. From the distribution of Fig. 3.40, the strains at different area percentages have been extracted for the loading Case D. As a matter of fact, more than 99 % of the skin area is subjected to strains lower than 0.47 %, and that only 1 % exceeds the limit strain of 0.5 %.

In this kind of analysis, it is necessary to keep in mind that the FE model is the result of a preliminary design approach, so all the parts of a given component are not obliged to be under the allowable value. For example, one can tolerate that 5 % (even 10 %) of the component area will be above the allowable value, because generally a large fraction of the component will be subjected to very small strains. Since the

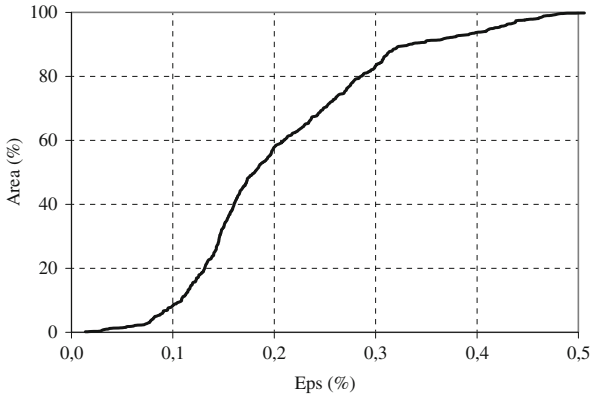

Fig. 3.40 Max strain distribution calculated for the upper skin and load case D

thickness was set to a constant value for a structural component, the mass surplus of the less strained areas could be reallocated to the higher strained areas, which leads to a mass redistribution without global mass variation.

3.3.7.4 Static Calculation Results

To illustrate the preceding step, the graph of Fig. 3.41 clearly highlights that in most of the components, 95 % of their area is under the allowable strain of 0.34 %. Some components should therefore be reinforced, but within the framework of this project and regarding the small percentages concerned by higher strains, this is more relevant for a detailed design.

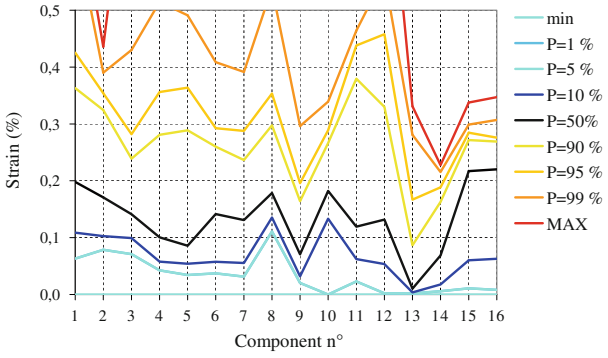

Fig. 3.41 Max strain distribution functions for the different fuselage parts for load Cases A, B, and C

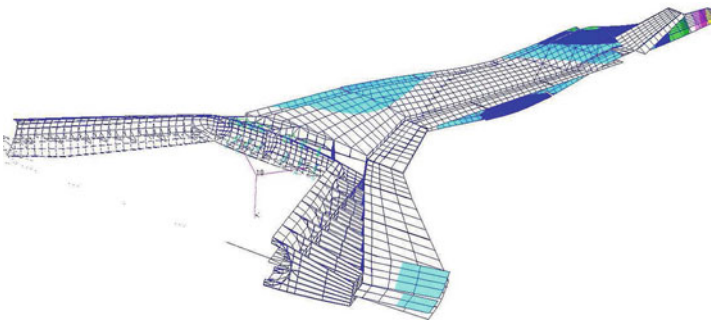

Fig. 3.42 An example of superimposition of global and local modes ($f = 8.8$ Hz)

3.3.7.5 Modal Analysis Results

Modal analysis has been performed under NASTRAN to check if there were no local modes which could lead to a more complicated flutter analysis. During this task, several analyses were performed, especially for the cabin floor, which was reinforced to eliminate most of the local modes. The first wing bending mode comes to lie at 1.16 Hz. Bending and torsion modes of the wing can be easily identified since they are not coupled. But at higher frequencies, some local modes can appear as shown in Fig. 3.42. The shown mode is a result of a superposition of a global wing mode and a local flap mode.

The first passenger floor mode is over 10 Hz, which is in agreement with the recommendations of the ACFA team. Since one of the goals of this project is to study the influence of the aircraft aeroelastic behavior on the passenger comfort, floor stiffness properties have also to be set by the following design tasks. This will be easily done in the FE model, where the main components are set in different element groups which can be clearly and quickly identified.

3.3.8 Mass Estimation

3.3.8.1 Weight Breakdown

Table 3.3 summarizes the weights estimated for the different aircraft configurations. It gives the weight breakdown of the BWB primary structure calculated from the FE model. This table includes some values estimated by TUM such as the engine and the landing gears.

MTOW and MZFW are respectively equal to 391 and 273 tons. These values can be compared to the values taken into account to determine the loading cases of Sect. 3.3.4, which were equal to 400 and 302 tons respectively. The calculation

Table 3.3 Weight summary for the half and complete BWB

Item	Item weight (kg)	Total (kg)
Structure	164,292	164,292
Equipments	21,170	(MWE) 185,462
Ops items	35,420	(operating empty weight (OWE)) 220,882
Freight and pax	52,582	(MZFW) 273,464
Fuel	116,800	(MTOW) 390,864

carried out with the initial values in Sect. 3.3.4.2 is thus slightly conservative and the weight difference is acceptable.

3.3.8.2 Aircraft Mass and Inertia Properties

The values of the half aircraft inertias given by the FE model at the CG, in the reference frame (Sect. 3.3.2), are given in Table 3.4. The position of CG is quite the same between both configurations, although inertias vary much more significantly because of the full tanks.

3.3.9 Conclusion

The initial model has been modified many times to take into account the suggestions of the different partners. In accordance with the remarks of TUM, some parts of the structure were reinforced with respect to buckling, and the material properties have been updated according to the technological constraints induced by the manufacturing process. The flutter preliminary calculations showed that it was crucial to reinforce the winglet and the surrounding attachment area at the wing tip, and to reduce the winglet area. The updated model was finally delivered to the partners responsible for model analysis and reduction.

Table 3.4 Inertia of the complete BWB calculated at the aircraft CG in the reference frame

	MTOW	MZFW
Inertia (kg m^2)		
XX	2.6224E+07	1.6127E+07
YY	3.0242E+07	2.4743E+07
ZZ	5.3114E+07	3.8209E+07
CG location (m)		
Xg	23.64	23.55

3.4 Aerodynamic Modeling

C. Breitsamter, M. Meyer, D. Paulus and T. Klimmek

Unconventional aircraft designs like BWB designs are a possible solution to achieve the ambitious economic and ecologic goals of future air transport systems to reduce the fuel consumption, CO_2-emissions by 50 % and the external noise by 4–5 dB. In previous project dealing with BWB configuration, like the EC-funded projects VELA (2002–2005) and NACRE (2005–2008), the high need for active control and related expertise has been identified. Since flight control design and flight performance are strongly influenced by the aircraft aerodynamics, it is inevitable to have accurate aerodynamic predictions even in the preliminary design process. Due to the strong nonlinear phenomena occurring on the BWB configuration, results of acceptable accuracy can only be obtained by high-fidelity simulations as opposed to simplified approaches, for example, empirical methods or linear aerodynamic methods without corrections. This section summarizes the aerodynamic computations carried out in task 2.2 of ACFA 2020. The goal is to provide a database of steady and unsteady aerodynamic data for task 2.3 that can be used for the setup of a reduced aerodynamic model in the frequency domain of the flight dynamics and the aeroelasticity of the ACFA BWB configuration. The data should cover the complete flight envelope, from low speed to cruise speed.

At first, the numerical methods used for the aerodynamic computations by the different partners, DLR-AE, FOI, NTUA, and TUM-AER, are explained with the focus on the fundamental concepts covering the flow physics.

3.4.1 Numerical Methods

In this subsection, the employed numerical methods are briefly described. Since potential flow methods are very robust and time efficient, they are the standard tools for aeroelastic simulations in industrial practice. Nevertheless, computational fluid dynamics (CFD) solvers provide much better accuracy in the transonic regime. Hence, several flow solvers based on different numerical methods are applied for the ACFA BWB configuration to provide the best fitted and most efficient solution approach according to different flight conditions. Furthermore, a comparison between independent flow solvers is valuable to assess the numerical results in lack of experimental data. DLR-AE used linear potential flow methods to predict the aerodynamic pressure distribution. FOI, NTUA, and TUM-AER solved the Euler equations, while FOI also conducted simulations based on the Reynolds-averaged Navier-Stokes (RANS) equations. The structured and unstructured meshes for solving the Euler equations were built with the commercial software ANSYS ICEM-CFD by FOI. The meshes for the RANS equations were built using the unstructured Euler meshes and an FOI-in-house software TRITET based on an advancing front

algorithm in order to create a hybrid mesh of prismatic and tetrahedral elements. The generation of the deflected fluid surface grids according to the structural eigenmodes was done by FOI.

3.4.1.1 Potential Flow Methods

In order to cover the low-speed regime ($M = 0.2$–0.6), the commercial surface panel method VSAERO was used by DLR-AE. VSAERO solves the three-dimensional potential flow equations by the boundary integral method (panel method) based on Morinos formulation [7]. Viscous boundary layer effects are calculated by integral methods which include convergence/divergence terms along streamlines and are coupled to the potential flow solution by surface transpiration. Wake models for wing trailing edge separation, bluff-body and cross-flow separation are available. Matrix solutions are obtained by a variety of methods which include Direct, Blocked Gauss-Seidel, Banded Jacobi, and GMRES solvers. An option to VSAERO is to calculate the aerodynamics of a structure oscillating with a prescribed shape, amplitude, and frequency. So the steady and oscillatory pressures including the in-phase (real) and out-of-phase (imaginary) pressures are determined. Linear analysis is used to achieve calculation times equivalent to steady-state calculations. The unsteady pressures can be linearized about the freestream, or for greater accuracy, linearized from the steady-state solution. Aeroelastic calculations of divergence and flutter are possible by generating the aerodynamic influence coefficients suitable for calculating pressures on a body undergoing arbitrary oscillations. A structured, multi-block surface grid of the ACFA BWB configuration was generated for VSAERO. The mesh is depicted in Fig. 3.43. The potential flow model needs also a geometry description of the trailing wakes. They are attached to the trailing edges of the wing-body shape including the winglets. The mesh consists of 19,398 body panels and 6,482 wake panels. For Mach numbers higher than $M = 0.6$, VSAERO is hardly applicable, because of the presence of aerodynamic shocks which cannot be captured correctly by this method. The grids are locally refined in areas where flaps are located. By modifying the boundary condition for panels representing a flap, static computations for deflected flaps can be conducted efficiently without modifying the actual geometry. VSAERO was also used to calculate the dynamic derivatives.

3.4.1.2 CFD Methods

All aerodynamic simulations by FOI were carried out using the in-house CFD code EDGE [1]. EDGE is a parallelized CFD flow solver system for solving 2D/3D viscous/inviscid, compressible flow problems on unstructured grids with arbitrary elements. The flow solver employs an edge-based formulation which uses a node-centered finite volume technique to solve the governing equations. The control volumes are nonoverlapping and are formed by a dual grid, which is computed from the control surfaces for each edge of the primary input mesh. In the flow solver,

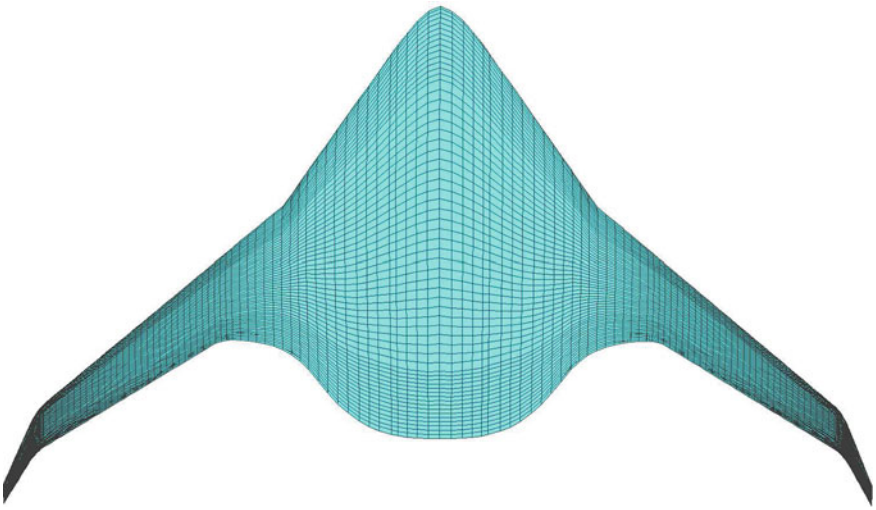

Fig. 3.43 Panel mesh by DLR-AE

the governing equations are integrated explicitly toward steady state with Runge-Kutta time integration. Convergence is accelerated using agglomeration multigrid and implicit residual smoothing. Time-accurate computations can be performed using a semi-implicit, dual time-stepping scheme which exploits convergence acceleration technique via a steady-state inner iteration procedure. EDGE solves the RANS compressible equations in either a steady frame of reference or in a frame with system rotation. Turbulence can be modeled with eddy viscosity models or explicit algebraic Reynolds stress models. Edge contains different spatial discretizations for the mean flow as well as the turbulence, different gas models, steady-state and time-accurate integration, low-speed preconditioning, etc. Applications include shape optimization and aeroelasticity. The used unstructured meshes comprise up to 1.37 million nodes for inviscid simulations and up to 12.2 million nodes for the viscous case. In Fig. 3.44, a surface mesh of the winglet is depicted.

In the TUM-AER flow solver AER-Eu, the Euler set of equations are discretized on structured finite volume grids [3]. The numerical convective fluxes are computed by the Roe scheme, and the diffusive fluxes are discretized by the Chakravarthy method. A total variation diminishing scheme prevents unphysical oscillations. For time advancement, the current calculations use a time-accurate scheme with lower-upper symmetric successive over relaxation (LU-SSOR). The numerical solver is second-order accurate in time and space. The AER-Eu has some special features. One is the ability to compute unsteady flows also forthright in the frequency domain, which guarantees high computational time efficiency in terms of CFD. It is based on a linear small disturbance approach applied to the Euler equations. Another feature is the extension to a Navier-Stokes set of equations in the AER-NS solver. With algebraic, 1- and 2-equation turbulence models RANS simulations can be carried out. These two features are not exploited in the ACFA 2020 project. However, an

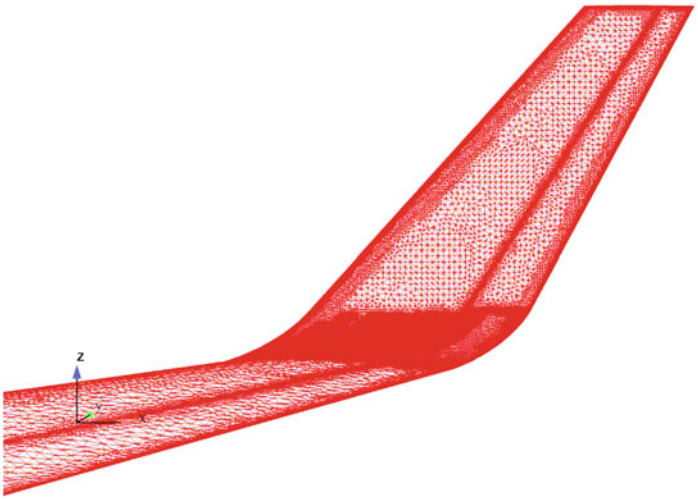

Fig. 3.44 Unstructured surface mesh at winglet by FOI

exploited feature is the ability to simulate deforming geometries. For calculations with deformed geometries, both deformed and undeformed spatial grids are required. The undeformed grid for the TUM-AER simulations was generated by TUM-AER in the commercial tool ANSYS ICEM-CFD and optimized by a TUM-AER in-house globally elliptic smoothing tool. This basic structured grid shows a favorable OO-block topology and consists of 1 million computational cells as depicted in Fig. 3.45. Domain extents are chosen such that farfield boundary conditions do not influence the flow physics near the aircraft. Grid independency was proven by grid convergence study. Besides the instantaneous and time-averaged aerodynamic derivatives, generalized aerodynamic forces (GAFs) are output of AER-Eu.

The NTUA flow solver is based on a vertex-centered finite volume scheme. The flow equations are cast in conservative form and integrated over finite volumes defined around the grid vertices. This solver may support unstructured or hybrid grids consisting of tetrahedra, hexahedra, pyramids, or prisms. The finite volumes are defined around each grid node, connecting the mass centers or circumcircles of the surrounding elements and the midnodes of the edges emanating from each node. For the given computational meshes, the second definition proved more efficient and, thus, is employed. Fluxes crossing the finite volume boundaries are all computed with second-order accuracy. The inviscid flux crossing the interface between the volumes centered at two adjacent nodes is computed by using the flux vector splitting scheme; second-order accuracy is obtained through variables extrapolation. The least squares method coupled with the Venkatakrishnan limiter was used for the reconstruction of the variables at the finite volumes interfaces. Dual (real and pseudo) time-stepping is employed. In the unsteady computations carried out, the computational mesh of each physical time step derives from the deformation of the previous real time step based on the selected mode or moving flap. The numerical solution of the discretized

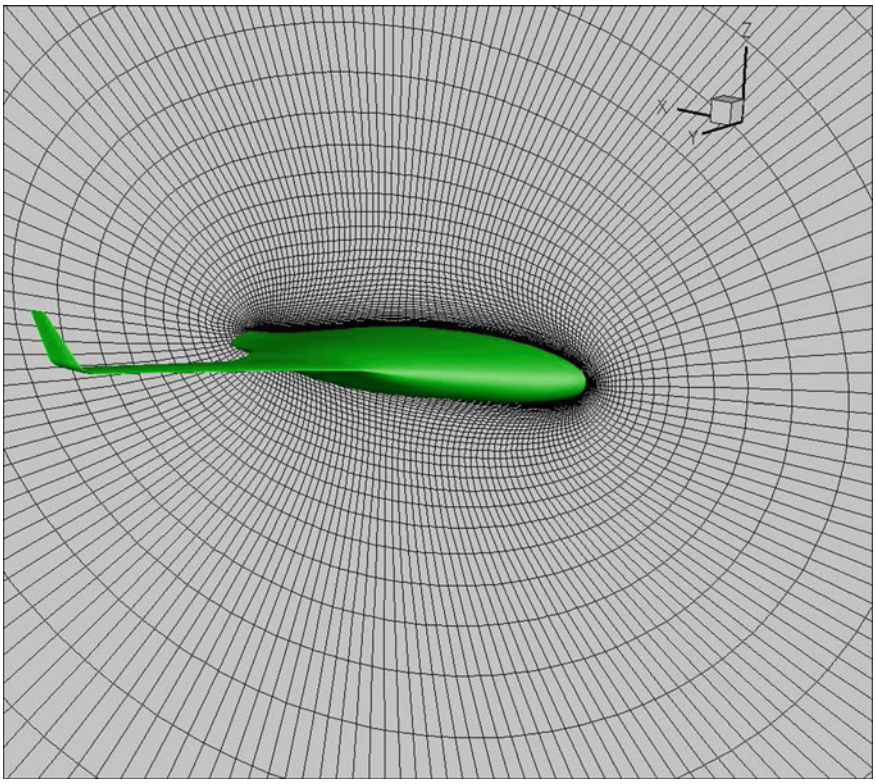

Fig. 3.45 Structured O–O-topology by TUM-AER

flow equations between two successive time steps is carried out by repetitively using the point implicit Jacobi method. The flow solver is fully parallelized, based on the multi-domain technique, and the PVM or MPI protocols. All the computations presented in this report have been carried out using the Euler equations solver.

3.4.1.3 Aeroelastic Coupling

Several procedures were tested for the fluid-structure coupling, especially procedures that do not require hand-selection of the nodes in the structural model in order to extrapolate the structure modal displacements to displacements of the CFD surface mesh. After several evaluations, the radial basis functions (RBF) were used for all computations. In the following, the eigenvectors or mode shapes, defined at the degrees of freedom of the FE model, are interpreted as deformations of the wetted surface, in terms of CFD mesh displacements. At first, the FE model and the CFD reference surface meshes were fitted to each other. The fluid mesh is translated and rotated so that leading and trailing edges in both grids fit each other. Denoting the

displacement vector by $\mathbf{V}$, the coupling between the structure and the fluid models is realized by

$$\mathbf{V}_{\mathrm{CFD}} = \mathbf{H}\mathbf{V}_{\mathrm{FEM}}. \tag{3.22}$$

The matrix $\mathbf{H}$ represents the spline matrix and is computed by RBF. The aerodynamic forces $\mathbf{F}$ acting on the structure and the fluid surface are also related by this spline matrix

$$\mathbf{F}_{\mathrm{FEM}} = \mathbf{H}^{\mathrm{T}}\mathbf{F}_{\mathrm{CFD}}. \tag{3.23}$$

This formulation defines a conservative fluid-structure coupling, which can be shown by

$$\mathbf{V}_{\mathrm{CFD}}^{\mathrm{T}}\mathbf{F}_{\mathrm{CFD}} = (\mathbf{H}\mathbf{V}_{\mathrm{FEM}})^{\mathrm{T}}\,\mathbf{F}_{\mathrm{CFD}} = \mathbf{V}_{\mathrm{FEM}}^{\mathrm{T}}\mathbf{H}^{\mathrm{T}}\mathbf{F}_{\mathrm{CFD}} = \mathbf{V}_{\mathrm{FEM}}^{\mathrm{T}}\mathbf{F}_{\mathrm{FEM}}. \tag{3.24}$$

The conservation of work is important for solving accurately aeroelastic problems. It guarantees that the GAFs computed by CFD are identical to the GAFs defined in the structure model. Unsteady aerodynamic methods can require scaling of the displacements in order to assure linear aerodynamic behavior and hence linear dependency of the GAFs with respect to the structural deformation. The CFD modes delivered by FOI were scaled such that the maximum displacement of each mode after scaling is 1/500 of the MAC. Finally, the GAFs Q due to harmonic oscillations in mode i and projected on mode j depend on the reduced frequency and are given by

$$Q_{ij} = \int_S c_{\mathrm{p}i}\,\mathbf{V}_j\,d\mathbf{S}_i\,. \tag{3.25}$$

$\mathbf{S}$ denotes the surface normal vector and c_{p} is the pressure coefficient.

3.4.2 Steady Simulation Results

The aim of this section is to give an overview of all computational results as well as a qualitative assessment of the data. Since experimental data are not available, a quantitative validation of the simulation results is not possible. But the results obtained by the different partners are compared. The next subsection deals with the assessment of the aerodynamic design based on steady simulation results.

3.4.2.1 Comparison of Numerical Models and Solvers

In terms of efficiency, the use of different flow models is common in aerodynamics because the relative viscosity, compressibility, and cross-flow effects vary with altitude and speed of the aircraft configuration. Different models are used in task 2.2 in order to build a database of aerodynamic data for the development of the flight control system.

In Fig. 3.46, global force and moment coefficients are plotted over the angle of attack for Mach numbers ranging from $M = 0.2$ to $M = 0.6$. Since no transonic flow effects are observed in this velocity range, steady-state results obtained by a RANS, using the Spalart-Almaras turbulence model, computed by FOI (FOI-R) are compared to semi-empirical results obtained with VSAERO (DLR-AE). Both models agree well regarding the lift coefficient. Differences appear for the drag and the pitching moment coefficient and vary with Mach number and angle of attack. The trend observed here is that results using VSAERO yield smaller absolute values

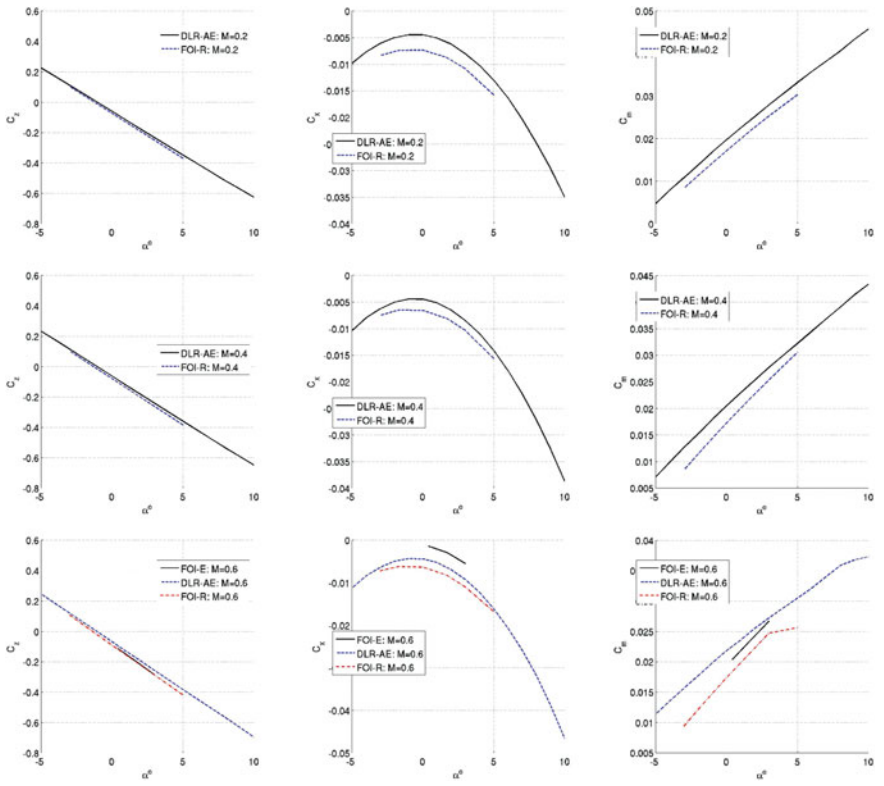

Fig. 3.46 Global force and moment coefficients for varying angle of attack and Mach number $M = 0.2$–0.6, DLR-AE (VSAERO), FOI-R (RANS), FOI-E (Euler)

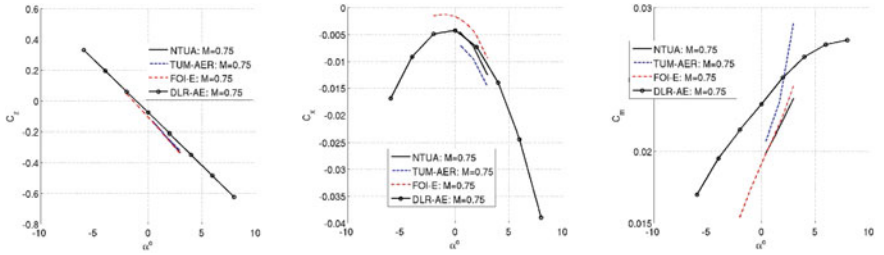

Fig. 3.47 Global force and moment coefficients for varying angle of attack and Mach number $M = 0.75$, DLR-AE (VSAERO), FOI-E (Euler), TUM-AER (Euler), NTUA (Euler)

than the simulations using the RANS solver in an interval of angles of attack from $\alpha = -4°$ to 5°. The Mach number does not seem to influence these differences in the present velocity range.

Transonic effects become important for Mach numbers greater than 0.6 for this aircraft configuration. This can be observed in Fig. 3.47, especially in the moment coefficient. Since compressibility and three-dimensional effects cannot be represented accurately by VSAERO the deviations between the results increase. Differences in the results are not always caused by the simplifications made on the flow equations as for instance neglecting viscosity. There are also differences due to the numerical scheme used for solving the flow equations. The flow solvers used by FOI and NTUA use a vertex-centered finite volume scheme, whereas TUM-AER uses a finite volume discretization that is cell-centered. Both NTUA and TUM-AER used a Roe scheme with flux limiters whereas FOI used the second- and fourth-order artificial dissipation model (JST model). The comparison between NTUA, FOI-E, and TUM-AER indicates a good agreement on the lift force but also significant differences on the drag prediction, see Fig. 3.47. The drag obtained by the Euler solvers of TUM-AER and NTUA is considerably larger than the drag obtained by the Euler solver of FOI (FOI-E). This can be caused by the size of the fluid domain between the mesh built by FOI where the farfield boundary conditions are typically 50 chords away from the aircraft, whereas for TUM-AER the domain is much smaller.

In Fig. 3.48, the pressure coefficient distribution is given in four spanwise sections. Compared are inviscid simulation results provided by FOI, NTUA, and TUM-AER on meshes of different size. Effects of the mesh resolution are determined to be very small and hence the solution can be regarded as grid-converged. Discrepancies occur concerning the shock position, especially in the two outer sections. The shock position computed by FOI and TUM-AER agrees quite well, while NTUA predicts a shock located further downstream.

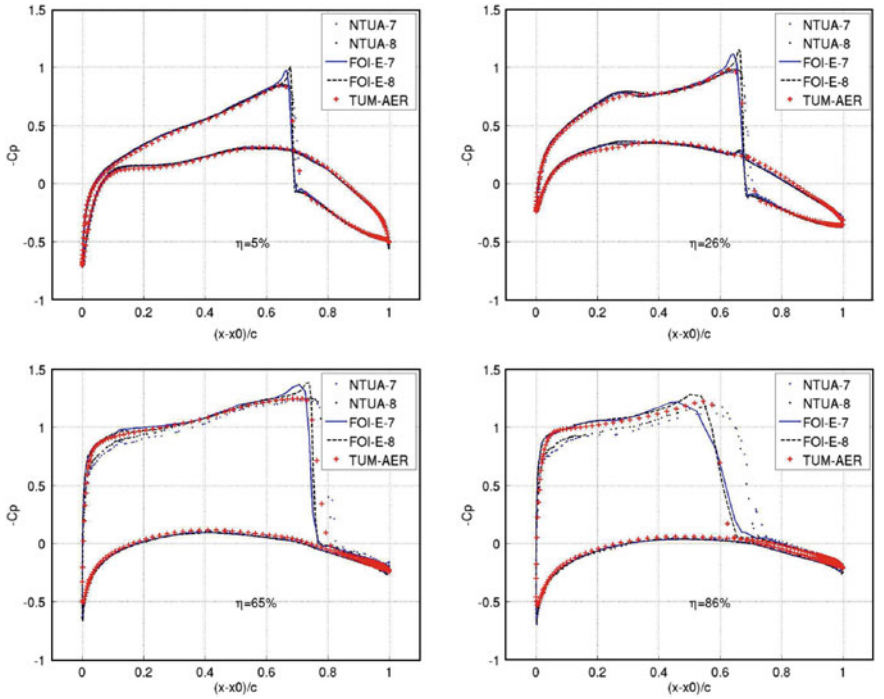

Fig. 3.48 Pressure coefficient distribution for $\alpha = 1.7°$ and $M = 0.85$ at different spanwise locations η, FOI-E-7 (Euler, mesh coarse), FOI-E-8 (Euler, mesh fine), TUM-AER (Euler), NTUA-7 (Euler, mesh coarse), NTUA-8 (Euler, mesh fine)

3.4.2.2 Aerodynamic Design Analysis

The aerodynamics on the BWB aircraft are determined by strong nonlinear effects. A complex shock system is built up on the lower and upper part of the wing and the winglet at cruise conditions, shown in Fig. 3.49. With increasing Mach number , the shock system moves toward the trailing edge. The shock position differs strongly in spanwise direction. Hence, the strong shocks and the spanwise variation in shock locations affects markedly the aerodynamic performance, but the project was not aimed on a fully optimized transonic aerodynamic design.

Figure 3.50 shows the effect of the Mach number on the lift, drag, and the pitching moment coefficient. At higher Mach numbers, shock systems dominate the flow physics of the aircraft and thus the aerodynamic coefficients. Due to the shock system, the suction region on top of the wing becomes larger. This leads to a higher lift and higher drag coefficient. The total drag coefficient is mainly increased due to the contribution of the wave-drag. With increasing Mach number and angle of attack, respectively, the shock strength increases and the shock system moves toward the trailing edge of the wing leading also to a change in the pitching moment coefficient. This shock movement is also visible in the pressure coefficient plots at the two mid-

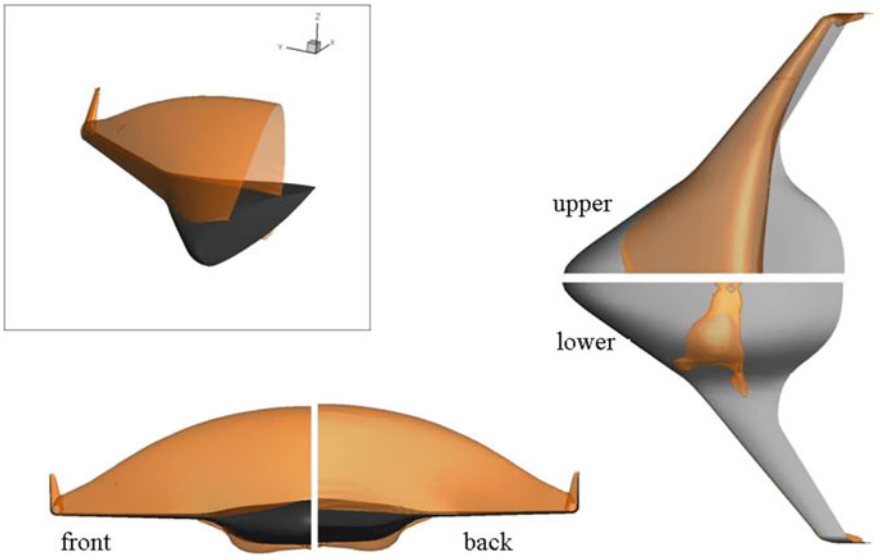

Fig. 3.49 Mach-isosurface ($M = 1$) for $M = 0.85$ and $\alpha = 1.7°$, TUM-AER (Euler)

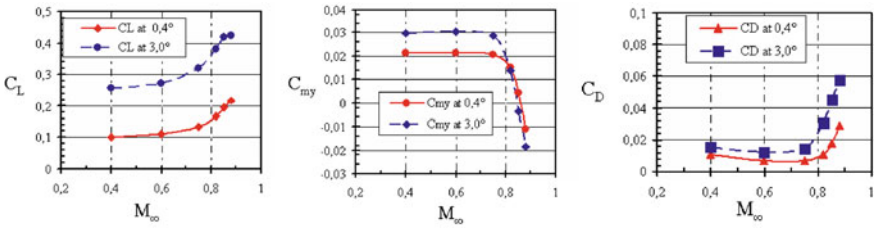

Fig. 3.50 Global force and moment coefficients for varying angle of attack and Mach number, TUM-AER (Euler)

flap positions in Fig. 3.51. The shock positions differ strongly in spanwise direction. Between $M = 0.85$ and $M = 0.88$, the shock position varies by 5 % on the inner wing, while it varies by 15 % on the outer wing. The respective shock strength shown by the pressure coefficient increase is 10 % higher on the outer wing then on the inner wing. At $M = 0.75$, no shock occurs on the wing. A slightly smaller variation occurs for different angles of attack, see Fig. 3.52. The variation of the shock position implies an undesirable unequally distributed aerodynamic loading and has a direct influence on the aircraft handling qualities. Improvement can be achieved by a more suitable airfoil selection or by adapting the wing twist and wing sweep.

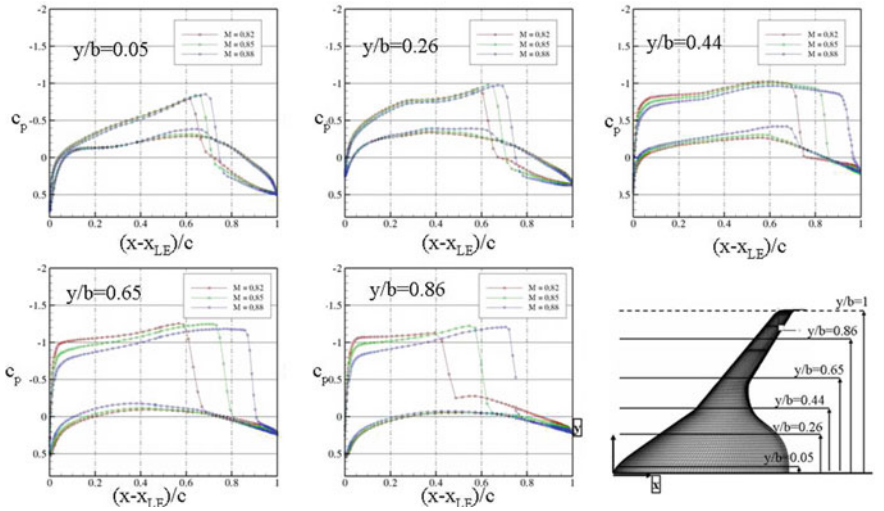

Fig. 3.51 Pressure coefficient distribution for $\alpha = 1.7°$ and three Mach numbers at different spanwise locations η, TUM-AER (Euler)

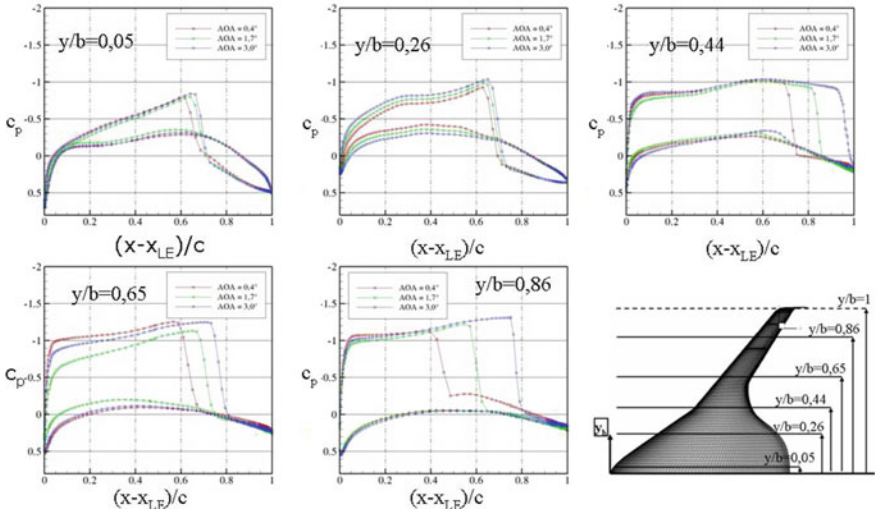

Fig. 3.52 Pressure coefficient distribution $M = 0.85$ and three angles of attack at different spanwise locations η, TUM-AER (Euler)

3.4.3 Unsteady Simulation Results

The steady simulations show that the Mach number has a significant influence on the aerodynamics and thus on the load distribution, particularly, on the outboard wing.

Therefore, the Mach number's influence for a wing bending mode at different reduced frequencies is investigated. The pressure coefficient's evolutions of the time-accurate simulations undergo a successive Fourier analysis. Figure 3.54 shows the real and imaginary parts of c_p for the previously used two mid-flap positions at two different Mach numbers and three different reduced frequencies for the bending mode. The pressure peaks indicate a shock position. The amplitude of the peak corresponds to the shock's strength and the width of the peak to the range of the shock movement due to the elastic bending motion. The three-dimensional bending motion can be considered as a plunge movement for a two-dimensional spanwise cut plane. The respective amplitude of the movement is higher on the outboard wing. The real part of c_p can be seen as quasi-stationary induced incidence α_0 locally at the deformation, while the imaginary part of c_p is due to the incidence α_i locally induced by the bending movement. The influence of the Mach number on both real and imaginary parts of c_p is larger on the suction side than on the lower side of the wing. Similar to the steady calculations, the c_p distribution on the outboard wing (at $y/b = 0.86$) is more susceptible to changes in the Mach number. At $M = 0.75$, the unsteady bending motion generates a double peak implying two recompression zones on the upper outboard wing close to the leading edge. A variation of the reduced frequency has also a higher impact on the c_p distribution along with the amplitude of the pressure peaks of the outboard wing. This is especially the case for the real part of c_p. For the imaginary part of c_p, a change in reduced frequency even leads to a local inversion in sign. However, this does not lead to global instabilities or to a respective change in sign of the global forces. To summarize, the c_p distribution, especially the one on the outboard wing, shows a very sensitive behavior to variations in Mach number and reduced frequency. These corresponding strong nonlinear phenomena can only be accounted for by the used high-fidelity simulations as opposed to simplified approaches based, for example, on potential theory.

In addition to the Euler computations, FOI carried out a number of viscous flow computations. Low Mach number computations with RANS allowed a more accurate comparison of the CFD results with VSAERO. Simulations with RANS at transonic Mach numbers ($M = 0.85$) complement the Euler CFD computations carried out by FOI (FOI-E), NTUA, and TUM-AER. The computations were carried out on two meshes, with different nodes densities, which allowed excluding grid convergence effects. All attempts at $M = 0.85$ were evident to suggest that the flow solution is unsteady. Therefore, for both grids, time-accurate solutions were computed. After passing the transient, the flow solutions converged to a harmonic flow regime oscillating at a frequency of $f = 0.7\,\text{Hz}$, apparently driven by shock-boundary layer interaction. The left plot in Fig. 3.53 illustrates the transient toward the harmonic regime. The right plot shows the relation between drag and lift. The amplitude variations of the drag and lift coefficient measure about 10 % of the absolute values.

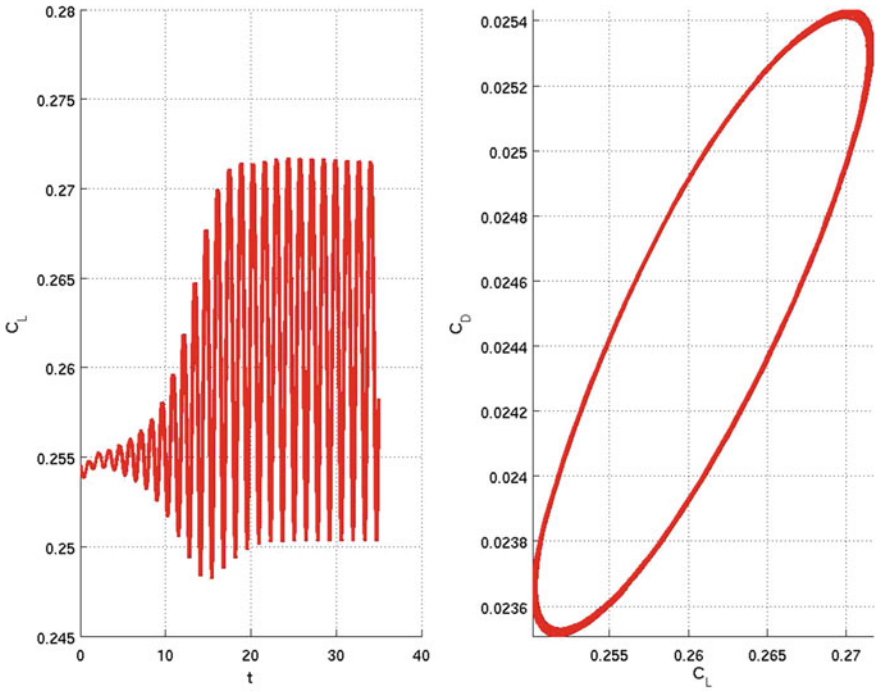

Fig. 3.53 Time-accurate computation of the lift and drag coefficient at $M = 0.85$ and $\alpha = 1.7°$, FOI (RANS)

3.4.4 Conclusions

The aerodynamics of the ACFA blended wing body (BWB) based on a number of test cases comprising steady and unsteady results using potential theory and high-fidelity Euler/RANS simulations were analyzed. The results show that the pressure distribution and aerodynamic loads, respectively, are susceptible to changes in Mach number in the steady simulations as well as changes in Mach number or in reduced frequency in the unsteady simulations. Severe load distribution variations are especially located at the outboard wing. Furthermore, oscillations in the aerodynamic loads are observed at cruise conditions. For improvement, it is recommended to incorporate high-fidelity aerodynamic analysis and design methods already in the conceptual design phase. A comparison between panel and CFD methods showed pertinent agreement at Mach numbers $M < 0.6$. But strong nonlinear phenomena at higher Mach numbers can only be accounted for by the use of high-fidelity CFD simulations (Fig. 3.54).

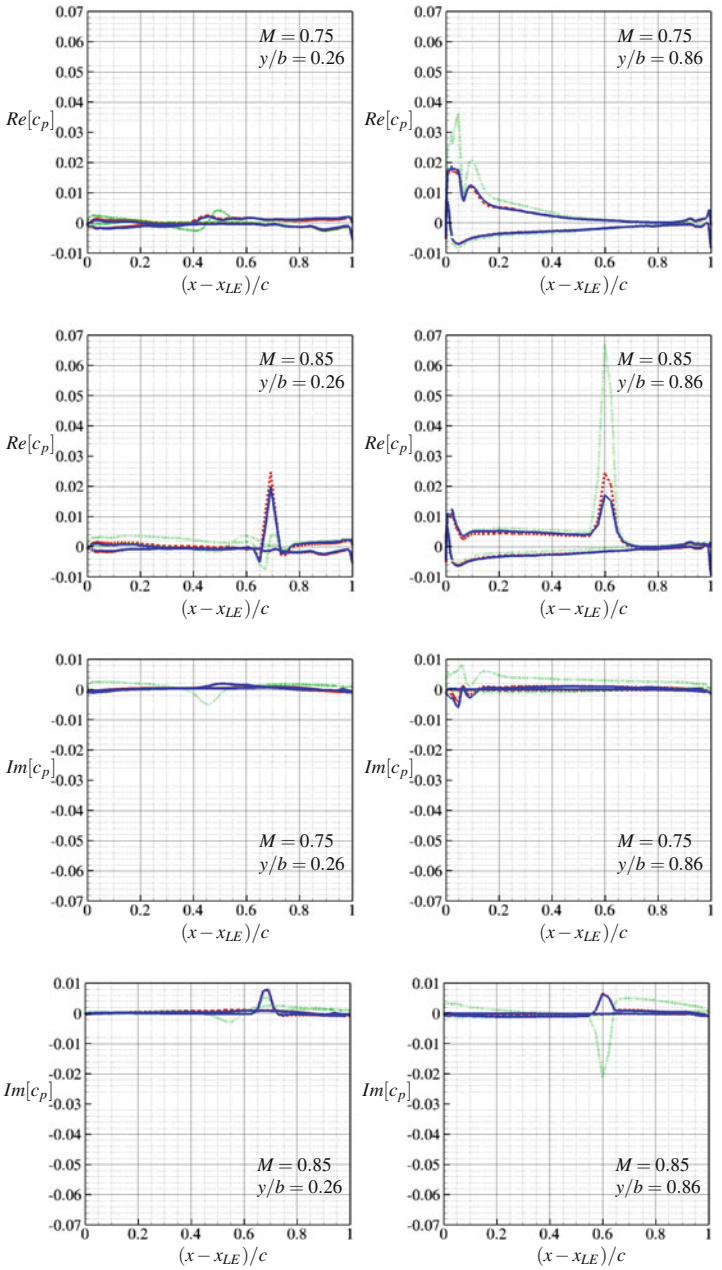

Fig. 3.54 Real and imaginary parts of the pressure coefficient, $\mathrm{Re}[c_\mathrm{p}]$ and $\mathrm{Im}[c_\mathrm{p}]$, in streamwise direction $(x - x_\mathrm{LE})/c$ at different spanwise positions y/b for symmetric bending at different Mach numbers and $\alpha = 1.7°$ (—: $k_\mathrm{red} = 0.05$; −− : $k_\mathrm{red} = 0.1$; $\cdots$: $k_\mathrm{red} = 0.5$)

3.5 Integrated Flight Dynamics and Aeroelastic Modeling

F. Stroscher and H. Baier

In the following, the modeling steps for the coupled flight dynamic and aeroelastic simulation model are described. The basis is the structural dynamic simulation model (Sect. 3.3) as well as the aerodynamic database (Sect. 3.4).

3.5.1 Structural Dynamics

Within the ACFA 2020 project, an FE model of the BWB aircraft primary structure was developed. The FE model level of detail is comparably low, but sufficient for the prediction of structural dynamic response in the considered frequency range. A full span model was applied in aeroelastic modeling, to directly take into account asymmetric turbulence excitation. The fuel tanks (Fig. 3.55) are represented by concentrated mass elements, rigidly connected to the structure.

The possible mass conditions of the aircraft are defined over the full range of fuel tank filling level, from empty to full. Further, the fuel distribution over tanks in wing and fuselage is considered, providing a useful margin of x-position of the aircraft center of gravity. Three configurations of fuel distributions are considered (CG1–3) for 11 steps of fuel filling (index 0 with 0 % filling to index 10 with 100 % filling), which yields 33 structural variants in total.

The natural modes for all mass configurations of the FE model are extracted by numerical solution of the vibration eigenvalue problem (3.26). Structural damping is neglected in this approach, resulting in noncomplex eigenvectors.

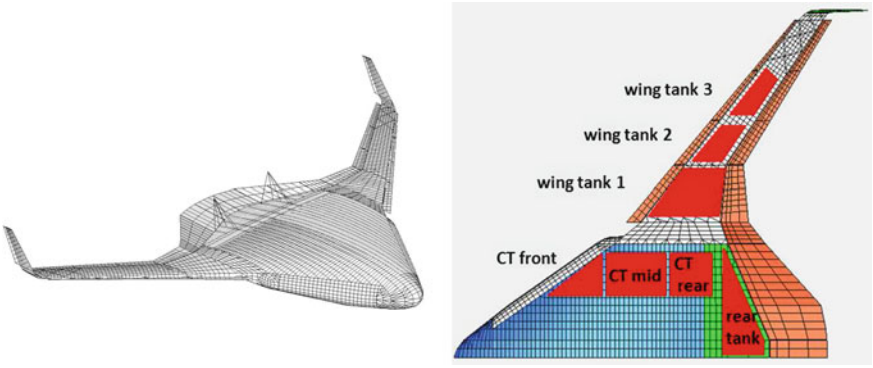

Fig. 3.55 FE model of the BWB aircraft structure (*left*) and fuel tank layout (*right*)

Fig. 3.56 First two symmetric elastic mode shapes

$$\left(-\omega^2 \mathbf{M}_{\text{struct}} + \mathbf{K}_{\text{struct}}\right) \mathbf{x}_{\text{struct}} = \mathbf{0} \tag{3.26}$$

The eigenvectors and natural frequencies are used as modal bases for each mass condition, comprised of 6 rigid-body (RB) modes Φ_{r} and a limited number of elastic modes Φ_{e}. The unit deflections of elastic modes are mass-normalized, leading to unitary modal mass matrices. To properly connect flight dynamic modes to RB modes, their deflections are normalized to 1m for translational modes, respectively 1rad for rotational modes (Fig. 3.56).

3.5.2 Aerodynamic Database

Steady aerodynamic analysis of the rigid aircraft, as well as unsteady aerodynamic analysis of the flexible aircraft has been performed with simplified, as well as high-order aerodynamic methods in subsonic and transonic regime. As usual in aeroelastic analysis, the unsteady aerodynamic database is computed for modal coordinates, that is, modal aerodynamic forces with respect to modal deflection. In order to account for the unsteady aerodynamics of control surfaces, additional control modes are introduced, which are defined by appropriate deflection of the aerodynamic degrees of freedom. Further, gust unsteady aerodynamic forces are included by a downwash distribution over the aircraft. The aeroelastic database is computed in frequency domain, assuming harmonic oscillation of mode shapes, control surface deflections, and gust downwash over a predefined frequency range. The reduced frequency k is applied here, which is a nondimensional quantity, usually applied in aeroelastic simulation, see (3.27).

$$k = \frac{\omega c}{2V_\infty} \tag{3.27}$$

Generalized aerodynamic forces (GAF), denoted by Q, are the unsteady aerodynamic forces on modal coordinates, normalized by dynamic pressure. The GAF Q_{h} are distinguished into forces due to modal perturbation Q_{hh}, control surface perturbation Q_{hc}, and gust excitation Q_{hg}. The modal forces in frequency domain can be

obtained by multiplication with modal deflections η, control surface deflections δ, and gust velocity w_g, see (3.28) as given in [9].

$$P_h(j\omega) = -q_\infty Q_{hh}(jk)\eta(j\omega) - q_\infty Q_{hc}(jk)\delta(j\omega) - q_\infty Q_{hg}(jk)\frac{w_g(j\omega)}{V_\infty} \tag{3.28}$$

3.5.3 Modification of GAF by Higher-Order Analysis Results

For the transonic regime, the GAF of some important structural modes are replaced with results from an unsteady CFD simulation, see Sect. 3.4. As the prescribed boundary motion in such unsteady aerodynamic computation has to be explicitly specified, one modal basis was selected.

By using a modal transformation rule, the GAF for the modal bases of all mass variants can be derived from the CFD-computed GAF of one modal basis. Let Q^a_{hh} be the GAF with respect to deflection of the mode shapes Φ^a_h and Q^a_{hc} with respect to control surface deflection. Then, the GAF Q^b_{hh} with respect to deflection of the mode shapes Φ^b_h, and Q^b_{hc} with respect to control surface deflection, are

$$\left[Q^b_{hh}(jk)\right] = \left[T^{ba}_\phi\right]^T \left[Q^a_{hh}(jk)\right]\left[T^{ba}_\phi\right] \tag{3.29}$$

$$\left[Q^b_{hc}(jk)\right] = \left[T^{ba}_\phi\right]^T \left[Q^a_{hc}(jk)\right] \tag{3.30}$$

with $\left[T^{ba}_\phi\right]$ as the least squares solution of the equation

$$\Phi^a_h T^{ba}_\phi = \Phi^b_h \tag{3.31}$$

By this transformation rule, the GAF of all modal bases in the transonic regime are replaced by CFD-computed results. The approximation error due to the linear transformation with a limited set of eigenvectors is comparably low.

3.5.4 Approximation of Aerodynamic Forces in the Laplace Domain

In order to derive equations of motion in the time domain, the GAF have to be expressed in Laplace domain first. This normally introduces a high number of additional degrees of freedom, to account for the time lags of aerodynamic forces. The minimum-state method, introduced by Karpel [5], is a rational function approximation method that accurately recovers the GAF in Laplace domain with only a

few additional degrees of freedom. The approximation rule of the GAF in Laplace domain, (3.32), is given in [9]:

$$Q_{\mathrm{h}}(p) = \mathbf{A}_0 + \mathbf{A}_1 p + \mathbf{A}_2 p^2 - \mathbf{D}(\mathbf{I}p - \mathbf{R}^{-1})\mathbf{E}p, \tag{3.32}$$

where $p = s\frac{c}{2V_\infty}$ is the nondimensional Laplace variable. The approximation matrices $\mathbf{A}_0$, $\mathbf{A}_1$, $\mathbf{A}_2$, $\mathbf{D}$, $\mathbf{E}$, and $\mathbf{R}$ are applied to form the equations of motion of the time-domain aeroelastic simulation model.

3.5.5 Structural Outputs

Several structural displacement, velocity, and acceleration outputs are integrated into the model, to be applied for load alleviation in active control design. Therefore, the entries of the eigenvectors at specific degree of freedom positions are multiplied by modal deflections and their time derivatives. The nodal locations of the structural outputs are shown in Fig. 3.57. Further, force and moment outputs are applied at several positions over wingspan for left and right part of the aircraft. These are intended for a quantification of load alleviation techniques, applied in the control design studies.

3.5.6 Equations of Motion

The basis of the flight dynamics modal is the nonlinear 6 degrees of freedom Newton-Euler flight dynamic equations of motion. These are described by the angular and linear momentum conservation laws, (3.33) and (3.34), which can be found in several bibliographic references, such as [6]. The flight dynamic translational and rotational

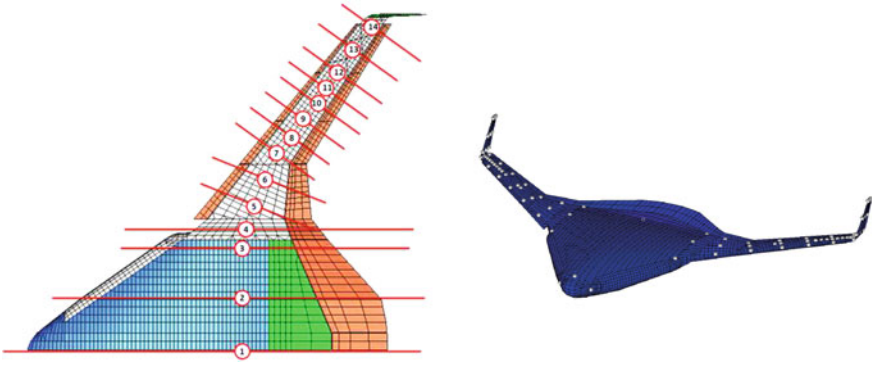

Fig. 3.57 Positions over wingspan for cut forces outputs (*left*), acceleration output positions over airframe (*right*)

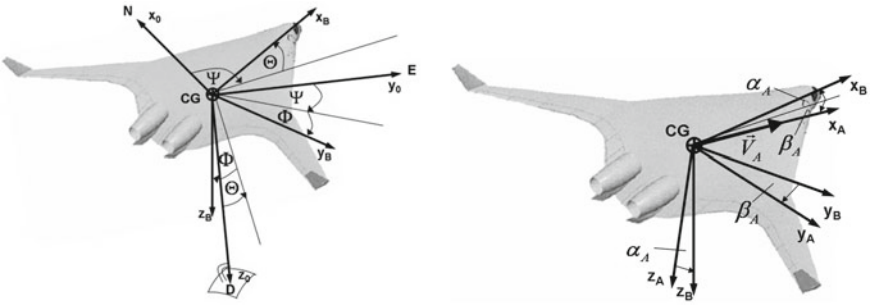

Fig. 3.58 Definition of NorthEastDown-System with inertial axes x_0, y_0, z_0, body axes x_B, y_B, z_B, Euler angles Φ, Θ, Ψ, wind axes x_A, y_A, z_A, angle of attack α_A and side-slip angle β_A

degrees of freedom, V_b and Ω_b, are defined over body axes. Figure 3.58 provides an overview on inertial, aerodynamic and body axes, as well as attitude, incidence, and side slip.

$$m\left\{\dot{V}_\mathrm{b} + \Omega_\mathrm{b} \times V_\mathrm{b} - T_\mathrm{be} g_\mathrm{e}\right\} = F^\mathrm{FD} + F^\mathrm{FD}_\mathrm{AE} + F^\mathrm{FD}_\mathrm{G} \tag{3.33}$$

$$J\dot{\Omega}_\mathrm{b} + \Omega_\mathrm{b} \times J\Omega_\mathrm{b} = M^\mathrm{FD} + M^\mathrm{FD}_\mathrm{AE} + M^\mathrm{FD}_\mathrm{G} \tag{3.34}$$

Here, m is the aircraft mass, J the inertial tensor, g_e gravitation acceleration in inertial axes and T_be the transformation matrix from inertial to body axes. The aerodynamic forces F^FD and moments M^FD from flight dynamic derivatives of the rigid aircraft are shown in (3.35) and (3.36).

$$F^\mathrm{FD} = q_\infty S_\mathrm{ref} T_{ba} \left(\begin{Bmatrix} C_D \\ C_Y \\ C_L \end{Bmatrix} + \begin{Bmatrix} C_{Dp} \\ C_{Yp} \\ C_{Lp} \end{Bmatrix} p + \begin{Bmatrix} C_{Dq} \\ C_{Yq} \\ C_{Lq} \end{Bmatrix} q + \begin{Bmatrix} C_{Dr} \\ C_{Yr} \\ C_{Lr} \end{Bmatrix} r + \begin{Bmatrix} C_{D\delta} \\ C_{Y\delta} \\ C_{L\delta} \end{Bmatrix} \delta \right) \tag{3.35}$$

$$M^\mathrm{FD} = q_\infty S_\mathrm{ref} \frac{c}{2} T_{ba} \left(\begin{Bmatrix} C_l \\ C_m \\ C_n \end{Bmatrix} + \begin{Bmatrix} C_{lp} \\ C_{mp} \\ C_{np} \end{Bmatrix} p + \begin{Bmatrix} C_{lq} \\ C_{mq} \\ C_{nq} \end{Bmatrix} q + \begin{Bmatrix} C_{lr} \\ C_{mr} \\ C_{nr} \end{Bmatrix} r + \begin{Bmatrix} C_{l\delta} \\ C_{m\delta} \\ C_{n\delta} \end{Bmatrix} \delta \right) + (\mathrm{ARP} - \mathrm{COG}) \times F^\mathrm{FD} \tag{3.36}$$

Here T_{ba} is the transformation matrix from aerodynamic to body axes, S_ref the aircraft reference surface, ARP and COG the coordinates of the aerodynamic reference point and center of gravity, and $C_{D,Y,L,l,m,p}$, etc., the flight dynamic derivatives. Aeroelastic coupling forces $F^\mathrm{FD}_\mathrm{AE}$ and moments $M^\mathrm{FD}_\mathrm{AE}$, due to elastic modal motion are expressed in (3.37) by the rational function approximation matrices, introduced in (3.32).

$$\begin{Bmatrix} F_{\mathrm{AE}}^{\mathrm{FD}} \\ M_{\mathrm{AE}}^{\mathrm{FD}} \end{Bmatrix} = -q_\infty T_{\mathrm{be}} \left(A_{\mathrm{re0}} \eta_{\mathrm{e}} + \left(\frac{c}{2V_\infty} \right) A_{\mathrm{re1}} \dot{\eta}_{\mathrm{e}} + \left(\frac{c}{2V_\infty} \right)^2 A_{\mathrm{re2}} \ddot{\eta}\mathrm{e} + D_{\mathrm{r}} x_{\mathrm{a}} \right) \tag{3.37}$$

Gust aerodynamic forces and moments are expressed analogously by (3.38).

$$\begin{Bmatrix} F_G^{\mathrm{FD}} \\ M_G^{\mathrm{FD}} \end{Bmatrix} = -q_\infty T_{\mathrm{be}} \left(A_{\mathrm{rg0}} \frac{w_{\mathrm{g}}}{V_\infty} + \left(\frac{c}{2V_\infty} \right) A_{\mathrm{rg1}} \frac{\dot{w}_{\mathrm{g}}}{V_\infty} \right) \tag{3.38}$$

The aeroelastic equations of motion are comprised by the modal inertial and elastic forces on the left-hand side, as well as aerodynamic forces due to flight dynamic, elastic, control surface , and turbulence perturbation, on the right-hand side of (3.39). Structural damping is neglected in this formulation.

$$\begin{aligned} &\mathbf{M}_{\mathrm{struct}} \ddot{\eta}_{\mathrm{e}} + \mathbf{K}_{\mathrm{struct}} \eta_{\mathrm{e}} \\ &\quad = A_{\mathrm{e0}} \begin{Bmatrix} \eta_{\mathrm{r}} \\ \eta_{\mathrm{e}} \\ \delta_{\mathrm{c}} \\ \frac{1}{V_\infty} w_{\mathrm{g}} \end{Bmatrix} + \left(\frac{c}{2V_\infty} \right) A_{\mathrm{e1}} \begin{Bmatrix} \dot{\eta}_{\mathrm{r}} \\ \dot{\eta}_{\mathrm{e}} \\ \dot{\delta}_{\mathrm{c}} \\ \frac{1}{V_\infty} \dot{w}_{\mathrm{g}} \end{Bmatrix} + \left(\frac{c}{2V_\infty} \right)^2 A_{\mathrm{e2}} \begin{Bmatrix} \ddot{\eta}_{\mathrm{r}} \\ \ddot{\eta}_{\mathrm{e}} \\ \ddot{\delta}_{\mathrm{c}} \\ 0 \end{Bmatrix} + D_{\mathrm{e}} x_{\mathrm{l}} \end{aligned} \tag{3.39}$$

For the coupling of flight dynamic motion to RB modes, η_{r} has to be transformed from inertial axes to body axes. The transformation rules are given by (3.40).

$$\eta_{\mathrm{r}} = \begin{Bmatrix} -X \\ Y \\ -Z \\ -\Phi \\ \Theta \\ -\Psi \end{Bmatrix}, \quad \dot{\eta}_{\mathrm{r}} = \begin{Bmatrix} -u \\ v + V_\infty \Psi \\ -w + V_\infty \Theta \\ -p \\ q \\ -r \end{Bmatrix}, \quad \text{and} \quad \ddot{\eta}_{\mathrm{r}} = \begin{Bmatrix} -\dot{u} \\ \dot{v} + V_\infty q \\ -\dot{w} + V_\infty r \\ -\dot{p} \\ \dot{q} \\ -\dot{r} \end{Bmatrix} \tag{3.40}$$

The aeroelastic equations of motion are augmented by a lag (3.41), which accounts for time delays of unsteady aerodynamic forces. The first-order differential equation is solved for the lag states, which are coupled to the aeroelastic equations of motion (3.39).

$$\dot{x}_{\mathrm{l}} = \left(\frac{2V_\infty}{c} \right) [R] x_{\mathrm{l}} + [E] \begin{Bmatrix} \dot{\eta}_{\mathrm{r}} \\ \dot{\eta}_{\mathrm{e}} \\ \dot{\delta}_{\mathrm{c}} \\ \frac{1}{V_\infty} \dot{w}_{\mathrm{g}} \end{Bmatrix} \tag{3.41}$$

3.5.7 State-Space Model

The state-space form of the equations of motion is constructed by linearization of the combined flight dynamic and aeroelastic model, (3.33)–(3.41), at specified trim points. The resulting state, input and output vectors are assembled as shown in (3.42)–(3.44).

$$x = \left[\eta_\mathrm{r},\ \dot{\eta}_\mathrm{r},\ \eta_\mathrm{e},\ \dot{\eta}_\mathrm{e},\ x_\mathrm{l}\right]^\mathrm{T}, \tag{3.42}$$

$$u = \left[\delta^\mathrm{right},\ \delta^\mathrm{left},\ \dot{\delta}^\mathrm{right},\ \dot{\delta}^\mathrm{left},\right.$$
$$\left.\eta^{2d},\ \eta^\mathrm{vertical},\ \eta^\mathrm{lateral},\ \dot{\eta}^{2d},\ \dot{\eta}^\mathrm{vertical},\ \dot{\eta}^\mathrm{lateral},\ F_\mathrm{Thrust},\ F_\mathrm{wingtip}\right]^\mathrm{T}, \tag{3.43}$$

$$y = \left[u^\mathrm{F},\ u^\mathrm{struct},\ \dot{u}^\mathrm{struct},\ \ddot{u}^\mathrm{struct},\ F^\mathrm{struct}\right]^\mathrm{T}. \tag{3.44}$$

References

1. Eliasson P (2002) EDGE a Navier-Stokes solver for unstructured grids. In: Proceedings of finite volumes for complex applications III, pp 527–534
2. European Commission (2014) Flying high with innovative aircraft concepts. http://ec.europa.eu/research/research-for-europe/transport-nacre_en.html
3. Fleischer D, Förster M, Breitsamter C (2011) Efficient CFD-based unsteady aerodynamics analysis. In: Proceedings of IFASD2011, international forum of aeroelasticity and structural dynamics, Stockholm
4. istworld (2014) Very efficient large aircraft. http://www.ist-world.org/ProjectDetails.aspx?ProjectId=bc5fe779da034fe4926c266e1c644b66&SourceDatabaseId=9cd97ac2e51045e39c2ad6b86dce1ac2
5. Karpel M (1981) Design for active and passive flutter suppression and gust alleviation, vol 3482. National Aeronautics and Space Administration, Scientific and Technical Information Branch
6. Lewis BL, Stevens FL (1992) Aircraft control and simulation. Wiley, New York
7. VSAERO—integral methods for potential and boundary layer flows (2014). http://www.ami.aero/software-computing/amis-computational-fluid-dynamics-tools/vsaero/ Accessed 19 May 2014
8. Wildschek A, Stroscher F, Klimmek T, Šika Z, Vampola T, Valášek M, Gangsaas D, Aversa N, Berard A (2010) Gust load alleviation on a large blended wing body airliner. In: 27th International congress of the aeronautical sciences (ICAS)
9. ZONA Technology (2010) ZAERO theoretical manual. http://www.zonatech.com/Documentation/ZAERO_THEORETICAL_MANUAL_8.5.pdf. Current version 8.5 (2011). Accessed 8 July 2014

Chapter 4
Reduced-Order Modeling

M. Valášek, Z. Šika, T. Vampola and S. Hecker

4.1 Model Order Reduction

M. Valášek, Z. Šika and T. Vampola

4.1.1 General Process of Generation of Parameterized Reduced-Order Models for Control Design

The output of the complex modeling process without reduction is the full model of the ACFA BWB aircraft predesign model in the original unreduced number of coordinates that is known for many discrete values of parameters $\mathbf{p}_\mathrm{d}$. It is supposed that the original models are linear and represented in the state-space form

$$\begin{aligned}\dot{\mathbf{x}}_\mathrm{F} &= \mathbf{A}_\mathrm{F}(\mathbf{p}_\mathrm{d})\mathbf{x}_\mathrm{F} + \mathbf{B}_\mathrm{F}(\mathbf{p}_\mathrm{d})\mathbf{u}\\ \mathbf{y} &= \mathbf{C}_\mathrm{F}(\mathbf{p}_\mathrm{d})\mathbf{x}_\mathrm{F} + \mathbf{D}_\mathrm{F}(\mathbf{p}_\mathrm{d})\mathbf{u}.\end{aligned} \tag{4.1}$$

The differential equations over structural and aerodynamic degrees of freedom (states) are given by the system matrix **A**. The state variables **x** are related to an input vector **u** containing input quantities, for example, control surface actuation moments, by the control matrix **B**. The transformation from states to outputs **y** is achieved by the observation matrix **C**. In case, inputs have a direct effect on the outputs, the feedthrough matrix **D** can be included. The index F indicates the full set of degrees of freedom.

M. Valášek (✉) · Z. Šika · T. Vampola
Czech Technical University in Prague, Prague, Czech Republic
e-mail: michael.valasek@fs.cvut.cz

S. Hecker
Munich University of Applied Sciences, Munich, Germany

M. Kozek and A. Schirrer (eds.), *Modeling and Control for a Blended Wing Body Aircraft*,
Advances in Industrial Control, DOI 10.1007/978-3-319-10792-9_4

Nevertheless, the unreduced version of the parameterized model is totally unusable for the control law synthesis. The suitable reduction can be done generally in two main steps. First, the full structural model is reduced based on the modal coordinates taken into account the relatively wide frequency range. The upper preserved frequencies after the first step of the reduction should be sufficiently high (for example, about 30 Hz). The rejected modes can either be completely neglected or partially taken into account by singular perturbation approximation (SPA), without enlarging the model order. All rigid body (RB) modes of the structure as a whole have to be preserved, since they are base for the flight mechanics states. Performing this first reduction step with the purely structural equations more radically (with low-frequency limit or using balanced reduction) can lead into errors due to subsequent modal aerodynamic coupling effects. Modes that are unimportant for inputs and outputs, that is, with low controllability and observability measures, may be important later for the aeroelasticity.

The model after the first reduction step is used for the derivation of generalized aerodynamic forces, including gust forces. Consequently, the complex model includes all flight mechanics states, all lag states, and the states of the preserved elastic modes. This complex model is further reduced based on the balanced reduction or using other methods as described within the further paragraphs. The final process of reduction is significantly influenced by the necessity of generation of the widely parameterized model, where the unambiguous continuation and tracking of particular states in the process of parameters variation is problematic. This inconvenience is especially substantial for the states corresponding to the elastic modes.

In any case, the result is the set of reduced models for the discrete values of parameters $\mathbf{p}_\mathrm{d}$ in the state-space form.

$$\begin{aligned} \dot{\mathbf{x}}_\mathrm{F} &= \mathbf{A}(\mathbf{p}_\mathrm{d})\mathbf{x} + \mathbf{B}(\mathbf{p}_\mathrm{d})\mathbf{u} \\ \mathbf{y} &= \mathbf{C}(\mathbf{p}_\mathrm{d})\mathbf{x} + \mathbf{D}(\mathbf{p}_\mathrm{d})\mathbf{u} \end{aligned} \tag{4.2}$$

Finally, a set of reduced models is replaced by one model with system parameters that are continuous functions of the parameter vector $\mathbf{p}$. The system parameters will be functions of parameters $\mathbf{p}$ in a form of rational functions.

$$\begin{aligned} \dot{\mathbf{x}}_\mathrm{F} &= \mathbf{A}(\mathbf{p})\mathbf{x} + \mathbf{B}(\mathbf{p})\mathbf{u} \\ \mathbf{y} &= \mathbf{C}(\mathbf{p})\mathbf{x} + \mathbf{D}(\mathbf{p})\mathbf{u} \end{aligned} \tag{4.3}$$

Such parameterized ROM can be processed by the Linear Fractional Transformation (LFT).

4.1.2 First Level of Model Reduction—Modal Reduction of Full Structural Model

4.1.2.1 Modal Decomposition

The basic operation of this decomposition is the well-known modal transformation and sequencing of the eigenfrequencies and corresponding modal coordinates. Starting from

$$\mathbf{M}\ddot{\mathbf{x}} + \mathbf{B}\dot{\mathbf{x}} + \mathbf{K}\mathbf{x} = \mathbf{f}, \tag{4.4}$$

the corresponding modal transformation $\mathbf{x} = \mathbf{V}\mathbf{q}$ and left multiplication by the modal matrix $\mathbf{V}^{\mathrm{T}}$ of (4.4) leads to

$$\mathbf{V}^{\mathrm{T}}\mathbf{M}\mathbf{V}\ddot{\mathbf{q}} + \mathbf{V}^{\mathrm{T}}\mathbf{B}\mathbf{V}\dot{\mathbf{q}} + \mathbf{V}^{\mathrm{T}}\mathbf{K}\mathbf{V}\mathbf{q} = \mathbf{V}^{\mathrm{T}}\mathbf{f}. \tag{4.5}$$

The elastic part (which belongs to nonzero eigenfrequencies) of the modal matrix $\mathbf{V}_{\mathrm{elast}}$ has been evaluated concerning the mass matrix normalization

$$\mathbf{V}_{\mathrm{elast}}^{\mathrm{T}}\mathbf{M}\mathbf{V}_{\mathrm{elast}} = \mathrm{I}. \tag{4.6}$$

The diagonal matrix of the structures eigenfrequencies $\boldsymbol{\Omega}$ in rad/s is then computed as

$$\mathbf{V}_{\mathrm{elast}}^{\mathrm{T}}\mathbf{K}\mathbf{V}_{\mathrm{elast}} = \boldsymbol{\Omega}^2. \tag{4.7}$$

Concerning proportional damping, also the third part of the equation system is diagonalized

$$\mathbf{V}_{\mathrm{elast}}^{\mathrm{T}}\mathbf{B}\mathbf{V}_{\mathrm{elast}} = 2\mathbf{b}_{\mathrm{d}}\boldsymbol{\Omega}, \tag{4.8}$$

where $\mathbf{b}_{\mathrm{d}}$ is the diagonal matrix of the modal damping ratios of separate eigenfrequencies. Concerning the flexible modes reduction, the first step of reduction simply preserves the eigenmodes corresponding to lowest eigenfrequencies bellow some chosen limit.

4.1.2.2 Computation of Rigid Body Modes

As mentioned above, all RB modes of the structure have to be included, since they are base for the flight mechanics states. The simplest version of the RB modes includes vertical (z-direction) and lateral (y- and x-direction) translations as well as roll, yaw and pitch rotation. Additional RB modes of the model are the deflections of control surfaces. Global RBM (structure as a whole), included in the modal basis, neither

have structural stiffness nor structural damping. The local RB modes (flaps, ailerons) may receive structural stiffness and damping if required. The RB modes describe the motion of the whole body without deformation. The correct RB modes applied to system coordinates must not induce elastic forces. This crucial property can simply be written in matrix form

$$\mathbf{K}\mathbf{V}_{\text{rigid}} = \mathbf{0}. \tag{4.9}$$

The RB modes are actually a special case of static constraint modes rather than the eigenmodes [2]. Based on this consideration, the RB modes can be evaluated based on

$$\begin{bmatrix} \mathbf{K}_{ii} & \mathbf{K}_{ir} \\ \mathbf{K}_{ri} & \mathbf{K}_{rr} \end{bmatrix} \begin{bmatrix} \mathbf{V}_{ir} \\ \mathbf{V}_{rr} \end{bmatrix} = \begin{bmatrix} \mathbf{0}_{ir} \\ \mathbf{0}_{rr} \end{bmatrix}. \tag{4.10}$$

The index r denotes an arbitrary set of coordinates $\mathbf{z}_{\text{rigid}}$ that is just sufficient to restrain RB motion of the system. The RB modes can be computed equating $\mathbf{V}_{rr} = \mathrm{I}_{rr}$ (each mode corresponds to particular coordinate from the set $\mathbf{z}_{\text{rigid}}$). The rest of RB mode elements can be evaluated afterwards from (4.10) as

$$\mathbf{V}_{ir} = \mathbf{K}_{ii}^{-1}\left(-\mathbf{K}_{ir}\mathbf{V}_{rr}\right) = \mathbf{K}_{ii}^{-1}\left(-\mathbf{K}_{ir}\right) \tag{4.11}$$

The complete motion in physical coordinates can be evaluated using the superposition of RB motion and flexible modes vibrations

$$\mathbf{x} = \mathbf{x}_r + \mathbf{x}_e = \mathbf{V}_{\text{rigid}}\mathbf{z}_{\text{rigid}} + \mathbf{V}_{\text{elast}}\mathbf{q}_{\text{elast}}. \tag{4.12}$$

Concerning condition of RB motion (4.9) the dynamic equations for the RB coordinates accelerations are

$$\mathbf{V}_{\text{rigid}}^{\text{T}}\mathbf{M}\mathbf{V}_{\text{rigid}}\ddot{\mathbf{z}}_{\text{rigid}} = \mathbf{V}_{\text{rigid}}^{\text{T}}\mathbf{f} \tag{4.13}$$

$$\ddot{\mathbf{z}}_{\text{rigid}} = \mu_{\text{rigid}}^{-1}\mathbf{V}_{\text{rigid}}^{\text{T}}\mathbf{f}, \quad \mu_{\text{rigid}} = \mathbf{V}_{\text{rigid}}^{\text{T}}\mathbf{M}\mathbf{V}_{\text{rigid}}. \tag{4.14}$$

4.1.2.3 Computation of Residual Modes

The cutoff eigenmodes which are not included in the ROM can be represented by the residual mode, which represents the feedthrough components. Strictly speaking, it is the application of the general SPA for the system described by the modal coordinates. The including of the residual mode is important for better preservation of the frequency value of the original system zeros (antiresonances). The reliability of the antiresonances is important for the feedback loop properties [18]. The structural part of the aircraft model is a free body including 6 RB modes, accordingly the flexibility

matrix $\mathbf{G} = \mathbf{K}^{-1}$ does not exist and the residual mode must be computed using the inertia-relief projection matrix [2, 18]. Concerning decomposition (4.12) and RB motion condition (4.9) the complete dynamic equation is

$$\mathbf{M}\mathbf{V}_{\text{rigid}}\ddot{\mathbf{z}}_{\text{rigid}} + \mathbf{M}\mathbf{V}_{\text{elast}}\ddot{\mathbf{q}}_{\text{elast}} + \mathbf{B}\mathbf{V}_{\text{elast}}\dot{\mathbf{q}}_{\text{elast}} + \mathbf{K}\mathbf{V}_{\text{elast}}\mathbf{q}_{\text{elast}} = \mathbf{f} \tag{4.15}$$

substitution from (4.14) the equation can be rewritten into the form

$$\begin{aligned}\mathbf{M}\mathbf{V}_{\text{elast}}\ddot{\mathbf{q}}_{\text{elast}} + \mathbf{B}\mathbf{V}_{\text{elast}}\dot{\mathbf{q}}_{\text{elast}} + \mathbf{K}\mathbf{V}_{\text{elast}}\mathbf{q}_{\text{elast}} &= \mathbf{f} - \mathbf{M}\mathbf{V}_{\text{rigid}}\mu_{\text{rigid}}^{-1}\mathbf{V}_{\text{rigid}}^{\text{T}}\mathbf{f} \\ &= \left(\mathrm{I} - \mathbf{M}\mathbf{V}_{\text{rigid}}\mu_{\text{rigid}}^{-1}\mathbf{V}_{\text{rigid}}^{\text{T}}\right)\mathbf{f}\end{aligned} \tag{4.16}$$

The matrix $\mathbf{P}^{\text{T}} = \mathrm{I} - \mathbf{M}\mathbf{V}_{\text{rigid}}\mu_{\text{rigid}}^{-1}\mathbf{V}_{\text{rigid}}^{\text{T}}$ is the so-called inertia-relief projection matrix. The matrix $\mathbf{P}$ operates as a filter which leaves unchanged the flexible modes and destroys RB modes. $\left(\mathrm{I} - \mathbf{M}\mathbf{V}_{\text{rigid}}\mu_{\text{rigid}}^{-1}\mathbf{V}_{\text{rigid}}^{\text{T}}\right)\mathbf{f} = \mathbf{P}^{\text{T}}\mathbf{f}$ is self-equilibrated superposition of the external forces and inertia forces from RB motion of the body. Thanks to the self-equilibrium and filter properties of $\mathbf{P}$, the self-equilibrium position in elastic physical coordinates can be written as

$$\mathbf{x}_e = \mathbf{P}\mathbf{G}_{ii}\mathbf{P}^{\text{T}}\mathbf{f} \tag{4.17}$$

$\mathbf{G}_{ii}$ is the flexibility matrix corresponding to arbitrary virtual suspension which restrain the RB motion. In our Nacre model, we have used again the suspension described in previous paragraph, $\mathbf{G}_{ii} = \mathbf{K}_{ii}^{-1}$.

The resulting residual matrix can be evaluated as

$$\mathbf{R} = \sum_{k=m+1}^{\infty} \frac{\mathbf{V}_{\text{elast},k}\mathbf{V}_{\text{elast},k}^{\text{T}}}{\Omega_k^2} = \mathbf{P}\mathbf{G}_{ii}\mathbf{P}^{\text{T}} - \sum_{j=1}^{m} \frac{\mathbf{V}_{\text{elast},j}\mathbf{V}_{\text{elast},j}}{\Omega_j^2} \tag{4.18}$$

where m is the number of nonzero eigenfrequencies retained in the ROM.

4.1.3 Second Level of Model Reduction—Reduction of Complete Aeroelastic Model

As mentioned above, the model after the first level of reduction is used for the preparation of the complete aeroelastic model including all flight mechanics states, all lag states, the states of the preserved elastic modes, and possibly also the residual mode. Preparation of this complex model is described in the Sects. 3.3–3.5. The second level of reduction is realized on this complex model.

There are several methods how to prepare the ROM of the system suitable for the control algorithm design [4, 13, 22]. Despite different reduction concepts being

used, there are always two basic possibilities: the state truncation (ST) or the SPA. Let the original state-space model be divided as follows (states corresponding to index 1 are the preserved ones, 2 are the eliminated ones):

$$\mathrm{SS}_{\mathrm{orig}} = \begin{bmatrix} \mathbf{A}_{11} & \mathbf{A}_{12} & \mathbf{B}_1 \\ \mathbf{A}_{21} & \mathbf{A}_{22} & \mathbf{B}_2 \\ \mathbf{C}_1 & \mathbf{C}_2 & \mathbf{D} \end{bmatrix}. \tag{4.19}$$

Then, the reduced-order state-space model obtained by ST of any type is

$$\mathrm{SS}_{\mathrm{trunc}} = \begin{bmatrix} \mathbf{A}_{11} & \mathbf{B}_1 \\ \mathbf{C}_1 & \mathbf{D} \end{bmatrix}. \tag{4.20}$$

The SPA variant of the reduced model preserves the static gains (DC gain) of an original system and generally can be written as

$$\mathrm{SS}_{\mathrm{spa}} = \begin{bmatrix} \mathbf{A}_{11} - \mathbf{A}_{12}\mathbf{A}_{22}^{-1}\mathbf{A}_{21} & \mathbf{B}_1 - \mathbf{A}_{12}\mathbf{A}_{22}^{-1}\mathbf{B}_2 \\ \mathbf{C}_1 - \mathbf{C}_2\mathbf{A}_{22}^{-1}\mathbf{A}_{21} & \mathbf{D} - \mathbf{C}_2\mathbf{A}_{22}^{-1}\mathbf{B}_2 \end{bmatrix}. \tag{4.21}$$

The preserving of the transfer functions for DC gain and for the low frequencies is important in the context of the low-order model approximation and consequently preserving of the RB and flight dynamics motion components. Therefore, the SPA [21] variant of the reduction has been preferentially chosen.

4.1.4 Balanced Reduction

The important concept of the generation of the ROM is the balanced reduction [13] based on the given inputs and outputs with the chosen model dimension. The balanced reduction has been used as the reference one. The general methods of the balanced reduction are based on solution of Lyapunov equation [4, 13]. The basic algorithm of the balanced ROM generation is as follows [4]. The unstable part of the original system must be included also in the ROM. The reduction is applied only to stable part of the system. Let the original system in the state-space form be

$$\mathrm{SS} = \begin{bmatrix} \mathbf{A} & \mathbf{B} \\ \mathbf{C} & \mathbf{D} \end{bmatrix}. \tag{4.22}$$

$$\mathrm{SS}_{\mathrm{b}} = \begin{bmatrix} \mathbf{Z}^{-1}\mathbf{A}\mathbf{Z} & \mathbf{Z}^{-1}\mathbf{B} \\ \mathbf{C}\mathbf{Z} & \mathbf{D} \end{bmatrix} = \begin{bmatrix} \mathbf{A}_{11} & \mathbf{A}_{12} & \mathbf{B}_1 \\ \mathbf{A}_{21} & \mathbf{A}_{22} & \mathbf{B}_2 \\ \mathbf{C}_1 & \mathbf{C}_2 & \mathbf{D} \end{bmatrix}. \tag{4.23}$$

The similarity transformation matrix $\mathbf{Z}$ is formally decomposed with regard to partitioning of the state matrix

$$\mathbf{Z} = \begin{bmatrix} \mathbf{T}, \mathbf{U} \end{bmatrix}, \quad \mathbf{Z}^{-1} = \begin{bmatrix} \mathbf{L} \\ \mathbf{V} \end{bmatrix} \tag{4.24}$$

The balancing-related model reduction methods are connected with the so-called controllability and observability gramians $\mathbf{P}$ and $\mathbf{Q}$ which can be computed from a pair of Lyapunov equations

$$\begin{aligned} \mathbf{AP} + \mathbf{PA}^{\mathrm{T}} + \mathbf{BB}^{\mathrm{T}} &= \mathbf{0} \\ \mathbf{A}^{\mathrm{T}}\mathbf{Q} + \mathbf{QA} + \mathbf{C}^{\mathrm{T}}\mathbf{C} &= \mathbf{0} \end{aligned} \tag{4.25}$$

The gramians of a stable system are positive semidefinite matrices which can be decomposed by Cholesky factorization $\mathbf{P} = \mathbf{SS}^{\mathrm{T}}$ and $\mathbf{Q} = \mathbf{R}^{\mathrm{T}}\mathbf{R}$. So-called Hankel singular values of the system are obtained by singular value decomposition

$$\mathbf{RS} = \begin{bmatrix} \mathbf{U}_1 \ \mathbf{U}_2 \end{bmatrix} \begin{bmatrix} \Sigma_1 & \mathbf{0} \\ \mathbf{0} & \Sigma_2 \end{bmatrix} \begin{bmatrix} \mathbf{V}_1 \\ \mathbf{V}_2 \end{bmatrix} \tag{4.26}$$

The singular values are ordered, first r largest singular values in $\mathbf{\Sigma}_1$ correspond to retained states, the rest $\mathbf{\Sigma}_2$ correspond to neglected states.

$$\mathbf{L} = \mathbf{\Sigma}_1^{-1/2}\mathbf{U}_1^{\mathrm{T}}\mathbf{R}, \quad \mathbf{T} = \mathbf{SV}_1\mathbf{\Sigma}_1^{-1/2} \tag{4.27}$$

The balanced reduction is very straightforward especially for the pure structural models with the proportional damping. The airplane model, however, also consists of the states with the high damping and even real poles. The evaluation of the final damping values of particular modes is relatively complex. The computational experiments show that the pure balanced reduction can discard some important states, like the first bending mode, some of the lag states, or even some flight mechanics states. Consequently, the combined reduction approaches have been tested.

4.1.4.1 Combined Model Reduction

Based on the control design requirements, the second level model has been reduced in two main versions. The first (control design) ROM contains all flight mechanics states, lag states and states of the first (lowest) 4 elastic modes. The SPA variant of the reduction has been chosen. The set of the small (4 elastic modes) models is prepared in the grid version and also in the parameterized version as described in the next paragraph about parameterization. In concrete, the 5th order of polynomial parameterization has been chosen. Besides the small model with 4 elastic modes,

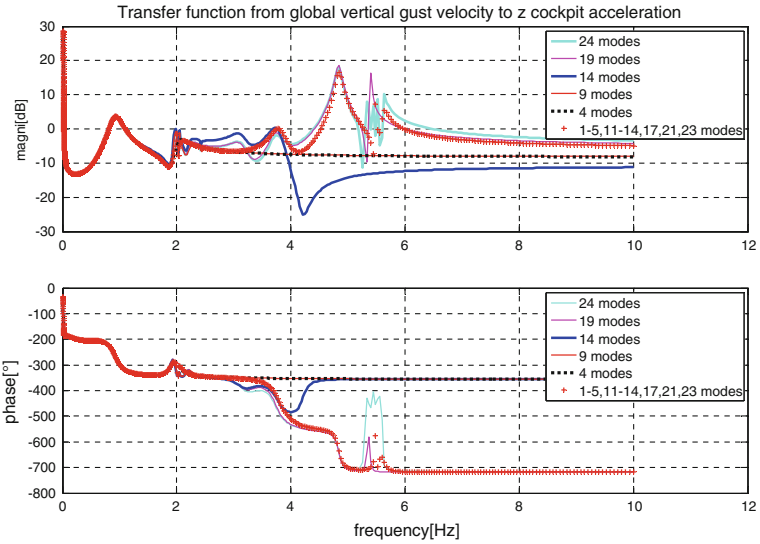

Fig. 4.1 TF from global vertical gust to z cockpit acceleration

also the larger testing model with selected set of 12 elastic modes or 19 elastic modes has been tested.

The choice starts from the balanced reduction and is modified based on the inspection of comparisons of many transfer functions for different levels of reduction (with first 4 elastic modes, first 9 elastic modes, first 14 elastic modes, first 19 elastic modes, first 24 elastic modes). The SPA variant of reduction has been chosen. The examples of the transfer functions are in Figs. 4.1 and 4.2. The larger model has been primarily prepared only in the grid version, the problems of tracking, and the final solution is described in next paragraphs.

4.1.5 Parameterization of Aircraft Models

The result of the reduction process is the set of reduced models (4.3) that are known for the values of parameters $\mathbf{p}_\mathrm{d}$. These models for the discrete values of parameters are to be replaced by one model the system parameters of which are some approximation continuous functions of the parameters. The system parameters are the elements of the system matrices $\mathbf{A}, \mathbf{B}, \mathbf{C}, \mathbf{D}$. The form of the approximation function must be a rational function, that is, a fraction of two polynomial functions. There are two groups of methods for construction of such approximations.

The first group is the approximation by splines and the second group is the approximation by radial basis functions (RBF). It is considered four parameters $\mathbf{p}_\mathrm{d}$

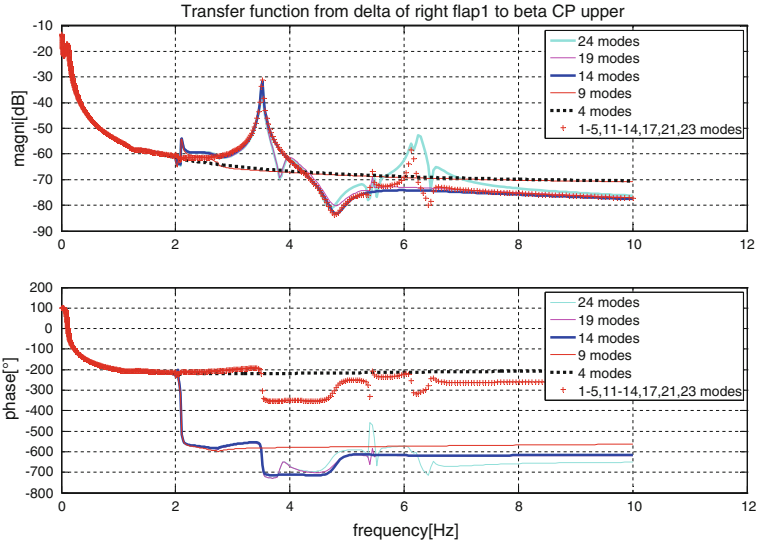

Fig. 4.2 TF from angle of right flap 1 to upper cockpit side-slip angle

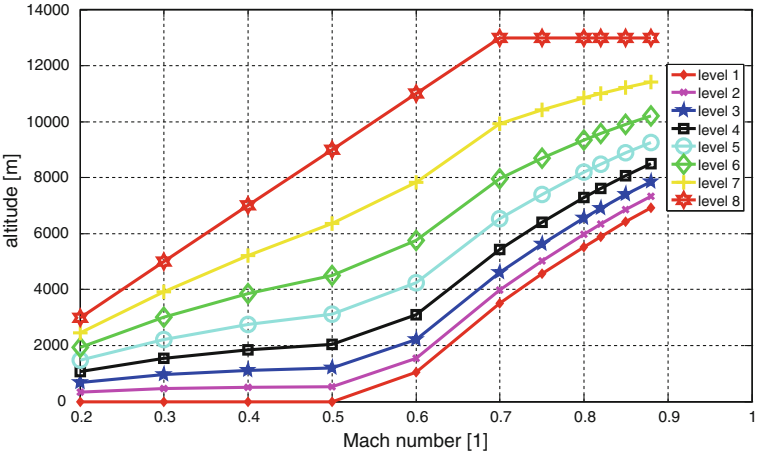

Fig. 4.3 Values of considered altitude levels and Mach numbers

- I_{Pass}—the number of the *passenger* variant (1, 2, 3)
- I_{Fuel}—the number of the *fuel* variant (1, 2, 3, 4, 5, 6, 7)
- I_{Mach}—the number of the *Mach* variant (1, 2, 3, 4, 5, 6, 7, 8, 9, 10, 11)
- I_{Alti}—the number of the *altitude level* variant (1, 2, 3, 4, 5, 6, 7, 8).

Values of considered altitude levels and Mach numbers are presented in Fig. 4.3.

4.1.6 Spline Interpolation

The splines can be divided into polynomial splines and rational splines (fraction of two polynomial splines). Each parameter p_i has the span $p_{i0} < p_i < p_{in_i}$ and the span is divided into n_i intervals $[p_{i,k-1}, p_{i,k}]$ in such way that $p_{i0} < p_{i1} < \cdots < p_{i,k-1} < p_{i,k} < \cdots < p_{i,n_i}$. The Cartesian product of the span consists of the Cartesian product of subintervals and each such Cartesian product of subintervals is for the system parameter S approximated by the Cartesian product of cubic polynomial splines

$$S = \sum_{i1=0}^{3} \sum_{i2=0}^{3} \sum_{i3=0}^{3} \sum_{i4=0}^{3} S_{i1,i2,i3,i4} p_1^{i1} p_2^{i2} p_3^{i3} p_4^{i4} \tag{4.28}$$

or by the Cartesian product of cubic rational splines

$$S = \frac{\sum_{i1=0}^{3} \sum_{i2=0}^{3} \sum_{i3=0}^{3} \sum_{i4=0}^{3} S^N_{i1,i2,i3,i4} p_1^{i1} p_2^{i2} p_3^{i3} p_4^{i4}}{\sum_{i1=0}^{3} \sum_{i2=0}^{3} \sum_{i3=0}^{3} \sum_{i4=0}^{3} S^D_{i1,i2,i3,i4} p_1^{i1} p_2^{i2} p_3^{i3} p_4^{i4}} \tag{4.29}$$

The particular splines can be created using the theory of geometric parametric splines for curves and surfaces like as B-splines and NURBS. The requirements on the approximation properties are here much fewer than in geometry.

4.1.6.1 Radial Basis Functions

The approximation by the RBF is based on the idea that the approximated function is approximated by the sum of its values (or weights) multiplied by the distance function from the function input. In the case of the system parameter S the approximation is

$$S = \sum_K S_K \Phi \left(\| \mathbf{p}_K - \mathbf{c}_K \| \right) \tag{4.30}$$

where Φ is the distance function, $\mathbf{c}_K$ is the input center, S_K the values or weights of the function. The distance functions are usually Gaussian functions. This theory has been developed specifically for system model approximations in the system LOLIMOT [12]. This original system has been reimplemented and extended at CTU [20] and modified by replacement of the Gaussian function by rational functions for the distance

$$\Phi \left(\| \mathbf{p}_K - \mathbf{c}_K \| \right) = \prod_K \frac{1}{\sum_{i=0}^{n} \left(\frac{p_K - c_K}{\sqrt{2}\sigma_K} \right)^{2n} \frac{1}{n!}} \tag{4.31}$$

The developed software CTU-MIMO-POLYNOMIAL-LOLIMOT has been used for continuous multidimensional approximation of the grid point data. CTU-MIMO-POLYNOMIAL-LOLIMOT in basic form generates approximation of any function in parameters p by locally linear functions and globally rational functions. For example, the formula for three dimensional parameterization ($\mathbf{p} = [p_1, p_2, p_3]^{\mathrm{T}}$) has a form

$$\begin{aligned} S &= \sum_{k=1}^{m} (w_{k,0} + w_{k,1} p_1 + w_{k,2} p_2 + w_{k,3} p_3) \Phi\left(\|\mathbf{p} - \mathbf{c}_k\|\right) \\ &= \sum_{k=1}^{m} (w_{k,0} + w_{k,1} p_1 + w_{k,2} p_2 + w_{k,3} p_3) \prod_{j=1}^{3} \frac{1}{\sum_{i=0}^{n} \left(\frac{p_j - c_{k,j}}{\sqrt{2}\sigma_K}\right)^{2i} \frac{1}{i!}} \end{aligned} \tag{4.32}$$

The local linear function can be generalized to local polynomial n-dimensional function

$$\begin{aligned} \mathrm{pol}(p_1, p_2, p_3) = w_{k,0} + w_{k,1} p_1 + w_{k,2} p_2 + w_{k,3} p_3 \\ + w_{k,4} p_1^2 + w_{k,5} p_2^2 + w_{k,6} p_3^2 + w_{k,7} p_1 p_2 + \cdots \end{aligned} \tag{4.33}$$

and if possible from the point of view of accuracy, one polynomial function can be used for the whole parameter interval. So, we can switch between these (rational/polynomial) types of approximation. The inherent trade-off between accuracy and complexity needs to be considered.

4.1.6.2 Parametrization Problems

The parametrization described in previous section can enter three kinds of problems. The first kind of problems is with the continuity of reduced coordinates. The reduction process can result into different coordinates for different values of parameters $\mathbf{p}_\mathrm{d}$. Such situation is presented in Fig. 4.4. The modal coordinates chosen to ROM by balanced reduction are marked by circles. The choices for the variant 00 (no fuel, no passengers) and for the variant 44 (full fuel tanks, all passengers) are different.

This results into discontinuities of the system parameters in model description $\mathbf{A}, \mathbf{B}, \mathbf{C}, \mathbf{D}$. Such parameterized ROM cannot be controlled. The change of coordinates within the reduction process for different values of parameters $\mathbf{p}_\mathrm{d}$ must be avoided. This means that many reduction techniques that are very efficient from the point of view of accurate reduction cannot be used.

The second kind of problems is with the parametrization of ROM between the values of parameters $\mathbf{p}_\mathrm{d}$. The parametrization can be separately very good, but the parameterized ROM between the values of parameters $\mathbf{p}_\mathrm{d}$ can be wrong. For example, the parameterized ROM model can be unstable between the values of parameters $\mathbf{p}_\mathrm{d}$.

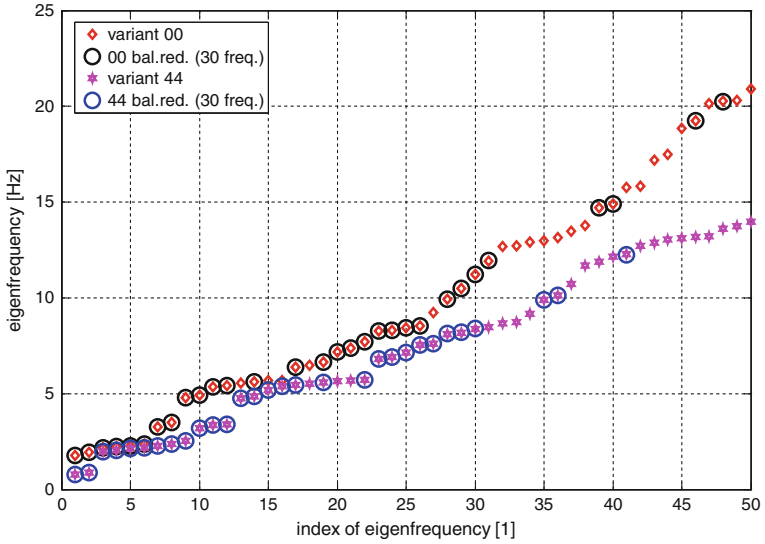

Fig. 4.4 Choice of modes to ROM for different variants based on balanced reduction

It is necessary to test basic properties (eigenvalues, stability, controllability, observability) for the interpolated matrices between original grid points.

The third kind of problems is the unique tracking of corresponding states during the parameters change. This problem is particularly problematic for the states corresponding to elastic modes. The modal assurance criterion can be used for testing of proximity of eigenmodes in adjacent grid points, but the reliable identification and tracking of all states across the wide parameter intervals is not easy. The final solution used within the project test gradually the consistency of states across all variants for the increasing number of preserved states.

4.1.7 Conclusion

The finally chosen solution of the reduction process comes from the testing of many variants and is highly influenced by the request of internally consistent parameterized model. The first level ROMs have been prepared with the 80 states. The second level of reduction process ends with two variants of models. The first variant of the control design ROM contains all flight mechanics states, all lag states, and states of the first (lowest) 19 elastic modes. The simplified variant of the control design ROM takes separately the symmetric and skew-symmetric component including all flight mechanics states, all lag states, and states of the first (lowest) 4 elastic modes. The example of comparison between original (80 states) and reduced input–output (only 2 symmetric modes) transfer function is in Fig. 4.5.

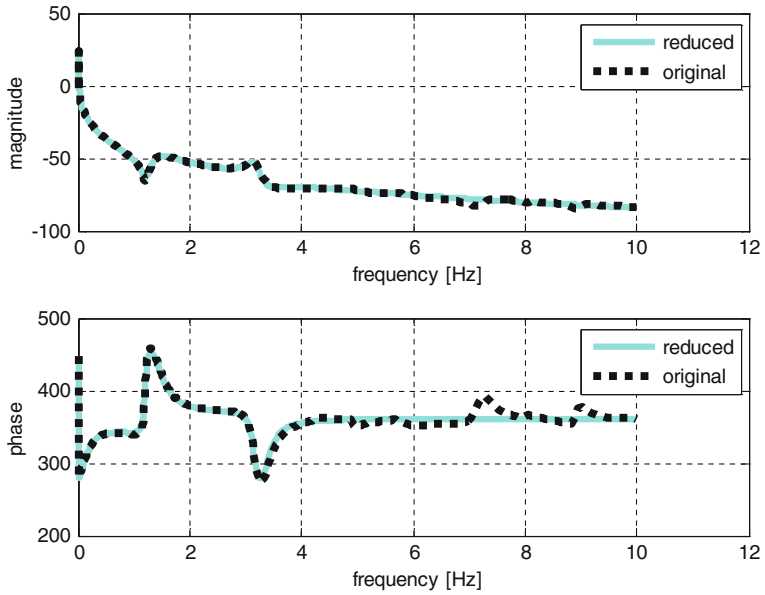

Fig. 4.5 Example of comparison between original and reduced transfer function

4.2 Linear Fractional Representation of Parametrized Models

S. Hecker

Over the last 20 years, a paradigm shift in the modeling of dynamic systems occurred with the introduction of modern robust control theory and its associated modeling framework, the LFT [14, 15]. A Linear Fractional Representation (LFR) is a representation of a nonlinear system as a linear system formed by a constant M matrix in linear feedback with a structured matrix $\mathbf{\Delta}$. The process of extracting the uncertainty into the structured matrix $\mathbf{\Delta}$ of this so-called $M - \mathbf{\Delta}$ form is called LFR realization, also known as "pulling out the delta", and is considered the fundamental LFR modeling step. From these initial LFT developments, it was immediately recognized that they were part of the larger set of linear parameter-varying (LPV) models but presenting a specific structure. This generated great interest and sparked the development of the (LPV)/(LFT) field [10, 11, 14–16, 19, 24].

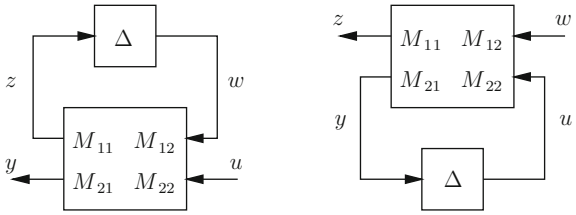

Fig. 4.6 Graphical representation of lower and upper LFTs

4.2.1 Linear Fractional Transformation

A LFT is a matrix function based on two matrix components,

$$\mathbf{M} = \begin{bmatrix} \mathbf{M}_{11} & \mathbf{M}_{12} \\ \mathbf{M}_{21} & \mathbf{M}_{22} \end{bmatrix}$$

and $\mathbf{\Delta}$, and a feedback interconnection. The matrix $\mathbf{M}$ represents the nominal, known, part of the system, while the matrix $\mathbf{\Delta}$ contains the time-varying, unknown, or uncertain components.

Depending on the feedback interconnection used, there are two possible types of LFTs, upper [see Fig. 4.6-left and (4.34)] and upper [see Fig. 4.6-right and (4.35)].

$$\mathscr{F}_{\mathrm{u}}(\mathbf{M}, \mathbf{\Delta}) = \mathbf{M}_{22} + \mathbf{M}_{21}(\mathrm{I} - \mathbf{\Delta}\mathbf{M}_{11})^{-1}\mathbf{\Delta}\mathbf{M}_{12} \tag{4.34}$$

$$\mathscr{F}_{\mathrm{l}}(\mathbf{M}, \mathbf{\Delta}) = \mathbf{M}_{11} + \mathbf{M}_{12}(\mathrm{I} - \mathbf{\Delta}\mathbf{M}_{22})^{-1}\mathbf{\Delta}\mathbf{M}_{21} \tag{4.35}$$

Remark 1 The matrix $\mathbf{\Delta}$ is typically norm-bounded $\|\mathbf{\Delta}\|_\infty \leq 1$ for design and analysis (without loss of generality by scaling of $\mathbf{M}$), but otherwise unrestricted in form (structured/unstructured) or type (nonlinear/time-varying/constant). If any of the components in $\mathbf{\Delta}$ is a scheduling parameter, an LPV system is obtained.

Remark 2 The order of the LFR is the number of parameters, including repetitions, contained in $\mathbf{\Delta}$ (for example, $\mathbf{\Delta} = \mathrm{diag}(p_1\mathrm{I}_2, p_2) \rightarrow$ LFR order is 3). Since many realistic robustness analysis problems can easily result in very-high-order LFRs, it is vital to have efficient and automated tools which can compute minimal, or at least close to minimal, representations of these systems.

Remark 3 A very important property of LFRs is that their interconnection results in another LFR (for example, sum, concatenation, etc. of LFRs result in LFRs) [5, 10].

4.2.2 Process of LFR Modeling

The most widespread, standard approach to obtain an LFR is based on the numerical Jacobian LPV approach augmented with the final LFR realization step of "pulling out the deltas". Hence the basis for the LFR modeling is a set of linear time-invariant (LTI) models generated by trimming and linearizing a nonlinear aircraft model at specific points within the flight envelope (Mach number and dynamic pressure) and for different parameter values (in ACFA2020 the fuel mass and center of gravity (CG) position parameters). These grid-point models are then interpolated using polynomial functions to obtain one single LPV model describing the full set of LTI models. Finally, the LPV model is transformed into an LFR.

This approach has the advantages of relying on well-known numerical techniques (to obtain equilibrium points and linearizations of plants) and of resulting in purely LTI models (once the components in the $\mathbf{\Delta}$ matrix are assigned numerical values). These advantages are highly relevant since most engineers are acquainted with numerical linearization and with linear analysis/synthesis techniques which are applicable due to the underlying LTI nature of the LFR. The drawback is a loss of modeling oversight as application of the numerical trim/linearization step transforms the modeling problem into a numerical black box approach. Furthermore, the results obtained from LTI synthesis/analysis need to be validated on the purely nonlinear model and there may exist a wide gap between the latter and the linear models used for design. The LFR modeling can be summarized in the following five-step process:

1. *Trimming and linearization*: the nonlinear aircraft model is trimmed and linearized at several values of the parameter vector $p = (p_1, \ldots, p_4)$, were the uncertain parameters are the fuel case (p_1 with 11 grid points), the position of center of gravity (p_2 with 3 grid points), the Mach number (p_3 with 8 grid points) and the dynamic pressure (p_4 with 13 grid points). The result was a set of 3432 LTI models.
2. *Model interpolation*: in order to accurately approximate the grid point LTI models with an LPV model, a usual way is to generate multivariable polynomials for all varying entries of the LTI state-space matrices $\mathbf{A}, \mathbf{B}, \mathbf{C}, \mathbf{D}$. This may result in very complex polynomial LPV models, which then may yield high-order LFRs. To avoid this, a general approach is presented in [17] to generate an LPV model, which approximates a set of linearized grid-point models with high accuracy and is optimally suited for LFT-based Robust Stability (RS) analysis and control design. The idea is to combine the polynomial fitting with a global optimization where the objective is to find an LPV model, which has the property to allow a transformation into an LFR of lowest possible order. A gap metric constraint is included during the optimization in order to guarantee a specified accuracy of the transfer function of the LPV model. As a result, only the varying state-space matrix entries that have a significant influence on the transfer function are fitted with polynomials, whereas the others are taken constant. In addition, the number of required monomials within each polynomial is optimized in order to

reduce complexity. Some recent applications [9, 17] of the method have shown its effectiveness.

3. *Symbolic preprocessing*: the role of symbolic preprocessing is to find equivalent representations of individual matrix elements, entire rows/columns or even the whole parametric state-space matrices, which lead to LFRs of lower order when realized with the object-oriented LFT realization approach. There exist many methods [8] such as the Horner form transformation, the structured tree decomposition [1], and the variable splitting factorization [7].
4. *Object-oriented LFR realization*: the method is described in [10] and in [5] it is extended to allow direct LFR realization of general rational parametric systems. The basic idea is to realize elementary LFRs for each uncertain parameter and to use basic LFR manipulation formulas for addition, subtraction, multiplication, inversion and row/column concatenation to build an LFR for a rational parametric matrix. The method is very flexible and can be easily automated, thus allowing an efficient and reliable implementation, which is available within the LFR Toolbox for MATLAB® Version 2 [6].
5. *Numerical order reduction*: in a last step it can be attempted to reduce the order of the LFR by using numerical multidimensional order reduction algorithms [3, 10], which are also implemented in [6]. There are papers [3] that discuss LFR minimality, but that is under the assumption that the uncertain parameters do not commute. The idea behind the numerical 1-D reduction method is to repeatedly perform standard 1-dimensional order reduction for each uncertain parameter. The *n*-D technique [3] works in a similar way but considers all parameters at once, and generally yields LFRs of lower orders compared to the 1D technique.

4.2.3 Generation of LFRs for the ACFA 2020 BWB Aircraft

In this section, the order and structure of the resulting LFRs that were used for controller synthesis are described. As the methods for LFT-based robust controller synthesis are computationally demanding, it is of prior interest to use LFRs of low order. This usually requires to reduce the order and complexity (number of states, inputs and outputs, number of uncertain parameters, number of LTI grid-point models covering a certain region of the flight envelope, …) of the underlying LTI grid-point models that are used for LFR generation.

Here, the ROMs created as outlined in Sect. 4.1 are the starting point to generate LFRs for control design. In the following, longitudinal LFR models are generated for the open-loop aircraft with and without modeled phugoid mode and utilized in system analysis and in the LPV feedback design in Sect. 6.5. Lateral LFR models of the open-loop dynamics controlled by a 1st-order initial stabilizing controller (designed in Sect. 6.2) are generated and utilized in the robust feedback design in Sect. 6.3.

4.2.3.1 A Priori Model Simplifications

The first step in LFR modeling is the interpolation of a set of LTI state-space models using polynomial functions for each element of the state-space system matrices **A**, **B**, **C**, and **D**. Hence the number of states, inputs and outputs, which define the dimension of these matrices play an important role in terms of the resulting LFR order. A lower number of states, inputs and outputs usually results in a lower LFR order. Therefore, in a first step, the overall aircraft model was split into two models describing the longitudinal and lateral dynamics only. In addition, the longitudinal model included only symmetric elastic modes and the lateral model included only asymmetric and antisymmetric elastic modes.

The number of elastic modes that were considered for controller synthesis was also drastically reduced and the LFRs usually included only between 2 and 6 elastic modes of lowest frequencies. Elastic modes of higher frequencies were only used for controller validation but due to the low bandwidth of the actuators and a roll-off of the controller, the excitation of these modes from the controller was very small.

An accurate description of the gust affecting the aircraft dynamics resulted in a large number of lag states that were included in the LTI aircraft models. For controlling the elastic modes, the robust controllers mainly used acceleration sensors, and no feed-forward system using a forward-looking sensor (for example, LIDAR) was used. Therefore, the way (gust or maneuver) and accuracy of how the elastic modes were excited was not of highest importance and most of the lag states could be neglected. The controller synthesis models included two lag states.

Furthermore, the control allocation for the large number of model inputs was usually fixed, that is, all controllers typically deflected several control surfaces in the same way. Hence, these control surfaces can be combined and considered as a single model input, which reduces the number of model inputs (columns in **B** and **D** state-space matrices).

Finally, only six model outputs were chosen for the controller synthesis model from the large number of outputs available from modeling.

The aircraft model includes four uncertain parameters, namely Mach number, position of center of gravity, fuel case, and dynamic pressure. For the LFRs, the Mach number and dynamic pressure were considered fixed and only the fuel case and the position of center of gravity were considered uncertain, resulting in an LFR with only two parameters. A reason for this simplification was that the Mach number and dynamic pressure can me measured very accurately and to high safety levels. Therefore, these parameters are used for gain scheduling, that is, several robust controllers (robust with respect to fuel case and CG position) for different Mach numbers and dynamic pressures will be synthesized and scheduled a posteriori.

4.2.3.2 LFRs for the Longitudinal Aircraft Model

The longitudinal aircraft model includes either 12- or 14- states: four states from two actuator models, two lag states, four states describing the two first (lowest frequency)

symmetric elastic modes and two RB states for the short-period mode. The 14-state model includes two more RB states describing the phugoid mode.

The model has three inputs, where the symmetric deflection of flaps 1 and flaps 2 are combined as one input and the other inputs are the symmetric deflection of flaps 3 and the global vertical gust input.

As outputs we have chosen the vertical load factor Nz_{CG} at the center of gravity, the pitch rate q_{CG} at the center of gravity, the true airspeed V_{TAS}, the combined output $Nz_{\mathrm{long.law}}$, the wing root bending moment M_x (here called M_y) and the vertical cut force Fz at the wing root.

For this model a given cruise condition with fixed Mach number, dynamic pressure and position of center of gravity was chosen and the fuel case parameter is allowed to vary within the full range. Therefore, the resulting LFRs include only one uncertain parameter.

Using the automated generation process described in Sect. 4.2.2, two LFRs were generated for the 14- states model. One accurate model with order 17, that is, $\Delta = p_4\, I_{17}$, and one less accurate model with order 4. During the LFR generation process, the accuracy of the LFR is measured using the ν-gap metric and is given by the maximum ν-gap metric between all the LTI grid-point models (given in the relevant flight domain) and the resulting LFR evaluated at the given grid points. Using the MATLAB® command `gapmetric.m` one obtains a value between 0 and 1, where 0 means that the models are equal and 1 indicates a large difference between the models. For the given LFRs, we obtained values of 0.08 for the accurate model and 0.15 for the less accurate model.

For the 12-state model, an accurate model of order 16 and a less accurate model of order 3 was generated. The maximum errors in terms of the ν-gap metric were given by 0.06 and 0.18.

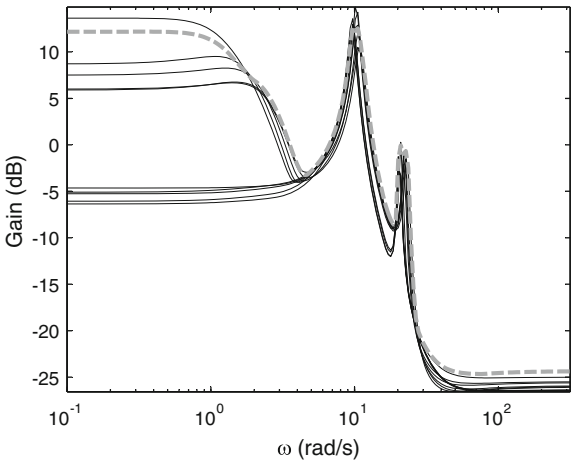

Fig. 4.7 Worst-case gain validation of 12-state model (LFR order 16, no phugoid)

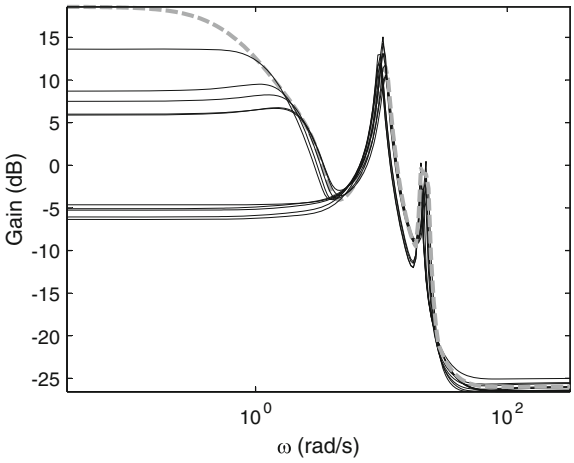

Fig. 4.8 Worst-case gain validation of 12-state model (LFR order 3, no phugoid)

Besides the ν-gap metrics, a further validation of the LFRs was performed by calculating the worst-case gains (MATLAB® function `wcgain.m`) of the LFRs for a given frequency range and comparing these values with the gains (maximum singular value over frequency) of the LTI models. Figures 4.7 and 4.8 show the worst-case gains (dashed gray line) and the gains of the LTI models for the 12-state models. It can be clearly seen that the higher order LFR yield a better approximation/coverage, especially at low and high frequencies the worst-case gain tightly covers the LTI model gains. The low-order LFR overestimates the low-frequency gain and underestimates the gains at the frequency of the first flexible mode. For the 14- states models shown in Figs. 4.9 and 4.10 a better approximation of the higher order LFR can be seen for the low-frequency RB aircraft modes.

4.2.3.3 LFRs for the Lateral Aircraft Model

The lateral aircraft model includes 33- states: six states from three actuator models, no lag states, 18 sensor states, four states describing the two first (lowest frequency) antisymmetric elastic modes, four states for the RB modes and one state for a simple controller that was already included in the model to stabilize the lateral RB modes (designed in Sect. 6.2).

The model has three inputs, where the symmetric deflection of flaps 3 and flaps 4 are combined as one input, the second and third inputs are the rudder and flaps 5.

As outputs, we have chosen the sideslip angle β, the angle φ, the roll rate p, the yaw rate r, the combined output $n_{z_{\text{law,lat}}}$ and the wing root bending moment Mx (here called My).

Two different cruise conditions with fixed Mach number and dynamic pressure were chosen. For the first cruise case, one LFR was generated for the full variation

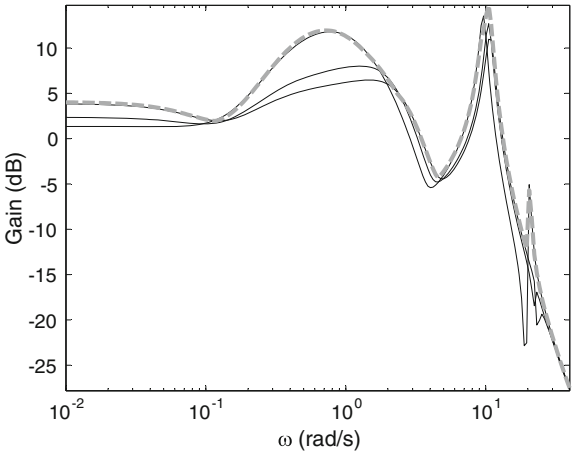

Fig. 4.9 Worst-case gain validation of 14-state model (LFR order 17, with phugoid)

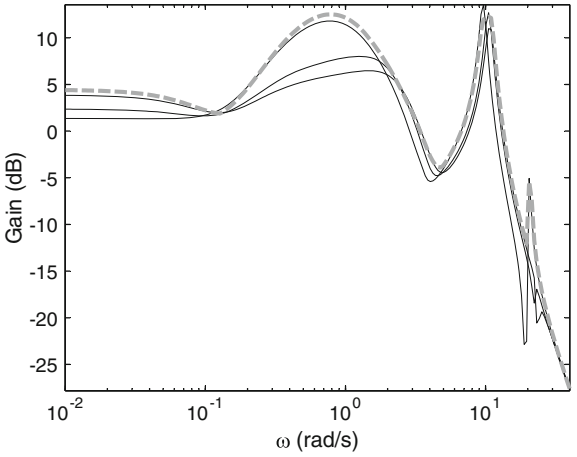

Fig. 4.10 Worst-case gain validation of 14-state model (LFR order 4, with phugoid)

of fuel cases and positions of center of gravity and a second LFR was generated covering all fuel cases but with fixed center of gravity position. For the model with two uncertain parameters, an LFR of order 16 was obtained and for the simpler one-parametric LFR, the order was 4. The corresponding ν-gap metric errors were 0.19 and 0.10. For the second cruise case only a two parametric LFR of order 13 covering all fuel cases and center of gravity positions was generated. The maximum ν-gap metric error of this model was 0.08. Figures 4.11, 4.12 and 4.13 again show that the LFRs tightly cover the LTI models in terms of the worst-case gain. All models were of reasonable complexity to be used for robust control design methods like μ-synthesis (in Sect. 6.3).

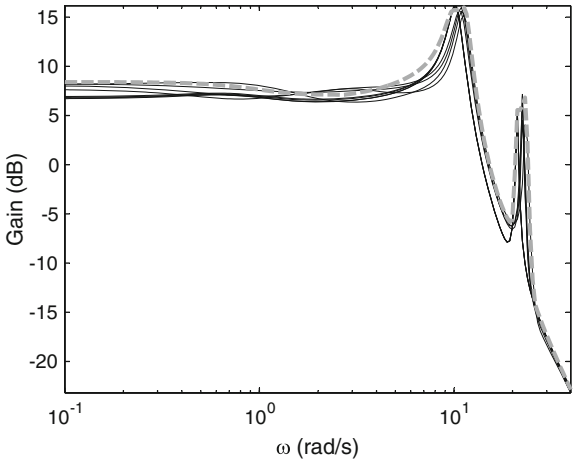

Fig. 4.11 Worst-case gain validation of lateral 33-state model (LFR order 16, parametrized in fuel and CG, cruise case A)

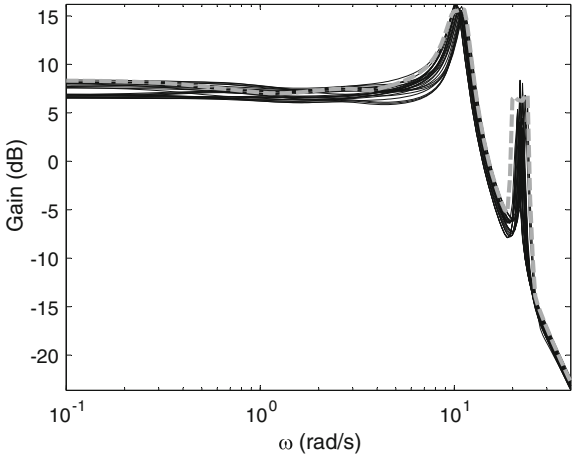

Fig. 4.12 Worst-case gain validation of lateral 33-state model (LFR order 4, parametrized in fuel only, cruise case A)

4.2.4 Summary

For the ACFA 2020 blended wing body (BWB) aircraft, parametric LFRs were generated to be used for robust controller synthesis. During the modeling phase of the project, much effort has been invested in finding models of reasonable complexity which can be used in conjunction with modern robust control design techniques.

One important step toward control-oriented aircraft models was the application of model reduction techniques to reduce the huge number of structural modes in the

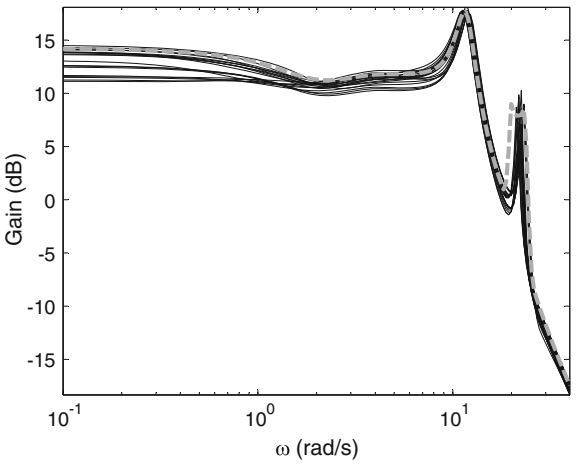

Fig. 4.13 Worst-case gain validation of lateral 33-state model (LFR order 13, parametrized in fuel and CG, cruise case B)

thousands of grid-point LTI models representing the aircraft dynamics for all fuel cases, CG positions, Mach numbers and dynamic pressures. As for LFR generation, the reduced-order grid-point LTI models are interpolated, one has to be very careful to guarantee consistency (number and physical meaning) of the states of the ROMs. Here, it may easily happen that the signs of the elements of the **A**, **B**, and **C** state-space matrices switch from grid point to grid point which does not affect the transfer function of a single grid-point model but makes an interpolation of neighboring grid-point models impossible. During the ACFA project, a fully automated process delivering ROMs that can be interpolated was not available and many sign correction had to be done manually. This is still an open problem and actual research tries to find order-reduction methods that allow the a posteriori interpolation of a set of reduced-order grid-point models [23].

As an alternative to the parametric uncertain models, one may also generate LFRs including an unstructured uncertainty. In this case, the sign problem is not important, however, a lot of structural information is lost and one may obtain more conservative controllers with less performance.

References

1. Cockburn JC, Morton BG (1992) Linear fractional representations of uncertain systems. Automatica 33(7):1263–1271
2. Craig RR (2000) Coupling of substructures for dynamic analyses: an overview. AIAA Paper 1573:2000
3. D'Andrea R, Khatri S (1997) Kalman decomposition of linear fractional transformation representations and minimality. In: Proceedings of the American control conference, Albuquerque, New Mexico, pp 3557–3561

4. Gawronski WK (2004) Advanced structural dynamics and active control of structures. Springer, New York
5. Hecker S, Varga A (2004) Generalized LFT-based representation of parametric uncertain models. Eur J Control 10(4):326–337
6. Hecker S, Varga A, Magni JF (2005) Enhanced LFR-toolbox for MATLAB. Aerosp Sci Technol 9:173–180
7. Hecker S, Varga A (2006) Symbolic techniques for low order LFT-modeling. Int J Control 79(11):1485–1494
8. Hecker S (2007) Generation of low order LFT representations for robust control applications, vol 1114. VDI-Verlag, Düsseldorf
9. Hecker S, Pfifer H (2010) Generation of LFRs for the COFCLUO nonlinear aircraft model. In: 2nd workshop on clearance of flight control laws, Stockholm, Sweden
10. Lambrechts P, Terlouw J, Bennani S, Steinbuch M (1993) Parametric uncertainty modeling using LFTs. In: American control conference, San Francisco
11. Leith DJ, Leithead WE (2000) Survey of gain-scheduling analysis and design. Int J Control 73(11):1001–1025
12. Nelles O (1998) Nonlinear system identification with local linear Neuro-Fuzzy models. PhD thesis, Technische Universitat Darmstadt, Darmstadt
13. Obinata GO, Anderson BDO (2001) Model reduction for control system design, communications and control engineering. Springer, London
14. Packard A, Doyle J (1993) The complex structured singular value. Automatica 29(1):71–109
15. Packard A (1994) Gain scheduling via linear fractional transformations. Syst Control Lett 22:79–92
16. Packard A, Becker G (1994) Robust performance of linear parameter varying systems using parametrically-dependent linear feedback. Syst Control Lett 23:205–215
17. Pfifer H, Hecker S (2008) Generation of optimal linear parametric models for LFT-based robust stability analysis and control design. In: IEEE conference on decision and control (CDC), Cancun, Mexico
18. Preumont A (2002) Vibration control of active structures: an introduction, 2nd edn., Solid mechanics and its application, vol 96. Kluwer Academic Publishers, Dordrecht
19. Shamma J, Cloutier J (1993) Gain-scheduled missile autopilot design using linear parameter varying transformations. J Guid Control Dyn 16(2):256–261
20. Stefan M, Valášek M (2007) CTU-MIMO-POLYNOMIAL-LOLIMOT. FME CTU in Prague, Prague
21. Šika Z, Zavřel J, Valášek M (2009) Residual modes for structure reduction and efficient coupling of substructures. Bull Appl Mech 5(19):54–59
22. Varga A, Anderson BDO (2003) Accuracy-enhancing methods for balancing-related frequency-weighted model and controller reduction. Automatica 39:919–927
23. Vuillemin P, Poussot-Vassal C, Alazard D (2013) A frequency-limited $\mathscr{H}_2$ model approximation method with application to a medium scale flexible aircraft. Euro-GNC, Delft (NL)
24. Wu F, Yang XH, Packard A, Becker G (1996) Induced $\mathscr{L}_2$-norm control for LPV systems with bounded parameter variation rates. Int J Robust Nonlinear Control 6:983–998

Part II
Control Design

Chapter 5
Control Goals

C. Westermayer and A. Schirrer

5.1 Analysis of Aircraft Dynamics

C. Westermayer and A. Schirrer

This section summarizes the open-loop dynamic behavior of the considered ACFA BWB aircraft predesign model as relevant for control design, both for longitudinal and lateral dynamics. The longitudinal analysis itself is based on the ROM from Chap. 4, has been developed in [13] and is summarized in the following from there. It starts with analyzing the system eigendynamics, where it is shown that longitudinal static stability does not exist over the entire parameter range. An investigation of the system response to control and disturbance inputs in both time-domain and frequency-domain exposes the constrained applicability of available control surfaces. Additionally, the effect of turbulence gusts on the system structural dynamics is shown and maximum load levels are determined. Based on a sensitivity analysis, the system dependency on flight parameters and fuel mass is evaluated, which provides essential insight for parameter dependent and robust control design. The influence of conventional feedback loops on the system dynamics is outlined using relevant root locus plots. A shortened lateral analysis taken from [10] follows in an analogous fashion.

5.1.1 Overview on the System Models for Control Design and Validation

Dynamic predesign models of the ACFA BWB 450-passenger aircraft configuration have been developed during the ACFA 2020 research project as described in Part 1

C. Westermayer · A. Schirrer (✉)
Vienna University of Technology, Vienna, Austria
e-mail: alexander.schirrer@tuwien.ac.at

M. Kozek and A. Schirrer (eds.), *Modeling and Control for a Blended Wing Body Aircraft*,
Advances in Industrial Control, DOI 10.1007/978-3-319-10792-9_5

of this book [12]. These integrated models represent the longitudinal as well as the lateral flight mechanics of the RB aircraft motion, the flexible structure mechanics, as well as the aeroelastic coupling of the RB and the flexible dynamics. The finite element method (FEM) has been utilized for structural design; panel- and computational fluid dynamics (CFD) methods have been applied to obtain aerodynamic data. Compared to earlier studies (see [6–9, 14]) based on the large 750-passenger NACRE BWB configuration (see Sect. 3.2 and [2]), the present models consider a redesigned, downsized BWB configuration.

Four relevant parameters are considered of having a major effect on the dynamic system behavior: the flight parameters *airspeed* and *dynamic pressure* as well as the two structure parameters *fuel-filling level* and *center of gravity (CG) position*. The longitudinal and lateral flight mechanics equations have been linearized about level trimmed flight conditions at fixed parameter gridpoints, and the flexible structure modes have been modeled and separated into symmetric and antisymmetric modes. Then, due to the symmetry of the aircraft configuration, the lateral dynamics is decoupled from the longitudinal dynamics for small perturbations of the flight mechanic variables (in particular, for sufficiently small perturbations of sideslip, roll, and yaw angles). In this predesign stage, no further quantification of lateral–longitudinal coupling effects has been done because the main objectives of the conducted studies target control design and loads alleviation in trimmed level flight conditions or in typical, moderate turn maneuvers.

5.1.2 Models of Longitudinal Dynamics

The longitudinal input/output (I/O) configuration of the BWB aircraft is depicted in Fig. 5.1.

The reduced longitudinal models $\boldsymbol{G}$ are given in state-space representation

$$\begin{bmatrix} \dot{\mathbf{x}}(t) \\ \mathbf{e}(t) \\ \mathbf{y}(t) \end{bmatrix} = \underbrace{\begin{bmatrix} \mathbf{A} & \mathbf{B}_1 & \mathbf{B}_2 \\ \mathbf{C}_1 & \mathbf{D}_{11} & \mathbf{D}_{12} \\ \mathbf{C}_2 & \mathbf{D}_{21} & \mathbf{D}_{22} \end{bmatrix}}_{\boldsymbol{G}_{\mathrm{ac}}} \begin{bmatrix} \mathbf{x}(t) \\ \mathbf{d}(t) \\ \mathbf{u}(t) \end{bmatrix} \tag{5.1}$$

with the corresponding state vector

$$\mathbf{x} = \left[X \; u \; Z \; w \; \Theta \; q \; \xi_1 \; \dot{\xi}_1 \; \ldots \; \xi_s \; \dot{\xi}_s \; x_{l_1} \; \ldots \; x_{l_t} \right]^{\mathrm{T}}, \tag{5.2}$$

where the first six states represent the RB states x-position X, body forward velocity u, z-position Z, body downward velocity w, pitch angle Θ and pitch rate q, respectively. If the integrator states X and Z are not considered, they are removed by truncation. The number of remaining rigid body (RB) states is then $r = 4$. The states ξ_j and $\dot{\xi}_j$ $(j = 1, \ldots, s)$ are the modal deflections and modal deflection rates of

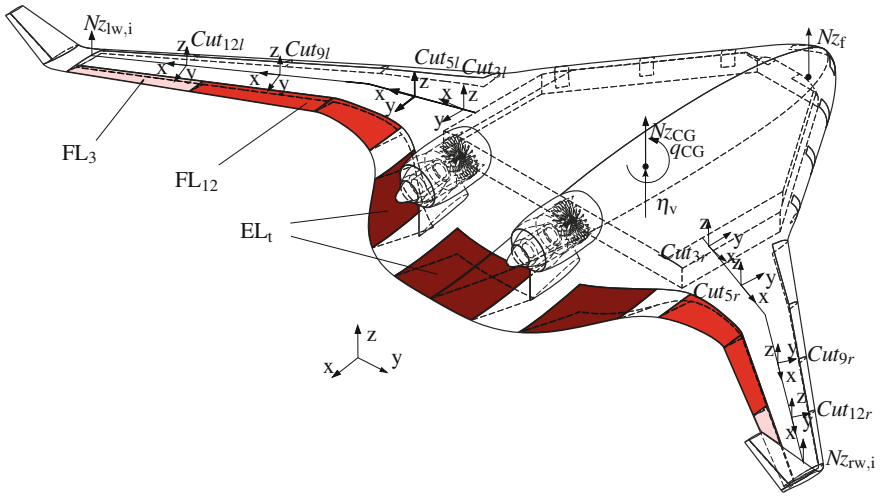

Fig. 5.1 Schematic sketch of BWB aircraft with relevant system inputs and outputs [13]

aeroelastic modes, respectively, and x_{l_k} $(k = 1, \ldots, t)$ are the lag states. The number of flexible modes and lag states are different for validation and design model, leading to the total numbers of states $n_{x,i}$:

- Validation model $\mathbf{G}_{\text{ac,val}}$: $r = 4, s = 19, t = 14 \Rightarrow \quad n_{x,\text{val}} = 62$
- Design model $\mathbf{G}_{\text{ac,des}}$: $r = 4, s = 2, t = 4 \quad \Rightarrow \quad n_{x,\text{des}} = 12$

The number of flexible modes is set to a comparatively low number due to the limited bandwidth of about 20 rad/s of the investigated control surfaces. However, within this range, the first two symmetrical flexible modes are located which are important in terms of structural loads and vibrations as will be shown in the open-loop system analysis in Sect. 5.1.3. Moreover, keeping only four lag states in the design model turned out to have only marginal effect on the considered system dynamics.

In general, it is reasonable to keep the system order of the aeroelastic design model as low as possible mainly for two reasons:

1. The controller order depends on the design system order when using $\mathscr{H}_\infty$-based design methodologies.
2. The system order strongly influences computational cost and conservativeness in control design.

The BWB aircraft is equipped with five flaps distributed along the trailing edge of the center body and the wing, all available for longitudinal control. Early investigations have shown that in order to obtain sufficient control authority for pitch control, all four flaps at the center body have to be used, forming together the combined elevator EL_t. Although the combined inner two flaps at the wing FL_{12} are mainly dedicated for lateral control [10], they also play an important role for longitudinal maneuver

load control. The outer flap at the wing FL_3 will be mainly used for aeroelastic control. The two engines of the aircraft are mounted at the rear, above the center body, and produce the symmetric thrust T_{12}. The control input vector of the system $\mathbf{u}$ is thus given by:

$$\mathbf{u} = \left[\delta_{\mathrm{EL}_t} \ \dot{\delta}_{\mathrm{EL}_t} \ \delta_{\mathrm{FL}_{12}} \ \dot{\delta}_{\mathrm{FL}_{12}} \ \delta_{\mathrm{FL}_3} \ \dot{\delta}_{\mathrm{FL}_3} \ T_{12} \right]^{\mathrm{T}}, \tag{5.3}$$

where δ_i and $\dot{\delta}_i$ is the symmetric deflection and deflection rate of the respective control surface. Besides these control inputs, the aircraft model is equipped with various exogenous inputs $\mathbf{d}$:

$$\mathbf{d} = \left[\eta_{\mathrm{v}} \ \eta_{\mathrm{2D},1} \ \dot{\eta}_{\mathrm{2D},1} \ \ldots \ \eta_{\mathrm{2D},33} \ \dot{\eta}_{\mathrm{2D},33} \right]^{\mathrm{T}}. \tag{5.4}$$

A global vertical gust velocity input η_{v} positioned at the CG is most relevant for the given study. Moreover, the model has zonal vertical gust velocity $\eta_{\mathrm{2D},i}$ and acceleration $\dot{\eta}_{\mathrm{2D},i}$ inputs distributed along the structure which can be fed by a 2D von-Kármán turbulence spectrum [4, 5].

The system model comprises 511 outputs which are basically divided into two groups: measurements $\mathbf{y}$ and exogenous outputs $\mathbf{e}$. Measurements utilized in this work are:

$$\mathbf{y} = \left[Nz_{\mathrm{CG}} \ q_{\mathrm{CG}} \ V_{\mathrm{TAS}} \ \Theta_{\mathrm{CG}} \ \alpha_{\mathrm{CG}} \ Nz_{\mathrm{f}} \ Nz_{\mathrm{rw},i} \ Nz_{\mathrm{lw},i} \ Nz_{\mathrm{long.law}} \right]^{\mathrm{T}}, \tag{5.5}$$

where Nz_{CG}, q_{CG}, Θ_{CG} and α_{CG} are the vertical acceleration, pitch rate, pitch angle and the angle of attack at the CG position, respectively, V_{TAS} is the true airspeed, Nz_{f} is the vertical acceleration at the front position (cockpit position) and $Nz_{\mathrm{rw},i}$, $Nz_{\mathrm{lw},i}$ are several vertical acceleration outputs distributed over the wing. The $Nz_{\mathrm{long.law}}$ output is a longitudinal modal wing bending acceleration signal used to separate the symmetric vertical wing bending from the RB motion

$$Nz_{\mathrm{long.law}} = \left(\frac{\left(Nz_{\mathrm{lw},k} + Nz_{\mathrm{rw},k} \right)}{2} - Nz_{\mathrm{CG}} \right), \tag{5.6}$$

where the index k refers to a selected pair of sensors obtained using a sensor placement optimization technique [3]. The exogenous output vector is given as follows:

$$\mathbf{e} = \left[My_1 \ \ldots \ My_{14} \ Fz_1 \ \ldots \ Fz_{14} \right]^{\mathrm{T}}, \tag{5.7}$$

where My_i represent the cut bending moments and Fz_i the cut vertical forces equally distributed along the wing as exemplarily shown in Fig. 5.1. From this set of structural load outputs, a subset is selected for controller design in order to formulate performance specifications concerning load minimization in turbulence gust and maneuvers. In the validation model, the entire set is utilized to evaluate closed-loop performance.

Table 5.1 Dynamical properties of control surface actuators for $\theta_q = 17{,}238$ and corresponding deflection and rate limits

	Frequency in rad/s	Relative damping (−)	Deflection limit in deg	Rate limit in deg/s
EL_t	2.72	0.71	$-30 \leq \eta_{EL_t} \leq 15$	$-30 \leq \dot{\eta}_{EL_t} \leq 30$
FL_{12}	4.44	0.71	$-25 \leq \eta_{FL_{12}} \leq 25$	$-40 \leq \dot{\eta}_{FL_{12}} \leq 40$
FL_3	7.80	0.71	$-25 \leq \eta_{FL_3} \leq 25$	$-40 \leq \dot{\eta}_{FL_3} \leq 40$

The aircraft model $\mathbf{G}_{\text{ac}}$ according to (5.1)–(5.7) has to be augmented with corresponding linear actuator $\mathbf{G}_{\text{act}}$ and sensor dynamics $\mathbf{G}_{\text{sen}}$ in order to finally obtain the model for controller design and validation:

$$\mathbf{G} = \mathbf{G}_{\text{act}}\, \mathbf{G}_{\text{ac}}\, \mathbf{G}_{\text{sen}}. \tag{5.8}$$

The dynamical properties of the linearized second-order control surface actuator models for the maximum dynamical pressure and the corresponding deflection and rate limits are provided in Table 5.1. The actuator matrix $\mathbf{G}_{\text{act}}$ therefore can be written as

$$\mathbf{G}_{\text{act}} = \begin{bmatrix} \frac{7.5}{s^2+3.9s+7.5} & 0 & 0 & 0 & 0 \\ \frac{7.5s}{s^2+3.9s+7.5} & 0 & 0 & 0 & 0 \\ 0 & \frac{19.7}{s^2+6.3s+19.7} & 0 & 0 & 0 \\ 0 & \frac{19.7s}{s^2+6.3s+19.7} & 0 & 0 & 0 \\ 0 & 0 & \frac{60.7s}{s^2+11.0s+60.7} & 0 & 0 \\ 0 & 0 & \frac{60.7s}{s^2+11.0s+60.7} & 0 & 0 \\ 0 & 0 & 0 & \frac{152e3}{5.8s+1} & 0 \\ 0 & 0 & 0 & 0 & \mathbf{I}_{\text{d}} \end{bmatrix}, \tag{5.9}$$

with $\mathbf{I}_{\text{d}}^{m\times m}$ as the identity matrix of appropriate dimensions according to the number of disturbance inputs m. As a result of the system extension by actuator dynamics, the input vector (5.3) is replaced by:

$$\mathbf{u} = \begin{bmatrix} \eta_{EL_t} & \eta_{FL_{12}} & \eta_{FL_3} & \eta_{T_{12}} \end{bmatrix}^{\text{T}}, \tag{5.10}$$

where η_{surf} are the respective symmetric control surface deflection and thrust inputs. The sensor delays are defined as 2nd-order Padé approximations, whereas for safety critical measurements, such as $\mathbf{y}(1, \ldots, 6)$ from (5.5), the delay is set to 160 ms and for measurements utilized for aeroelastic control $\mathbf{y}(7, \ldots, 9)$, a delay of 60 ms is

assumed. Moreover, measurements $\mathbf{y}(1, \ldots, 6)$ are filtered by low-pass Butterworth filters given by the transfer function

$$\mathbf{G}_{\mathrm{BW}} = \frac{1}{0.00281s^2 + 0.075s + 1}. \tag{5.11}$$

In case of the design models, sensor delays and Butterworth filters are further approximated with only 1st-order Padé approximations and PT1 elements, leading to

$$\mathbf{G}_{\mathrm{sc}} = \frac{-15(s - 12.5)}{(s + 15)(s + 12.5)} \tag{5.12}$$

for safety critical measurements and to

$$\mathbf{G}_{\mathrm{ae}} = \frac{-(s - 33.3)}{(s + 33.3)} \tag{5.13}$$

for aeroelastic measurements. The sensor transfer function matrix is therefore given by:

$$\mathbf{G}_{\mathrm{sen}} = \mathrm{diag}\{\, \mathbf{G}_{\mathrm{sc}}\mathbf{I}^{r\times r}\ \mathbf{G}_{\mathrm{ae}}\mathbf{I}^{s\times s}\ \mathbf{I}^{t\times t}\,\}, \tag{5.14}$$

where r and s are the numbers of safety critical and aeroelastic measurements, respectively, and t the number of load outputs.

5.1.3 Open-Loop Analysis of Longitudinal Dynamics

5.1.3.1 System Eigendynamics

The longitudinal RB motion of the BWB aircraft is characterized by the short-period mode (SPM) and the phugoid mode (PM). Moreover, in the low-frequency region up to 3 rad/s the slowest lag state (LAG) and actuator mode actuator mode (AM) of the combined elevator EL_t appear. Depending on the considered parameter case, basically three different constellations of SPM and PM appear. Those are presented in Fig. 5.2, where in the left plot the full RB dynamics, that is, SPM and PM, are presented while in the right plot the corresponding SPM approximation due to omitted states u and Θ is shown.

1. The SPM forms a conjugate complex pole pair and the PM is given by two real poles, whereby one of them is unstable.
2. The SPM is given by two real stable poles while one phugoid pole is again stable and one is unstable.

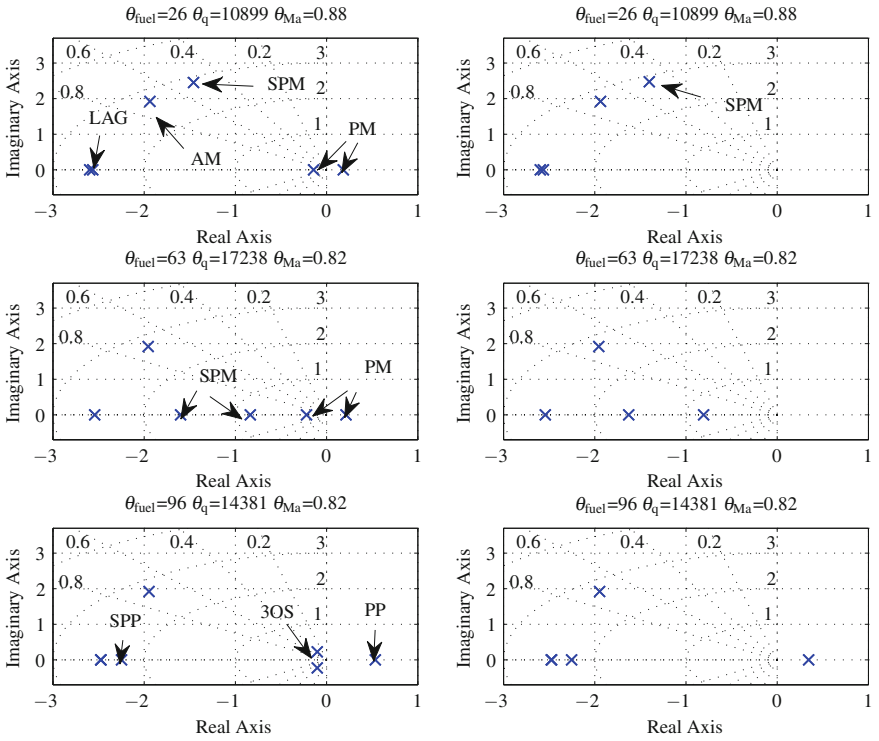

Fig. 5.2 Pole map of low-frequency poles for various parameter cases: model with RB states u, w, Θ, q (*left*) and with RB states w, q (*right*)

3. SPM and PM merge forming a so-called 3rd oscillation (3OS). The remaining two poles are real. One of them is faster and stable (SPP) and the other one is unstable (PP).

This development of pole constellations from 1 to 3 is attained with parameter settings toward higher fuel mass θ_{fuel}, increased dynamic pressure θ_q and lower Mach numbers θ_{Ma}. The EL_t actuator mode AM is hardly changed for varying pressure parameters θ_q, however, it is located rather close to the SPM. This can lead to undesirable interaction of those two modes due to feedback control.

In the first two cases, a similar position for the SPM is visible. In the third case, the SPM is given by two real poles, where one of them is stable and one unstable. Therefore, for parameter settings corresponding to the third case, the system dynamics is characterized by a fast and unstable SPM, which in turn indicates longitudinal static instability of the aircraft.

The pole distribution of the flexible modes is shown in Fig. 5.3 for the whole parameter envelope.

The design model contains only two flexible modes, the first and second wing bending mode WB_1 and WB_2, respectively. Considering Fig. 5.3, it can be seen that

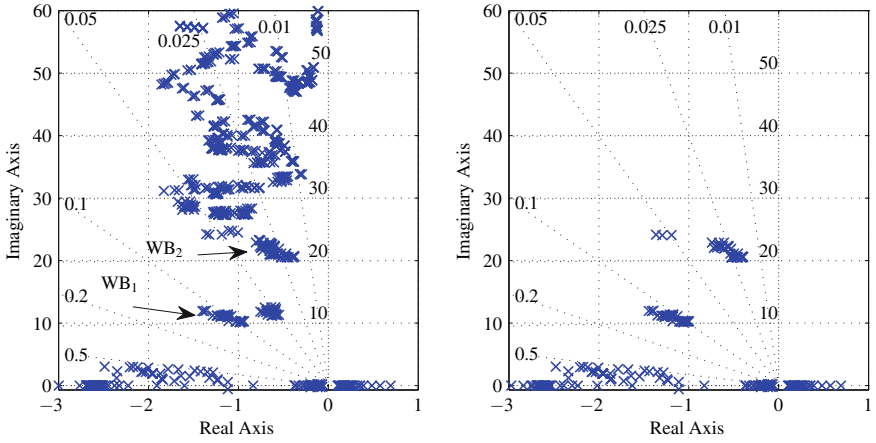

Fig. 5.3 Flexible mode pole distribution for entire envelope: validation model (*left*) and design model (*right*)

for both models WB_1 and WB_2 come to lie at similar positions which is an important requirement for control design. The remaining flexible modes in the validation model are located between 10 and 60 rad/s. However, these modes' frequencies are significantly above the actual bandwidth of the actuators and therefore out of scope of this study.

5.1.3.2 Input Response

Time-Domain Response

The following time-domain analysis provides a representative overview on system characteristics for both control surface inputs as well as disturbance inputs.

Control surface inputs: In Fig. 5.4 the unit step response from the control surfaces η_{EL_t}, $\eta_{FL_{12}}$ and η_{FL_3} to the flight mechanic outputs $Nz_{\text{long.law}}$, q_{CG} and to My_5 are shown. Note that the time responses drift away as a result of the unstable phugoid mode. The $Nz_{\text{long.law}}$ output extracts clearly the wing oscillations. In the lower plot, the structural load output My_5 is shown where high loads given by the pitch-down maneuver are notable. The general qualitative statements on system response hold for the entire parameter range despite the presence of strong variations in system dynamics.

Turbulence gust inputs: For evaluation of the system response in terms of the maximum arising structural loads and vibrations caused by turbulence, a standardized disturbance velocity signal given by the one-minus-cosine $(1-\cos)$ gust will be utilized throughout this work. This signal basically depends on two parameters, the integral scale length L_{gust} and the maximum vertical gust velocity

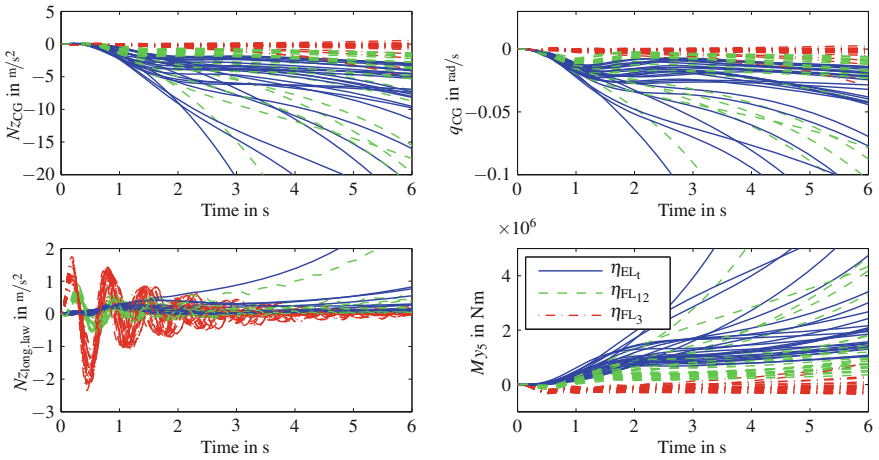

Fig. 5.4 Time response of selected relevant outputs to unit step inputs on combined elevator η_{EL_t}, combined inner flap $\eta_{FL_{12}}$ and outer flap η_{FL_3} for a representative set of parameter cases

$v_{z,\max} = v_{z,\max}(\theta_{Ma}, q)$. Shorter gusts excite mainly the flexible structure modes, while long gusts lead to excitation of the RB dynamics. It is noticeable that the gust of highest length corresponding to excitation in the low-frequency region leads to maximum acceleration and pitch rate values. Depending on the parameter case, maximum accelerations of 20 m/s^2 and above can occur. Similar to the flight mechanic outputs, also structural loads are maximal for long gusts. Shorter gusts, on the contrary, strongly excite flexible modes, resulting in long-lasting, weakly damped vibrations. Considering the $Nz_{long.law}$ output, for example, it turns out that a gust with length $L_{gust} = 30.5$ m causes the maximum wing bending acceleration. It is important to determine the parameter combination for aircraft and gust leading to maximum dynamical structural loads. The cut forces Fz_i and moments My_i at three different positions along the wing are evaluated. It turns out that the maximum structural loads at cut positions closer to the center are typically caused by the longest gusts. At outside cut positions, shorter gusts are more relevant.

Frequency-Domain Response

Considering the Nz_{CG} and q_{CG} responses, it turns out that the responses for the η_{EL_t} and $\eta_{FL_{12}}$ inputs is dominated by the low-frequency short-period mode. For pitch maneuver control, it is important that the elevator hardly excites the flexible modes. This also becomes evident when considering the responses for $Nz_{long.law}$ and My_5. The outer flap FL_3 shows highest magnitude at the frequency of the first wing bending mode WB_1. The controllability of the second wing bending mode WB_2 is low for this flap. FL_{12} appears to be an effective control input for both, flight mechanics and aeroelastics control.

The response for varying parameter cases from vertical gust input η_v to Nz_{CG} shows a flat characteristics until about 10 rad/s, while above it is dominated by the weakly damped WB_2 and a higher frequency flexible mode at around 50 rad/s. The $Nz_{long.law}$ response shows high-pass behavior, dominated by WB_1, WB_2, and again the flexible mode at 50 rad/s. For inside cut positions the cut load outputs Fz_i and My_i show high gain in the low-frequency region. The maximum magnitude is present at WB_2. Load outputs further outside show high-pass behavior, dominated by WB_1, WB_2, and modes at higher frequencies.

Root Locus of Relevant Feedback Loops

Before starting a multiobjective multi-input multi-output (MIMO) controller design, it is of utmost importance to understand the effects of single-input single-output (SISO) feedback loops. Effective loops for modification of the short-period mode and the phugoid mode are shown, and present limitations due to the slow actuator dynamics and sensor delays are outlined. The basic characteristics described in the following also hold for the remaining parameter cases.

In Fig. 5.5, the root locus for positive static feedback from q_{CG}, Nz_{CG} and Θ_{CG} on η_{EL_t} and negative static feedback from V_{TAS} on η_{EL_t} are shown. As can be seen from the top left plot, a q_{CG} feedback on EL_t significantly increases SPM damping.

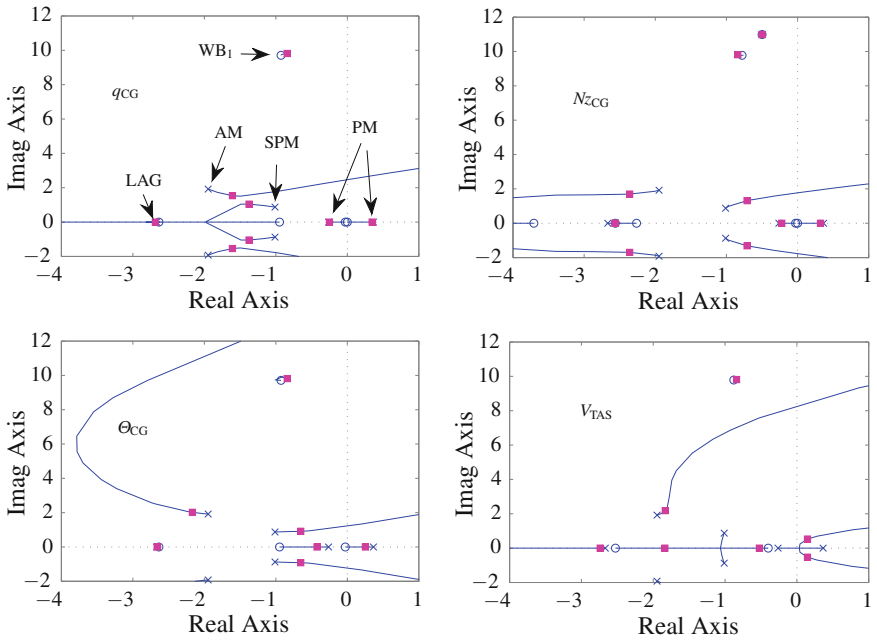

Fig. 5.5 Low-frequency root locus plots for $+q_{CG}$, $+Nz_{CG}$, $+\Theta_{CG}$ and $-V_{TAS}$ static feedback on η_{EL_t} for modification of SPM and PM

Likewise, the damping of the actuator mode is reduced to a similar extent. The location of the PM and the WB_1 is hardly changed. The latter also holds for Nz_{CG} feedback. Notably, this measurement has a destabilizing effect on the SPM, while the frequency is only slightly increased. A similar behavior can be detected for a Θ_{CG} feedback, with the exception that this output also slightly modifies the PM. The PM can be even more shifted by a negative feedback of V_{TAS} on η_{EL_t}. For the optimum static feedback gain, both poles are real and close to the imaginary axis. The SPM, on the contrary, forms two real poles, where one of them becomes significantly slower with increased feedback gain. Finally, the slowest lag state (LAG) is marginally modified due to the presented feedback loops.

The effectiveness of the wing trailing-edge control surfaces FL_{12} and FL_3 concerning flexible mode damping is evaluated using the modal wing bending acceleration signal $Nz_{long.law}$. The damping of the flexible mode WB_1 can be increased due to static feedback solely by the outer flap FL_3. Limitations due to the 60 ms delay become clearly evident: In the case of WB_2, the root locus even changes its direction when including the sensor delay. However, the actual pole shifting of WB_2 is rather moderate. This is different for feedback on FL_{12}, where the root locus for WB_2 is almost horizontal. Nevertheless, an increase of damping using static feedback is related to reduced damping of WB_1.

5.1.3.3 Sensitivity Analysis

The main results of the sensitivity analysis are summarized in the following from [13]. Evaluating the ν-gap metric as a control-oriented measure of plant variation for different parameter points θ_{Ma} and v for the range of fuel-mass parameters (potentially unknown to the controller), it can be seen that high values of the metric arise for flight parameter $\theta_{Ma} = 0.85$ which suggests this to be the most difficult θ_{Ma} parameter for obtaining robustness against uncertain fuel mass. Conversely, no strong correlation to the θ_q parameter is evident. For the considered flight control architectures, the flight parameters θ_{Ma} and θ_q are potential scheduling parameters for the BWB aircraft.

It can be concluded that an increased θ_{Ma} parameter is characterized by a faster SPM of reduced damping. Moreover, it turns out that the DC gain changes nonlinearly with the θ_{Ma} parameter and the maximum gain occurs for the low θ_{Ma} number case. For both parameters, ω and ζ, in general a linear dependency appears, however, with varying slope for different θ_q and θ_{fuel} parameters. Noticeable is specifically the different characteristic of the magnitude plot for same θ_{fuel} parameter but changing θ_{Ma} parameter. Generally, with increasing θ_q parameter, the frequency and the damping of the SPM is moderately increased. It can be concluded that the SPM pole location depends approximately linearly on flight parameters θ_q and θ_{Ma}, while the system input–output behavior deviates, partly significantly, from linear behavior.

5.1.4 Models of Lateral Dynamics

The lateral dynamics model is comprised of lateral flight mechanic states, antisymmetric flexible structure dynamic states, as well as lag states. The corresponding dynamic models are utilized to design and validate the lateral control laws in Chaps. 6 and 7 at various flight cases (defined by the parameters airspeed and dynamic pressure) and mass cases (defined by the parameters fuel-filling level and CG position).

Some comprehensive studies (for example, sizing loads alleviation performance, see Chap. 8) have been carried out for a total of several hundred aircraft parameter cases within a defined grid for these four parameters.

Many detail studies have been carried out at a selected flight case corresponding to cruise conditions. Then, a set of $k = 30$ linearized state-space systems $\mathbf{P}_i$, $i = 1, \ldots, k$ for various parameter values of fuel-filling level and CG position is studied:

$$\dot{\mathbf{x}} = \mathbf{A}_i \mathbf{x} + \mathbf{B}_i \mathbf{u} \tag{5.15}$$

$$\mathbf{y} = \mathbf{C}_i \mathbf{x} + \mathbf{D}_i \mathbf{u}. \tag{5.16}$$

The lateral state vector $\mathbf{x}$ is composed of 4 flight mechanic states (sideslip angle β, roll rate p, yaw rate r, roll angle ϕ), 12 elastic states (6 structural antisymmetric modes), as well as 7 lag states. The integrator states ψ (yaw angle) and y (horizontal displacement) are neglected in this study. These systems are augmented by actuator and sensor dynamics.

Utilized inputs $\mathbf{u}$ for control design are:

1. Symmetric rudder deflection and rate u_{RU}, $\dot{u}_{\mathrm{RU}}$
2. Combined antisymmetric trailing-edge control surface deflections and rates:
   a. u_{TE12}, $\dot{u}_{\mathrm{TE12}}$: middle and inner elevons (deflected equally)
   b. u_{TE3}, $\dot{u}_{\mathrm{TE3}}$: outer elevon

The actuator dynamics $\mathbf{G}_{\mathrm{act}}$ are modeled via 2nd-order low-pass filters as a low-order approximation of physically modeled control surfaces and actuation system dynamics. These models provide both the actual surface deflections as well as their rates as outputs $\left([u_j, \dot{u}_j]^{\mathrm{T}} = \mathbf{G}_{\mathrm{act},j}\, u_{\mathrm{command},j}\right)$.

Utilized outputs $\mathbf{y}$ for control design are:

1. Sideslip angle β
2. Roll angle ϕ
3. Roll rate p
4. Yaw rate r
5. Antisymmetric wingtip acceleration signal $Nz_{\mathrm{lat.law}} = Nz_{\mathrm{r.wingtip}} - Nz_{\mathrm{l.wingtip}}$ where $Nz_{\mathrm{r.wingtip}}$ and $Nz_{\mathrm{l.wingtip}}$ are vertical accelerations at the right and left wingtips, respectively,

which are each considered subject to time delays due to signal processing latencies (160 ms for outputs (1–4), 60 ms for output (5)), modeled via 2nd-order Padé

Table 5.2 System modes of the lateral open-loop dynamics

Aircraft system mode	Pole characteristics	Frequency (rad/s)
DR mode	Oscillatory, low-damped/unstable	1
Roll resilience mode	Real, stable	2...3
Spiral mode	Real, slow, unstable	0.001
1st anti-sym. flexible mode	Oscillatory, low-damped	10
2nd anti-sym. flexible mode	Oscillatory, low-damped	20

approximations. Additionally 2nd-order low-pass Butterworth filters are applied to outputs (1–4). Note that output (5) acts as an effective, simplified modal sensor for the antisymmetric flexible modes. It amplifies these modes' amplitudes, however, it is not compensated for the effect of roll rate change (RB motion) for simplicity. The sensor dynamics is collected into $\mathbf{G}_{\text{sens}}$, and the augmented system $\widetilde{\mathbf{P}}_i = \mathbf{G}_{\text{sens}}\mathbf{P}_i\mathbf{G}_{\text{act}}$ is of order 47.

Additional exogenous input and output signals are considered for system analysis and validation: a wind gust disturbance input is modeled by an aggregated lateral wind speed input signal

$$d = v_{\text{lat}}, \tag{5.17}$$

as well as a structure load output (a cut moment at the wing)

$$z = M y_{\text{wing}}. \tag{5.18}$$

5.1.5 Open-Loop Analysis of Lateral Dynamics

The open-loop system eigendynamic parameters can be seen in Table 5.2: A low-damped or unstable Dutch Roll mode (DR mode) and the two real flight mechanic modes (spiral, roll resilience) are present. The first two antisymmetric flexible modes are located around 10 and 20 rad/s, respectively. Table 5.3 lists the pole locations of the dominating PT2 behavior of the linearized actuator models for the actuators of

Table 5.3 Eigenfrequencies of the linearized actuator models

Linearized control surface mode (dominant 2nd-order dynamics)	Pole characteristics
Flaps 3, 4	Damping $\zeta = \sqrt{2}/2$ at $\omega_{\text{d}} = 4.4$ rad/s
Flaps 5	Damping $\zeta = \sqrt{2}/2$ at $\omega_{\text{d}} = 7.8$ rad/s
Rudder	Damping $\zeta = \sqrt{2}/2$ at $\omega_{\text{d}} = 10.3$ rad/s

flaps 3, 4, 5, and the rudder. As seen from these numbers, the control design task is expected to be challenging for flexible modes control because these are located at or above the actuators' bandwidth. Open-loop responses for the lateral dynamics are given in the lateral control design sections (Sects. 6.2, 6.3, and 7.2).

5.2 Control Goals

A. Schirrer and C. Westermayer

This section lists the primary control goals formulated for the ACFA BWB aircraft predesign model both for the longitudinal and lateral dynamics. Subsets or specific variants of these goals are treated later in the respective control design sections of Chaps. 6 (feedback designs) and 7 (feed-forward designs).

5.2.1 Longitudinal Control Design Goals

The following general set of goals are addressed in the longitudinal control designs:

1. Stabilize the unstable short-period mode.
2. Slow down the unstable phugoid, such that the pole pair stays real and the maximum real part of the unstable pole p is limited by $\max(\mathrm{Re}(p)) < 0.1$.
3. Track the reference command input given by the vertical acceleration at the CG position Nz_{CG}. The rise time of Nz_{CG} to a unit step command input must be between 3 and 5 s and no overshoot is tolerated.
4. Overshoot of accompanying pitch rate response at the CG position, q_{CG}, must be lower than 30 %.
5. Reject disturbances from control inputs and external excitations within 5–7 s.
6. Unify the system dynamical behavior throughout the considered operating range in order to obtain similar closed-loop response.
7. Minimize maximum vertical accelerations of Nz_{CG} and Nz_{f} due to turbulence gust.
8. Constrain the demanded control signals by maximum deflection and deflection rate limits according to Table 5.1.
9. Investigate and demonstrate robustness against uncertainties of the fuel-mass parameter.
10. All control surfaces on the trailing edge can be utilized as actuators. However, the combined inner flap FL_{12} is also utilized for lateral control, consequently only restricted use for longitudinal control is possible.
11. Besides Nz_{CG} also q_{CG}, Nz_{f}, V_{TAS} and Θ_{CG} are available as flight mechanic measurements. Generally, the number of utilized measurement signals for the controller must be kept as low as possible.

Table 5.4 Control goals for the lateral control design tasks

General and tracking specifications	
DR mode	$\zeta_{DR} > 0.7$, ω_{DR} unchanged
Decoupling	Generate inputs with high coupling to roll and sideslip angles and low cross-coupling
Roll angle ϕ	DC gain similar for all mass cases, rise time to 90 % in $t_{rise} < 7$ s, max. 5 % overshoot
Sideslip angle β	DC gain similar for all mass cases, $t_{rise} < 5$ s
Robustness	Stable controller, Robust Stability (RS) and Robust Performance (RP) for all mass cases
Disturbance rejection specifications	
Minimize the influence of lateral gust on roll, sideslip, and lateral acceleration, while obeying the tracking specifications above. Moreover, the loads must not be increased	
Maneuver loads alleviation specifications	
Robustly minimize sizing *Fz*, *Mx*, and *My* loads along the wing in 60° roll maneuvers	

The requirements 1–7 are typical design goals of a so-called stability augmentation system (SAS) [1, 11] in order to align the closed-loop RB motion to pilot needs. Moreover, fulfilling these requirements provides an improved basis for subsequent autopilot design. Requirements 1, 2 and 6 are directly linked to closed-loop pole location and can therefore be addressed only by a feedback control approach, while requirements 3, 4 are also main goals of feed-forward design (see Chap. 7). Disturbance rejection (4) and acceleration minimization (7) based on a disturbance feed-forward concept is not investigated in this work. The limited actuator bandwidth (8) and the robustness requirements regarding fuel-mass uncertainty (9) are further essential aspects for an integrated flexible aircraft design which have to be considered at an early design phase.

5.2.2 Lateral Control Design Goals

The goals followed in lateral control design for the considered BWB aircraft are specified in Table 5.4.

References

1. Brockhaus R (2001) Flugregelung (English: Flight control). Springer, Berlin
2. European Commission (2014) Flying high with innovative aircraft concepts. http://ec.europa.eu/research/research-for-europe/transport-nacre_en.html
3. Hemedi M, Schirrer A, Westermayer C, Kozek M (2011) Integrated input-output selection strategy for robust control of complex parameter depending systems. J Syst Des Dyn (Special Issue of Motion and Vibration Control 2010) 5(5):1106–1118. Invited

4. Imbert N, Mouyon P, Montseny G (2000) State representation and simulation of 2nd turbulent wind. In: AIAA modelling and simulation technologies, Denver
5. Mouyon P, Imbert N (2002) Identification of a 2nd turbulent wind spectrum. Aerosp Sci Technol 6:599–605
6. Schirrer A, Westermayer C, Hemedi M, Kozek M (2010) LQ-based design of the inner loop lateral control for a large flexible BWB-type aircraft. In: 2010 IEEE multi-conference on systems and control, Yokohama, Japan
7. Schirrer A, Westermayer C, Hemedi M, Kozek M (2010) Robust control design parameter optimization via genetic algorithm for lateral control of a BWB type aircraft. In: IFAC workshop on intelligent control systems, Sinaia, Romania
8. Schirrer A, Westermayer C, Hemedi M, Kozek M (2011) Multi-model convex design of a scheduled lateral feedforward control law for a large flexible BWB aircraft. In: Preprints of the 18th IFAC world congress, Milano, Italy, pp 2126–2131
9. Schirrer A, Westermayer C, Hemedi M, Kozek M (2011) Robust convex lateral feedback control synthesis for a BWB aircraft. In: Preprints of the 18th IFAC world congress, Milano, Italy, pp 7262–7267
10. Schirrer A, Westermayer C, Hemedi M, Kozek M (2013) Robust lateral blended-wing-body aircraft feedback control design using a parameterized LFR model and DGK-iteration. In: Progress in flight dynamics, guidance, navigation, control, fault detection, and avionics, vol 6. EDP Sciences, pp 749–766
11. Stevens BL, Lewis FL (2003) Aircraft control and simulation. Wiley, New York
12. Stroscher F, Petersson Ö, Leitner M (2010) Aircraft structural optimization subject to flight loads—application to a wide body commercial aircraft configuration. In: EASN international workshop on aerostructures, Oct 2010
13. Westermayer C (2011) 2DOF parameter-dependent longitudinal control of a blended wing body flexible aircraft. PhD thesis, Vienna University of Technology
14. Westermayer C, Schirrer A, Hemedi M, Kozek M (2010) Linear parameter-varying control of a large blended wing body flexible aircraft. In: 18th IFAC symposium on automatic control in aerospace, Nara, Japan

Chapter 6
Feedback Control Designs

A. Schirrer, M. Kozek, F. Demourant and G. Ferreres

6.1 Introduction

A. Schirrer and M. Kozek

6.1.1 General Properties of Feedback Control

The general concept of feedback control is characterized by utilizing system output signals (measurements) to determine the control signal, thus closing a control loop by a feedback interconnection. For linear systems, this generally alters the system's eigendynamics, and this is in fact the central feature that feedback systems possess in contrast to feed-forward (input-shaping) concepts. Consequently, the main conceptual goals of feedback control concepts for linear dynamic systems are the following:

Stabilization: If stabilizability conditions are met, unstable systems can be stabilized by a suitable control law when the control loop is closed.
Shaping of the eigendynamics: The system's eigendynamics can be altered in terms of a shift of eigenvalues and/or a change of the eigenvectors, which corresponds for example, to changing system time constants or to decoupling responses.
Increase robustness: Feedback control has the potential to decrease the effects of unknown model errors or perturbations or unknown disturbances to the system's responses. This is commonly known as *disturbance rejection*. As an example, a feedback controller could achieve accurate tracking of reference signals even

A. Schirrer (✉) · M. Kozek
Vienna University of Technology, Vienna, Austria
e-mail: alexander.schirrer@tuwien.ac.at

F. Demourant · G. Ferreres
ONERA-Toulouse, Toulouse, France

M. Kozek and A. Schirrer (eds.), *Modeling and Control for a Blended Wing Body Aircraft*,
Advances in Industrial Control, DOI 10.1007/978-3-319-10792-9_6

though the system gain may be uncertain or disturbance input signals unknown to the controller. A purely feed-forward input-shaping concept cannot address these uncertainties by design.

Note, however, that these properties can also produce disadvantages because a feedback controller could also destabilize an otherwise stable system, for example, if critical model errors occur and if the feedback control law is not suitable under these conditions. Thus, the design of a feedback controller requires in-depth system analysis, design tuning, and validation to ensure that the critical requirements (stability, signal magnitude bounds, validity region of the model) are also met in reality.

Additionally, feedback control can address time- and frequency-domain specifications (rise time, overshoot, bandwidth, response magnitudes), which can also be affected by feed-forward concepts. Depending on the application and on the available design methods, the control engineer needs to be decide on the most efficient concept(s) to address these requirements. Often, a combination of methods which exploits their benefits yields high-performance, modular solutions.

6.1.2 Feedback Design Methods in the Flight Control Context

Flexible aircraft control is subject of broad research (see for example [41, 46, 48, 90], or [92]) and it bears the potential of additional weight savings and thus increased fuel efficiency. Novel concepts in civil aviation such as BWB aircraft introduce numerous new challenges to this class of multiobjective control design problems (see [57]): potential (cross-)coupling of longitudinal and lateral motion (and low-frequency flexible modes), possible open-loop instability, as well as high-performance demands in loads alleviation, vibration reduction, and maneuver shaping.

This chapter presents several state-of-the-art feedback flight control design methods for the lateral as well as the longitudinal dynamics of the considered large, flexible BWB transport aircraft model. Numerous stringent constraints and goals are given in terms of eigendynamic requirements and specifications in the time and frequency domains. The considered design methods typically address a subset of the design specifications given in Chap. 5. The control performance is validated and discussed for each approach. The following design methods are considered:

- Partial eigenstructure assignment (ACFA 2020 BWB configuration, lateral control, see Sect. 6.2).
- μ synthesis via DGK-iteration based on a parametrized linear fractional transformation (LFT) model (ACFA 2020 BWB configuration, lateral control, see Sect. 6.3).
- Convex control design via the Youla parametrization and a parametrized observer (ACFA 2020 BWB configuration, longitudinal control, see Sect. 6.4).
- Linear parameter-varying (LPV) feedback control design by a linear matrix inequality (LMI) approach (ACFA 2020 BWB configuration, longitudinal control, see Sect. 6.5).

- Structured low-order $\mathscr{H}_\infty$ design (NACRE BWB lateral control in Sects. 6.6.1–6.6.3; ACFA 2020 BWB longitudinal control in Sect. 6.6.4).

Partial eigenstructure assignment is utilized as an initial controller for the lateral control task (see robust modal control design [54, 73]) to achieve some of the lateral control goals most efficiently addressed by eigenstructure assignment, including basic damping of flexible modes. Based on this pre-shaping, the linear fractional representations (LFRs) of the parametrized, pre-shaped aircraft dynamics are obtained as shown in Sect. 4.2 and a μ synthesis design is carried out to maximize robust damping performance for the relevant flexible modes by exploiting the structured change of system dynamics as functions of the physical parameters.

The longitudinal control task is addressed by convex controller synthesis, which starts out from an linear quadratic Gaussian (LQG)-controlled plant in which rigid-body (RB) requirements are addressed. The observer-based realization is directly suited to put the system into a Youla-parametrized form, that is, to express closed-loop transfers affinely in the Youla controller parameter. A convex optimization problem for heterogenous time- and frequency-domain objectives and constraints can now be formulated and solved efficiently. Finally, the plant model within the observer is parametrized, yielding a globally LPV control law. The controller achieves high performance in terms of handling qualities, critical loads, and comfort.

Next, longitudinal control is once again addressed, however, via a direct design of an LPV controller for an LPV plant description. After a thorough open-loop analysis, the design weighting functions are prepared and optimized by considering a series of standard $\mathscr{H}_\infty$ designs at fixed parameter values. This also allows to directly tune robustness of the controller family. Then these design data are utilized in a direct LPV control design to obtain an optimized LPV controller. This allows to consider parameter rate of change bounds and to exploit the structure of the parameter dependency already in the control design and yields excellent performance in validation.

Finally, both lateral and longitudinal control tasks are addressed in the investigation of design methods of $\mathscr{H}_\infty$ and $\mathscr{H}_2/\mathscr{H}_\infty$ controllers with prescribed controller structure and (arbitrarily) low dynamic order. The involved optimization problems are generally difficult to solve (non-smooth, non-convex). However, well-performing results could be achieved via the $\mathscr{H}_\infty$ fixed-order optimization toolbox ($\mathscr{H}_\infty$ fixed-order optimization) in MATLAB®. These designs have been developed for the NACRE BWB configuration (lateral design) and for the ACFA BWB configuration (longitudinal design).

The multitude of control design studies in this context yields the important conclusion that multistage design approaches that combine the benefits of several different design methods allow to address a multitude of heterogenous specifications efficiently. These composite control concepts typically contain feedback control laws, but also complementary feed-forward controller blocks to address command shaping or (measurable) disturbance compensation. These concepts are often referred to as *two degrees of freedom control architecture*. Here, several such concepts have been developed:

- Design of a lateral comprehensive load alleviation control system as a combination of eigenstructure assignment, robust $\mathscr{H}_\infty$-control feedback design and a scheduled feed-forward command shaper.
- Design of a longitudinal gust loads alleviation by LQG pre-shaping and convex controller synthesis.
- Design of a longitudinal comprehensive load alleviation control concept combining $\mathscr{H}_\infty$ designs/LPV feedback control design with an $\mathscr{H}_\infty$ full-information feed-forward concept.

6.1.3 State of the Art

Flight and structural control laws are commonly built using optimal or robust control design methods to maximize control performance also in the presence of plant uncertainties. The DK-iteration and more recently the DGK-iteration or mixed-μ-synthesis are well-known design tools to generate robust control laws when the plant's uncertainty or possible perturbations can be modeled well by structured uncertainties [5, 76, 95].

An additional, central challenge for a control engineer is to translate the given specifications efficiently and effectively into design parameters for the utilized synthesis methods (usually from optimal or robust control). Typically, these constraints are either stated as weighting functions in the frequency-domain ($\mathscr{H}_\infty/\mathscr{H}_2$ control, DK-iterations) or as objective function weightings (as in linear quadratic (LQ) control). One design method with the capability of considering both time- and frequency-domain constraints and objectives at the same time is convex synthesis.

Convex design for the control of conventional flexible aircraft has been studied, among others, in the PhD thesis of [20] as well as by [64] (with subsequent controller order reduction), and [84] (a self-scheduling approach). In robust control applications, robust stability (RS) of the closed loop is usually the most fundamental requirement. One additional, important requirement for reliable control is the stability of the controller itself (referred to as strong stabilization, see for example [45, 86]), which is not guaranteed by standard optimal and robust design methods. This is however imperative in the case of potential actuator or sensor faults, and simple tuning often does not suffice to obtain stable controllers.

Convex synthesis of a feedback controller using the Youla parameterization has been designed based on the large 750-passenger NACRE BWB aircraft predesign model in [72]. An linear matrix inequality (LMI) formulation is taken to optimize directly for the time- and frequency-domain goals not addressed by the initial controller. A heuristic algorithm to achieve strong stabilization is proposed and allows to obtain a stable feedback law which is validated successfully on all considered parameter cases (mass cases). High control performance is achieved, including direct time-domain specifications.

A general integrated methodology for multiobjective robust control design has been presented in [69]. Previous, closely related studies have been carried out on the

large 750-passenger NACRE BWB aircraft predesign model: for LQ-based lateral control designs see [70], the application of a genetic algorithm for parameter optimization of a multiobjective $\mathscr{H}_\infty$ DK-iteration design has been treated in [71]. Using a Youla parameterization of the feedback control loop, a convex controller synthesis for lateral BWB control has been performed in [73] with a subsequent scheduled feed-forward control design in [72]. Longitudinal BWB control using LPV control concepts has been studied in [89]. All these works investigate control designs on the large 750-passenger NACRE BWB aircraft predesign model and represent the early results achieved in the ACFA 2020 project.

The subsequent feedback control designs reported in this chapter have initially been published in the following papers: the lateral designs in Sects. 6.2 and 6.3 are adopted from [74], the longitudinal convex synthesis design in Sect. 6.4 has been shown in [24], and the LPV feedback design approach in Sect. 6.4 is detailed in [88]. Finally, the structured longitudinal design in Sect. 6.6.4 has been published in [42].

6.2 Robust Eigenstructure Assignment

A. Schirrer and M. Kozek

6.2.1 Methodology

Methods of robust eigenstructure assignment extend classical pole placement control design in several ways [54]: First, only a partial eigenstructure assignment of a few, relevant system poles to desired closed-loop positions is possible. The remaining system poles will generally be shifted slightly as well, but this can be met by an iterative design procedure. The advantage is that no artificial design requirements (for example, pole pinning) need to be introduced, and that the remaining degrees of freedom can be utilized to improve insensitivity to model errors. Also, no full state vector estimation may be necessary and methods exist to derive only those elementary estimates necessary to perform the partial assignment, yielding low-complexity dynamic output feedback controllers.

In the following, an initial controller in the form of an output feedback control law is designed by robust eigenstructure assignment using the techniques and tools given in [54].

Given a state-space system $\mathbf{P}$ as in (5.15) and (5.16) (subscript i omitted for brevity), q triplets $(\lambda_i, \boldsymbol{v}_i, \boldsymbol{w}_i)$ (eigenvalue, input, and output directions, respectively) are assigned in closed loop (with $q \leq p$ where p is the number of measurements). Let $\mathbf{X} = \mathbf{CV} + \mathbf{DW}$, $\mathbf{V} = [\boldsymbol{v}_1, \ldots, \boldsymbol{v}_q]$, and $\mathbf{W} = [\boldsymbol{w}_1, \ldots, \boldsymbol{w}_q]$ hold. The output feedback gain to assign the given eigenstructure is

$$\mathbf{K} = \mathbf{W}\mathbf{X}^{\dagger} \tag{6.1}$$

where the pseudo-inverse $(\cdot)^{\dagger}$ of $\mathbf{X}$ yields the norm-minimal feedback gain for $q < p$. If $q = p$ and $\mathbf{X}$ is non-singular, the inverse of $\mathbf{X}$ can be used instead.

6.2.2 Control Goals

The specific control goals for this lateral inner-loop control design are a subset of the goals in Table 5.4:

1. stabilize the aircraft,
2. obtain high damping $\zeta \geq 0.7$ of the Dutch Roll mode (DR mode) while keeping the mode's undamped eigenfrequency unchanged,
3. obtain sufficiently fast real/aperiodic remaining system dynamics to fulfill rise-time requirements on roll/side-slip responses in 7 and 5 s, respectively, and
4. improve damping of the first flexible mode.

Note that in the present setting, goal 1 also includes a significant shift of the spiral mode's pole to the left which otherwise is realized by an outer (auto-)pilot control loop.

These requirements all have to be fulfilled robustly for all 30 considered parameter cases in the viewed parameter space. They will all be addressed, as far as possible, by the control law which is designed through robust/insensitive eigenstructure assignment.

6.2.3 Feedback Control Design

To fulfill the listed control goals, an initial controller is designed by robust partial eigenstructure assignment (utilizing the MATLAB® Robust Modal Control Toolbox supplied with the book [54]). This is done in two steps:

1. Assign low-frequency (rigid-body) dynamics using low-pass output feedback,
2. Increase the damping of high-frequency flexible modes via a bandpass-filtered output feedback through eigenvector projection.

For step 1, an input/output (I/O)- and state-reduced RB model was extracted from the design ROMs at a chosen parameter case:

- Input reduction to 1 combined rudder command and 1 combined anti-symmetric command on flaps 3 and 4 ("inner" and "middle" ailerons). This was chosen because flaps 3, 4 do not reverse their effect on the aircraft over the envelope and they are fast enough for RB control.

- Output reduction to measurements of β (side-slip angle), φ (roll angle), p (roll rate), and r (yaw rate).
- State reduction by truncation of all flexible modes and lag states, leaving only states β (side-slip angle), p (roll rate), r (yaw rate), φ (roll angle), and the rudder- and flap 3, 4 second-order dynamics. The actuator dynamics of flaps 3 and 4 were modeled by a single filter because they behave sufficiently similarly.
- Augmentation of each of the 4 measurements by a fourth-order dynamics (second-order Padé approximation of 160 ms delay and a second-order low-pass filter).

The relevant plant open-loop poles lie close to the respective poles of the full-order model. The RB poles can be identified as a low-damped (in some parameter cases unstable) DR mode (frequency between 0.7 and 1 rad/s), a marginally stable or unstable real spiral mode and a stable real pole at around -2. The desired DR pole location is obtained by increasing its damping ζ to $\sqrt{2}/2$ with constant frequency.

The DR mode damping requirement and the decoupling specifications (and partially the performance specifications) are cast into eigenstructure constraints, see [54]:

$$p_{\text{rig,des},1} = -0.6 \qquad v_1 = [0, *, 0, *, \ldots]^{\mathrm{T}} \tag{6.2}$$

$$p_{\text{rig,des},2,3} = p_{\text{DR,des},1,2} \qquad v_{2,3} = [*, 0, *, 0, \ldots]^{\mathrm{T}} \tag{6.3}$$

$$p_{\text{rig,des},4} = -1.3 \qquad v_4 = [0, *, 0, *, \ldots]^{\mathrm{T}}, \tag{6.4}$$

where the remaining eigenvector elements (marked by $*$ in (6.2)–(6.4)) are unconstrained. The computed feedback gain robustly assigns a high DR mode damping. The loop is closed with the resulting static output feedback law, and this shaped plant comprises the design plant for step 2.

Design step 2 aims to increase the damping of the first (low-damped) flexible mode at around 10 rad/s. The controller takes the modal measurement $Nz_{\text{lat.law}}$ and generates a combined flap 3, 4 and a separately actuated flap 5 control signal. In order to obtain enough degrees of freedom to shift the two flexible mode (complex-conjugated) poles, a first-order observer is necessary. The mentioned toolbox offers a robust observer design method for this task. The observation dynamics is chosen real and near the relevant modes' frequency at $p_{\text{obs}} = -10$. After such observer is synthesized, a static output feedback gain is computed to shift the flexible mode poles to the left. Hence, they are reassigned at the location

$$p_{\text{flex,desired},1,2} = p_{\text{flex,actual},1,2} - 0.5 \tag{6.5}$$

using a minimal-energy criterion, yielding a Bode magnitude peak reduction of about 6 dB in the closed-loop transfer path from lateral gust to $Nz_{\text{lat.law}}$.

The final partial eigenstructure assignment controller is combined into a single linear time-invariant (LTI) system of first order, 3 outputs (combined flap 3, 4; flap 5; rudder), and 5 inputs (measurements of side-slip angle, roll angle, roll rate, yaw rate, and $Nz_{\text{lat.law}}$) and is successfully validated on all fuel and center of gravity (CG)

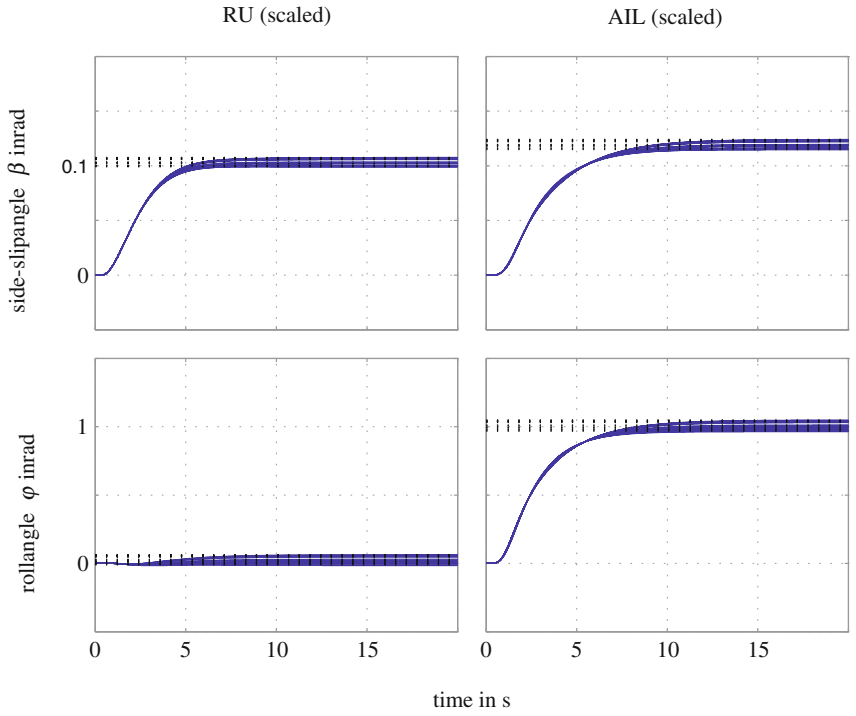

Fig. 6.1 Step responses of the pre-shaped plants from rudder and ailerons to side-slip and roll angles at random CG and fuel parameter values

parameter cases of the design flight condition (fixed Mach and dynamic pressure case).

6.2.4 Basic Feed-Forward Decoupling Design

For basic pilot input shaping, a simple feed-forward control law of PT1-structure is synthesized that

- maximizes decoupling of the two reference signals (roll reference φ_{ref} and side-slip reference β_{ref}) and
- ensures that rate limits on the control surface inputs are obeyed for the test maneuvers ($-30° \rightarrow +30°$ roll reference step, $0 \rightarrow 0.1$ rad side-slip reference step).

This is solved by a linear programing (LP) problem that directly shapes the feed-forward controller coefficients to optimize decoupling Decouplingover all fuel and CG cases and a suitable choice of the PT1 time constants.

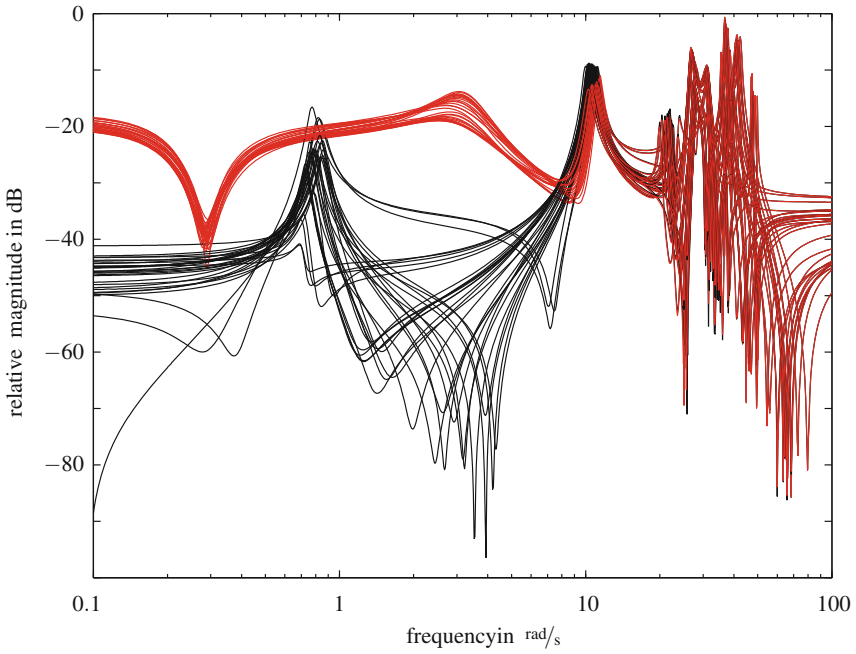

Fig. 6.2 Bode magnitude plot of gust-wing cut moment for all mass cases (*black* open loop; *red* closed loop with initial controller)

6.2.5 Initial Control Law Validation

Figures 6.1 and 6.2 validate the performance of the designed initial control law for all CG and fuel cases for the high-speed central flight case (cruise conditions). Figure 6.1 shows that the closed-loop validation step responses fulfill the required RB specifications robustly. Moreover, the aircraft is robustly stabilized, and the damping ratios of the DR mode and the first flexible (wing bending) modes are increased as shown in Fig. 6.2, but also an overall increase in the low-frequency magnitude of the disturbance-loads transfer becomes evident. The first flexible mode can be robustly attenuated by about 6 dB in all CG/fuel cases with this simple control law.

Further studies on the issue of the increased low-frequency disturbance-load magnitude shows that this effect mainly occurs at parameter configurations far from the design point. When solely assigning one aircraft mode to the desired location while keeping the others fixed at their open-loop locations, it is unveiled that shifting the roll mode and the flexible mode does not affect low-frequency loads; however, both DR mode shaping as well as shifting the spiral mode are responsible to a similar degree to the observed increase in loads. Further optimization of the low-frequency disturbance behavior of the aircraft is not studied in this work, but represents an interesting area for follow-up studies.

6.3 DK-Iteration Design

A. Schirrer and M. Kozek

6.3.1 Methodology

Based on the pre-shaped plant obtained by closing the loop with the initial controller from Sect. 6.2, a parameterized high-accuracy parameterized linear fractional representation (LFR) is built (see Sect. 4.2.3.3), which serves as basis for robust feedback control design by DGK-iteration [74]. Due to high-dimensional parameter dependency and loose bounds in current μ analysis tools, this synthesis task faces computational difficulties given today's workstation computing performance and numeric properties of the algorithms. Thus, ways to reduce design complexity and improve resulting robust control performance are tested and assessed in terms of performance, robustness, tractability, and problem size. A high-accuracy parametric LFR as well as various simplified LFR formulations are utilized in subsequent design attempts.

6.3.1.1 Initial Controller

The output feedback controller $\mathbf{K}_{\text{init}}$ of dynamic order 1 is obtained as shown in Sect. 6.2. The initial controller is interconnected to the aircraft system models, forming a set of pre-shaped plants (each of dynamic order 48). As described in Sect. 6.2.5, this initial controller achieves a robust reduction of the first anti-symmetric wing bending mode amplitude by about 6 dB. Note that it is not possible to directly and robustly increase flexible mode damping further with the eigenstructure assignment design methodology.

6.3.1.2 Linear Fractional Representation of the Parametrized, Pre-shaped Plants

By exploiting the structure of the parameter dependency of the plant, the damping of the first flexible modes is attempted to be further increased, without altering the other already satisfied control goals (RB response, stability). Therefore, an LFR description of this set of pre-shaped plants in the two parameters CG and fuel filling has been generated from the model grid (5.15) and (5.16) and validated by the authors' project partners analogous to the procedure in [43], see Sect. 4.2.3.3. The lag states were removed for the LFR generation. A first, high-accuracy LFR has been generated which has 41 states and a Δ block size of 40 $\times$ 40 (in which the two real-valued

parameters are 9 and 31 times repeated, respectively). Later, due to computational difficulties with this level of complexity, a simplified parameterization has been generated which leads to a reduced-accuracy LFR with 33 states and a 13×13 Δ block (8 and 5 times repeated, respectively).

Figure 6.1 shows scaled, typical step responses (as modeled by the high-accuracy LFR) for several randomly sampled parameter values. The RB response is considered satisfactorily shaped by the initial controller.

6.3.2 Control Goals

In addition to the initial control law designed in Sect. 5.4, a lateral inner-loop control design should be carried out to are:

1. retain the achieved goals from Table 5.4 (stabilization, RB control), and
2. maximize damping of the first two flexible modes.

Note that the initial control law already provides vibration damping functionality; however, further improvement of the vibration damping performance (goal 2) is possible only when exploiting knowledge on the parameter dependency. Thus, the μ synthesis method (via the D(G)K-iteration algorithm) is employed to address this goal.

6.3.3 Control Design

DGK-iteration is employed with the aim to generate a robust controller that fulfills the targeted control goals: to attenuate the first and second flexible modes, and thus reduce the gust-induced wing loads. For details on the involved robust control theory, fundamental definitions of linear fractional transforms/representation (LFTs/LFRs), the structured singular value (μ), robust stability (RS), robust performance (RP), or the DK- and DGK-iteration algorithms, the reader is referred to [5, 37, 76, 95].

The control design architecture for control design via DGK-iteration is outlined in Fig. 6.3 (left). The system LFR $\mathbf{G}_{\text{LFR}}$ is augmented by the design weights $\mathbf{W}_{\text{a}}$, $\mathbf{W}_{\boldsymbol{n}}$, $\mathbf{W}_{\boldsymbol{u}}$, and $\mathbf{W}_z$ to obtain the augmented plant $\mathbf{G}_{\text{aug}}$, and $\mathbf{K}$ is the robust feedback LTI controller to be designed. The modeled signals are disturbance input $d = v_{\text{lat}}$, feedback control commands $\boldsymbol{u} = [u_{\text{RU,FB}}, u_{\text{TE12,FB}}, u_{\text{TE3,FB}}]^{\text{T}}$, the performance outputs $\boldsymbol{z} = [My_{\text{wing}}, Nz_{\text{lat.law}}]^{\text{T}}$, the measured outputs $\boldsymbol{y} = [\beta, \phi, p, r, Nz_{\text{lat.law}}]^{\text{T}}$ with measurement noise $\boldsymbol{n}$, as well as the weighted output signals $\boldsymbol{z_u}$ and $\boldsymbol{z_p}$. The measurement noise weighted $\mathbf{W}_n$ and the additive uncertainty weight $\mathbf{W}_{\text{a}}$ serve as problem regularization terms and are chosen small and constant. The remaining weights are chosen with the aim to

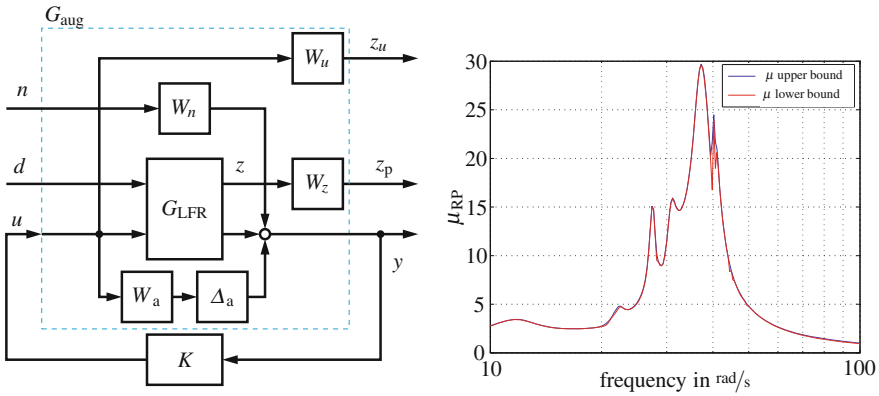

Fig. 6.3 Design architecture for DGK-iteration (*left*), robust performance (RP) μ analysis results (*right*)

- ensure well-scaled I/O magnitudes (via scaling inside $\mathbf{G}_{\text{LFR}}$),
- emphasize the first and second wing bending modes in the performance path (via $\mathbf{W}_z$), and to
- limit the control input magnitudes to the admissible input range (via $\mathbf{W}_u$).

6.3.3.1 DGK-Design Attempt with High-Accuracy LFR

The results of a DGK-iteration run based on the high-accuracy LFR are shown in Fig. 6.3 (right). The RP μ value is much larger than 1 at all considered frequencies—it is clearly evident that the closed loop fails to achieve satisfactory control performance. In further studies, it becomes evident that the bounds of the open-loop robust stability (RS) μ value are very loose. This problem of convergence and the resulting conservativeness in the **D**- and **G**-scalings yield unsatisfactory results of the design. Note that only static scalings could be utilized in DGK-iteration design due to the problem size: The $\boldsymbol{\Delta}$-block contains $40 \times 40 = 1{,}600$ entries. Fitting these with dynamic **G**- and **D**-scalings inflates the controller order quickly well above 1,000 which is numerically and computationally infeasible.

One common heuristics to improve mixed-μ convergence is to add small, complex uncertainties to the existing real uncertainties. This was attempted first, however no improvement in μ bound convergence could be observed.

To overcome the encountered computational difficulties, two simplification approaches will be taken and compared in the following.

6.3.3.2 DGK-Design Attempt with AdHoc Uncertainty Model

Based on the observation that the perturbations of the flexible mode parameters are the main source of uncertainty, an adhoc uncertainty parameterization is attempted

(see [8, 90, 95] for similar attempts). The aircraft models are close to a modal form [36] in which a low-damped flexible mode is represented by a 2×2 submatrix of the system matrix $\boldsymbol{A}$:

$$\boldsymbol{A}_{\mathrm{m}i} = \begin{bmatrix} 0 & 1 \\ -\omega_i^2 & -2\zeta_i\omega_i \end{bmatrix}. \tag{6.6}$$

By replacing the (2, 1) and (2, 2) matrix elements with real-valued uncertain parameters which are confined to the intervals occurring across the model set, an efficient uncertainty representation with a small uncertainty matrix $\boldsymbol{\Delta}$ of size 2×2 per mode is obtained. Note that no other variations in the plant are considered, hence the uncertainty model is rather crude. The architecture shown in Fig. 6.3 is reused, but the plant LFR is replaced by its simplified version (with a $\boldsymbol{\Delta}$-block of 4×4). The achieved RP μ value is 2.7.

The obtained controller is of dynamic order 117 (due to dynamic D- and G-scalings) after few minutes of computation time on a standard office PC. This controller complexity is in general too high for implementation, so controller order reduction is needed subsequently.

Figure 6.4 shows the performance singular values of the open- and closed-loop systems with the validation plants. An input turbulence model according to a 1D von-Kármán vertical turbulence model has been utilized to include information on the expected low-pass characteristics of turbulence excitation, assuming that a similar turbulence characteristics can be observed in a lateral direction. It is evident that for most models the obtained controller performs well and achieves strong attenuation (about -7 dB) of the first and second flexible modes. However, in two (extremal) parameter cases, the second flexible mode of the respective validation plant is destabilized. No simple means are available to ensure stability with these plants except for enlarging the uncertainty ranges, which quickly destroys the obtained nominal performance.

6.3.3.3 DGK-Design with Reduced-Accuracy LFR

In order to obtain a computationally manageable problem size, but still to obtain a robustly stabilizing and performing control law, a reduced-accuracy parameterized LFR has been generated. The weight shapes are chosen as depicted in Fig. 6.5 to emphasize the control effect on the first flexible mode. After several design iterations, it became clear that the large variation of the second flexible mode is a limiting factor in the design—therefore, the weightings are adapted to avoid control action at the second flexible mode's frequency range.

Figure 6.6 shows the unweighted and the weighted performance singular values of the unweighted (scaled) LFR and of the weighted design plant, randomly sampled in the uncertain set. The effect of the chosen weightings is clearly visible—the strongly

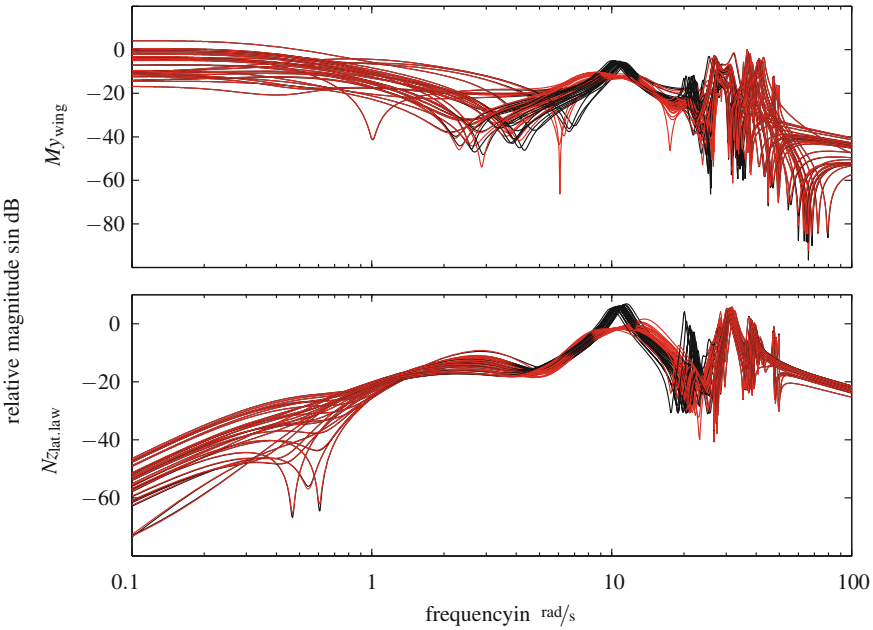

Fig. 6.4 Bode magnitude plots of von-Kármán low-pass filtered lateral wind v_{lat} to wing cut moment My_{wing} and anti-symmetric wingtip acceleration signal $Nz_{\text{lat.law}}$ for all mass cases. *Black* Pre-shaped design plant; *red* closed loop with robust controller, obtained by DGK-iteration on a simplified design LFR

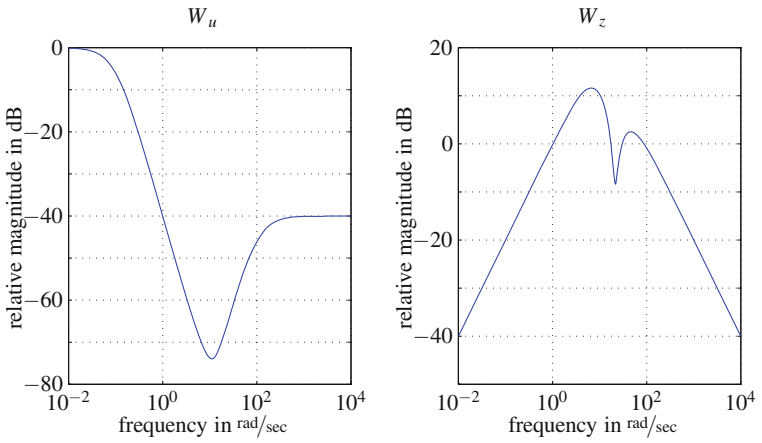

Fig. 6.5 Weight shapes of $\mathbf{W}_u$ (*left*) and $\mathbf{W}_z$ (*right*) the control action is focused on the first wing bending mode (notch in $\mathbf{W}_u$, peak in $\mathbf{W}_z$). Additionally, the 2nd flexible mode must be attenuated in the performance path to obtain RP

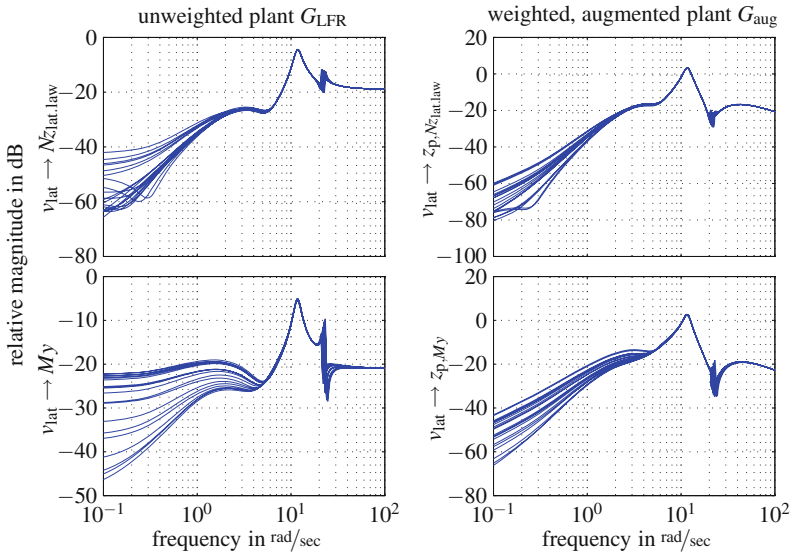

Fig. 6.6 Scaled, unweighted (*left*), and weighted (*right*) magnitude plot of lateral gust—performance outputs as modeled by the reduced-complexity LFR, sampled at 20 random parameter points

varying second mode is decreased in importance; the control design task focuses on the first flexible mode.

After the DGK-iteration run (20 iterations, **D**- and **G**-scalings up to order 4, grid of 284 frequencies, augmented design plant $\mathbf{P}_{\mathrm{aug}}$ of order 59, 135 min computation time), an RP μ of 1.44 is obtained (as compared to an open-loop RP μ of 2.0), which is still larger than 1, but, as shown in Fig. 6.7, the RS μ value is less than 1. The figure shows also the nominal performance singular values (single weighted load performance outputs and all outputs combined) of the nominal closed loop **M** and thus shows the closed-loop system variation bounds as gap between the nominal singular values and the RP μ bound. The controller dynamic order is very high with 253 states. For implementation, (robust) controller order reduction must be performed, see [21] for a μ-based approach. The high-order control law can be reduced by the `reduce` command of MATLAB® [5] with the option `'ErrorType','mult'` to order 30 virtually without performance loss. The underlying algorithm is a balanced stochastic model truncation (BST) via Schur's method [67].

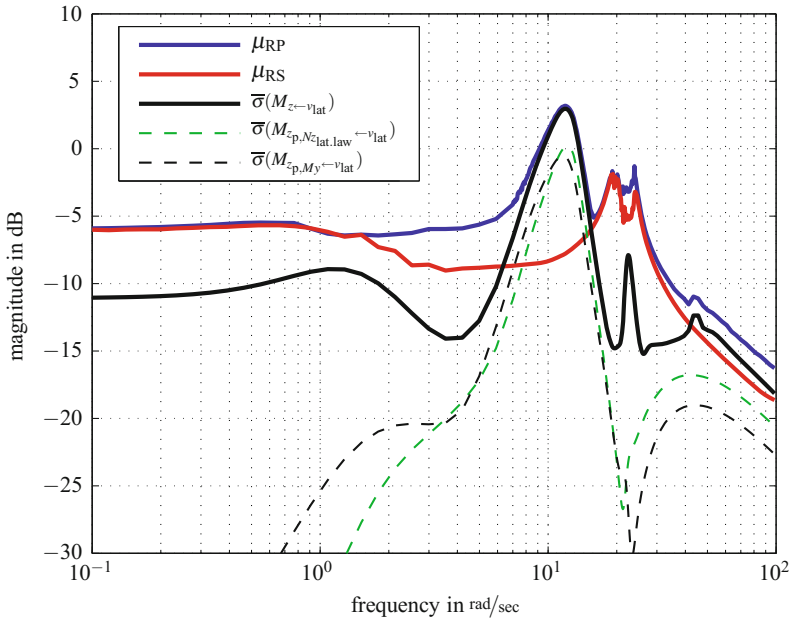

Fig. 6.7 Nominal performance singular values and μ upper bounds for RP and RS

6.3.4 Validation and Discussion

6.3.4.1 Validation of Control Performance and Robustness

The control law obtained in Sect. 6.3.3.3 is validated with all grid models (5.15) and (5.16). All closed-loop systems are stable. While the μ analysis results in Fig. 6.7 proves RS for the utilized LFR formulation of the problem (up to LFR approximation errors), this enumeration of the set of all closed-loop systems proves RS in terms of the provided model set.

Figure 6.8 shows the magnitude plots of the disturbance—performance paths: the first flexible mode can robustly be reduced to 2–3 dB below the level provided by the initial control law. Note that this does not contradict the evident lack of RP in the LFR sense (which is based on the performance formulation according to Fig. 6.3).

The controller obtained by DGK-iteration does not interfere with low-frequency roll and side-slip behavior of the BWB aircraft, so the final closed-loop responses are virtually unchanged compared to Fig. 6.1 and control goals 2 and 3 in Sect. 6.2 remain fulfilled.

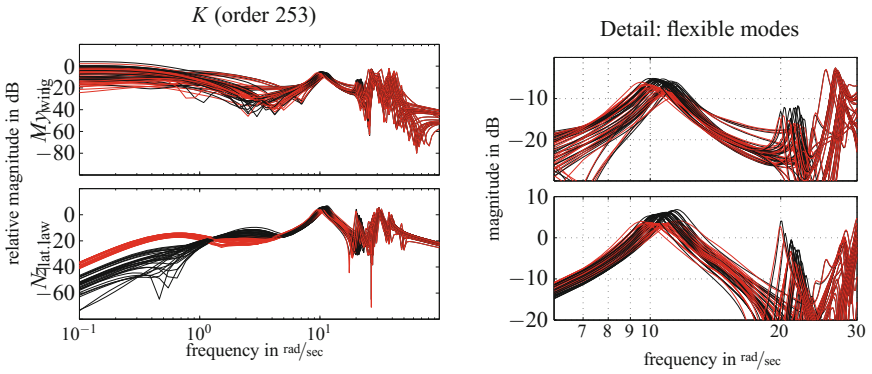

Fig. 6.8 Bode magnitude plots of von-Kármán low-pass filtered lateral wind v_{lat} to the wing cut moment My_{wing} and to the anti-symmetric wingtip acceleration signal $Nz_{\text{lat.law}}$ for all mass cases. *Black* Aircraft model with initial control law only; *Red* closed loop with initial controller and robust controller, obtained by DGK-iteration with the reduced-accuracy design LFR

6.3.4.2 Discussion

A highly detailed modeling process yields accurate system models for a parameter grid of relevant system parameters. For high parameterization accuracy, the obtained parameterized linear fractional representation turns out to be prohibitively complex for current μ analysis and synthesis algorithms. Several ways to solve the design task have been attempted, including well-known problem regularization techniques ("complexification" of the uncertainty description) and simplification of the linear fractional representation.

Adhoc uncertainty modeling yields simple LFRs and high control performance for the design plant, but it destabilizes some parameter-extremal validation plant cases in closed loop. No straightforward remedy is found without compromising control performance significantly.

Subsequently, a reduced-accuracy parameterized LFR is generated which leads to a successful, albeit computationally demanding design. The obtained control law can be reduced to order 30 without performance degradation and yields stable closed loops with all validation cases. Its performance is significantly lower than the nominal performance achieved through the adhoc approach, but in turn it provides an actually robust solution. Considering that significant damping is already introduced by the initial control law it is plausible that further improvement comes at high cost—both in terms of design complexity and numeric complexity of the control law.

As an outlook to possible future research, several other approaches could be attempted in such high-complexity designs. To meet the numeric challenges associated with μ bounds calculation, especially in the present case where a low number of parameters is repeated often, it seems reasonable to attempt numeric search methods to empirically find improved μ bounds. Also, μ computation algorithms without the need of fine frequency gridding could alleviate the encountered difficulties [34].

This study considers only the lateral motion of the BWB aircraft which is decoupled from the longitudinal motion as long as the deviation of the flight mechanic variables remain sufficiently close to trimmed level flight conditions and the linearized system models remain valid. However, even without longitudinal/lateral coupling in the underlying system models, it is important to simulate both dynamics simultaneously in order to verify that control surface deflection/rate limitations are obeyed also in combined maneuvers (such as in coordinated turns).

In conclusion, the findings of this work underline the importance of efficient LFR modeling for DK-/DGK-iteration-based control design. The encountered challenges demonstrate the need for algorithms which allow to generate efficient LFRs whose parameterization accuracy is optimized for the envisaged control task, for example through frequency-weighted error minimization.

6.3.4.3 Conclusions

This section presents results for an incremental robust feedback control design of a lateral inner-loop control law for the 450-passenger ACFA BWB aircraft predesign model. Starting with an initial control law that already provides basic response shaping and flexible mode damping, the main design goal of this work is to further increase the damping of the flexible modes robustly despite the presence of strong parameter-dependent plant variation. The DGK-iteration synthesis procedure is utilized and several LFR formulations of the aircraft model parameter dependency are tested. The highest-complexity attempt involving a high-accuracy parametric LFR cannot be handled computationally. A simple, manual adhoc uncertainty formulation leads to quick results with high nominal performance but fails to provide robustness in validation. Finally, a reduced-accuracy parametric LFR is utilized which leads to a computationally demanding design, but yields a control law that robustly stabilizes and attenuates the flexible dynamics above the level provided by the initial control law. High-fidelity validation studies of these control laws via simulations are necessary at a later stage of control design in order to quantify the effects of model uncertainties and errors as well as longitudinal and lateral coupling.

6.4 Convex Synthesis Design

F. Demourant, G. Ferreres and A. Schirrer

6.4.1 Introduction

Numerous requirements are to be fulfilled to control a flexible aircraft. The corresponding specifications can be very different: handling qualities, load alleviation in the frequency- and/or time-domain representations, command effort including saturation and rate limiters, comfort and robustness [23, 33, 84]. To meet these

different kinds of specifications the Youla parameter design, namely the convex synthesis [12] is involved. This approach is very interesting for several reasons. All stabilizing controllers can be parametrized thanks to the Youla parameter and the closed-loop transfer functions are affine with respect to the Youla parameter. Then all specifications that correspond to constraints on closed-loop transfer functions can be rewritten as convex optimization problem. Finally, the problem solved is convex which guarantees the globality of the optimum found and good tractability of the optimization algorithm. This last point is all the more important in that a specific property of a flexible aircraft is the high dynamic order of the models. In brief, the convex synthesis is clearly a multiobjective/multicriterion control law design approach.

The second important point is to ensure achieving the required performance level for the full flight domain and different mass/fuel cases. This point leads to schedule a control law with measurable parameters which impact the behavior of the aircraft. An useful representation to make the Youla parameter appear naturally is the estimated state feedback structure. By this representation, a natural LPV controller is obtained since a parametrized model is embedded in the observer. A typical parametrization is an LFR of the model to control, whereby the Δ block contains scheduling parameters. Let us point out two important points. Firstly, it is not necessary to schedule the observer and state gains and/or the Youla parameter if the closed-loop behavior is satisfactory. Secondly, the LFR, which can be difficult to determine with high-order models and/or numerous scheduling/robustness parameters [83], is one possible representation, but other parametrizations such as a polynomial parametrization, can be used for the observer.

The studied control design task for the flexible ACFA BWB aircraft is aimed at 3 sets of specifications. The first set of specifications concerns the handling qualities, that is, the behavior of the aircraft with pilot and flight control law. Thereby, it is important to note that it is not expected that all handling qualities specifications are satisfied by the feedback. If the feedback design is considered satisfactory, it is possible and necessary to use a feed-forward control law to shape time-domain responses in order to fully meet handling qualities specifications. The second set of specifications concerns the load alleviation in critical load outputs. Typically, the main objective is to decrease the load level for the wing root bending moment (WRMX) under the constraint to satisfy actuators saturations and rate limiters and not to increase the wing root vertical force (WRFz). The last specification set concerns the improvement of passenger comfort. Here, this specification is formulated as reduction of the $\mathscr{H}_2$ norm of cabin accelerations.

For the rigid part, an LQG methodology is involved. This methodology is very interesting in our context because it makes the structure of the estimated state feedback appear naturally. Of course, from theoretical point of view, any dynamic feedback output can be put under an estimated state-feedback form [1]. However, this additional step is not straightforward to carry out and can lead, in the context of an LPV control law, to controllers which are not interpolable with a suitable behavior. Results obtained in terms of closed-loop pole placement and time-domain simulations are satisfactory without scheduling observer and state gains. Still, this controller is an LPV controller due to the fact that the observer is parametrized. This controller

represents the initial stabilizing LPV controller. Now the Youla parameter is designed to meet specification on the flexible part. Finally, the load alleviation, which is the main objective, is obtained while satisfying constraints on WRFz and actuators together with a comfort improvement. Finally, after the feedback has been synthesized, a feed-forward is designed to satisfy handling qualities specifications completely.

The results of this control design strategy are taken from [24].

6.4.2 Methodology

A convex representation of the feedback control design problem is obtained via the Youla parameterization [94]. This allows one to express closed-loop transfer functions affinely in basis functions of the Youla parameter and thus allows direct convex optimization of closed-loop time- or frequency-domain responses. This so-called convex synthesis [12, 20], as a Youla-parameter-based technique, is similar to the $\mathscr{H}_\infty$ synthesis in the sense that it allows to weigh closed-loop transfer matrices. Additionally, mixed frequency- and time-domain constraints or objectives ($\mathscr{H}_\infty$, $\mathscr{L}_\infty$, $\mathscr{H}_2$, etc.) can be considered simultaneously. However, closed-loop plant poles become immobile under this parametrization, so an initial stabilizing controller is required which already has to produce a well-placed closed-loop plant pole structure.

6.4.2.1 Affinity of Closed-Loop Transfer Functions

Let us consider the classical standard form where $\mathbf{y}(t)$ and $\boldsymbol{u}(t)$ are the inputs/outputs of the control law and $\boldsymbol{w}(t)$ and $\boldsymbol{z}(t)$ are the closed-loop inputs/outputs to control. Typically, $\boldsymbol{w}(t)$ are reference inputs, measure noise and non-measured perturbations. Outputs $\boldsymbol{z}(t)$ represent any closed-loop weighted signals which must be controlled by the control law. $\mathbf{P}(s)$ represents the synthesis model with weighting functions and $\mathbf{K}_0$ represents an available control law. Two hypothesizes are necessary to use of convex synthesis methodology:

- the transfer matrix $\mathbf{P}(s)$ should be proper;
- the initial controller $\mathbf{K}_0$ should ensure closed-loop stability.

Let us split transfer matrix $\mathbf{P}$ in the following way:

$$\mathbf{P} = \begin{bmatrix} \mathbf{P}_{11} & \mathbf{P}_{12} \\ \mathbf{P}_{21} & \mathbf{P}_{22} \end{bmatrix} \tag{6.7}$$

It is possible to write the transfer matrix between $\boldsymbol{w}$ and $\boldsymbol{z}$ as a function of $\mathbf{P}$ and any controller $\mathbf{K}$ by the lower linear fractional transformation $\mathscr{F}_l(\mathbf{P}, \mathbf{K})$:

$$\mathbf{T}_{w\to z} = \mathscr{F}_l(\mathbf{P}, \mathbf{K}) = \mathbf{P}_{11} + \mathbf{P}_{12}\mathbf{K}(\mathrm{I} - \mathbf{P}_{22}\mathbf{K})^{-1}\mathbf{P}_{21} \tag{6.8}$$

In our synthesis problem, it is necessary to write the set of time- and frequency-domain specifications under mathematical criteria. For instance, frequency-domain specifications can be written as the minimization of $\gamma_{i,j}$ under the frequency-domain constraint:

$$\| \mathbf{T}_{w_i \to z_j}(j\omega) \|_\infty \leq \gamma_{i,j} \Leftrightarrow \| \mathscr{F}_1(\mathbf{P}, \mathbf{K})_{i,j} \|_\infty \leq \gamma_{i,j} \tag{6.9}$$

The problem is to determine the control law $\mathbf{K}$ which satisfies specifications (6.9), which is deeply nonlinear in $\mathbf{K}$. We will now show that the Q-parameterization allows to express the closed-loop constraints as a linear expression in $\mathbf{Q}$:

$$\mathscr{F}_1(\mathbf{P}, \mathbf{K}) = \mathbf{T}_1 - \mathbf{T}_2 \mathbf{Q} \mathbf{T}_3 \tag{6.10}$$

where $\mathbf{Q}$ becomes the synthesis parameter and $\mathbf{T}_1$, $\mathbf{T}_2$ and $\mathbf{T}_3$ contain the poles of the initial closed-loop system. In fact, the Q-parameterization allows to substitute $\mathbf{Q}$ to $\mathbf{K}$ to make the optimization problem convex. The Q-parameterization allows to describe all the $\mathbf{K}(s)$ which stabilize the closed loop: if a control law satisfying the specifications exists then it is possible to find it by optimizing the $\mathbf{Q}$ parameter.

We have shown that the closed-loop transfer matrix is affine in $\mathbf{Q}$ for an (LFT). $\mathbf{Q}$ can be parameterized as follows:

$$\mathbf{Q} = \sum_{i=1}^{n} \theta_i \mathbf{Q}_i \tag{6.11}$$

$\mathbf{Q}_i$ are filters whose poles are determined a priori and θ_i are optimization parameters. The set of these filters is a base which is used to build $\mathbf{Q}$. Then the (LFT) can be written in the following way:

$$\mathscr{F}_1(\mathbf{P}, \mathbf{K}) = \mathbf{T}_1 - \sum_{i=1}^{n} \theta_i \mathbf{T}_2 \mathbf{Q}_i \mathbf{T}_3 \tag{6.12}$$

Let us assume $\mathbf{F}_{l_0} = \mathbf{T}_1$ and $\mathbf{F}_{l_i} = -\mathbf{T}_2 \mathbf{Q}_i \mathbf{T}_3$, we obtain:

$$\mathscr{F}_1(\mathbf{P}, \mathbf{K}) = \mathbf{F}_{l_0} + \sum_{i=1}^{n} \mathbf{F}_{l_i} \theta_i = \mathbf{F}_{l_0} + \mathbf{F}^t \Theta \tag{6.13}$$

where the closed-loop transfer matrix is affine in Θ, vector of the decomposition of $\mathbf{Q}$ over the base. We can show that frequency- and time-domain responses are also affine in Θ. The problem can then be efficiently solved with the cutting-planes method.

6.4.2.2 Choice of a Base

To choose a base for Q comes down to determine poles. Is important to note that poles of filters are poles of the final closed loop by property of Q-parameterization. In the field of system identification, numerous studies exist about the generation of these bases. Theoretically, an infinite number of base elements is needed, but as the control law order depends on the base order, a base which order is compatible with specifications is chosen. An orthonormal base is used, called Takenaka and Malmquist base, which combines properties of Laguerre and Kautz base. The decomposition of $Q_i(s)$ is given by (6.14).

$$Q_i(s) = \frac{\sqrt{2\,\mathrm{Re}(a_i)}}{s + a_i} \prod_{k=1}^{i-1} \frac{s - \overline{a_k}}{s + a_k}, \quad Q_0(s) = 1, \quad a_k \in \mathbb{C}^+ \tag{6.14}$$

where a_k are the filters poles and are determined a priori to cover the frequency domain of the bandwidth, and $Q = \sum_{i=1}^{N} \theta_i Q_i$.

6.4.2.3 A Structure for the Youla Parameter

One method to obtain a Youla parametrization is to design an initial stabilizing observer-based state feedback which is a posteriori augmented with the inputs $\boldsymbol{e}$ and outputs $\boldsymbol{v}$ of $\mathbf{Q}(s)$:

$$\begin{aligned} \dot{\hat{\mathbf{x}}} &= \mathbf{A}\hat{\mathbf{x}} + \mathbf{B}\boldsymbol{u} + \mathbf{L}(\mathbf{y} - \mathbf{C}\hat{\mathbf{x}} - \mathbf{D}\boldsymbol{u}) \\ \boldsymbol{u} &= -\mathbf{K}\hat{\mathbf{x}} + \boldsymbol{v} \\ \boldsymbol{e} &= \mathbf{y} - \mathbf{C}\hat{\mathbf{x}} - \mathbf{D}\boldsymbol{u} \end{aligned} \tag{6.15}$$

where $\mathbf{K}$ and $\mathbf{L}$ respectively represent the state feedback and the observer gain. Finally, the control law order $\mathbf{K}(\mathbf{Q})$ is the sum of the order of the initial control law $\mathbf{K}_0$ and the order of $\mathbf{Q}$.

6.4.3 Control Design

The utilized longitudinal model of the ACFA 2020 BWB aircraft (a variant of the reduced-order model (ROM) as generated in Sect. 4.1) is of order 23. This model includes 4 rigid states (pitch oscillation and phugoid modes), 6 flexible modes, hence 12 flexible states and 7 lag states. This model is composed of 2 parts: A rigid part which corresponds to the handling qualities model and a flexible part which corresponds to the aeroelastic model.

The structure of the closed loop for the longitudinal control of a civil aircraft is the following one. The measurement signals used by the controller are $Nz_{\text{long.law}}$, q, and Nz_{CG}. The signals q and Nz_{CG}, respectively, represent the pitch rate and the vertical acceleration on the center of gravity. These two outputs are used to obtain satisfactory results for the handling qualities. $Nz_{\text{long.law}} = (Nz_{\text{l.wingtip}} + Nz_{\text{r.wingtip}})/2 - Nz_{\text{CG}}$ where $Nz_{\text{l.wingtip}}$ and $Nz_{\text{r.wingtip}}$ represent respectively the vertical acceleration on the left and right wing allows to catch the symmetric flexible modes of the wing in order to control them and then to decrease the load level and to improve the comfort for passengers. The outputs used by the controller correspond to the elevators (inner and outer) and the outer ailerons. The elevators allow to obtain good handling qualities and the ailerons allow to control the symmetric flexible modes. As just the longitudinal dynamics is investigated ailerons and elevators are deflected in a symmetric way. The last input, Nz_{com}, corresponds to the reference input.

A second-order actuator is used for each input. Besides, a second-order Padé model of a 160 ms delay with an additional low-pass second-order filter is added on q and Nz_{CG}. A second-order Padé model of a 60 ms delay is added on $Nz_{\text{long.law}}$. These actuators have specific characteristics since the dynamics of these actuators are very slow as indicated by Table 6.1. This kind of dynamics leads to a high amplitude of controller output signals. Besides, as rate limiters and saturations are situated before actuators on the controller outputs, rate limiters represent strong constraints for the command effort. Data about saturations and rate limiters are given in Table 6.1.

Globally the system to control is of order 37 (aircraft 23 + actuators 4 + sensors 10). Of course, it is necessary to add other inputs and outputs which are not used by the controller but essential to satisfy specifications such as the wind and derivative wind inputs, WRMX and WRFz outputs, and cabin accelerations to improve comfort.

The considered flight domain is defined by 3 Mach numbers and 3 dynamic pressures. Tables 6.2 and 6.3 provide the different flight cases in altitudes and true air speed. Eight fuel cases have been considered from the case 20 % to the case full fuel tank by step of 10 %. Finally, 9 flight cases and 9 fuel/mass cases are obtained which correspond to 81 models.

To evaluate the load level, two kinds of signal for perturbations can be considered. The first one is the turbulence which is usually represented by a linearized von-Kármán filter. In our application, this perturbation does not represent the critical perturbation in the sense that it does not lead to a high load level. The second one is the discrete gust which is modeled by the following relation:

Table 6.1 Actuators characteristics

	Damping	Frequency (rad/s)	Position limits (°)	Velocity limits (°/s)
Elevators	0.707	2.71	[−30, +15]	[−30, +30]
Outer ailerons	0.707	7.77	[−25, +25]	[−40, +40]

Table 6.2 True air speed V_{TAS} in m/s

	Mach case 1	Mach case 2	Mach case 3
V1	243.6	251.6	259.8
V2	248.6	256.1	263.7
V3	252.9	260.3	267.7

Table 6.3 Altitude in m

	Mach case 1	Mach case 2	Mach case 3
H1	10,871	11,335	11,777
H2	9,031	9,513	9,973
H3	7,793	8,287	8,761

$$U = \frac{U_{ds}}{2} \times \left[1 - \cos\left(\frac{\pi\, V_{\mathrm{TAS}}}{H} t\right)\right] \tag{6.16}$$

where V_{TAS} is the true airspeed of the aircraft, U_{ds} the amplitude which varies from 11.9 to 19 m/s and H the scale which lies between 9 and 152.4 m. This kind of perturbation leads to sizing load levels.

6.4.3.1 The Initial Stabilizing Controller

The initial stabilizing controller has been designed by a classical LQG approach. Let us remind that this approach is based on the minimization of the following criterion:

$$\int_{-\infty}^{+\infty} \left(\mathbf{x}^{\mathrm{T}}\mathbf{Q}\mathbf{x} + \boldsymbol{u}^{\mathrm{T}}\mathbf{R}\boldsymbol{u}\right) \mathrm{d}t \tag{6.17}$$

where $\mathbf{x}$ is the state vector and $\boldsymbol{u}$ is the input signal of the system to control such as:

$$\begin{aligned} \dot{\mathbf{x}} &= \mathbf{A}\mathbf{x} + \mathbf{B}\boldsymbol{u} \\ \mathbf{y} &= \mathbf{C}\mathbf{x} + \mathbf{D}\boldsymbol{u} \end{aligned} \tag{6.18}$$

Matrices $\mathbf{Q}$ and $\mathbf{R}$ are design parameters and are chosen to satisfy specifications. Finally, a state feedback $\mathbf{K}$ such as $\boldsymbol{u} = -\mathbf{K}\mathbf{x}$ is obtained. A similar formulation exists to synthesize the observer gain $\mathbf{L}$.

6.4.4 Validation and Discussion

As indicated previously, convex synthesis is done in two steps. The first one is to obtain an initial stabilizing LPV controller. From methodological point of view, this

initial controller is designed to satisfy specifications on the rigid part. The rigid part is a fourth-order model with two dynamics: the pitch oscillation and the phugoid modes.

6.4.4.1 Handling Qualities

Specifications concern the pitch oscillation since the phugoid is treated thanks to an auto-throttle which is not the objective here. But a hard constraint must be respected since the pitch oscillation control do not make the phugoid too unstable, that is, the phugoid must remain real and the possible instability inferior to +0.1 rad/s. In other words, the phugoid can be unstable but real and very slow to be controllable by the pilot. Specifications are the following ones:

- A static error null between the Nz command Nz_{com} and Nz_{CG} for a step input;
- Perturbation rejection must be ensured;
- A correct closed-loop pole placement, that is, the control law is able to reject a non-measured perturbation in 5 or 6 s;
- A first-order behavior for Nz_{CG} with a step reference input on Nz_{com}. A rising time of 3–6 s is expected with a very limited overshoot on Nz and an overshoot maximum of 30 % on q.

The first three specifications can be and must be satisfied only by the feedback. In fact, it is necessary to have an integrator in the controller to ensure the perturbation rejection and the null static error. Besides, the closed-loop pole placement cannot be modified by a feed-forward, hence it is necessary to satisfy with the feedback the specification concerning the perturbation rejection in 5 or 6 s. The last specification is treated thanks to a feed-forward. However, to make easier the design of the feed-forward, it is interesting to have, with only the feedback, time-domain response as closed as possible to this specification.

The structure of the 2DOF controller is given by Fig. 6.9. Let us notice the integrator pole in the controller to ensure a perturbation rejection, the feed-forward which acts on only the elevators to satisfy handling qualities specifications and the Youla parameter which uses the estimation error.

Design of the State-Feedback Controller

The design model corresponds to the most unstable model with pitch oscillation and phugoid modes. The phugoid mode is unstable (-0.133 and $+0.206$), while the damping ratio of the short-period mode, namely 0.527, is close to the minimum value over the operating range.

The design model for the state-feedback controller is the 21 state integral model (with a second-order rigid part only corresponding to the pitch oscillation) + actuator and sensor models + an integrator on the Nz_{CG} output. Only the elevators are used.

An LQ method is used as written previously to design the initial stabilizing controller. $R = 1$ for the weighting matrix on u_1 and the weighting matrix Q for the

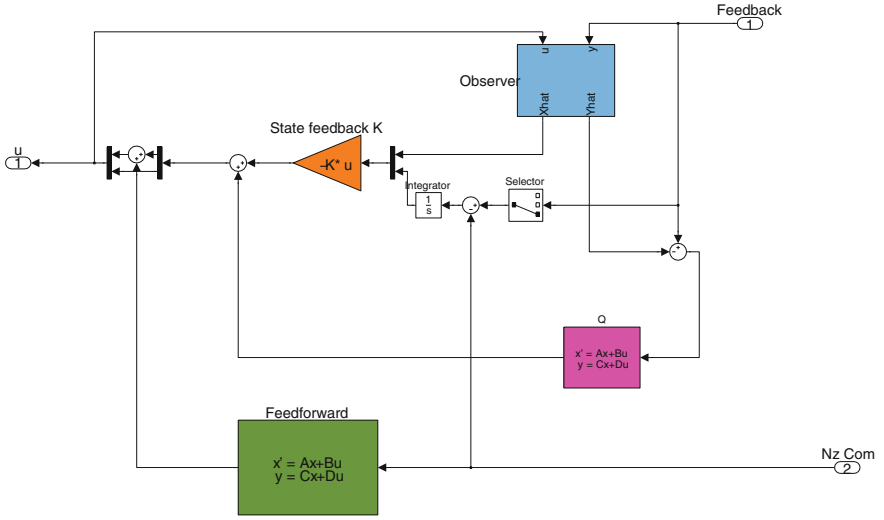

Fig. 6.9 Structure of the 2DOF controller

states corresponds to $Q = \mu_1 c_1 c_1^{\mathrm{T}} + \mu_2 c_2 c_2^{\mathrm{T}}$. The output $y_1 = c_1^{\mathrm{T}} x$ corresponds to the integrator on the Nz_{CG} output, while $y_2 = c_2^{\mathrm{T}} x$ corresponds to the Nz_{CG} output itself. For the application, $\mu_1 = \mu_2 = 0.01$.

Finally, the results in terms of closed-loop pole placement are the following ones for all models over the operating range with only the pitch oscillation:

- The integrator pole remains real in closed loop;
- The open-loop real lag pole remains real in closed loop;
- The pitch oscillation mode, with a damping ratio of about 0.5 in open loop, is accelerated and a bit more damped.

The previous results are not modified by the phugoid, that is, with a 23rd-order model. Besides for all models over the operating range, the worst-case stability degree for the phugoid is $+0.007$, which is very satisfactory since widely inferior to 0.1 rad/s which is the limit imposed by specifications.

To illustrate these results, time-domain responses of the closed loop between Nz_{com} and Nz_{CG} are given by Fig. 6.10a, b. Let us notice that results without phugoid are rather close to the final specifications expected with a feed-forward. Then it is reasonable to assume that it will be possible to satisfy specifications on all models with a simple multi-model feed-forward. The state-feedback controller is globally (very) satisfactory.

Design of the Observer Gain

The model embedded inside the observed state-feedback controller is chosen to be the integral 21 state model (with only a second-order rigid part corresponding to the pitch

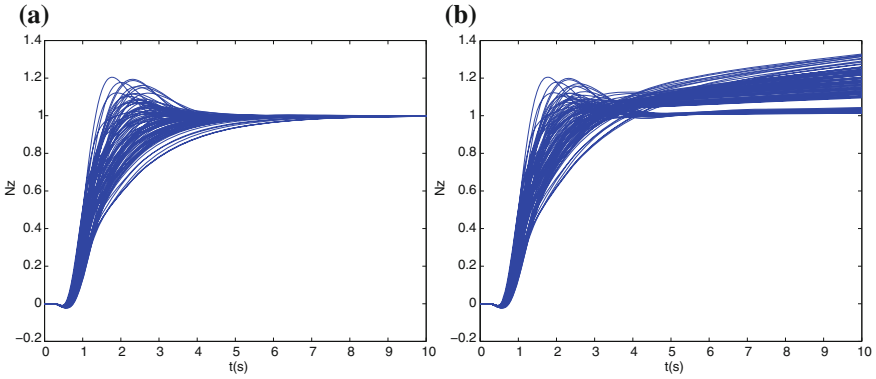

Fig. 6.10 Time-domain response of Nz_{CG} for a step input on Nz_{com}. **a** Time-domain response without phugoid. **b** Time-domain response with phugoid

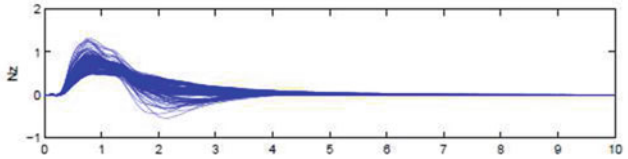

Fig. 6.11 Step response to the filtered wind input on all models without phugoid

oscillation mode) as well as actuator and sensor models. There is no integrator on the Nz_{CG} output since this state is directly available for the state-feedback controller. Remember that the pitch oscillation mode is correctly damped, so that the observer gain is simply chosen as zero. The resulting observed state-feedback controller is first tested on all models without phugoid mode, for the step response to a filtered wind input. More precisely, a filter $1/(1+0.05\text{s})$ is applied to the wind input w and a filter $s/(1+0.05\text{s})$ is applied to $\mathrm{d}w/\mathrm{d}t$. The result seems satisfactory (see Figs. 6.11 and 6.12). The step response to a reference acceleration input is the same as the one obtained with the state-feedback controller, and the closed-loop poles correspond to those obtained with the state feedback and observer gains, so that they need not be checked. Then the estimated state-feedback controller is applied to all models with phugoid mode:

- As for the closed-loop poles, the worst-case stability degree is $+1.951\text{e}{-}02$, which means that the phugoid mode has been essentially stabilized (remember its worst-case open loop value is $+0.206$).
- The step responses to a reference acceleration input are displayed in Fig. 6.13.

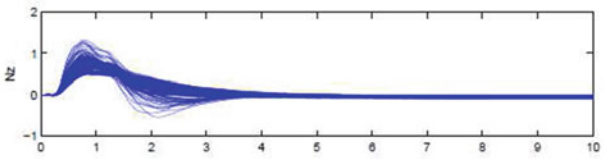

Fig. 6.12 Step response to the filtered wind input on all models with phugoid

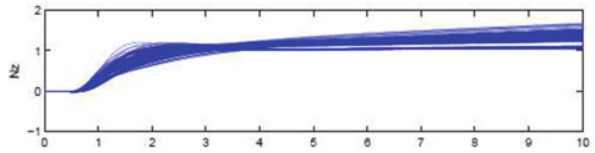

Fig. 6.13 Time-domain response of Nz_{CG} for a step input on Nz_{com} with phugoid mode for all models

6.4.4.2 Control of the Flexible Part

Specifications on the flexible part are treated thanks the Youla parameter design. Let us remind that the closed-loop transfer functions are parametrized with respect to the Youla parameter of the following way:

$$\mathbf{T}_{w\to z} = \mathbf{T}_1 + \mathbf{T}_2\mathbf{Q}\mathbf{T}_3 \tag{6.19}$$

where $\mathbf{T}_{w\to z}$ represents the closed-loop transfer function to minimize or to constrain, $\mathbf{T}_1$ the initial closed-loop transfer function, $\mathbf{T}_2$ and $\mathbf{T}_3$ closed-loop transfer functions which depend on the initial stabilizing controller. Specifications on the flexible model are the following ones:

- To minimize the WRMX load level for sizing cases with critical perturbations;
- A command effort to minimize the WRMX compatible with saturations and rate limiters;
- A WRFz preserved with minimization of the WRMX load level;
- Improvement of the passengers comfort.

Load Level Alleviation

The first specification is the main specification and the most difficult one. Typically, the perturbation is either a turbulence or a discrete gust. However, generally speaking, the discrete gust is the perturbation which leads to the maximum load level for the WRMX. For discrete gusts, the load level is evaluated as an $\mathscr{L}_\infty$ norm on the output WRMX for a specific discrete gust. For each flight and mass case, 10 different discrete gusts, which correspond to 10 different amplitudes U_{ds} and scales H, are applied. Besides when the WRMX load level is decreased for one discrete gust, one mass and one flight case, the load level must represent the maximum load level for all

other discrete gusts and flight/fuel cases. In other words, it is difficult to guarantee a maximum load level for all cases. Of course, as indicated previously, it must be done while satisfying saturations and rate limiters with a limited WRFz load level.

Another and last point is to take into account the 1 g load. This static load is specific to the longitudinal dynamic and perfectly natural since it corresponds to the compensation of the weight of the aircraft. In brief, the total load level is the result of a static part and a dynamic part. But if the dynamic load is obtained by the linear time-domain simulations, it is not the case of the 1 g load. For all that it is the total load which must be minimized and if the same constraint is imposed for all dynamic load it is not relevant because the total load can be very different due to the 1 g load. A solution is to impose a constraint different for each dynamic load in order to have the same constraint for the total load level.

To decrease the WRMX load level sizing fuel and flight cases have been determined. Besides discrete gusts which lead to the highest WRMX load level are determined too. These discrete gusts are called critical discrete gusts. In brief, just sizing flight and fuel cases with critical discrete gusts are used in the optimization problem. But the analysis a posteriori is done with all fuel and flight cases and all discrete gusts.

For all figures, constraints are represented by red lines, static load levels by green lines and dynamic or total load levels by blue lines. For a upward discrete gust , the bending moment is negative, so the sizing value is represented by the negative part. A constraint on the dynamic load is evaluated for each fuel and flight sizing case (Fig. 6.14a). The Youla parameter is designed and finally the result on the dynamic load level is given by Fig. 6.14b. Results on total load level are given by Fig. 6.15b where we notice that the constraint is the same for all cases (Fig. 6.15a, b) since the constraint on the dynamic part has been evaluated for this. Finally, a load alleviation of 17 % is obtained on the total load level (Fig. 6.15b). An important point is to check that WRMX load level for all flight and mass cases and all discrete gusts satisfy constraints, which represent 81 models $\times$ 10 discrete gusts totalling 810 time-domain simulations for each figure. These responses are presented in Fig. 6.16a, b. Thanks to these figures we notice that the constraints are satisfied for all cases.

Command Effort

Let us remind that in the nonlinear scheme, saturations and rate limiters are situated before the actuators and consequently on the controller outputs. Then the signals which are considered for the synthesis and the analysis are controller outputs. Critical constraints are imposed by rate limiters since the deflection velocity before actuator is very high due to limited actuators bandwidth.

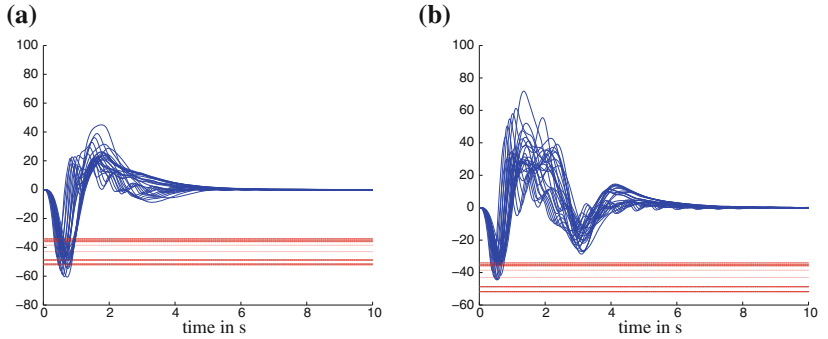

Fig. 6.14 Time-domain response of the WRMX *dynamic* load level with discrete gust. **a** WRMX time-domain response without Youla parameter. **b** WRMX time-domain response with Youla parameter

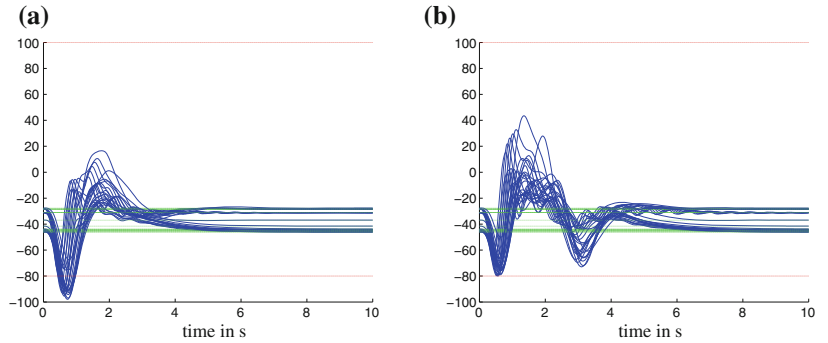

Fig. 6.15 Time-domain response of the WRMX *total* load level with discrete gust. **a** WRMX time-domain response without Youla parameter. **b** WRMX time-domain response with Youla parameter

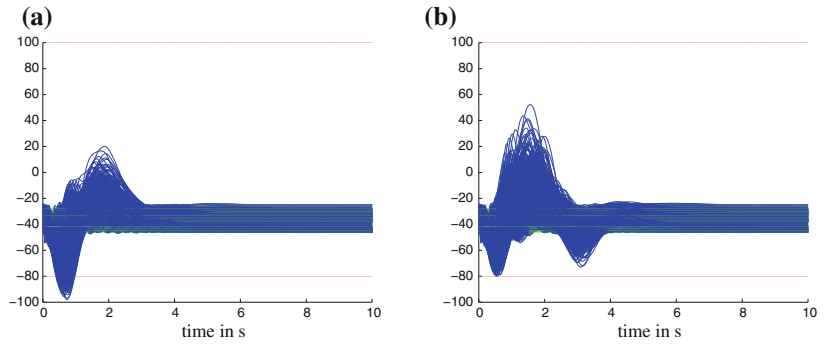

Fig. 6.16 Time-domain response of the WRMX *total* load level with all discrete gusts and all fuel and mass cases. **a** WRMX time-domain response without Youla parameter. **b** WRMX time-domain response with Youla parameter

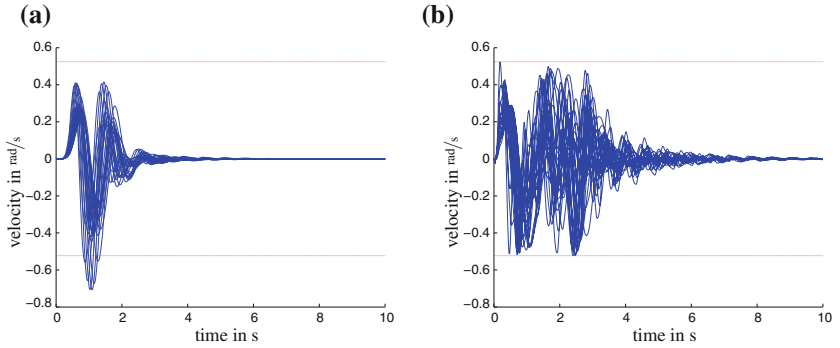

Fig. 6.17 Deflection velocity of elevators for sizing mass and flight cases and critical discrete gusts. **a** Deflection velocity of elevators without Youla parameter. **b** Deflection velocity of elevators with Youla parameter

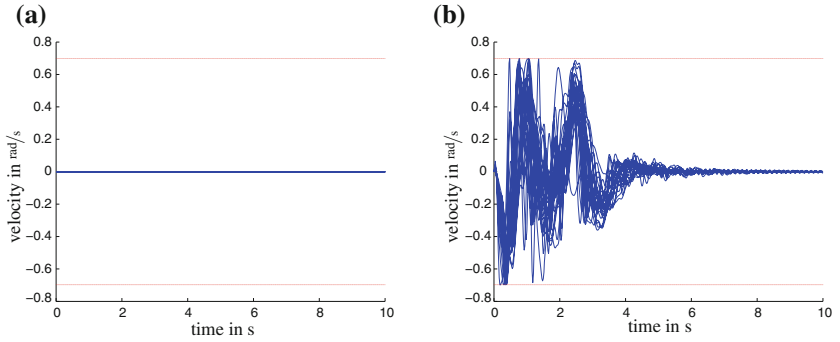

Fig. 6.18 Deflection velocity of outer ailerons for sizing mass and flight cases and critical discrete gusts. **a** Deflection velocity of outer ailerons without Youla parameter. **b** Deflection velocity of outer ailerons with Youla parameter

Figures 6.17, 6.18, 6.19 and 6.20 represent deflections (in rad) and deflection velocity (in rad/s) of outer ailerons and elevators for sizing flight and mass cases and critical gusts with respect to time in seconds. We notice that the constraints represented by red lines are satisfied. These constraints are given by Table 6.1. Let us notice that the initial stabilizing controllers whose the objective is to satisfy handling qualities does not use ailerons, so the result without Youla parameter is 0.

Wing Root Vertical Force Load Level

A specification concerns the WRFz which must be preserved with minimization of the WRMX load level.

In Fig. 6.21, the WRFz load level has been represented for all discrete gusts, mass and flight cases. The red lines on these figures represent the maximal positive and

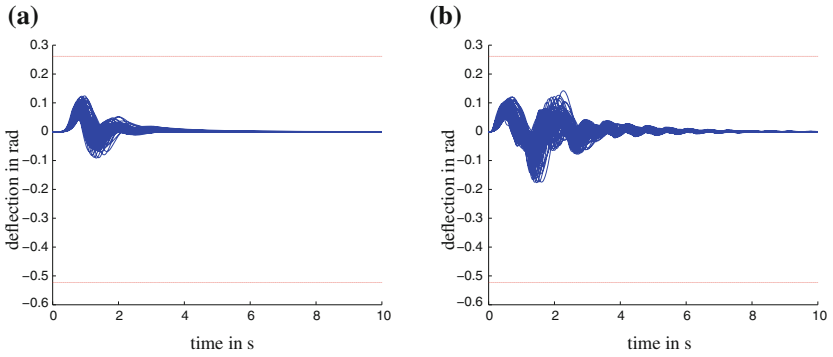

Fig. 6.19 Deflection of elevators for sizing mass and flight cases and critical discrete gusts. **a** Deflection of elevators without Youla parameter. **b** Deflection of elevators with Youla parameter

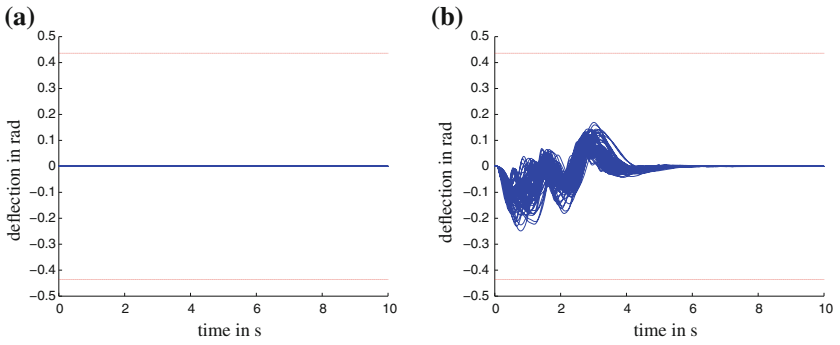

Fig. 6.20 Deflection of outer ailerons for sizing mass and flight cases and critical discrete gusts. **a** Deflection of outer ailerons without Youla parameter. **b** Deflection of outer ailerons with Youla parameter

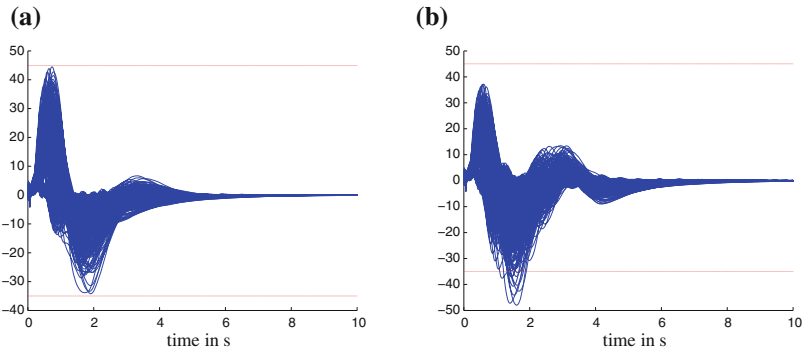

Fig. 6.21 Time-domain response of the WRFz load level with all discrete gusts and all fuel and mass cases. **a** WRFz load level without Youla parameter. **b** WRFz load level with Youla parameter

negative value without Youla parameter. We notice that results with Youla parameter are satisfactory because not only the WRFz is preserved, but also it is decreased for the positive value. The absolute value of the negative part increases but it is not a problem since the 1 g force is positive.

Passenger Comfort

Figures 6.22 and 6.23 represent comfort cabin with two kinds of filters: seasickness and vibration filters. The comfort criterion is based on the $\mathscr{H}_2$ norm of the transfer function. Only result with one comfort cabin output has been represented but 5 comfort cabin outputs have been used in the design scheme. On each figure, the 81 fuel and flight cases have been represented. The input signal is a white noise filtered by a linearized von-Kármán filter. Globally, since 5 comfort cabin outputs are used, the $\mathscr{H}_2$ norm of $5 * 81 = 405$ transfer functions are considered. Of course, it is not possible to represent all these transfer functions but the global reduction of the $\mathscr{H}_2$

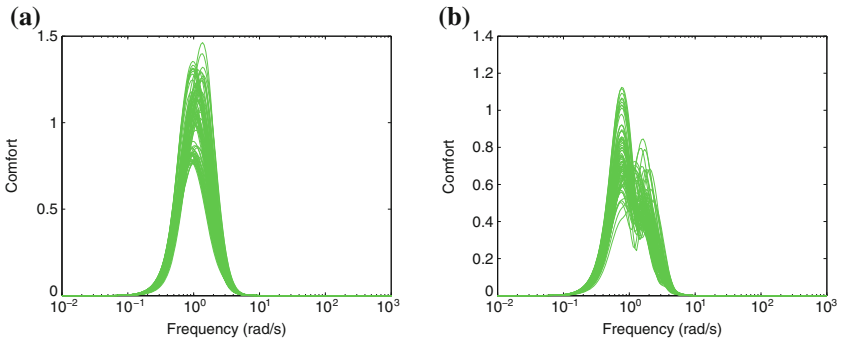

Fig. 6.22 Comfort cabin with seasickness filters. **a** Transfer functions of comfort cabin without Youla parameter. **b** Transfer functions of comfort cabin with Youla parameter

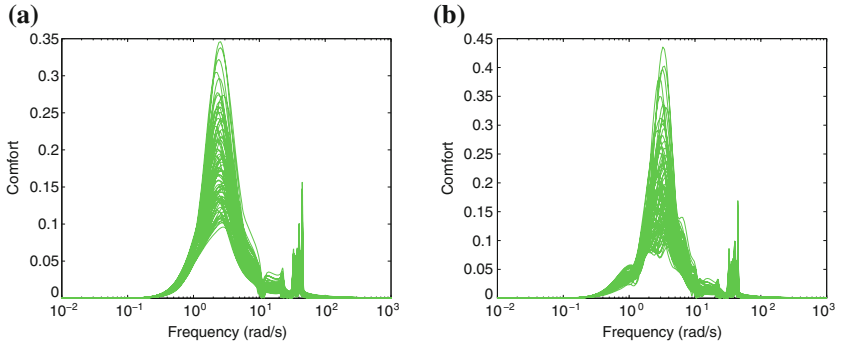

Fig. 6.23 Comfort cabin with vibration filters. **a** Transfer functions of comfort cabin without Youla parameter. **b** Transfer functions of comfort cabin with Youla parameter

norm is 20 %, that is, the comfort has been improved by 20 %. This global reduction can lead to a rise in some transfer functions as it is possible to see in Fig. 6.23b.

6.4.4.3 Feed-Forward

Let us remind handling qualities specifications that we have to satisfy with the feed-forward:

- A rise time of 3–6 s is expected with a very limited overshoot on Nz;
- A maximum overshoot of 30 % on q.

Figure 6.24 represents handling qualities when the feed-forward law is designed and implemented. We can notice that specifications are fully satisfied now since:

- The overshoot on Nz_{CG} is limited to 1 % for the worst case with a mean of 0.45 %;
- The rising time on Nz_{CG} is 5.95 s at 95 % of the wanted value or 4.95 s at 90 % of the wanted value for the worst case. Mean values are respectively of 4.0 and 3.4 s.
- The overshoot on q is limited to 21.5 % for the worst case with a mean value of 5.7 %.

Besides, this feed-forward law is multi-model, that is, a simple transfer function of order 4 allows to satisfy specifications for all fuel and flight cases. Of course, all these results on Nz_{CG} and q are obtained with a limited command effort since we can see in Fig. 6.25 that firstly, only elevators are used by the feed-forward law as shown by Fig. 6.9 and secondly that deflection and deflection velocity are widely inferior to constraints represented by saturations and rate limiters.

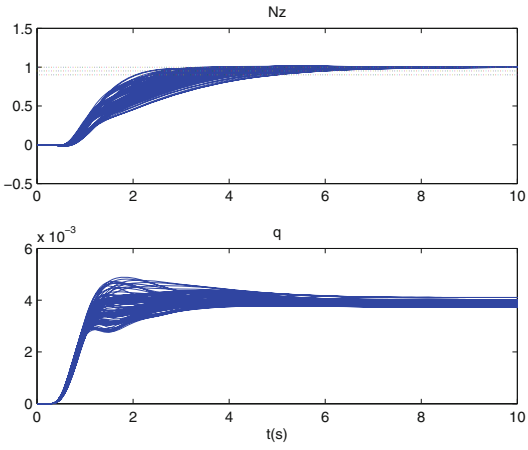

Fig. 6.24 Step response for Nz and q

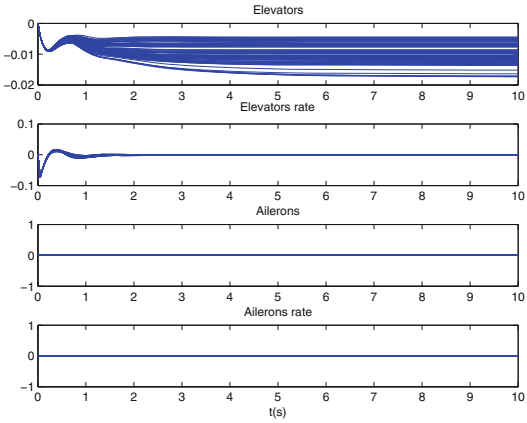

Fig. 6.25 Elevator and aileron responses to step

6.5 LPV Feedback Design

C. Westermayer, A. Schirrer and M. Kozek

The LPV feedback control design presented in this section has been developed in [88] for the longitudinal dynamics of the ACFA 2020 BWB aircraft. Over the design steps, including preliminary and optimized $\mathscr{H}_\infty$ LTI designs, as well as the overall LPV design, both, a linearization family of the ROMs (Sect. 4.1) and a parametrized model in an LFR obtained in Sect. 4.2 has been utilized for analysis, design, and validation tasks.

6.5.1 Methodology—LPV Design Using Parameter-Dependent Lyapunov Functions

In this section, the theoretical background for controller design using parameter-dependent Lyapunov functions is outlined. It follows the derivations in [93], where the information given by upper bounds on parameter variation rates are utilized for controller design of parameter-varying systems in order to obtain less conservative results. An outline of this methodology can also be found in [66], where also the connection to other scheduling approaches is provided. The methodology was already successfully applied to some practical applications [4, 61, 85, 89], which was decisive to use it also for the given problem formulation. More specifically, an LPV design toolbox developed by and kindly provided by Prof. Gary Balas [4], which is based on the methodology of parameter-dependent Lyapunov functions, is utilized for feedback control design of the aeroelastic BWB aircraft.

6.5.1.1 Stability and Performance Analysis of Parameter-Dependent Systems

Starting point for the following considerations is the description of the nonlinear plant

$$\begin{aligned} \dot{\boldsymbol{x}}(t) &= \boldsymbol{f}\left(\boldsymbol{x}(t), \boldsymbol{u}(t), \boldsymbol{d}(t), \boldsymbol{\rho}(t)\right) \\ \boldsymbol{y}(t) &= \boldsymbol{g}\left(\boldsymbol{x}(t), \boldsymbol{d}(t), \boldsymbol{\rho}(t)\right) \\ \boldsymbol{z}(t) &= \boldsymbol{h}\left(\boldsymbol{x}(t), \boldsymbol{u}(t), \boldsymbol{d}(t), \boldsymbol{\rho}(t)\right) \end{aligned} \tag{6.20}$$

where $\boldsymbol{x}(t)$ denotes the state vector, $\boldsymbol{u}$ is the control input, $\boldsymbol{d}$ is the disturbance input, $\boldsymbol{y}$ is the measurement output, $\boldsymbol{z}$ is the error output. Additionally, $\boldsymbol{\rho}(t)$ is the exogenous variable, or also denoted as the parameter vector. This vector is assumed piecewise continuously differentiable and is defined over the compact set $\mathscr{P} \subset \mathbb{R}^s$:

$$\boldsymbol{\rho}(t) = [\rho_1(t)\ \rho_2(t)\ \cdots\ \rho_s(t)]^{\mathrm{T}} \qquad \boldsymbol{\rho} \in \mathscr{P} \subset \mathbb{R}^s. \tag{6.21}$$

Moreover, the parameter vector rate of variation is bounded such that

$$|\dot{\rho}_i(t)| \leq \nu_i, \quad i = 1, \ldots, s. \tag{6.22}$$

holds. Linearization of (6.20) for a set of fixed parameters in an equilibrium point with respect to $\boldsymbol{x}$, $\boldsymbol{u}$ and $\boldsymbol{d}$ leads to a linear parameter-dependent description for the nonlinear plant

$$\begin{bmatrix} \dot{\boldsymbol{x}} \\ \boldsymbol{z} \\ \boldsymbol{y} \end{bmatrix} = \begin{bmatrix} \boldsymbol{A}(\boldsymbol{\rho}) & \boldsymbol{B}_1(\boldsymbol{\rho}) & \boldsymbol{B}_2(\boldsymbol{\rho}) \\ \boldsymbol{C}_1(\boldsymbol{\rho}) & \boldsymbol{D}_{11}(\boldsymbol{\rho}) & \boldsymbol{D}_{12}(\boldsymbol{\rho}) \\ \boldsymbol{C}_2(\boldsymbol{\rho}) & \boldsymbol{D}_{21}(\boldsymbol{\rho}) & \boldsymbol{D}_{22}(\boldsymbol{\rho}) \end{bmatrix} \begin{bmatrix} \boldsymbol{x} \\ \boldsymbol{d} \\ \boldsymbol{u} \end{bmatrix} \tag{6.23}$$

Utilizing the assumptions that $\boldsymbol{D}_{22}(\boldsymbol{\rho}) = \boldsymbol{0}$, $\boldsymbol{D}_{12}(\boldsymbol{\rho})$ has full column rank and $\boldsymbol{D}_{21}(\boldsymbol{\rho})$ full row rank for all $\boldsymbol{\rho} \in \mathscr{P}$, the open-loop system representation (6.23) can without loss of generality be transformed in a simplified form for synthesis:

$$\begin{bmatrix} \dot{\boldsymbol{x}} \\ \boldsymbol{z}_1 \\ \boldsymbol{z}_2 \\ \boldsymbol{y} \end{bmatrix} = \begin{bmatrix} \boldsymbol{A}(\boldsymbol{\rho}) & \boldsymbol{B}_{11}(\boldsymbol{\rho}) & \boldsymbol{B}_{12}(\boldsymbol{\rho}) & \boldsymbol{B}_2(\boldsymbol{\rho}) \\ \boldsymbol{C}_{11}(\boldsymbol{\rho}) & \boldsymbol{D}_{1111}(\boldsymbol{\rho}) & \boldsymbol{D}_{1112}(\boldsymbol{\rho}) & \boldsymbol{0} \\ \boldsymbol{C}_{12}(\boldsymbol{\rho}) & \boldsymbol{D}_{1121}(\boldsymbol{\rho}) & \boldsymbol{D}_{1122}(\boldsymbol{\rho}) & \mathrm{I}_{n_{z2}} \\ \boldsymbol{C}_2(\boldsymbol{\rho}) & \boldsymbol{0} & \mathrm{I}_{n_{d2}} & \boldsymbol{0} \end{bmatrix} \begin{bmatrix} \boldsymbol{x} \\ \boldsymbol{d}_1 \\ \boldsymbol{d}_2 \\ \boldsymbol{u} \end{bmatrix}. \tag{6.24}$$

The parameter vector $\boldsymbol{\rho}$ and its derivative $\dot{\boldsymbol{\rho}}$ are assumed to be measurable in real time and therefore can be used as an additional information for the controller. This leads to the system representation of the controller

$$\begin{bmatrix} \dot{\boldsymbol{x}}_{\mathrm{K}} \\ \boldsymbol{u} \end{bmatrix} = \begin{bmatrix} \boldsymbol{A}_{\mathrm{K}}(\boldsymbol{\rho}, \dot{\boldsymbol{\rho}}) & \boldsymbol{B}_{\mathrm{K}}(\boldsymbol{\rho}, \dot{\boldsymbol{\rho}}) \\ \boldsymbol{C}_{\mathrm{K}}(\boldsymbol{\rho}, \dot{\boldsymbol{\rho}}) & \boldsymbol{D}_{\mathrm{K}}(\boldsymbol{\rho}, \dot{\boldsymbol{\rho}}) \end{bmatrix} \begin{bmatrix} \boldsymbol{x}_{\mathrm{K}} \\ \boldsymbol{y} \end{bmatrix}, \tag{6.25}$$

which is also parameter-dependent. Using a lower (LFT), the closed loop can be built

$$\begin{bmatrix} \dot{\boldsymbol{x}}_{\mathrm{cl}} \\ \boldsymbol{z} \end{bmatrix} = \begin{bmatrix} \boldsymbol{A}_{\mathrm{cl}}(\boldsymbol{\rho}, \dot{\boldsymbol{\rho}}) & \boldsymbol{B}_{\mathrm{cl}}(\boldsymbol{\rho}, \dot{\boldsymbol{\rho}}) \\ \boldsymbol{C}_{\mathrm{cl}}(\boldsymbol{\rho}, \dot{\boldsymbol{\rho}}) & \boldsymbol{D}_{\mathrm{cl}}(\boldsymbol{\rho}, \dot{\boldsymbol{\rho}}) \end{bmatrix} \begin{bmatrix} \boldsymbol{x}_{\mathrm{cl}} \\ \boldsymbol{d} \end{bmatrix}, \tag{6.26}$$

with

$$\boldsymbol{A}_{\mathrm{cl}} = \begin{bmatrix} \boldsymbol{A}(\boldsymbol{\rho}) + \boldsymbol{B}_2(\boldsymbol{\rho})\boldsymbol{D}_{\mathrm{K}}(\boldsymbol{\rho}, \dot{\boldsymbol{\rho}})\boldsymbol{C}_2(\boldsymbol{\rho}) & \boldsymbol{B}_2(\boldsymbol{\rho})\boldsymbol{C}_{\mathrm{K}}(\boldsymbol{\rho}, \dot{\boldsymbol{\rho}}) \\ \boldsymbol{B}_{\mathrm{K}}(\boldsymbol{\rho}, \dot{\boldsymbol{\rho}})\boldsymbol{C}_2(\boldsymbol{\rho}) & \boldsymbol{A}_{\mathrm{K}}(\boldsymbol{\rho}, \dot{\boldsymbol{\rho}}) \end{bmatrix}, \tag{6.27}$$

$$\boldsymbol{B}_{\mathrm{cl}} = \begin{bmatrix} \boldsymbol{B}_{11}(\boldsymbol{\rho}) & \boldsymbol{B}_{12}(\boldsymbol{\rho}) + \boldsymbol{B}_2(\boldsymbol{\rho})\boldsymbol{D}_{\mathrm{K}}(\boldsymbol{\rho}, \dot{\boldsymbol{\rho}}) \\ \boldsymbol{0} & \boldsymbol{B}_{\mathrm{K}}(\boldsymbol{\rho}, \dot{\boldsymbol{\rho}}) \end{bmatrix}, \tag{6.28}$$

$$\boldsymbol{C}_{\mathrm{cl}} = \begin{bmatrix} \boldsymbol{C}_{11}(\boldsymbol{\rho}) & \boldsymbol{0} \\ \boldsymbol{C}_{12}(\boldsymbol{\rho}) + \boldsymbol{D}_{\mathrm{K}}(\boldsymbol{\rho}, \dot{\boldsymbol{\rho}})\boldsymbol{C}_2(\boldsymbol{\rho}) & \boldsymbol{C}_{\mathrm{K}}(\boldsymbol{\rho}, \dot{\boldsymbol{\rho}}) \end{bmatrix}, \tag{6.29}$$

$$\boldsymbol{D}_{\mathrm{cl}} = \begin{bmatrix} \boldsymbol{D}_{1111}(\boldsymbol{\rho}) & \boldsymbol{D}_{1112}(\boldsymbol{\rho}) \\ \boldsymbol{D}_{1121} & \boldsymbol{D}_{1122}(\boldsymbol{\rho})\boldsymbol{D}_{\mathrm{K}}(\boldsymbol{\rho}, \dot{\boldsymbol{\rho}}) \end{bmatrix}. \tag{6.30}$$

In order to test stability of the parameter-dependent systems such as (6.24) or (6.26), the Lyapunov stability test [40] can be used. However, this test is based on a quadratic, parameter-independent Lyapunov function

$$\mathbf{V}(\boldsymbol{x}) = \boldsymbol{x}^{\mathrm{T}}\mathbf{X}\boldsymbol{x}, \quad \mathbf{X} = \mathbf{X}^{\mathrm{T}} \tag{6.31}$$

and proves stability for arbitrarily fast changing parameters. Therefore, utilizing this analysis test as a basis for controller synthesis of parameter-varying systems leads to either conservative results or in terms of an LMI optimization even to infeasibility although a feasible result could exist. Instead of the quadratic Lyapunov function, a parameter-dependent Lyapunov function of the form

$$\mathbf{V}(\boldsymbol{x}, \boldsymbol{\rho}) = \boldsymbol{x}^{\mathrm{T}}\mathbf{X}(\boldsymbol{\rho})\boldsymbol{x}, \quad \mathbf{X}(\boldsymbol{\rho}) = \mathbf{X}^{\mathrm{T}}(\boldsymbol{\rho}) \tag{6.32}$$

can be introduced. Its time derivative is given by

$$\begin{aligned} \frac{\mathrm{d}}{\mathrm{d}t}\mathbf{V}(\boldsymbol{x}, \boldsymbol{\rho}) &= \dot{\boldsymbol{x}}^{\mathrm{T}}\mathbf{X}(\boldsymbol{\rho})\boldsymbol{x} + \boldsymbol{x}^{\mathrm{T}}\mathbf{X}(\boldsymbol{\rho})\dot{\boldsymbol{x}} + \frac{\mathrm{d}}{\mathrm{d}t}\mathbf{X}(\boldsymbol{\rho}) \\ &= \dot{\boldsymbol{x}}^{\mathrm{T}}\mathbf{X}(\boldsymbol{\rho})\boldsymbol{x} + \boldsymbol{x}^{\mathrm{T}}\mathbf{X}(\boldsymbol{\rho})\dot{\boldsymbol{x}} + \sum_{i=1}^{s}\left(\dot{\rho}_i \frac{\partial \mathbf{X}(\boldsymbol{\rho})}{\partial \rho_i}\right). \end{aligned} \tag{6.33}$$

Using this Lyapunov function, the stability test for parameter-dependent systems can be defined as follows.

Definition 6.1 (*Parameter-dependent stability* [93]) For a given compact parameter set $\boldsymbol{\rho} \in \mathscr{P} \subset \mathbb{R}^s$ and non-negative upper bounds of parameter variation rates $\{\nu_i\}_{i=1}^s$, consider a linear parameter-varying system

$$\dot{\boldsymbol{x}} = \boldsymbol{A}(\boldsymbol{\rho}, \dot{\boldsymbol{\rho}})\boldsymbol{x}, \quad \boldsymbol{x}(t_0) = \boldsymbol{x}_0, \tag{6.34}$$

which is called parametrically dependent stable if $\lim_{t\to\infty} \boldsymbol{x}(t) = 0$ for all $\boldsymbol{x}_0$. Using the parameter-dependent Lyapunov function (6.32), then $\boldsymbol{A}(\boldsymbol{\rho}, \dot{\boldsymbol{\rho}})$ is parametrically dependent stable over $\mathscr{P}$ if there exists a continuously differentiable function $\mathbf{X}(\boldsymbol{\rho})$: $\mathbb{R}^s \to \mathbb{S}^{n\times n}$, such that $\mathbf{X}(\boldsymbol{\rho}) = \mathbf{X}^{\mathrm{T}}(\boldsymbol{\rho}) > 0$ and

$$\boldsymbol{A}^{\mathrm{T}}(\boldsymbol{\rho}, \dot{\boldsymbol{\rho}})\mathbf{X}(\boldsymbol{\rho}) + \mathbf{X}(\boldsymbol{\rho})\boldsymbol{A}(\boldsymbol{\rho}, \dot{\boldsymbol{\rho}}) + \sum_{i=1}^{s} \left(\dot{\rho}_i \frac{\partial \mathbf{X}}{\partial \rho_i} \right) < 0 \tag{6.35}$$

for all $\boldsymbol{\rho} \in \mathscr{P}$ and $|\dot{\rho}_i| \leq \nu_i$ holds.

The proof is given in [93]. This parameter-dependent stability criterion incorporates bounds on the maximum parameter rates of variation and therefore is less conservative than the quadratic stability criterion. In order to obtain a similar stability and performance test as given by the classical Bounded Real Lemma [68] for LTI systems, this lemma has to be generalized for parameter-varying systems using the parameter-dependent Lyapunov function (6.32). An appropriate corresponding performance measure for LPV systems is given by the induced $\mathscr{L}_2$-norm which is defined for the performance transfer path as

$$||T_{zd}||_{i,2} = \sup_{\substack{\rho\in\mathscr{P} \\ |\dot{\rho}|\leq \boldsymbol{\nu}}} \sup_{\|\boldsymbol{d}\|_2 \neq 0} \frac{||\boldsymbol{z}||_2}{||\boldsymbol{d}||_2}. \tag{6.36}$$

This norm is equivalent to the largest amplification of the disturbance norm $||\boldsymbol{d}||_2$ to the error norm $||\boldsymbol{z}||_2$ for all parameter trajectories that satisfy $\boldsymbol{\rho} \in \mathscr{P}$ and hence represents a generalization of the $\mathscr{H}_\infty$-norm for LTI systems to LPV systems [93]. Consequently, the following theorem is derived which provides a sufficient condition for parameter-dependent stability and a prescribed bound for the induced $\mathscr{L}_2$-norm of a linear parameter-dependent system.

Theorem 6.1 [93] *For a given compact parameter set $\boldsymbol{\rho} \in \mathscr{P} \subset \mathbb{R}^s$ and non-negative upper magnitude bounds of parameter variation rates $\{\nu_i\}_{i=1}^s$, consider the linear parameter-varying system (6.26). If there exists a continuously differentiable matrix function $\mathbf{X}(\boldsymbol{\rho}) = \mathbf{X}^{\mathrm{T}}(\boldsymbol{\rho})$ such that*

$$\begin{aligned} &\mathbf{X}(\boldsymbol{\rho}) > 0, \\ &\begin{bmatrix} \boldsymbol{A}_{\mathrm{cl}}^{\mathrm{T}}(\boldsymbol{\rho}, \dot{\boldsymbol{\rho}})\mathbf{X}(\boldsymbol{\rho}) + \mathbf{X}(\boldsymbol{\rho})\boldsymbol{A}_{\mathrm{cl}}(\boldsymbol{\rho}, \dot{\boldsymbol{\rho}}) + \sum_{i=1}^{s} \left(\dot{\rho}_i \frac{\partial \mathbf{X}}{\partial \beta_i} \right) \mathbf{X}(\boldsymbol{\rho})\boldsymbol{B}_{\mathrm{cl}}(\boldsymbol{\rho}, \dot{\boldsymbol{\rho}}) \\ \boldsymbol{B}_{\mathrm{cl}}^{\mathrm{T}}(\boldsymbol{\rho}, \dot{\boldsymbol{\rho}})\mathbf{X}(\boldsymbol{\rho}) \qquad\qquad\qquad\qquad \mathbf{0} \end{bmatrix} \\ &\quad + \begin{bmatrix} \mathbf{0} & \mathbf{I} \\ \boldsymbol{C}_{\mathrm{cl}}(\boldsymbol{\rho}, \dot{\boldsymbol{\rho}}) & \boldsymbol{D}_{\mathrm{cl}}(\boldsymbol{\rho}, \dot{\boldsymbol{\rho}}) \end{bmatrix}^{\mathrm{T}} \begin{bmatrix} -\gamma^2\mathbf{I} & \mathbf{0} \\ \mathbf{0} & \mathbf{I} \end{bmatrix} \begin{bmatrix} \mathbf{0} & \mathbf{I} \\ \boldsymbol{C}_{\mathrm{cl}}(\boldsymbol{\rho}, \dot{\boldsymbol{\rho}}) & \boldsymbol{D}_{\mathrm{cl}}(\boldsymbol{\rho}, \dot{\boldsymbol{\rho}}) \end{bmatrix} < 0 \end{aligned} \tag{6.37}$$

holds for all $\boldsymbol{\rho} \in \mathscr{P}$ and $|\beta_i| \leq \nu_i$, then

1. *the function $\boldsymbol{A}_{cl}(\boldsymbol{\rho}, \dot{\boldsymbol{\rho}})$ is parametrically dependent stable over $\mathscr{P}$ and*
2. *the closed-loop performance transfer fulfills $||T_{zd}||_{i,2} < \gamma$.*

In Theorem 6.1 purposely the closed-loop system as given by (6.26) was considered, indicating that this theorem serves as a basis for controller design. Using the Schur complement, the LMI (6.37) can be also written in compact form as

$$\begin{bmatrix} \boldsymbol{A}_{\mathrm{cl}}^{\mathrm{T}}(\boldsymbol{\rho},\dot{\boldsymbol{\rho}})\mathbf{X}(\boldsymbol{\rho}) + \mathbf{X}(\boldsymbol{\rho})\boldsymbol{A}_{\mathrm{cl}}(\boldsymbol{\rho},\dot{\boldsymbol{\rho}}) + \sum_{i=1}^{s}\left(\beta_i \frac{\partial \mathbf{X}}{\partial \rho_i}\right) & \mathbf{X}(\rho)\boldsymbol{B}_{\mathrm{cl}}(\boldsymbol{\rho},\dot{\boldsymbol{\rho}}) & \gamma^{-1}\boldsymbol{C}_{\mathrm{cl}}{}^{\mathrm{T}}(\boldsymbol{\rho},\dot{\boldsymbol{\rho}}) \\ \boldsymbol{B}_{\mathrm{cl}}{}^{\mathrm{T}}(\boldsymbol{\rho},\dot{\boldsymbol{\rho}})\mathbf{X}(\rho) & -\mathrm{I} & \gamma^{-1}\boldsymbol{D}_{\mathrm{cl}}{}^{\mathrm{T}}(\boldsymbol{\rho},\dot{\boldsymbol{\rho}}) \\ \gamma^{-1}\boldsymbol{C}_{\mathrm{cl}}(\boldsymbol{\rho},\dot{\boldsymbol{\rho}}) & \gamma^{-1}\boldsymbol{D}_{\mathrm{cl}}(\boldsymbol{\rho},\dot{\boldsymbol{\rho}}) & -\mathrm{I} \end{bmatrix} < 0. \tag{6.38}$$

This LMI (6.38) can be used as starting point for the derivation of an adequate controller synthesis formulation. For the sake of brevity, the solvability condition for the parameter-dependent γ-performance problem is not presented here and the reader is kindly referred to [93].

The matrix functions $\mathbf{X}(\boldsymbol{\rho})$ represent an infinite-dimensional function space which has to be approximated by a finite-dimensional subspace using a set of continuously differentiable basis functions f_i:

$$\mathbf{X}(\boldsymbol{\rho}) := \sum_{i=1}^{N} f_i(\boldsymbol{\rho})\mathbf{X}_i. \tag{6.39}$$

A guideline for the selection of the basis functions is to choose functions that reflect the parameter dependency of the open-loop plant as close as possible [4, 61, 85]. Moreover, the synthesis LMIs have to be satisfied for all $\boldsymbol{\rho} \in \mathscr{P}$ which would require to solve an infinite number of LMIs. Hence, for computational tractability, the entire parameter space has to be approximated by a representative finite set of grid point models. It is important to keep in mind that both, the selection of basis functions and the gridding density strongly affects computational complexity, since the number of decision variables increases with a higher number of basis functions and grid point models.

6.5.1.2 Design Process

Based on the theoretical aspects outlined above and the information that needs to be gathered from nominal $\mathscr{H}_\infty$ grid point design as will be shown in Sect. 6.5.3, the LPV design process can be described by the following steps:

1. Derive the linearized models from the nonlinear system parameterized by the scheduling variables $\boldsymbol{\rho}$ (see Sect. 4.2). Thereby, attention should be paid on the model order to simplify the subsequent LMI optimization process.
2. Analyze the open-loop model with special emphasis on the effect of varying parameters on the system properties (see Sect. 5.1).

3. Select an appropriate $\mathscr{H}_\infty$ controller design architecture which addresses the required design specifications and define appropriate weighting functions (see Sect. 6.5.3.1).
4. Optimize LTI $\mathscr{H}_\infty$ controllers over the entire parameter space by adjusting the performance weighting functions (see Sect. 6.5.3.2). Preferably, this is done in an automatic way by defining a cost function based on relevant design specifications which have to be optimized (see Sect. 6.5.3.3).
5. Validate the LTI controllers on a representative validation model. If specifications are not satisfied, go back to step 3 and try a different design architecture or different frequency weighting functions.
6. Scale the determined performance weighting functions for each parameter grid point by corresponding obtained γ_{LTI} values in order to avoid over-emphasizing of some grid points in the LPV optimization. At the same time, the finally obtained γ_{LPV} value provides information about the performance degradation in comparison to the LTI design.
7. Select suitable basis functions according to the plant dynamics dependency on scheduling parameters [93], and determine a grid of fixed parameter settings representing the parameter space (see Sect. 6.5.4.1).
8. Define lower and upper bounds for the parameter variation rates representative for the considered application (see Sect. 6.5.4.2).
9. Run of LMI optimization using the linearized models, the design architecture, and the scaled performance weighting functions determined in the previous steps.
10. Split the entire parameter space into smaller subspaces, if the entire parameter space is too large for controller optimization in one step or strong discontinuities in a certain parameter region are present.

If more than one scheduling parameter has to be considered at once, it is to recommend that a priori designs for a single parameter are carried out to develop an understanding about the necessary density of the parameter grid and the effect of various basis functions. With the information gathered, a stepwise enlargement of the parameter space is preferable.

If the LMI optimization leads to a feasible solution, the following steps are necessary to obtain the final LPV control law:

1. Preparation of a fine gridding of linearized models such that several grid points in between the design grid points are available.
2. Linear interpolation of the performance weightings and the γ_{LTI} values between the design grid points.
3. Interconnection of the finely gridded linearized models with the corresponding interpolated and scaled performance weightings.
4. The LPV controller matrices for the fine gridding are obtained as presented in [93], where the system matrix $\mathbf{A}_{\mathrm{LTI}}$ depends on the parameter rate.
5. Optional removal of parameter rate dependency according to [66].

In order to obtain a control law representation which continuously depends on the parameter vector, the finely gridded controller matrices can be linearly interpolated element-wise as in [4].

6.5.2 Design Goals

In this feedback design, the feedback control goals as a subset of the goals listed in Sect. 5.2 are addressed. Especially, robust stabilization, pole placement, and rejection of turbulence or gust disturbances are focused on. Partially, the maneuverability is addressed to improve maneuver performance with the final feed-forward command shaping.

6.5.3 Preceding $\mathscr{H}_\infty$ Design Optimization

6.5.3.1 Design Model and Closed-Loop Interconnection Architecture

As described in Sect. 6.5.1.2, the overall complexity of the feedback control process demands a stepwise design procedure starting with nominal $\mathscr{H}_\infty$ designs. Using the results gathered during the open-loop analysis as presented in Sect. 5.1, an adequate control design architecture needs to be defined.

Initial preliminary designs have revealed that the architecture as proposed in Fig. 6.26 is suitable to successfully address the design goals as formulated in

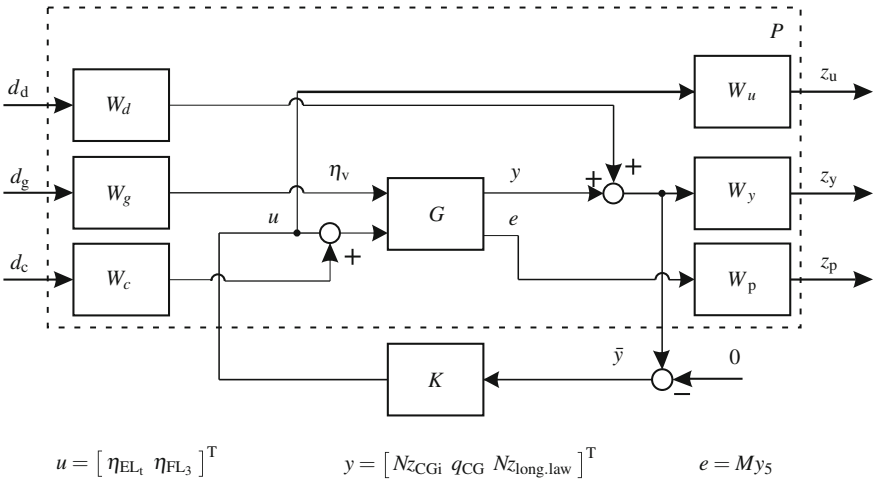

Fig. 6.26 Extended closed-loop interconnection structure

Sect. 6.5.2 in an highly efficient manner. In this architecture, $\mathbf{G}$ is the state-space model of the aircraft

$$\begin{bmatrix} \dot{\boldsymbol{x}}(t) \\ \boldsymbol{e}(t) \\ \boldsymbol{y}(t) \end{bmatrix} = \underbrace{\begin{bmatrix} \boldsymbol{A} & \boldsymbol{B}_1 & \boldsymbol{B}_2 \\ \boldsymbol{C}_1 & \boldsymbol{D}_{11} & \boldsymbol{D}_{12} \\ \boldsymbol{C}_2 & \boldsymbol{D}_{21} & \boldsymbol{D}_{22} \end{bmatrix}}_{\mathbf{G}} \begin{bmatrix} \boldsymbol{x}(t) \\ \boldsymbol{d}(t) \\ \boldsymbol{u}(t) \end{bmatrix}, \tag{6.40}$$

and $\mathbf{K}$ is the feedback controller to be designed. The corresponding state vector $\boldsymbol{x}$ of $\mathbf{G}$ is given by

$$\boldsymbol{x} = \left[u \; w \; \Theta \; q \; \xi_1 \; \dot{\xi}_1 \; \ldots \; \xi_s \; \dot{\xi}_s \; x_{l_1} \; \ldots \; x_{l_t} \right]^{\mathrm{T}}, \tag{6.41}$$

where the first four states represent the RB states body forward velocity u, body downward velocity w, pitch angle Θ and pitch rate q. Neglecting the states u and Θ in (6.41) results in the short-period mode approximation of the aircraft. Using this approximation prevents the $\mathscr{H}_\infty$ optimization algorithm from directly stabilizing the phugoid mode in favor of overall improved closed-loop performance. The states ξ_j and $\dot{\xi}_j$ $(j = 1, \ldots, s)$ are the modal deflections and modal deflection rates of aeroelastic modes, respectively, and x_{l_k} $(k = 1, \ldots, t)$ are the lag states. The number of flexible modes and lag states are different for validation and design models:

- Validation model $\mathbf{G}_{\mathrm{val}}$: $s = 19, \quad t = 14$
- Design model $\mathbf{G}_{\mathrm{des}}$: $s = 2, \quad t = 4$

The number of flexible modes in the design model is set to a comparatively low number due to the limited bandwidth of about 20 rad/s of the investigated control surfaces. However, within this range, the first two symmetrical flexible modes are located which are important in terms of structural loads and vibrations. Moreover, keeping only four lag states for the design turned out to have only marginal effect on the considered system dynamics.

The utilized control inputs $\boldsymbol{u}$ of $\mathbf{G}$ are the combined elevator $\eta_{\mathrm{EL_t}}$ and the fast actuating outer flap $\eta_{\mathrm{FL_3}}$. The first is the control surface most efficient for pitch motion control, while the latter is mainly used for aeroelastics control. In terms of aeroelastics control, the exogenous input η_{v} is a further important input to the system, representing the global vertical gust velocity input positioned at the CG.

The measurement signals available to the controller to fulfill control goals that are mainly related to the RB dynamics of the aircraft, are the vertical acceleration at CG, Nz_{CG}, and the pitch rate q_{CG}. Zero tracking error on Nz_{CG} is guaranteed by an approach as presented in [50], where the open loop is directly augmented by an integrator as indicated by the index i in Fig. 6.26. The q_{CG} output turned out to be an effective lever for tuning of the short-period mode damping. Initial designs also revealed that Nz_{CG} and q_{CG} feedback signals are able to significantly shift the unstable phugoid mode. For that reason, an additional V_{TAS} measurement signal was not directly included in the $\mathscr{H}_\infty$ design, but instead a static V_{TAS} outer feedback loop was added to further improve the phugoid mode. For aeroelastic control, the modal

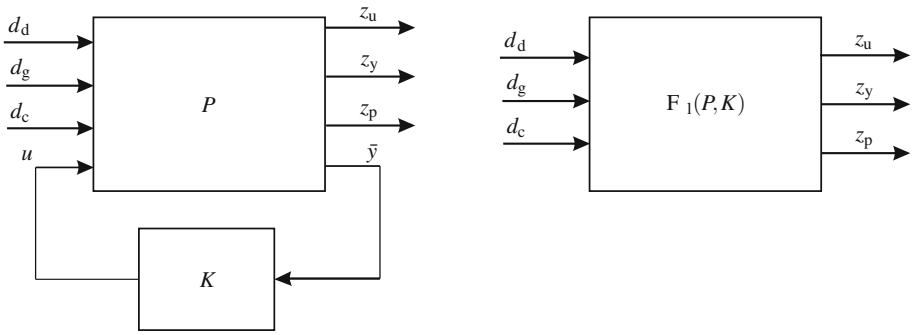

Fig. 6.27 Generalized closed-loop and lower LFT

wing bending signal $Nz_{\text{long.law}}$ is used to separate the vertical wing bending from the RB motion:

$$Nz_{\text{long.law}} = \left(\frac{\left(Nz_{\text{lw,k}} + Nz_{\text{rw,k}}\right)}{2} - Nz_{\text{CG}} \right), \tag{6.42}$$

The cut moment output My_5 serves as the only performance output during design and is selected to formulate performance specifications concerning load minimization in turbulence gust and maneuvers.

The design architecture in Fig. 6.26 represents a standard $\mathscr{H}_\infty$ mixed-sensitivity problem [76], with the corresponding generalized closed-loop representation as shown in Fig. 6.27. The main goal of the optimization is to minimize the cost function

$$\left\| \mathscr{F}_l(\mathbf{P}, \mathbf{K}) \right\|_\infty < \gamma, \tag{6.43}$$

where the transfer paths from the exogenous inputs $\boldsymbol{d}$ to the exogenous outputs $\boldsymbol{z}$ correspond to the single elements of the cost function matrix (6.43) and represent important performance paths of the closed loop. These are additionally weighted by suitable weighting functions $\mathbf{W}_i$ as indicated in Fig. 6.26 and represent the tuning knobs of the $\mathscr{H}_\infty$ mixed-sensitivity design. Therefore, a good understanding of the weighting functions and the actual closed-loop behavior is a prerequisite for a successful LPV design over a large parameter space. However, the choice of weighting function definition and the tuning process itself is extensive. Here, exemplarily the optimization with respect to limited control energy and the tuning of aeroelastic control is presented only.

6.5.3.2 Performance Weighting Function Definition

When trying to improve disturbance attenuation or tracking performance, it is of utmost importance to incorporate constraints concerning available control energy in a similar degree. In terms of a mixed-sensitivity problem, this can easily be ensured by including the control input $\boldsymbol{u}$ in the performance output vector [76]. Thereby, the function $\mathbf{KS}_\mathrm{o}$ appears in the cost function (6.43), where $\mathbf{S}_\mathrm{o} = (\mathbf{I} + \mathbf{GK})^{-1}$ is the output sensitivity function. In the low-frequency region, the singular value of $\mathbf{KS}_\mathrm{o}$ must be limited in order to avoid large control signals beyond saturation limits demanded by the controller $\mathbf{K}$. On the other hand, the bandwidth of control inputs must be constrained to avoid exceeding the corresponding rate limits. Since the output sensitivity function $\mathbf{S}_\mathrm{o}$ typically shows proportional behavior in the high-frequency region, the controller roll-off itself determines the roll-off of the closed-loop transfer function $\mathbf{KS}_\mathrm{o}$. Appropriate controller roll-off is obtained using a high-pass filter as performance weighting

$$\mathbf{W}_u = \begin{bmatrix} t_{u1}\frac{s+t_{u2}\cdot 1}{s+t_{u2}\cdot 100}, & 0 \\ 0 & t_{u3}\frac{s+t_{u4}\cdot 1}{s+t_{u4}\cdot 100}, \end{bmatrix}, \tag{6.44}$$

where t_{u1}, t_{u3} and t_{u2}, t_{u4} as the corresponding tuning factors to define the static gain (DC gain) and the corner frequency. For the control input $\eta_{\mathrm{EL_t}}$, the singular value plot of $\mathbf{KS}_\mathrm{o}$ for a nominal plant as well as exemplarily the inverse of the corresponding weighting function $\mathbf{W}_u^{-1}$ is shown in Fig. 6.28 (left).

As evident from that figure, the low-pass behavior of $\mathbf{W}_u^{-1}$ ensures the desired roll-off behavior of the closed loop. Increasing t_{u1} leads to both reduced bandwidth and reduced maximum control signals.

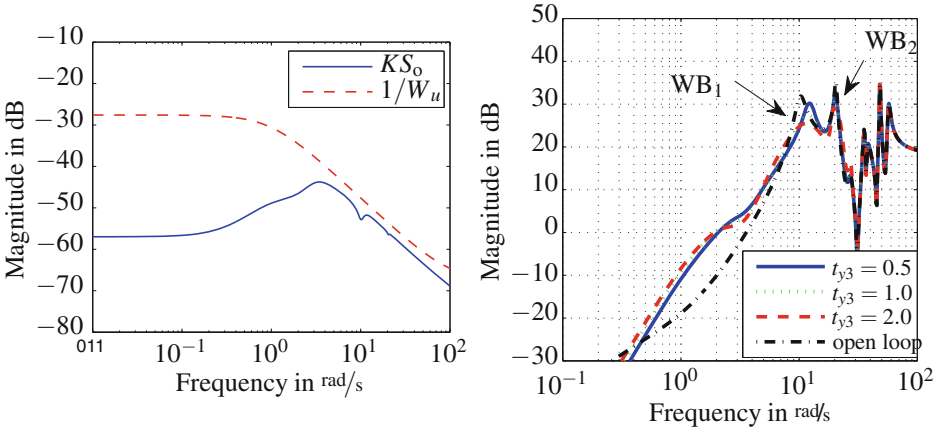

Fig. 6.28 $\mathbf{KS}_\mathrm{o}$ and $1/\mathbf{W}_u$ (*left*); effect on the singular value plot from η_v to $Nz_{\mathrm{long.law}}$ given by varying weighting factors t_{y3} (*right*)

The design requirements regarding reduction of structural loads and maximum vertical accelerations due to vertical gusts has proven to be difficult to achieve by frequency domain weighting without deterioration of the remaining specifications. Therefore, instead of minimization, an increase of these quantities is tried to be avoided by an appropriate selection of tuning weights. The damping of structural vibrations, on the contrary, is effectively addressed by shaping the output sensitivity function $\mathbf{S}_\mathrm{o}$ from the disturbance input at the output d_d to the measurement $Nz_{\mathrm{long.law}}$ and the disturbance transfer path from the vertical gust input η_v to $Nz_{\mathrm{long.law}}$. Therefore, the output disturbance weighting function matrix $\mathbf{W}_d$ and the output weighting function matrix $\mathbf{W}_y$,

$$\mathbf{W}_d = \begin{bmatrix} t_{d1} & 0 & 0 \\ 0 & t_{d2} & 0 \\ 0 & 0 & t_{d3} \end{bmatrix}, \quad \mathbf{W}_y = \begin{bmatrix} t_{y1} & 0 & 0 \\ 0 & t_{y2} & 0 \\ 0 & 0 & t_{y3} \end{bmatrix}, \tag{6.45}$$

at the corresponding position are both defined as a constant weight t_{d3} and t_{y3}. Constant weights have proven to be sufficient, due to the localized high gains of the flexible modes in the corresponding transfer functions. For controller tuning, the factors t_{d3} and t_{y3} are both increased until a slight shift of WB_1 respectively WB_2 is visible. Subsequently, t_{d3} is kept constant and t_{y3} is used for tuning of the structural damping of these two modes. This is presented in the singular value plot from η_v to $Nz_{\mathrm{long.law}}$ in Fig. 6.28 (right), where the results for a varying tuning factor t_{y3} are shown and $t_{y3} = 1$ represents a nominal setting. As can be seen, the damping is extremely sensitive on variations of t_{y3}. Considering WB_1, variations of the nominal setting $t_{y3} = 1$ by a factor of 2 respectively 0.5 leads to changes of the relative damping of around $\pm 50\,\%$. However, as expected not only modifications in the modes' damping ratios but also in their frequencies are apparent.

6.5.3.3 Robustness Against Fuel Uncertainty and Automated Tuning

In the previous section, aspects of nominal design were considered mainly. A subsequent step is to investigate the design optimization with respect to the robustness requirement for fuel-mass uncertainty. Basically, two different approaches were considered. First, a μ-synthesis design was investigated using an (LFT) model with a structured uncertainty block of order three. The high-accuracy and simultaneously low-order (LFT) model was provided by the project partner DLR (see Sect. 4.2). The obtained RP of the closed loop was compared to a second approach, a multi-model $\mathscr{H}_\infty$ approach. Despite the slightly deteriorated performance of the latter, the multi-model approach is chosen due to the reduced optimization complexity. Moreover, the closed-loop robustness against frequency and damping parameter uncertainty of the first two flexible modes was analyzed. Thereby, it turned out that the sensitivity to frequency uncertainty is higher than for damping parameter variations. However, basically a good robustness against these two uncertain parameters was revealed.

The manual tuning process is a time-consuming task for the large operating range to be considered. Therefore, an automatic tuning approach based on quality functions appropriate for performance specifications related to command response shaping and pole placement were defined. The resulting optimization function was minimized using the genetic algorithm of the optimization toolbox in MATLAB®. Using the automatic tuning approach, the weighting functions over the entire considered parameter space required for the subsequent LPV optimization were effectively determined, see [88].

6.5.4 Preliminary LPV Feedback Design

With the information gathered from the nominal $\mathscr{H}_\infty$ designs as described in the previous Sect. 6.5.3, the LPV controller optimization can be started. The LPV design is again divided into several sub-steps in order to improve the overall design process. First, several preliminary designs with single scheduling parameters are necessary in order to determine appropriate basis functions and an adequate gridding density, both with respect to closed-loop performance and computational complexity. Furthermore, closed-loop performance is investigated with respect to changing upper bounds for parameter rates. Finally, the LPV design optimization over the entire parameter space is presented and key items are discussed.

6.5.4.1 Basis Functions Selection and Gridding Density

For a successful LPV control optimization over a large parameter space, the effect of gridding density and the selection of basis function are essential aspects of the design. It is advantageous to consider always only one scheduling parameter for the parameter range of interest at the beginning. Exemplarily, the θ_{Ma} parameter is investigated in the following.

The solution matrices $\mathbf{X}(\boldsymbol{\rho})$, $\mathbf{Y}(\boldsymbol{\rho})$ of the LPV synthesis problem as outlined in Sect. 6.5.1.1 are matrix functions depending on the parameter vector $\boldsymbol{\rho}$. This leads to an infinite-dimensional optimization problem, so these matrices have to be approximated by a finite set of basis functions. Though much importance is attached to the choice of basis functions, a clear analytical procedure is not available. A general rule is to select the basis functions according to the parameter dependency of the open-loop system to be considered [93]. In previous works [4, 61, 85], where the LPV design methodology is applied to industrial applications, the matrix functions were defined by constant, linear and quadratic basis functions as

$$\mathbf{X}(\boldsymbol{\rho}) = \mathbf{X}_1 + \rho\mathbf{X}_2 + \rho^2\mathbf{X}_3,\ \mathbf{Y}(\boldsymbol{\rho}) = \mathbf{Y}_1 + \rho\mathbf{Y}_2 + \rho^2\mathbf{Y}_3. \tag{6.46}$$

For a larger subproblem in [85], only a constant and a linear term are utilized.

According to the results obtained from the open-loop analysis in Sect. 5.1, the parameter dependency of the short-period mode (SPM) on the θ_{Ma} parameter for the given parameter range $0.82 \leq \theta_{\mathrm{Ma}} \leq 0.88$ is nearly linear. Therefore, in a first step, constant and linear basis functions, $\mathbf{X}(\theta_{\mathrm{Ma}}) = \mathbf{X}_1 + \theta_{\mathrm{Ma}}\mathbf{X}_2$ and $\mathbf{Y}(\theta_{\mathrm{Ma}}) = \mathbf{Y}_1 + \theta_{\mathrm{Ma}}\mathbf{Y}_2$, were tested. Moreover, the parameter range was approximated by two finite parameter vectors $\mathbf{P}_{\theta_{\mathrm{Ma}},i}$ of different grid density:

$$\begin{aligned} \mathbf{P}_{\theta_{\mathrm{Ma}},1} &= [0.820, 0.832, 0.844, 0.856, 0.868, 0.880] \\ \mathbf{P}_{\theta_{\mathrm{Ma}},2} &= [0.820, 0.850, 0.880] \end{aligned} \tag{6.47}$$

The effect of the different gridding density on the controller is shown in Fig. 6.29, where a frequency magnitude response plot of the controller from Nz_{CG} to η_{EL_t} and the corresponding pole/zero map on a fine parameter validation grid $\mathbf{P}_{\theta_{\mathrm{Ma}},\mathrm{val}} = [0.820, 0.826, \ldots, 0.880]$ is presented. In the low-frequency region up until 5 rad/s, the magnitude curves lie denser for the finer gridding indicating the advantage given by the additional information of intermediate grid points. In the higher frequency region, on the contrary, the magnitude curves are similar, which can be explained by the restricted control authority of the elevator in this region. The pole/zero map shows a smooth characteristics for poles and zeros along the parameter variation for the fine gridding. For the rough gridding, however, sometimes poles and zeros form a cluster. The obtained γ values are $\gamma_{\mathrm{LPV,fine}} = 1.15$ and $\gamma_{\mathrm{LPV,rough}} = 1.25$ for

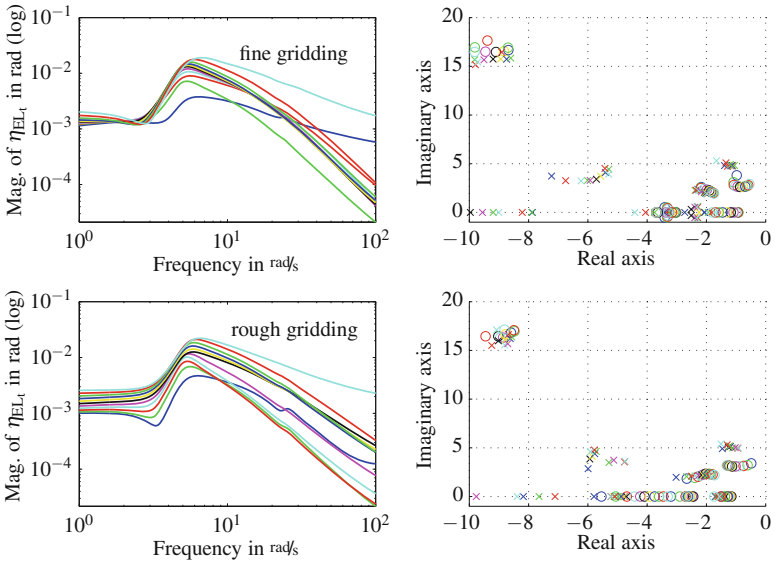

Fig. 6.29 Evaluation of LPV control law (depends on θ_{Ma} parameter only) dependency on different gridding density: frequency magnitude response plot from Nz_{CG} to η_{EL_t} (*left*) and corresponding pole zero map (*right*)

the fine and rough gridding, respectively, which emphasizes the advantage given by denser gridding.

A similar investigation was conducted with the matrix functions extended by the quadratic basis function terms $\theta_{\mathrm{Ma}}^2\mathbf{X}_3$ and $\theta_{\mathrm{Ma}}^2\mathbf{Y}_3$. Thereby, it turned out that the design is much more sensible to gridding density as in the linear case. Using a gridding according to $\mathbf{P}_{\theta_{\mathrm{Ma}},2}$ did not lead to useful results for intermediate points even though the design γ value $\gamma_{\mathrm{LPV,rough}} = 1.08$ was significantly lower than for the linear case. With $\mathbf{P}_{\theta_{\mathrm{Ma}},1}$, better results could be achieved, however, at few intermediate points the obtained control law was still defective. The same analysis was carried out for the θ_q parameter which lead to similar results.

6.5.4.2 Parameter Rate Setting

Additionally, the effect of the parameter rate setting on the optimization result was tested. Therefore, starting from a nominal setting of $|\dot{\theta}_{\mathrm{Ma}}| = 0.02\,1/\mathrm{s}$ and $|\dot{\theta}_{\mathrm{q}}| = 80\,\mathrm{Pa/s}$ was stepwise increased respectively decreased. Increasing the rate values leads to more conservative results indicated by an increased γ_{LPV} value and deteriorated overall performance. However, the basic characteristics of the control law and the resulting closed-loop behavior did not change.

6.5.5 Final LPV Design

With the information gathered from preliminary LPV designs, the parameter space was enlarged step-by-step. The $\mathscr{H}_\infty$ multi-model approach as shown in Sect. 6.5.3.3 has shown good RP results for an uncertain fuel-mass parameter and fixed θ_{Ma} and θ_q parameters. However, for varying θ_{Ma} and θ_q parameters, achieving robustness for the entire fuel-mass range turned out to be hard. Therefore, the fuel-mass parameter is included as additional parameter in the LPV design process, which is possible according to the design specifications, leading to a three-dimensional parameter space for the LMI optimization.

The associated high complexity of the optimization problem leads to either long computation times or to infeasibility of the problem. Therefore, the entire parameter space is split up into several subspaces. The rate of parameter variation is comparatively higher for θ_{Ma} and θ_q in comparison with θ_{fuel}, which makes robustness guarantees for those two parameters important. Moreover, the control law must provide sufficient robustness against fuel-mass uncertainty. Therefore, the fuel-mass parameter range was divided into three subspaces, where each subspace of θ_{fuel} is described by two grid points:

$$\mathbf{P}_{\theta_{\mathrm{fuel}},1} = [38, 63] \quad \mathbf{P}_{\theta_{\mathrm{fuel}},2} = [63, 91] \quad \mathbf{P}_{\theta_{\mathrm{fuel}},3} = [96, 100] \tag{6.48}$$

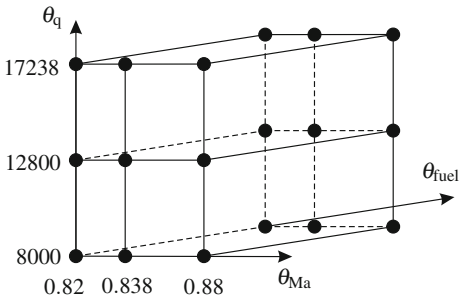

Fig. 6.30 Gridding of the parameter spaces used for design

Those fuel parameter regions which are not included in the optimization have to be robustly covered by the designed control laws $\mathbf{K}_{\theta_{\text{fuel}},i}(\theta_{\text{Ma}}, \theta_q, \theta_{\text{fuel}})$, $i = 1, 2, 3$. Especially in the low-fuel-mass region $\theta_{\text{fuel}} \leq 50\,\%$, it has been shown that $\mathbf{K}_{\theta_{\text{fuel}},1}$ fulfills the RP requirements to full extent. A continuously scheduled control law even for the fuel-mass parameter would have to be blended. However, blending of the control laws was not carried out in this work.

The parameter ranges of θ_{Ma} and θ_q parameter are described by three grid points, where the grid point vectors $\mathbf{P}_i$ are defined as

$$\mathbf{P}_{\theta_{\text{Ma}}} = [0.820, 0.838, 0.880] \quad \mathbf{P}_{\theta_q} = [8{,}000, 12{,}800, 17{,}238] \tag{6.49}$$

Therefore, each subspace is described through 18 grid point models as can be also seen in Fig. 6.30. The matrix functions $\mathbf{X}(\theta_{\text{Ma}}, \theta_q, \theta_{\text{fuel}})$, $\mathbf{Y}(\theta_{\text{Ma}}, \theta_q, \theta_{\text{fuel}})$ are approximated by constant and linear basis functions in θ_{Ma}, θ_q and θ_{fuel} according to:

$$\begin{aligned} \mathbf{X}(\theta_{\text{Ma}}, \theta_q, \theta_{\text{fuel}}) &= \mathbf{X}_1 + \theta_{\text{Ma}}\mathbf{X}_2 + \theta_q\mathbf{X}_3 + \theta_{\text{fuel}}\mathbf{X}_4 \\ \mathbf{Y}(\theta_{\text{Ma}}, \theta_q, \theta_{\text{fuel}}) &= \mathbf{Y}_1 + \theta_{\text{Ma}}\mathbf{Y}_2 + \theta_q\mathbf{Y}_3 + \theta_{\text{fuel}}\mathbf{Y}_4 \end{aligned} \tag{6.50}$$

The parameter rate of variation was set to $|\dot{\theta}_{\text{Ma}}| = 0.005\,1/\text{s}$, $|\dot{\theta}_{\text{q}}| = 240\,\text{Pa/s}$, and $|\dot{\theta}_{\text{fuel}}| = 0.1\,\%/\text{s}$. For the middle subspace represented by $\mathbf{K}_{\theta_{\text{fuel}2}}$, it has been shown that a reduction of the maximum rate for $\dot{\theta}_{\text{Ma}}$ and $\dot{\theta}_{\text{q}}$ to a quarter of the given value is necessary. Basically, this subspace has shown to be the computationally most demanding which could be relaxed through a further splitting.

With this optimization setup, one optimization run on an Intel® Core™ i7 PC takes between 6 and 17 h when using the LMI solver `mincx` from the Robust Control Toolbox of MATLAB® [5].

The obtained γ values are $\gamma_{\text{LPV},\theta_{\text{fuel}1}} = 6.9$, $\gamma_{\text{LPV},\theta_{\text{fuel}2}} = 4.9$ and $\gamma_{\text{LPV},\theta_{\text{fuel}3}} = 2.4$. Basically, an increase of the γ values in comparison with the LTI values is to be expected due to the given rate bounds and the approximation of the function space by the basis functions. However, these comparatively high values can be traced back to chosen high-gain performance weights at distinct parameter regions in order to enforce the desired performance specifications. Since the closed-loop validation

results are satisfactory as will be shown in Sect. 6.5.6, no further attempts were taken to reduce the obtained $\gamma_{\mathrm{LPV},\theta_{\mathrm{fuel}\,i}}$ values.

6.5.6 Validation of LPV Feedback Design

Basically, the validation models feature the following characteristics:

- The linear aircraft model comprises 19 aeroelastic modes and 14 lag states.
- The actuator dynamics is given by a θ_q-dependent nonlinear model.
- Control inputs are limited by nonlinear saturation and rate limits.
- Second-order Padé approximations for sensor delays.
- Second-order Butterworth filters for control measurement signals.

6.5.6.1 Closed-Loop Poles

One of the key performance requirements is the stabilization of the partly unstable SPM. Moreover, the open-loop poles must be shifted by the feedback law such that they provide satisfactory absolute and relative stability in the closed loop, except for the phugoid mode (PM), where an unstable real pole with a maximum real part of $\max(\mathrm{Re}(\lambda_{\mathrm{PM}})) < 0.1$ is still acceptable.

6.5.6.2 Command Response Behavior

For evaluation of the pitch response to a reference step command, essential flight mechanic data as well as the corresponding demanded control signals are presented in this section for the system response to a $r = 1.5\,\mathrm{g}$ reference command, where $g = 9.81\,\mathrm{m/s^2}$ is the gravity constant. Such large reference step represents a required validation maneuver leading to operation off the linearization point used for design.

The final command response behavior is available only if the feedback loop is connected with the feed-forward controller $\mathbf{K}_{\mathrm{ff}}$ where the results will be presented in a later section. The following results show the attainable tracking performance given by $\mathbf{K}_{\mathrm{fb}}$ alone and highlight the requirements which are not fully satisfied and therefore have to be improved by $\mathbf{K}_{\mathrm{ff}}$.

First, the command response is presented in Fig. 6.31 where the validation model does not contain the phugoid mode. Besides the outputs Nz_{CG}, q_{CG}, and Nz_{f}, the so-called C^* quantity is provided. This is a weighted linear combination of the vertical acceleration at the pilot position Nz_{f} and pitch rate q_{CG} and can be defined according to [13]:

$$C^* = Nz_{\mathrm{f}} + \dot{q}_{\mathrm{CG}} \frac{x_{\mathrm{CG}}}{\mathrm{g}} + q_{\mathrm{CG}} \frac{V_{\mathrm{m}}}{\mathrm{g}}, \tag{6.51}$$

where $V_m = 122\,\mathrm{m/s}$ [80] is an average velocity and x_{CG} is the distance from the CG to the pilot position.

Considering Nz_{CG}, which is the quantity to be tracked, in the upper left plot, it turns out that differences in the rise time as well as the maximum overshoot appear for the various parameter cases. Mainly the high Mach cases tend to yield slower command response. As it can be seen, it takes up to $t = 8\,\mathrm{s}$ for some systems to reach the desired end value. However, a large part fulfills the requirement of a rise time between 3 and 5 s with little overshoot.

The spread of the time characteristics of the pitch rate q_{CG} is, on the contrary, comparatively small over the parameter cases. The rise time is shorter than for Nz_{CG} and the maximum overshoot of 50 % is higher than the given requirement of 30 %. Considering the vertical acceleration at the cockpit position Nz_f, only moderate differences to the Nz_{CG} output appear. Also the C^* response is dominated by the shape of the Nz_f response.

The control signals demanded by the controller corresponding to Fig. 6.31 are provided in Fig. 6.32.

Comparing the obtained results with the actual limits for deflection and deflection rates

$$-30^\circ \le \eta_{EL_t} \le 15^\circ \quad -25^\circ \le \eta_{FL_{12}} \le 25^\circ \quad -25^\circ \le \eta_{FL_3} \le 25^\circ \tag{6.52}$$

$$-30^\circ/\mathrm{s} \le \dot{\eta}_{EL_t} \le 30^\circ/\mathrm{s} \; -40^\circ/\mathrm{s} \le \dot{\eta}_{FL_{12}} \le 40^\circ/\mathrm{s} \; -40^\circ/\mathrm{s} \le \dot{\eta}_{FL_3} \le 40^\circ/\mathrm{s} \tag{6.53}$$

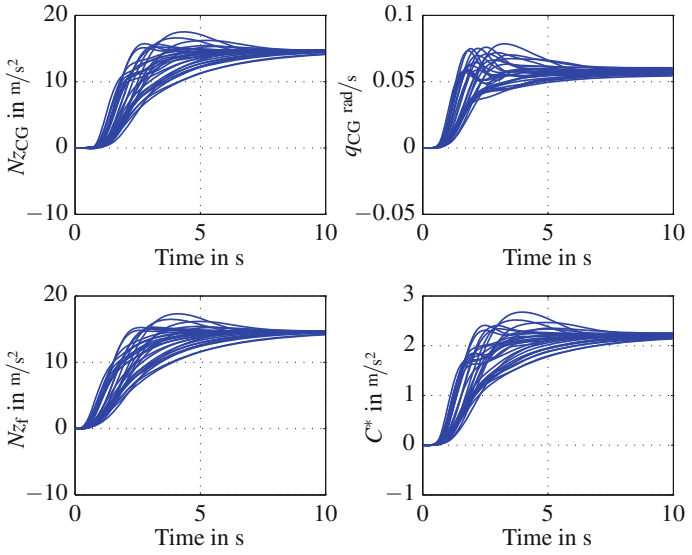

Fig. 6.31 Flight mechanic data time response to an $r = 1.5\,\mathrm{g}$ reference step command for representative validation models chosen from the parameter envelope

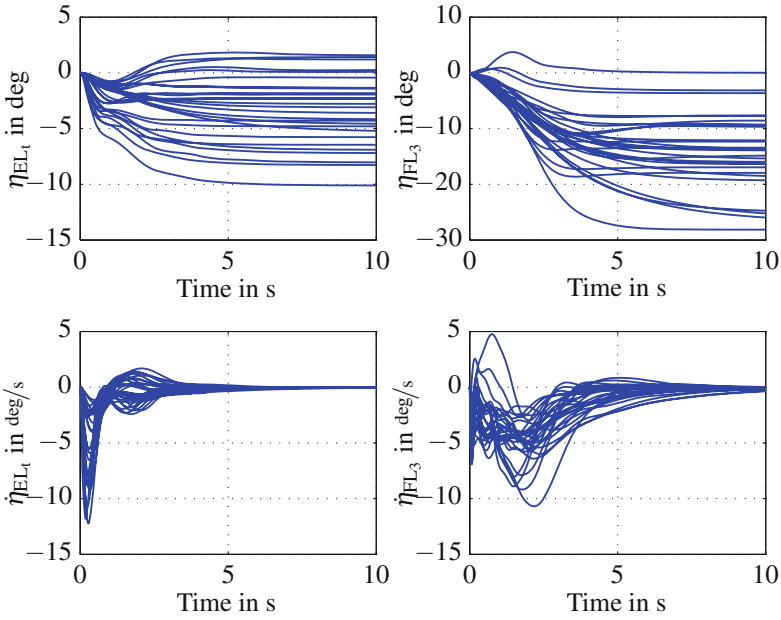

Fig. 6.32 Control input deflection and deflection rate time responses to an $r = 1.5$ g reference step command for representative validation models chosen from the parameter envelope

it turns out that the demanded values stay below the limits except for a few outliers. Especially the deflection rates are significantly lower for both actuators than the given limits, indicating that there is still enough potential left to make the pitch response faster. This was one of the main goals for feed-forward control law design, see Sect. 7.3.

6.5.7 Disturbance Response Behavior

In this section, the system disturbance response is validated using two representative $1 - \cos$ gusts input signals. In Fig. 6.33, the closed-loop and open-loop time responses for the longest considered gust length $L_{\text{gust}} = 152.4$ m are compared. This gust is the most important one in terms of maximum vertical accelerations and structural loads. The maximum acceleration respectively maximum load is given by their first peak in the time response. For a reduction of these peaks, it has been shown that feedback control requires high control effort in terms of maximum deflections and rates. Moreover, due to the corresponding necessary higher bandwidth, the robustness against high-frequency flexible modes deteriorates. Therefore, instead of minimizing of these maximum values, closed-loop acceleration and structural load levels equivalent to the open-loop level were aimed for.

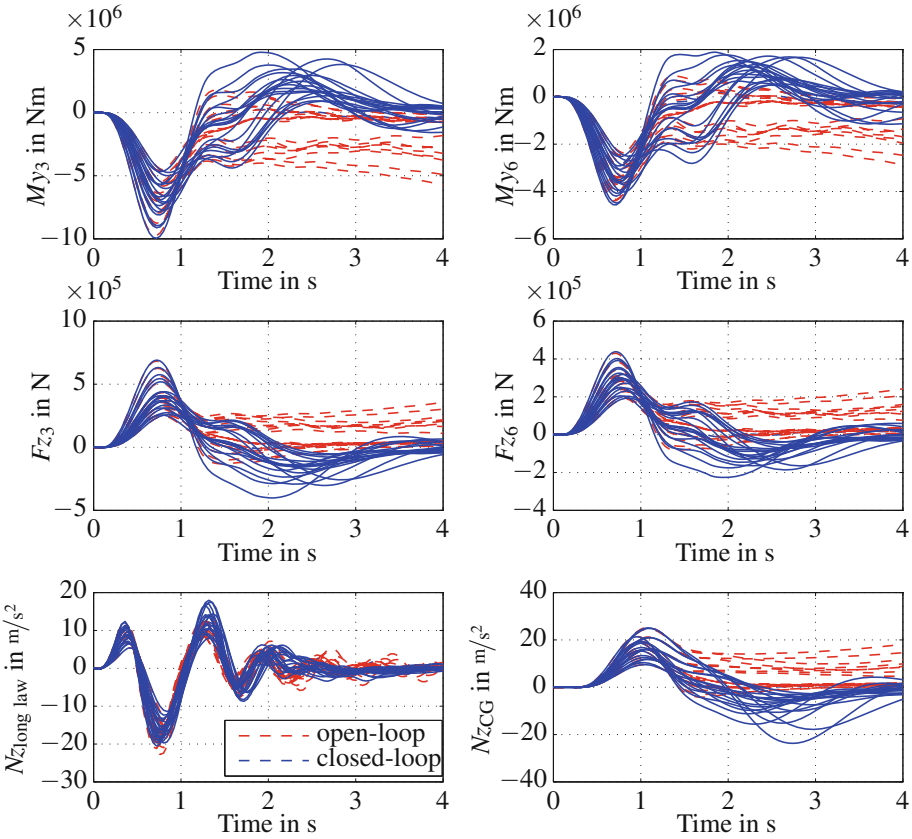

Fig. 6.33 Closed-loop and open-loop system time responses to gust number 10 for representative validation models chosen from the envelope

Considering the vertical acceleration Nz_{CG} response in the lower right plot of Fig. 6.33, it can be seen that the maximum closed-loop acceleration for various parameter cases is equivalent to those of the open-loop, represented by the dashed lines. For evaluation of structural loads, the load outputs My_3, My_6, Fz_3, and Fz_6 are exemplarily selected. Considering the responses it turns out that the design goal to avoid an increase of the load level is satisfied for both, the wing bending moment and the vertical force outputs.

The demanded control input time responses are provided in Fig. 6.34. During the design process, it has been shown that exceeding the rate limit of the elevator severely deteriorates the disturbance response and can even lead to instability. Therefore, special attention was paid to avoid too fast controller action of this control flap by appropriate frequency weighting. As can be seen in this figure, the maximum rate value for the elevator is $|\dot{\eta}_{EL_t}| = 28°/s$ and for the majority of cases $|\dot{\eta}_{EL_t}| < 20°/s$

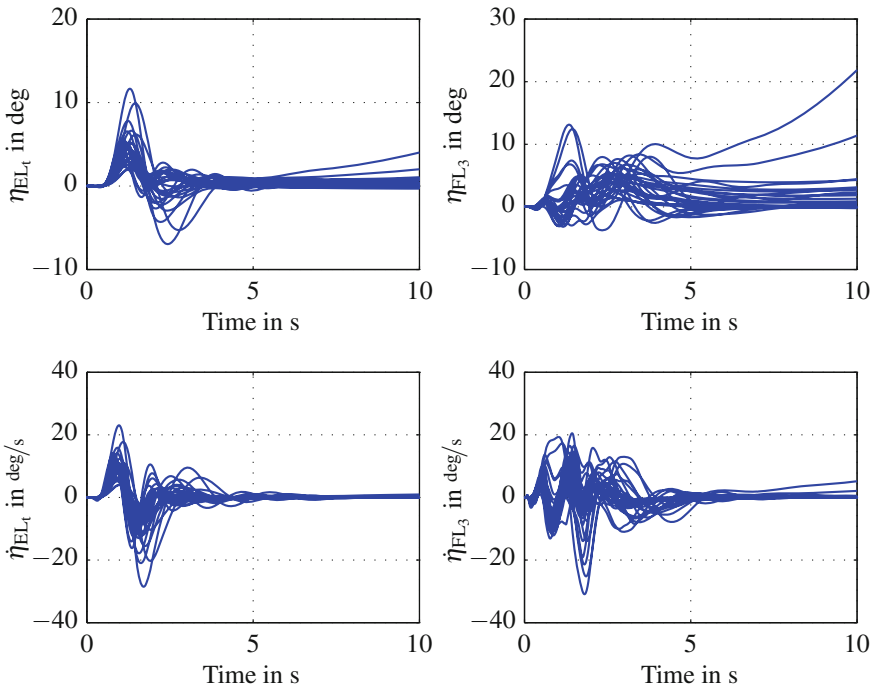

Fig. 6.34 Control input deflection and deflection rate time response to gust number 10 for representative validation models chosen from the envelope

holds, while $|\dot{\eta}_{FL_3}| < 29°/s$ holds. The maximum deflections $|\eta_{EL_t}| \leq 12°$, $|\eta_{FL_3}| \leq 13°$ also stay well within the limits.

Finally, the performance of aeroelastic damping is evaluated in the frequency domain. In Fig. 6.35, an open-loop/closed-loop comparison of the singular value plots is presented for several load outputs as well as Nz_{CG} and $Nz_{long.law}$ measurements. As can be seen from these plots, the damping of WB_1 is significantly increased and its magnitude significantly reduced for all considered outputs. The damping of WB_2, on the contrary, is hardly changed. No spillover effects arise for the modes not included in the design due to sufficient roll-off of the control law. There possibly exists some potential to further increase the control law bandwidth which can also have a positive effect on the damping performance for WB_2. This could be investigated in a subsequent design iteration step.

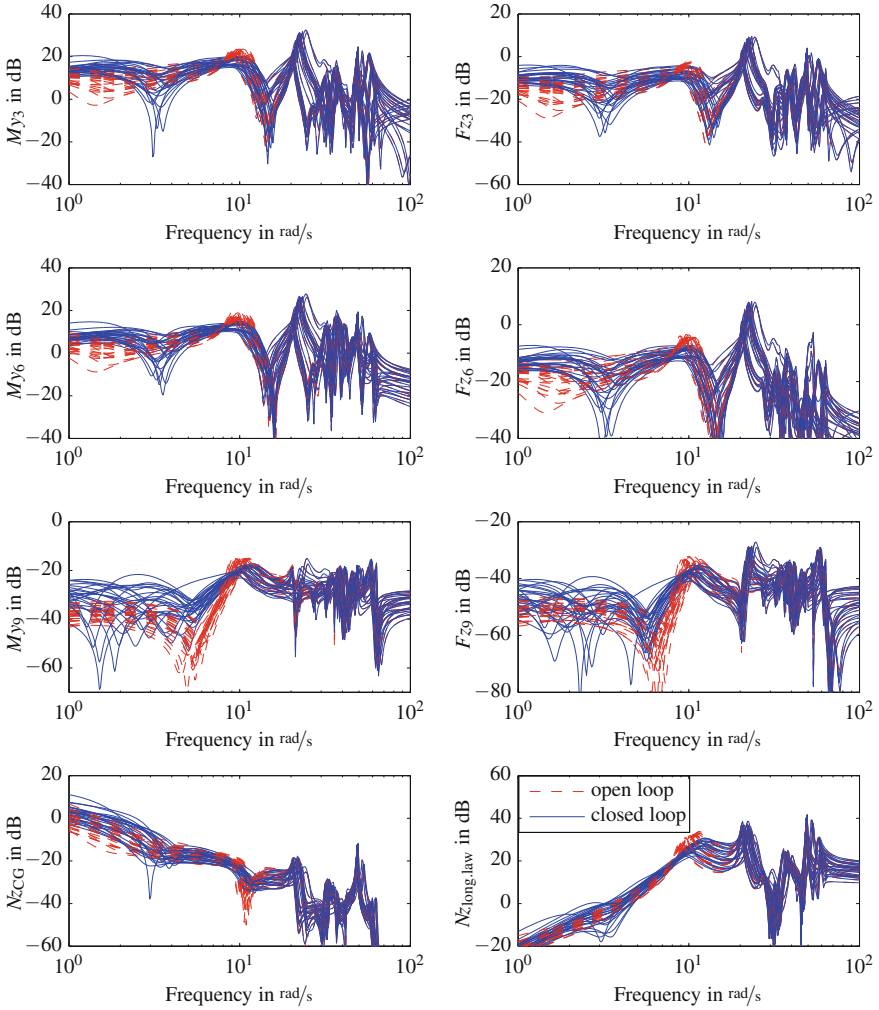

Fig. 6.35 Evaluation of aeroelastic control performance based on singular value analysis plots for several representative outputs

6.6 Low-Order Control Law Design

M. Hromčík and T. Haniš

6.6.1 Lateral $\mathscr{H}_\infty$-Optimal Control Law

Two different design approaches for design of lateral control augmentation system (CAS) for large BWB aircraft with flexible structure are elaborated and assessed in

this section. The most challenging design issues are related to coupling of rigid-body (RB) mechanics and flexible dynamics. First, a classical approach is employed giving rise to separate flight dynamics controller ($\mathscr{H}_2$-optimal, with sufficient roll-off at higher frequencies to avoid spillover) and an active damper for most prominent lateral flexible modes on top of that (mixed-sensitivity $\mathscr{H}_\infty$ design). This approach proves successful and has obvious advantages related to the design process complexity and to implementation/verification/testing. On the other hand, there is always a risk of potentially significant performance loss compared to a fully integrated design. For this reason, a fully integrated design is also presented in the form of a fixed-order multi-input multi-output (MIMO) $\mathscr{H}_\infty$-optimal flight control system (FCS) controller, obtained by means of direct non-convex non-smooth optimization using the dedicated software package HIFOO. Performance of both approaches is discussed. This design is carried out for the lateral motion of the NACRE BWB 750-passenger aircraft predesign model.

6.6.1.1 Introduction

Large lightweight aircraft structures and novel concepts, such as the BWB aircraft configurations, typically feature low-frequency structural vibrations modes, and their coupling with the flight mechanics modes may occur. Combined with significant dependency of the aircraft dynamics on flight parameters (Mach number / altitude / passengers / fuel volume and its distribution), severe flight control laws design challenges are to be expected.

Traditional methods for flight control design typically use nested single-input single-output (SISO) control loops and strongly structured control architectures [79]. These methods are based on detailed aircraft system analysis and exploit paths with weak coupling to obtain good results for conventional flight control design. However, multivariate methods, such as optimal control and particularly robust control design methods, are state-of-the-art for more complex flight control designs nowadays, especially useful for coupled and/or uncertain system dynamics. Two large groups of control design methodologies are optimal control design methods (for example, LQG control and the Kalman estimator [52]), as well as robust control design methods (see [76, 95] for fundamentals, or [7] for an aerospace-specific overview).

Two different approaches to lateral MIMO feedback CAS for NACRE BWB aircraft are presented in the following sections. They are namely a robust MIMO $\mathscr{H}_2/\mathscr{H}_\infty$ mixed-sensitivity controller and a low-order robust MIMO $\mathscr{H}_\infty$-optimal controller designed by direct fixed-order control design techniques. All controllers are designed to guarantee the desired closed-loop RB response (namely rise time and no-overshoot behavior to the reference change of the bank angle set point, attenuation of side-slip disturbance, and required damping ratio of the DR mode), and to dampen the first two anti-symmetric wing bending flexible modes. Performance and robustness of all controllers is demonstrated by means of MATLAB/Simulink® simulations, and their advantages and drawbacks are discussed.

6.6.1.2 BWB Aircraft Lateral Mathematical Model

The mathematical model of the BWB aircraft used for control law design consists of the flight mechanics model combined with the models of actuators and sensors. Actuator models are considered as second-order linear models augmented by saturations and rate limiters. Sensors are modeled as second-order Butterworth filters with time delays approximated by second-order Padé approximations. The mathematical model of the aircraft consists of the RB description (modeled as a 12th-order linear system separated into longitudinal and lateral dynamics), flexible modes (for design purposes just four modes are considered, depicted by an eighth-order linear model) and lag states. The overall model used for control law design is of order 52.

6.6.1.3 $\mathscr{H}_2/\mathscr{H}_\infty$ Mixed-Sensitivity Controller

A two-stage control law is devised—a separate CAS taking care of the flight dynamics (robust $\mathscr{H}_2$-optimal roll autopilot, with roll-off at higher frequencies), and an active damper for selected flexible modes ($\mathscr{H}_\infty$-optimal mixed-sensitivity controller tuned to first two anti-symmetric wing bending modes). Such an arrangement has obvious advantages—regarding tuning (both parts are designed/tuned independently), future flight testing (the active damper can be tested after the roll autopilot is implemented and approved, and it can be turned on/off at any time while keeping the aircraft well-controlled), safety (loss of the damper's functionality, for example, due to sensors failure, does not take the airplane out of control). The drawback is the potential reduction of performance compared to a fully integrated design where both flight dynamics and vibrational issues are handled by a single large MIMO controller.

Design Method

The lateral CAS (roll autopilot) is designed by $\mathscr{H}_2$ norm minimization of the generalized plant, encompassing the lateral RB dynamics itself (four states/outputs), two integrators (to ensure perfect steady-state tracking of a roll angle set point command and perfect steady-state attenuation of a side-slip disturbance), and two low-pass filters (for the required roll-off at higher frequencies—so that the flexible modes are left untouched and not excited by the controller). As all the RB states are measured, no observer needs to be implemented in fact and the resulting order of this CAS can be kept quite small (six states). Resulting controller features RS/RP for all considered mass cases (three passengers and five fuel cases).

On top of that, a robust MIMO controller is built by minimization of the $\mathscr{H}_\infty$ norm of the frequency-weighted mixed-sensitivity function. The wings' modal anti-symmetric sensor and anti-symmetric flaps make up the I/O groups. Loosely speaking, the closed-loop sensitivity function is kept small at selected frequency regions (in our case covering the wings' anti-symmetric modes) to assure for good performance (disturbance attenuation), while the complementary sensitivity function is kept small everywhere else (to ensure robustness—the design model becomes invalid outside the selected frequency region). A simple design model of eighth order was constructed

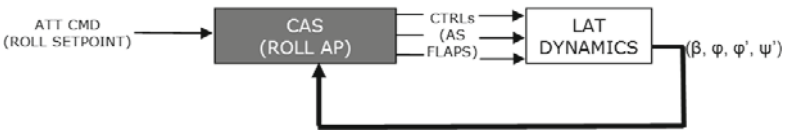

Fig. 6.36 Control augmentation system for $\mathscr{H}_2$ controller design. Anti-symmetrically operated wings ailerons are considered as control surfaces

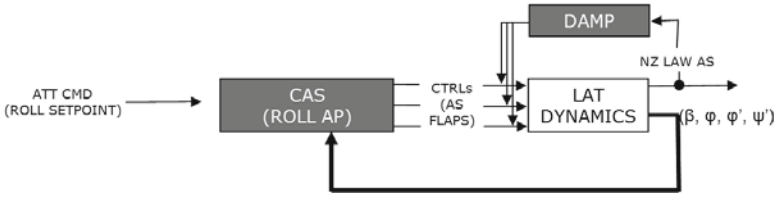

Fig. 6.37 Control augmentation system for $\mathscr{H}_2/\mathscr{H}_\infty$ controller design. Anti-symmetrically operated wings ailerons are considered as control surfaces

(modeling accurately the two modes and close region in the I/O channels). Two resonant weighting filters of second order are tuned to the frequencies and dampings of the anti-symmetric wing bending modes of a selected representative case for this purpose. The resulting $\mathscr{H}_\infty$ controller has 20 states.

The resulting damper (and also the overall CAS/damper combination) provides RS for all mass cases, significant improvement regarding damping of structural vibrations for most mass cases (more than 5 dB attenuation), and no effect on vibration damping for the remaining cases. These findings and the overall performance of the designed controller and its respective parts are visualized in Figs. 6.36 and 6.37.

$\mathscr{H}_2/\mathscr{H}_\infty$ Control Results

Brief assessment of the controller performance is given in the text above (regarding robustness and performance). A set of selected characteristics is now given to document these findings.

Note that very good performance is achieved for those cases that do not vary much in the frequency of the targeted modes (Fig. 6.38 left). However, even for the other cases (Fig. 6.38 right), some performance improvement is achieved, and RS is assured (Figs. 6.39, 6.40, and 6.41).

Required response to bank angle set point is achieved. Note marginal improvement of the response when the damping system is connected (though it was not intended to influence the flight dynamics in fact). As stated above, the flight dynamics part contains integrated yaw damper and side-slip compensator. Gain and phase margins for the complete designed controller have been evaluated. RS of the closed loop for all mass cases is achieved. For simultaneous, independent, worst-case variations in the individual channels the gain margin ranges from 1.9 to 3.7 dB, and the phase margin ranges from 12 to 23°, depending on the mass case.

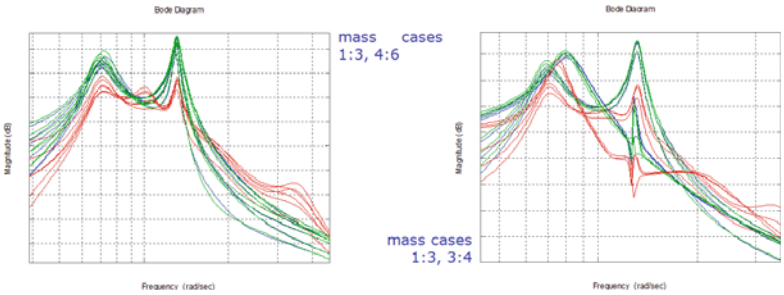

Fig. 6.38 Wing bending modes attenuation. Open loop (*green*), $\mathscr{H}_2$ control (*blue*), and $\mathscr{H}_2/\mathscr{H}_\infty$ control (*red*)

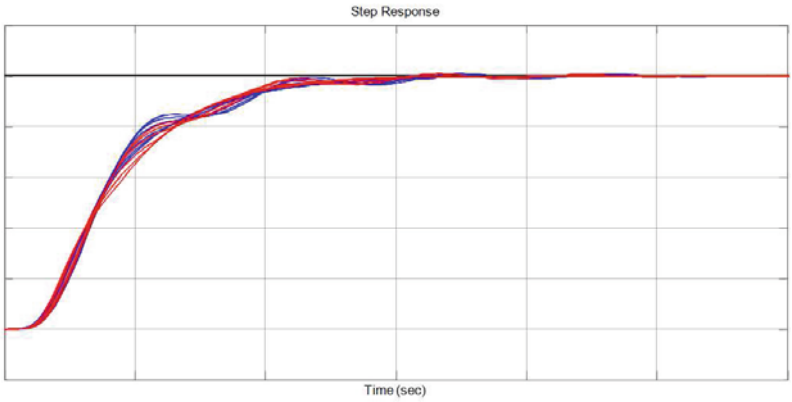

Fig. 6.39 Roll reference tracking. $\mathscr{H}_2$ control (*blue*) and $\mathscr{H}_2/\mathscr{H}_\infty$ control (*red*)

6.6.2 Non-convex Non-smooth Optimization

In recent years, great progress has been made in the challenging area of non-convex non-smooth optimization solvers. In contrast to more traditional setups, such problems are highly non-convex and no differentials or Jacobians can be used to navigate the search for even a local optimum. The solvers rely on a Broyden–Fletcher–Goldfarb–Shanno (BFGS) variable metric (quasi-Newton) method [16, 17, 51], or non-smooth modifications of Virginia Torczon's multidirectional search (MDS) [2, 81, 82].

Related numerical software has been soon delivered in the form of freeware and commercial package like Hybrid Algorithm for Non-Smooth Optimization (HANSO) based on the BFGS method.

As people from the systems and control community quickly realized, such algorithms and tools can be successfully applied to resolve some control design challenges that are otherwise almost untractable for real-life-size data. Didier Henrion and Mike Overton seem to get furthest, proposing a new methodology for direct design of

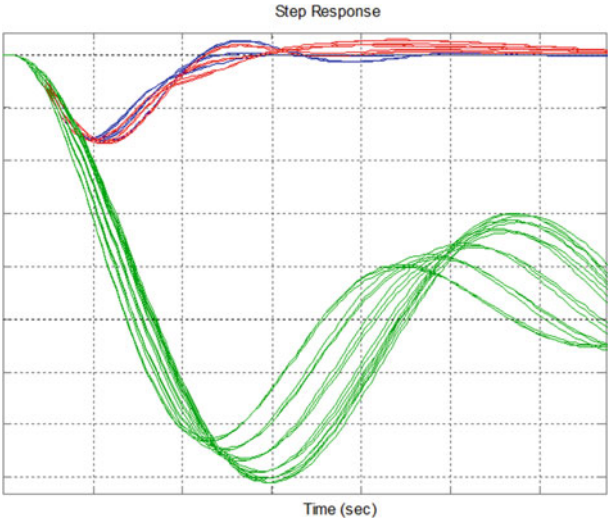

Fig. 6.40 Side-slip disturbance rejection. Open loop (*green*), $\mathscr{H}_2$ control (*blue*), and $\mathscr{H}_2/\mathscr{H}_\infty$ control (*red*)

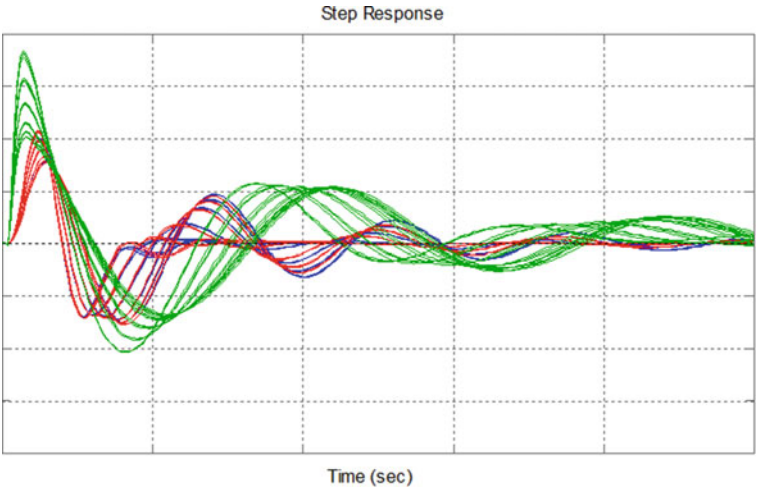

Fig. 6.41 Yaw rate damper. Open loop (*green*), $\mathscr{H}_2$ control (*blue*) and $\mathscr{H}_2/\mathscr{H}_\infty$ control (*red*)

low-order $\mathscr{H}_\infty$-optimal controllers in the 2000s [3, 15, 38, 39, 59], and delivering a related freeware package HIFOO.

The HIFOO package has already attracted attention of controls designers in the miscellaneous field [22, 25, 47, 63, 65, 87]. Regarding flight controls design, the first attempt was made in master thesis [59], where the applicability of the package

was approved by a means of a textbook example of a wing-leveler controller for an F-16 aircraft.

In this section, this approach and software will be employed to design, at one-shot, a robust, full-featured, $\mathscr{H}_\infty$-optimal longitudinal control law for a BWB highly flexible near-future airliner concept, following the recommended and industry-approved structure for this CAS. Performance of the result is assessed by means of high-fidelity simulations and classical, industry-standard robustness analysis results.

6.6.3 Direct Approach to Fixed-Order $\mathscr{H}_\infty$-Optimal Control Design

For reader's reference, the basic principles of the underlying algorithms used for direct $\mathscr{H}_\infty$ fixed-order control design are summarized in brief in this section, adopted from [38]. Interested readers are advised to consult the original paper for a more detailed and rigorous treatment.

The aim of the HIFOO algorithm is to deliver a stabilizing $\mathscr{H}_\infty$-optimal controller for given n LTI systems. The criterion for $\mathscr{H}_\infty$ optimization is expressed by the generalized plant setup. The algorithm has two phases. In each phase, the main workhorse is the BFGS optimization algorithm, which is surprisingly effective for non-convex, non-smooth optimization. The user can provide an initial guess for the desired controller; if this is not provided, HIFOO generates randomly generated initial controllers, and even when an initial guess is provided, HIFOO generates some additional randomly generated initial controllers in case they provide better results. The first phase is stabilization: BFGS is used to minimize the maximum of the spectral abscissa of the closed-loop plants. This process terminates as soon as a controller is found that stabilizes these plants, thus providing a starting point for which the objective function for the second phase is finite. The second phase is optimization: BFGS is used to look for a local minimizer of the controllers found in the first phase. The HIFOO control design method searches for locally optimal solutions of a non-smooth optimization problem that is built to incorporate minimization objectives and constraints for multiple plants. The optimization problem is introduced as a set of augmented plants, see Fig. 6.42, commonly used in robust control approaches. First, the controller order is fixed at the start, allowing for low-order controller design. Second, Lyapunov or lifting variables are introduced to deal with the conflicting specifications. The resulting optimization problem is formulated on the controller coefficients only, resulting in a typically small-dimensional non-smooth non-convex optimization problem that does not require the solution of large convex sub-problems, relieving the computational burden typical for Lyapunov LMI techniques. An algorithm that searches only for local minimization is used for the sake of computational time. While no theoretical guarantee can be given on the result's quality, in practice it often yields surprisingly efficient control laws.

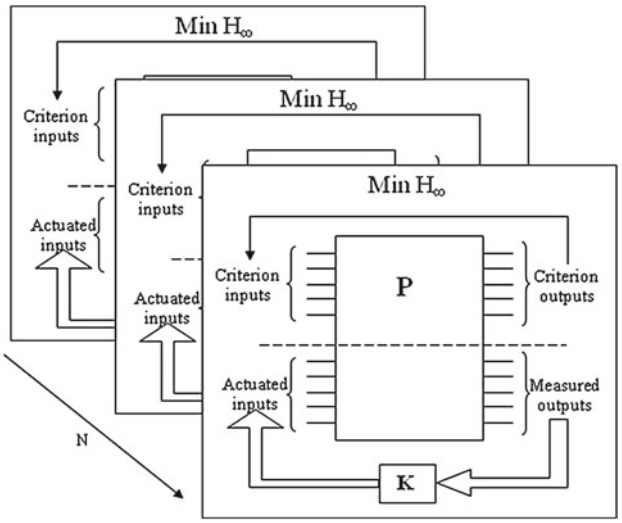

Fig. 6.42 $\mathscr{H}_\infty$ fixed-order optimization setup

6.6.3.1 Lateral Fixed-Order $\mathscr{H}_\infty$-Optimal MIMO Robust Controller

Similar as in the previous section, the two different control goals are targeted, but this time by one integrated controller. One job of the control law is to provide autopilot functionality. The autopilot consists of a stability augmentation system (SAS) (a DR mode damper) and a CAS (roll and side-slip angle reference tracking). Other roles of the control law are related to vibrations and loads attenuation.

The lateral integrated CAS was designed as a 2DoF architecture using the fixed-order optimization approach to keep control law order low. The resulting, extremely simple controller (in this case, just third-order control law was used) was calculated using the HIFOO toolbox. The overall lateral CAS consists of a RB autopilot (roll and side-slip tracker with DR mode damper) and an active feedback damper for structural modes. The lateral CAS setup can be seen from Fig. 6.43. Two reference signals are used as inputs into the feed-forward part of the controller (roll and side-slip setpoints). The side-slip reference signal is usually set to zero, and then the CAS provides coordinated turn functionality.

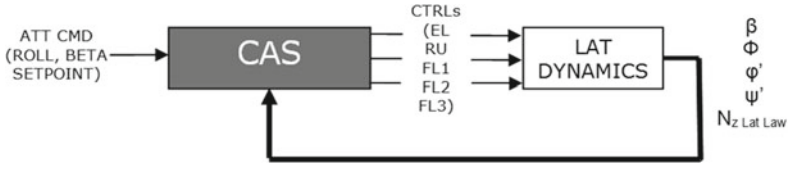

Fig. 6.43 Control augmentation system for HIFOO

The control surfaces used by the CAS are all ailerons (anti-symmetrically actuated FL1–FL3), rudders (RU) and elevators (symmetrically actuated EL). Measured signals are lateral RB variables at CG (side-slip angle, roll angle, roll rate and yaw rate), for structural modes control we have selected a lateral wing bending acceleration modal sensor in an anti-symmetrical setup. The resulting control law (autopilot and structural modes controller) provides RS as well as RP for all 18 cruise condition cases (six fuel and three passenger cases).

6.6.3.2 HIFOO Control Results

The achieved improvement of damping of the first and second wing bending modes can be seen from Fig. 6.44. Simultaneously, the DC gain is preserved for all cases. RP can be approved by the bank angle reference signal tracking response plotted in Fig. 6.45 (left). Responses for a sequence of two steps are shown and one can see sufficiently fast response with acceptably small overshoot.

Side-slip disturbance attenuation functionality is investigated in Fig. 6.46 (left). One can see complete vanishing of side wing influence in a few second and without inducing oscillation for major part of cases. DR mode damping is investigated in Fig. 6.46 (right).

Gain and phase margins for the complete designed controller have been evaluated. RS of the closed loop for all mass cases is achieved. For simultaneous, independent,

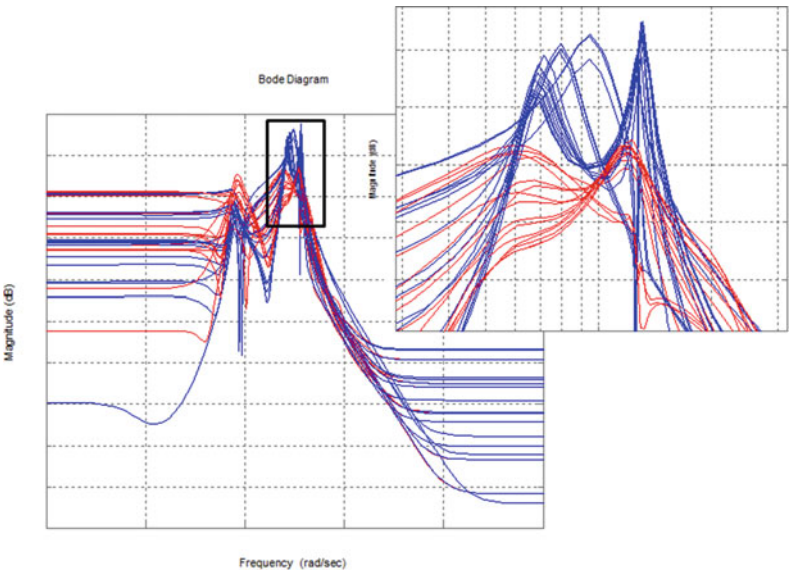

Fig. 6.44 Wing bending mode attenuation. Open loop (*blue*), closed loop (*red*)

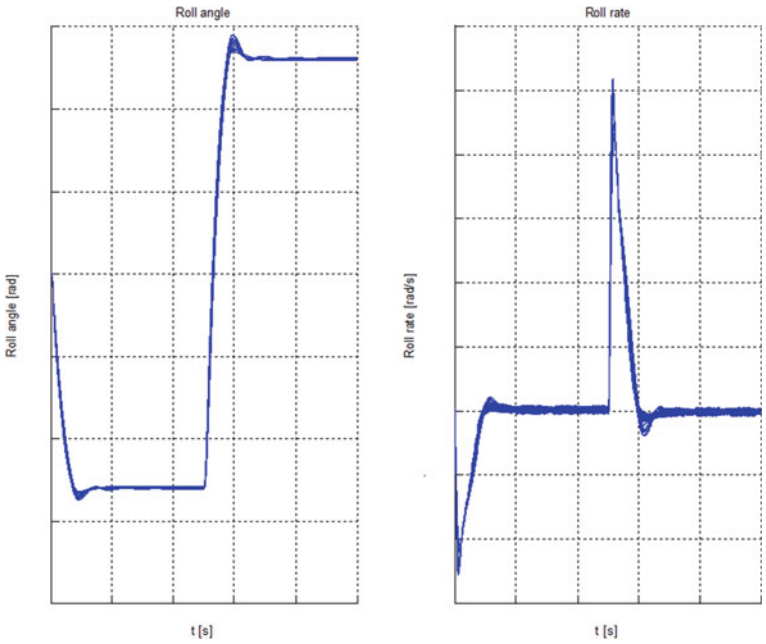

Fig. 6.45 Bank angle and roll rate reference signal tracking

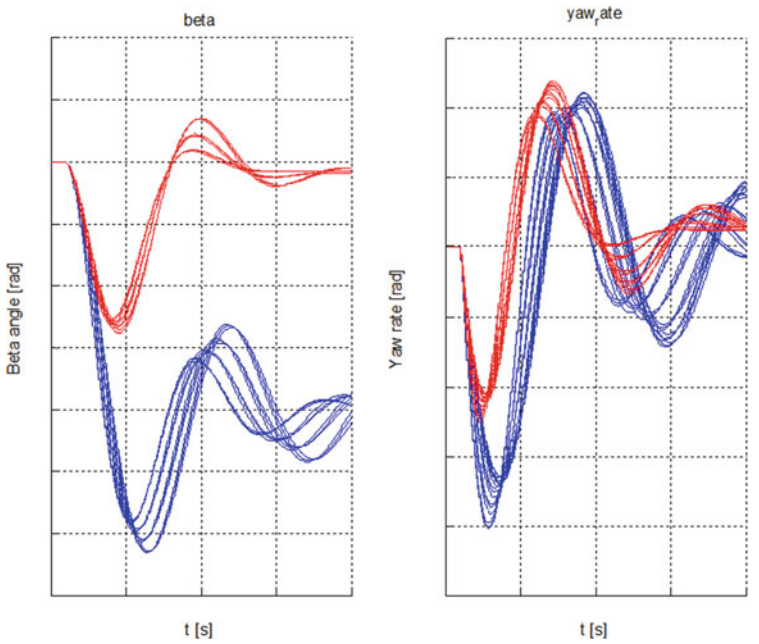

Fig. 6.46 Side-slip angle disturbance attenuation (*left*) and Yaw rate damping (*right*). Open loop (*blue*), closed loop (*red*)

worst-case variations in the individual channels the gain margin ranges from 0.8 to 2.6 dB, and the phase margin ranges from 5 to 16°, depending on the mass case.

6.6.4 Longitudinal $\mathscr{H}_\infty$-Optimal Control Law of Prescribed Structure

Advanced non-convex non-smooth optimization techniques for fixed-order $\mathscr{H}_\infty$ robust control are proposed in this part for design of FCSs with prescribed structure. Compared to classical techniques—tuning of and successive closures of particular SISO loops like dampers, attitude stabilizers, etc.—all loops are designed simultaneously by means of quite intuitive weighting-filters selection. In contrast to standard optimization techniques, such as $\mathscr{H}_2$ or $\mathscr{H}_\infty$ optimization, the resulting controller respects the prescribed structure in terms of engaged channels and orders (for example, P, PI, PID controllers). In addition, robustness with respect to multi-model uncertainty is also addressed which is of most importance for aerospace applications as well. Such a way, robust controllers for various Mach numbers, altitudes, or mass cases can be obtained directly, based only on particular mathematical models for respective combinations of the flight parameters.

6.6.4.1 Introduction

The flight dynamics, exhibiting many oscillatory or unstable modes for a typical aircraft, as well as the automatic or semi-automatic regimes of modern autopilots call for control synthesis methods that can effectively address these issues. Traditionally, classical tools for SISO loops tuning are used successively to deliver a complex FCS composed of a few smartly pre-selected channels, such as pitch, roll, or yaw dampers for suitable dynamics modifications (stability augmentation), subsequent attitude hold autopilots, automatic navigation loops, etc. Typically, a significant number of iterations and "backstepping" is required as the higher-level loops interact partially with the lower-level predesigned parts. Historically, frequency response methods were developed first in the 1930s and 1940s [11, 32, 56, 58, 60], and they remain arguably the most commonly used methods until today [14].

Since the 1960s, results of optimal control theory have been used extensively for aircraft control design as a powerful alternative to the classical approach. The methods are typically purely multi-input multi-output (MIMO) in nature, delivering all channels of the resulting controller in "one shot". The design procedure is controlled indirectly by means of selection of some weightings, being it constant matrices for LQ or LQG approach [53, 95], or LTI shaping filters for the $\mathscr{H}_2$ or $\mathscr{H}_\infty$-optimal control [7, 76, 95]. Nevertheless, the structure of the FCS is typically very hard or impossible to imprint, and the order (complexity) of the resulting controller can

become unacceptably large as well. In this regard, the classical methods still have quite a lot to offer.

Robustness of the flight controller is of utmost importance. The flight dynamics changes considerably as the aircraft properties vary over time (fuel amount, center of gravity position) and as the flight parameters change (altitude, airspeed, attitude angles). Classical and optimal controllers must fulfill the robustness requirements which is typically acknowledged by means of stability margins analysis (gain margin, phase margin [10, 18, 19, 53, 76, 95]) and extensive simulations for selected important points of the flight envelope. Nevertheless, neither of these methodologies supports incorporating the robustness requirements explicitly into the design procedure. In contrast, the robust control design approach, developed in the 1980s through the 2000s [26, 30, 31, 95] relies on the mathematical formulation of the uncertainty as one of the control design parameters. Most prominent methods are unstructured $\mathscr{H}_\infty$ optimization [7, 76, 95], structured $\mathscr{H}_\infty$ control (μ-synthesis, DK-iterations [6, 27–29, 95], robust loopshaping [55], and others). They all have been naturally accepted by the aerospace controls community, giving rise to significant implementations [9, 35, 44, 62].

One may ask if there is not a way to combine the benefits of the classical, optimal, and robust approaches—the convenient weighting-filters formulation of the optimal control synthesis, hierarchical and comprehensive structure of the classical controllers, and insensitivity to parameters uncertainties of the robust control designs. Indeed, some attempts have been made, based either on linear quadratic optimization (static output feedback design [77–79]), based on mixed-sensitivity $\mathscr{H}_\infty$ optimization with static output constraints [49, 75], or by designing a mixed $\mathscr{H}_2/\mathscr{H}_\infty$-optimal controller of fixed order based on a homotopy algorithm [91].

In this section, a completely different approach toward this goal is suggested, though. Thanks to the practical availability of computer-aided control systems design (CACSD) tools based on most recent non-convex non-smooth optimization techniques, direct synthesis methods can be employed to deliver a complex FCS that is structured (features pre-selected channels only), of fixed low order (consisting of, for example, P, PI, or lead-lag controllers), optimal in the $\mathscr{H}_\infty$ norm sense (for bandwidth setting, reference tracking, disturbance attenuation requirements), and robust with respect to a multi-model uncertainty (covering a selected number of airspeed, mass, altitude, or other cases).

The rest of this section is structured as follows. In Sect. 6.6.4.2, the method of formulating and solving a structured longitudinal CAS design process with HIFOO is shown. The main result of the paper is the case study presented in Sect. 6.6.4.3 (where advanced case study is presented). The procedure toward a structured, low complexity, and robust lateral FCS is elaborated in detail for a nonlinear model of a BWB-type aircraft, as a proof of practical usefulness of the proposed modern techniques for flight controls design purposes.

6.6.4.2 Longitudinal Structured Control Law with HIFOO

We propose a systematic methodology for a one-shot, robust, full-featured, $\mathscr{H}_\infty$-optimal longitudinal control design, for a multi-model case covering substantial points of the flight envelope. This methodology literally combines advantages from modern controller design techniques involving $\mathscr{H}_\infty$ or $\mathscr{H}_2$ optimization with a hierarchical approach for aircraft control system design. The HIFOO toolbox allows to preserve the property of physical meaning of each control system loop (which is one reasonable argument of aircraft control system engineers) and removes disadvantages of loop-by-loop tuning of control systems. On the other hand, the well-known robust control design approach based on the generalized plant setup and a corresponding criterion definition (for example, in the $\mathscr{H}_\infty$ sense) in the frequency domain can be followed also in the HIFOO formulation. Thereby, weighting filters like those used in [70, 71, 89, 90] can be included to produce MIMO controllers. Still, the HIFOO toolbox can be understood as an extension to the classical control design techniques. Due to the local optimization carried out by HIFOO, providing a suitable starting point in terms of an initial controller can significantly save computation time. Standard hierarchical approaches can then be used as a promising initial control law.

Algorithm:
Given:

- Set of systems for control design
- Structure of resulting control law
- Optimization criterion.

Output:

- Robust LTI control law with predefined structure.

- **Step 1:** Specify generalized plant set up (define measurable outputs/actuated inputs and criterion by performance inputs/outputs).
  - **Recommendations:** It is needed to select measurable outputs/actuated inputs in correspondence with structure to be designed.
- **Step 2:** Specify performance requirements by weighting filters.
  - **Recommendations:** Depends on the control problem. Typically, low-pass filters are used for reference signal tracking, and bandpass filters are used for vibration modes attenuation.
- **Step 3:** Specify the control law structure.
  - **Recommendations:** The structure needs to be defined by the controller's Rosenbrock matrix. There can be more than one representation, whereby a minimal realization should be aimed for.
- **Step 4:** Specify the starting control law if any is available, otherwise it will be generated randomly.

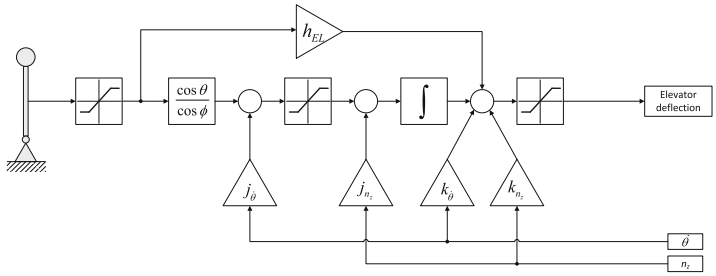

Fig. 6.47 Longitudinal control augmentation system (adopted from [13])

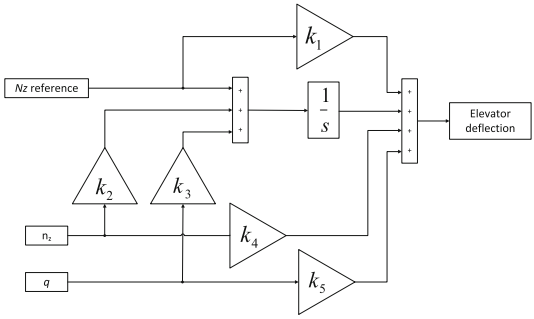

Fig. 6.48 Normal acceleration reference signal tracking control augmentation system with structure

  - **Recommendations:** The suitable choice of a starting point is critical to save optimization time. Control laws designed by classical approaches can be a suitable choice.

- **Step 5:** Solve the design problem using the HIFOO toolbox.
  - **Recommendations:** The involved optimization does not guarantee global optimality; therefore, it is usually required to run the optimization several times to reduce the risk of getting caught in mediocre local optima.

A longitudinal CAS of extremely low order (first-order control law) with imprinted structure was designed by the HIFOO toolbox. The structure of the control law is shown in Fig. 6.47, respectively Fig. 6.48 (with mapping of constants (6.54)).

$$\begin{aligned} k_1 &= h_\eta \\ k_2 &= j_{nz} \\ k_3 &= j_{\dot{\theta}} \\ k_4 &= k_{nz} \\ k_5 &= k_{\dot{\theta}} \end{aligned} \tag{6.54}$$

It is a common hierarchical control law used for an asymptotic tracking of the aircraft normal acceleration reference signal (see [13, 79]). The hierarchical control law design was usually done in an iterative manner, using background knowledge

of the physical meaning of the single loop to reach the required performance. The optimization technique is addressed now to design the overall control law in one shot. $\mathscr{H}_\infty$-performance criteria can be introduced to design robust control laws with predefined structure and order. The extremely low-order and structural complexity of the overall control law (with preserved robust behavior and control performance of full MIMO high-order control laws) is very important for final on-board implementation. It reduces necessary computational effort and therefore hardware demands for on-board equipment, which is closely connected with reliability and price of implementation. For other possibilities of high-order MIMO CAS designs, see [70, 71, 89, 90]. Control surfaces used by CAS are symmetrically actuated beaver tails (denoted as BT) and elevator (denoted as EL), in our case both flaps are collectively actuated as one. Measured signals are longitudinal RB variables at CG, namely normal acceleration (denoted as Nz_{CG}) and pitch rate (q). Highly valuable feature of $\mathscr{H}_\infty$ optimization is the possibility to introduce the concept of robustness. The HIFOO toolbox will be used, in this particular case, to cover multiple plants, each representing different fueling points in the flight envelope to end up with a longitudinal CAS robust with respect to fueling. The augmented plant used for control law design is shown in Fig. 6.49.

The signals in the augmented plant are divided into exogenous inputs and outputs (which represent control law performance by definition of the optimization criterion), as well as measured outputs and actuated inputs according to Fig. 6.42. The plant G represents aircraft longitudinal dynamics itself and weighting filters W represent the definition of performance criterion in the frequency domain. At this point, the structure of the controller can be introduced into HIFOO by prescribing zero entries in the controller's Rosenbrock matrix. Let the state-space representation of the controller be $K \cdot a$, $K \cdot b$, $K \cdot c$, and $K \cdot d$, then its Rosenbrock matrix is:

$$K = \begin{bmatrix} K \cdot a & K \cdot b \\ K \cdot c & K \cdot d \end{bmatrix}, \tag{6.55}$$

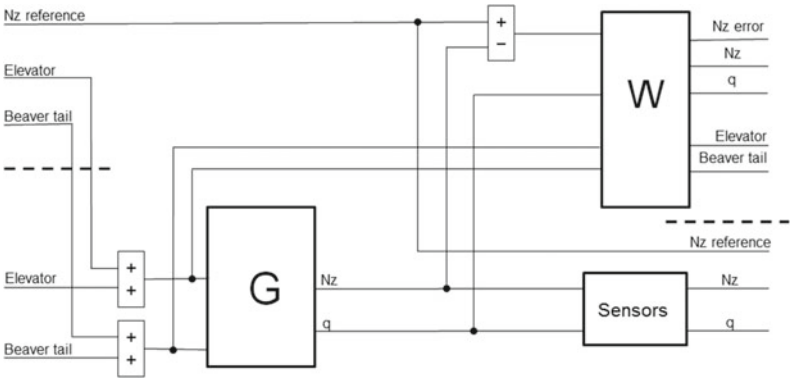

Fig. 6.49 Augmentation plant set up used for longitudinal control law design

with the augmented plant setup shown in Fig. 6.49 and the desired structure of the controller as shown in Figs. 6.47 and 6.48 the controller can be written in the form:

$$A_K = 0 \tag{6.56}$$

$$B_K = \begin{bmatrix} 1 & -k_2 & k_3 \end{bmatrix} \tag{6.57}$$

$$C_K = \begin{bmatrix} 1 \end{bmatrix} \tag{6.58}$$

$$D_K = \begin{bmatrix} k_1 & k_4 & k_5 \end{bmatrix}. \tag{6.59}$$

Consequently, the controller's Rosenbrock matrix is

$$K = \begin{bmatrix} 0 & 1 & -k_2 & k_3 \\ 1 & k_1 & k_4 & k_5 \end{bmatrix}. \tag{6.60}$$

The HIFOO toolbox is applied now to carry out the fixed-order optimization with a predefined structure of the controller. The final control law is an integrated first-order multi-input single-output (MISO) controller with predefined structure and can be used as an integrated longitudinal CAS. However, because of the structure it is possible to disassemble it into a hierarchical structure of SISO loops, which can be used one-by-one as a SAS itself (pitch rate damper and normal acceleration damper) as it is known from text books and longitudinal CAS, in this case a normal acceleration reference signal tracker.

6.6.4.3 BWB Case Study

Mathematical Model of Longitudinal Aircraft Dynamics

This longitudinal CAS control design is carried out for the ACFA 2020 BWB aircraft. A variant of the longitudinal ROMs obtained in Sect. 4.1 are utilized in the following. They contain both flight mechanics and aeroelastic effects as well as their coupling. A set of linearized state-space systems for various parameter values of fuel and payload mass (at fixed cruise altitude and airspeed) is available:

$$\begin{aligned} \dot{\mathbf{x}} &= \mathbf{A} \cdot \mathbf{x} + \mathbf{B} \cdot \boldsymbol{u} \\ \mathbf{y} &= \mathbf{C} \cdot \mathbf{x} + \mathbf{D} \cdot \boldsymbol{u}, \end{aligned} \tag{6.61}$$

where the state vector $\mathbf{x}$ is composed of the six flight mechanic states (x-position X, body forward speed u, altitude Z, body down speed w (it is proportional to angle of attack α), pitch angle θ and pitch rate q), 12 elastic states (six symmetrical structural

modes), as well as seven aerodynamic lag states. The states X (x-position) and Z (altitude) are neglected in this study. Utilized inputs u for control design are:

- Symmetric Extended Elevator deflection δ_{EEL} (in rad) and deflection rate $\dot{\delta}_{\mathrm{EEL}}$ (in rad/s).
- Symmetric Elevator deflection δ_{EL} (in rad) and deflection rate $\dot{\delta}_{\mathrm{EL}}$ (in rad/s).

The Extended Elevator and Elevator control surfaces are coupled and actuated simultaneously (will be notated as δ_{EL}) in case of longitudinal control law. The actuator dynamics are modeled via second-order low-pass filters.
Utilized outputs for control design are:

- Pitch rate q (in rad/s)
- Normal acceleration Nz_{CG} (in $\mathrm{m/s^2}$)

where in both sensor signals 160 ms time delay (due to signal processing latency, modeled via a second-order Padé approximation) and low-pass Butterworth filters of second order were considered.

Simulations

The resulting longitudinal control law performance is presented in this section. First are presented linear model simulation in MATLAB® and than nonlinear MATLAB/Simulink® model is involved to demonstrate longitudinal control law capabilities. Position of the closed-loop poles is constrained by required relative damping of 0.5 for all RB poles, the only exception is for the phugoid mode, which can have even one real unstable pole with time period less than 0.1. The closed-loop pole locations can be seen in Fig. 6.50.

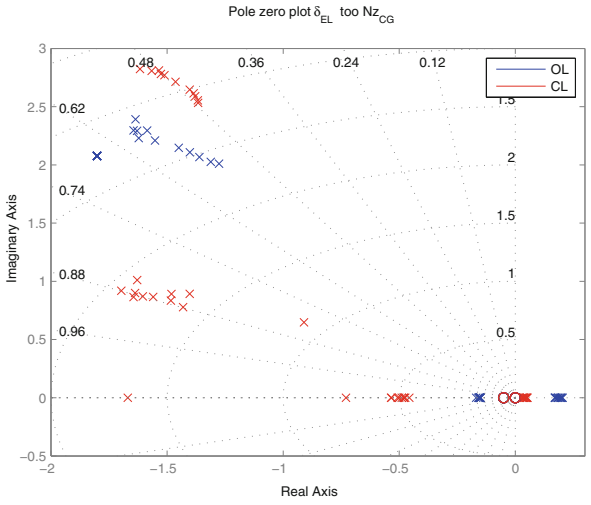

Fig. 6.50 Poles and zeros of Nz_{CG} reference signal to Nz_{CG} output signal channel (10 fueling cases are plotted)

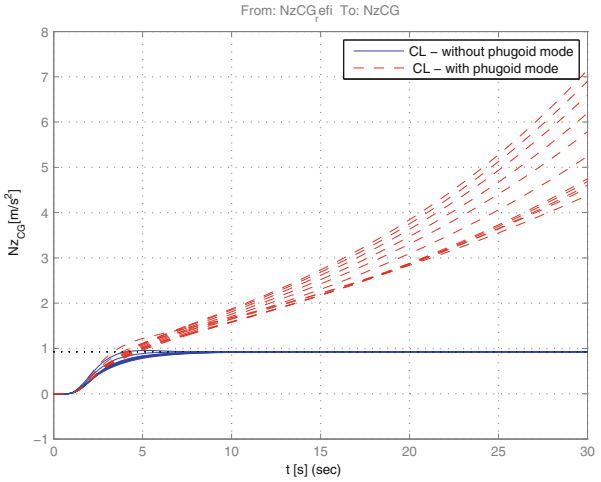

Fig. 6.51 Normal acceleration step response—linear simulation (10 fueling cases are plotted)

The aircraft normal acceleration step response can be seen in Fig. 6.51, where the design plant (without phugoid mode) response as well as the validation plant (with phugoid mode) responses are plotted for all fuel cases (which is one of the robust behavior requirements).

The robustness of control law with respect to unmodeled uncertainty is presented. The uncertainty is here illustrated by diamonds in a Nichols charts, as standard margins or robustness evaluation measures among aircraft controls designers for decades. Uncertainty in this case should be understood as a phase lag and gain variance insensitiveness. One Nichols chart is used for each opened loop (closed loop is disconnected at controller inputs or its output) of the multiple inputs and single-output control law to validate controller robustness. There are different robustness requirements for predefined frequency regions of control law, bounded by phugoid mode frequency (solid line diamond), short-period frequency (dot and dash line diamond) and the first wing bending mode frequency (doted line diamond). First, the robustness is investigated with respect to unmodeled uncertainty at system input, represented by diamonds in a Nichols chart of open-loop transfer function from system δ_{EL} input to controller δ_{EL} output, see Fig. 6.52 and its zoom in Fig. 6.53. One can see that all curves are outside of the prescribed diamonds which guarantees the required robustness.

Similarly, robustness with respect to output unmodeled uncertainty is investigated. The open-loop system has two inputs pitch rate q and normal acceleration Nz (controller inputs) and two measurements of the same notations (plant outputs). Nichols charts of open-loop transfer functions are plotted in Fig. 6.54, and its zoom for Nichols diamonds are plotted in Fig. 6.55.

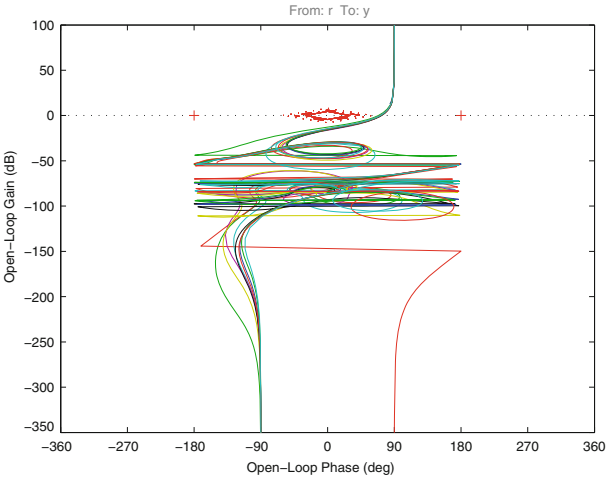

Fig. 6.52 Nichols charts of the closed loops (disconnected at actuators). Ten fueling cases are depicted

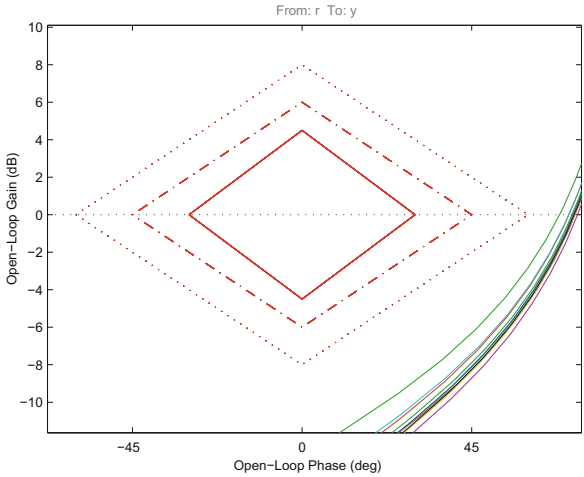

Fig. 6.53 Nichols charts of the closed loops (disconnected at actuators). Ten fueling cases are depicted. Zoomed in for Nichols *diamonds*

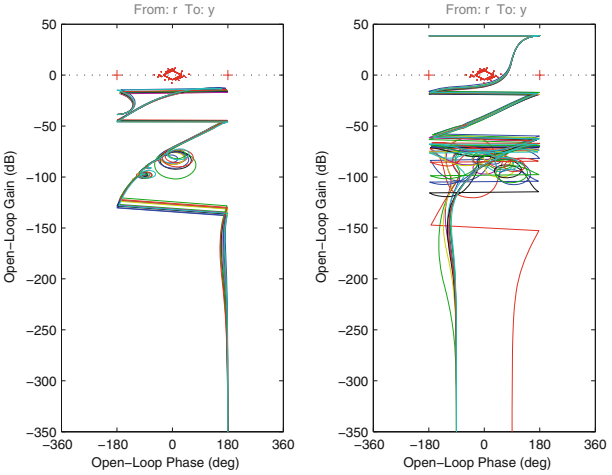

Fig. 6.54 Nichols charts of closed loop disconnected at sensors, pitch rate (*left*) and Nz_{CG} (*right*) (10 fueling cases are plotted)

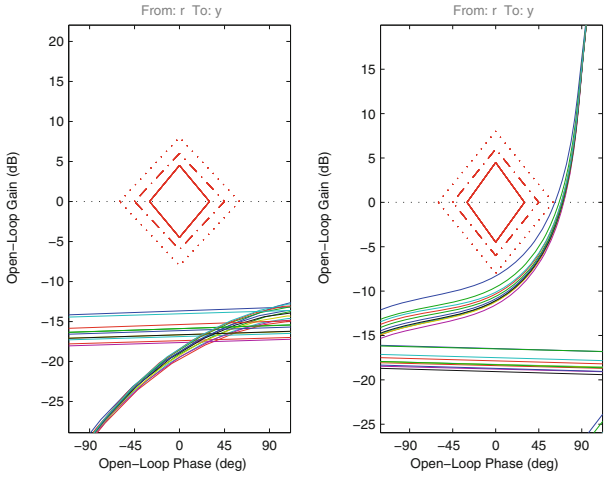

Fig. 6.55 Nichols charts of closed loop disconnected at sensors, pitch rate (*left*) and Nz_{CG} (*right*), zoomed for Nichols *diamonds* (10 fueling cases are plotted)

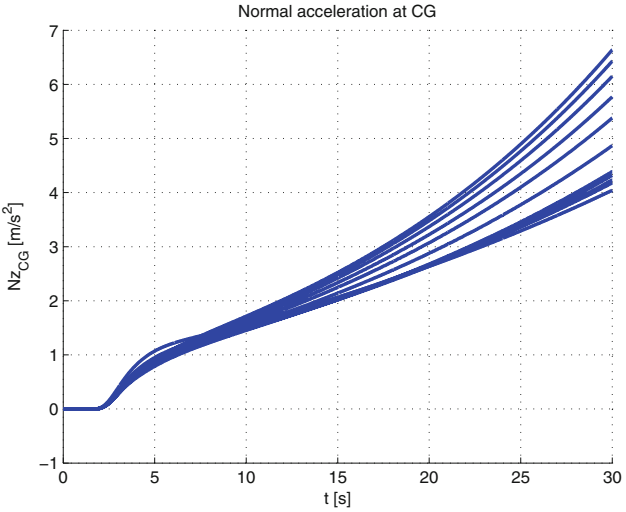

Fig. 6.56 Normal acceleration step response (10 fueling cases are plotted)

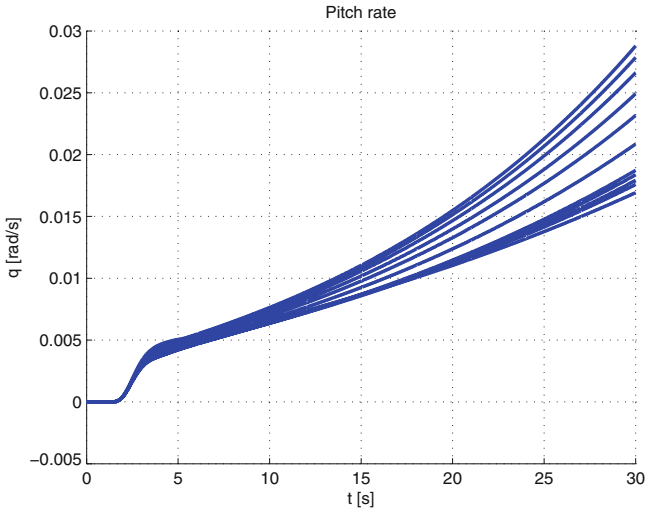

Fig. 6.57 Pitch rate response to step in normal acceleration reference signal (10 fueling cases are plotted)

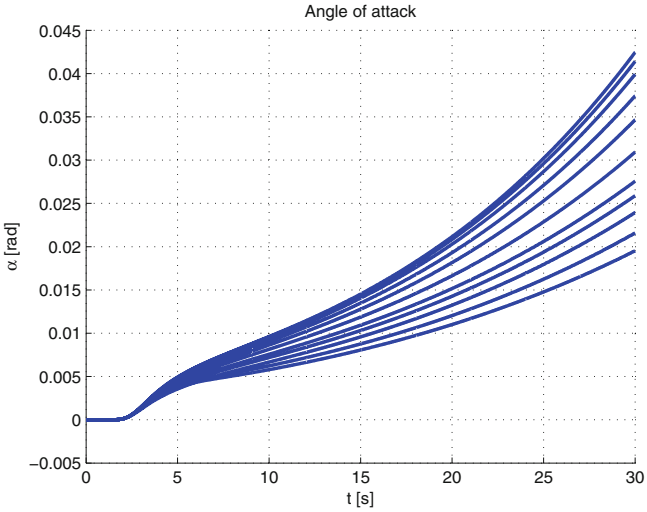

Fig. 6.58 Angle of attack response to step change in normal acceleration reference signal (10 fueling cases are plotted)

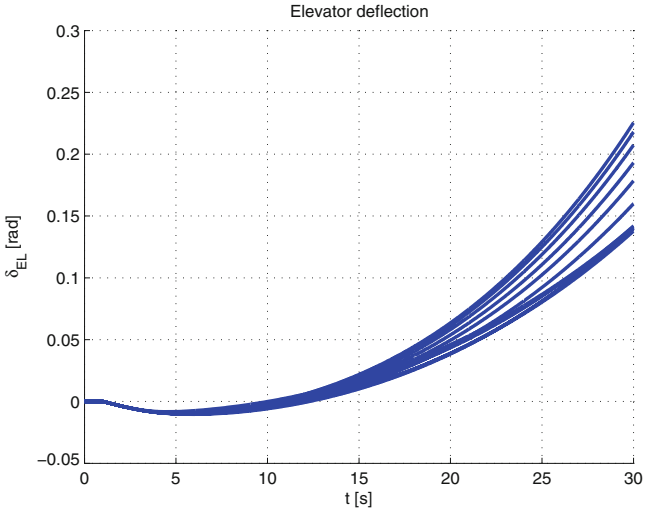

Fig. 6.59 Elevator command induced by step change in normal acceleration reference signal tracking (10 fueling cases are plotted)

Eventually, a MATLAB/Simulink® nonlinear model has been involved. Main sources of nonlinearity come from a fully nonlinear model of actuators, which considers control surface maximal deflections, maximal deflection rates, and aerodynamic effects. All nonlinear simulations are influenced by the unstable phugoid mode, but with a time constant of instability of less than 0.1 s it does not violate control constraints or requirements. Time responses of the aircraft's normal acceleration for all considered aircraft fuel cases are plotted in Fig. 6.56. The pitch rate and angle of attack responses are plotted in Figs. 6.57 and 6.58, again plotted for all considered cases. Finally, control law effort needed for such a maneuver, for all fuel cases, is plotted in Fig. 6.59.

References

1. Alazard D, Apkarian P (1999) Observer-based structures of arbitrary compensators. Int J Robust Nonlinear Control 9(2):101–118
2. Apkarian P, Noll D (2006) Controller design via nonsmooth multidirectional search. SIAM J Control Optim 44:1923–1949
3. Arzelier D, Deaconu G, Gumussoy S, Henrion D (2011) H_2 for HIFOO. In: IFAC world congress on automatic control
4. Balas GJ (2002) Linear, parameter-varying control and its application to a turbofan engine. Int J Robust Nonlinear Control 12:763–796
5. Balas G, Chiang R, Packard A, Safonov M (2010) MATLAB robust control toolbox 3, user's guide. MathWorks
6. Balas G, Doyle JC, Glover A (1991) The mu analysis and synthesis toolbox, Math Works and MUSYN
7. Bates D, Postlethwaite I (2002) Robust multivariable control of aerospace systems. DUP Science, Ios Pr Inc
8. Benatzky C (2006) Theoretical and experimental investigation of an active vibration damping concept for metro vehicles. Dissertation, Vienna University of Technology, Vienna
9. Bennami S, Looye G (1998) Design of flight control laws for a civil aircraft using mu synthesis. In: Proceedings of the AIAA conference on guidance, navigation and control
10. Bing-Fei Wu, Perng Jau-Woei (2004) Gain and phase margin analysis of pilot-induced oscillations for limit-cycle prediction. J Guidance Control Dyn 27:59–65
11. Blakelock JH (1965) Automatic control of aircraft and missiles. Wiley, New York
12. Boyd S, Barrat C (1990) Linear controller design: limits of performance. Prentice Hall, Englewood Cliffs
13. Brockhaus R (2001) Flugregelung (English: Flight control). Springer, Berlin
14. Bryson AE (1994) Control of spacecraft and aircraft. Princeton University Press, Princeton
15. Burke JV, Henrion D, Lewis AS, Overton ML (2006) HIFOO—a MATLAB package for fixed-order controller design and $\mathscr{H}_\infty$ optimization. In: IFAC symposium on robust control design, 2006
16. Burke JV, Lewis AS, Overton ML (2005) A robust gradient sampling algorithm for nonsmooth, nonconvex optimization. SIAM J Optim
17. Burke JV, Lewis AS, Overton ML (2006) Stabilization via nonsmooth, nonconvex optimization. IEEE Trans Autom Control 51:1760–1769
18. Chang Che-Hsu, Hant Kuang-Wei (1990) Gain margins and phase margins for control systems with adjustable parameters. J Guidance Control Dyn 13:404–408
19. Chopra I, Ballardf J (1981) A method for measuring the stability of a full-scale rotor control system. J Guidance Control Dyn

20. Dardenne I (1999) Développement de méthodologies pour la synthèse de lois de commande d'un avion de transport souple. Ph.D. thesis, Ecole Natrionale Supérieure de l'Aéronautique et de l'Espace (SUPAERO), France, 1999. (English: Development of methodologies for control law synthesis for a flexible transport aircraft)
21. Dehkordi VR, Boulet B (2009) Robust controller order reduction. In: Proceedings of the american control conference, pp 3083–3088
22. Delwiche T (2009) Contribution to the design of control laws for bilateral teleoperation with a view to applications in minimally invasive surgery. PhD thesis, Free University of Brussels
23. Demourant F, Ferreres G (2002) A frequency domain identification-control approach for a flexible aircraft. In: IEEE CCA'02
24. Demourant F, Ferreres G (2013) A linear parameter-varying multiobjective control law design based on Youla parametrization for a flexible blended wing body aircraft. In: Progress in flight dynamics, guidance, navigation, control, fault detection, and avionics, vol 6. EDP Sciences, pp 729–748
25. Dotta D, Silva AS, Decker IC (2009) Design of power systems controllers by nonsmooth, nonconvex optimization. In: IEEE power and energy society general meeting
26. Doyle JC (1979) Robustness of multiloop linear feedback systems. In: Proceedings of the 17th IEEE conference decision and control
27. Doyle JC, Mall J, Stein G (1982) Performance and robustness analysis for structured uncertainty. In: IEEE conference on decision and control
28. Doyle JC, Packard A (1987) Uncertain multivariable systems from a state space perspective. In: Proceedings of American control conference, Minneapolis
29. Doyle JC, Packard A, Zhou K (1987) Review of LFT's LMIs and mu. In: Proceedings of 30th IEEE conference on decision and control
30. Doyle JC (1982) Analysis of feedback systems with structured uncertainties. IEE Proc Part D 129(6):242–250
31. Doyle JC, Glover K, Khargonekar PP, Francis BA (1989) State-space solutions to standard $\mathscr{H}_2$ and $\mathscr{H}_\infty$ control problems. IEEE Trans Autom Control 34(8):831–847
32. Evans WR (1948) Graphical analysis of control systems. Trans AIEE 67:547–551
33. Ferreres G, Puyou G (2006) Flight control law design for a flexible aircraft: limits of performance. J Guidance Control Dyn 29(4):870–878
34. Ferreres G, Biannic JM (1998) A μ analysis technique without frequency gridding. In: American control conference. Proceedings of the 1998, vol 4. IEEE, pp 2294–2298
35. Fialho I, Balas G, Packard A, Renfrow J, Mullaney C (1997) Linear fractional transformation control of the F-14 aircraft lateral-direction axis during powered approach landing. In: Proceedings of the American control conference
36. Gawronski W (2004) Advanced structural dynamics and active control of structures. Springer, New York
37. Gu DW, Petkov PH, Konstantinov MM (2005) Robust control design with MATLAB, vol 1. Springer, London
38. Gumussoy S, Henrion D, Millstone M, Overton M (2009) Multiobjective robust control with HIFOO 2.0. In: IFAC symposium on robust control design
39. Gumussoy S, Millstone M, Overton ML (2008) $\mathscr{H}_\infty$ strong stabilization via HIFOO, a package for fixed-order controller design. In: Proceedings of CDC
40. Haddad WM, Chellaboina V (2008) Nonlinear dynamical systems and control: a Lyapunov-based approach. Princeton University Press, Princeton
41. Hanel M (2001) Robust integrated flight and aeroelastic control system design for a large transport aircraft. Number 866 in 8. VDI-Verlag, Düsseldorf
42. Haniš T, Kučera V, Hromčík M (2013) Low order $\mathscr{H}_\infty$ optimal control for ACFA blended wing body aircraft. In: Progress in flight dynamics, guidance, navigation, control, fault detection, and avionics, vol 6. EDP Sciences, pp 671–684
43. Hecker S (2006) Generation of low order LFT representations for robust control applications. PhD thesis, Technische Universität München, Lehrstuhl für Steuerungs- und Regelungstechnik
44. Hyde RA (1995) $\mathscr{H}_\infty$ aerospace control design: a VSTOL flight application. Springer, Berlin

45. Ito H, Ohmori H, Sano A (1993) Design of stable controllers attaining low $\mathscr{H}_\infty$ weighted sensitivity. IEEE Trans Autom Control 38(3):485–488
46. Jeanneau M, Lamolie J, Puyou G, Aversa N (2005) AWIATOR's design of multi-objectives control laws. IFAC
47. Knittel D, Henrion D, Millstone M, Vedrines M (2007) Fixed-order and structure $\mathscr{H}_\infty$ control with model based feedforward for elastic web winding systems. In: Proceedings of the IFAC/IFORS/IMACS/IFIP symposium on large scale systems
48. Kron A, de Lafontaine J, Alazard D (2003) Robust 2-DOF H-infinity controller for highly flexible aircraft: design methodology and numerical results. Can Aeronaut Space J 49:19–29
49. Kureemun R, Bates DG (2001) Aircraft flight controls design using constrained output feedback–a $\mathscr{H}_\infty$ loopshaping approach. In: AIAA guidance, navigation, and control conference
50. Kwakernaak H (2002) Mixed sensitivity design. In: Proceedings of the 15th IFAC world congress, Barcelona
51. Lewis AS, Overton ML (2009) Nonsmooth optimization via BFGS. SIAM J Optim
52. Lewis F (1986) Optimal estimation. Wiley, New York
53. Lewis FL, Vrabie D, Syrmos VL (2012) Optimal control. Wiley, New York
54. Magni J-F (2002) Robust modal control with a toolbox for use with MATLAB. Kluwer Academic Publishers, New York
55. McFarlane D, Glover K, Khargonekar PP, Francis BA (1992) A loop-shaping design procedure using $\mathscr{H}_\infty$ synthesis. In: IEEE transactions on automatic control
56. McRuer D, Ashkenas I, Graha D (1973) Aircraft dynamics and automatic control. Princeton University Press, Princeton
57. Mialon B, Hepperle M (2005) Flying wing aerodynamics studies at ONERA and DLR. In: CEAS Katnet conference on key aerodynamic technologies, Braunschweig
58. Miller JE (1966) Space navigation, guidance and control. AGARDograph
59. Millstone M (2006) HIFOO 1.5: structured control of linear systems with a non-trivial feedthrough. Master's thesis, Department of Mathematics, Courant Institute of Mathematical Sciences—New York University
60. Perkins CD (1970) Development of airplane stability and control. J Aircr 7:290–301
61. Pfifer H, Hecker S (2010) LPV controller synthesis for a generic missile model. In: IEEE international conference on control applications, Yokohama, pp 1838–1843
62. Postlethwaite I, Smerlas A, Walker A, Gubbels AW, Baillie S, Strange ME, Howitt J (1999) $\mathscr{H}_\infty$ control of the NRC Bell 205 fly-by-wire helicopter. J Am Helicopter Soc 44:276–284
63. Pouly G, Lauffenburger J-P, Basset M (2010) Reduced order $\mathscr{H}_\infty$ control design of a nose landing gear steering system. In: 12th IFAC symposium on control in transportation systems
64. Puyou G, Ferreres G, Chiappa C, Menard P (2004) A multiobjective method for flight control law design. In: AIAA guidance, navidation, and control conference, Providence
65. Robu B, Budinger V, Baudouin L, Prieur C, Arzelier D (2010) Simultaneous $\mathscr{H}_\infty$ vibration control of fluid/plate system via reduced-order controller. In: Proceedings of CDC
66. Rugh WJ, Shamma JS (2000) Survey paper: research on gain scheduling. Automatica 36:1401–1425
67. Safonov MG, Chiang RY (1988) Model reduction for robust control: a Schur relative error method. Int J Adapt Control Signal Process 2(4):259–272
68. Scherer C, Weiland S (2004) Linear matrix inequalities in control. Lecture notes. http://www.dcsc.tudelft.nl/cscherer/lmi.html, Accessed 16 May 2014
69. Schirrer A, Westermayer C, Hemedi M, Kozek M (2010) A comprehensive robust control design and optimization methodology for complex flexible-structure systems. In: Proceedings of the 18th mediterranean conference on control and automation, Marrakech
70. Schirrer A, Westermayer C, Hemedi M, Kozek M (2010) LQ-based design of the inner loop lateral control for a large flexible BWB-type aircraft. In: 2010 IEEE multi-conference on systems and control, Yokohama
71. Schirrer A, Westermayer C, Hemedi M, Kozek M (2010) Robust $\mathscr{H}_\infty$ control design parameter optimization via genetic algorithm for lateral control of a BWB type aircraft. In: IFAC workshop on intelligent control systems, Sinaia

72. Schirrer A, Westermayer C, Hemedi M, Kozek M (2011) Multi-model convex design of a scheduled lateral feedforward control law for a large flexible BWB aircraft. In: Preprints of the 18th IFAC world congress, Milano, pp 2126–2131
73. Schirrer A, Westermayer C, Hemedi M, Kozek M (2011) Robust convex lateral feedback control synthesis for a BWB aircraft. In: Preprints of the 18th IFAC world congress, Milano, pp 7262–7267
74. Schirrer A, Westermayer C, Hemedi M, Kozek M (2013) Robust lateral blended-wing-body aircraft feedback control design using a parameterized LFR model and DGK-iteration. In: Progress in flight dynamics, guidance, navigation, control, fault detection, and avionics, vol 6. EDP Sciences, pp 749–766
75. Skelton RE, Stoustrup J, Iwasaki T (2007) The hinf control problem using static output feedback. Int J Robust Nonlinear Control 4:449–455
76. Skogestad S, Postlethwaite I (2005) Multivariable feedback control: analysis and design, 2nd edn. Wiley, New York
77. Stevens BL, Vesty P, Heck BS, Lewis FL (1983) Loop shaping with output feedback. In: American control conference
78. Stevens BL, Lewis FL, Al-Sunni F (1992) Aircraft flight controls design using output feedback. J Guidance Control Dyn 15:238–246
79. Stevens BL, Lewis FL (2003) Aircraft control and simulation. Wiley, New York
80. Tobie HN, Elliot EM, Malcolm LG (1966) A new longitudinal handling qualities criterion. In: Proceedings of the annual national aerospace electronics conference, pp 93–99
81. Torczon V (1991) On the convergence of the multidirectional search algorithm. SIAM J Optim
82. Torczon V (1997) On the convergence of pattern search algorithms. SIAM J Optim
83. Torralba J, Demourant F, Puyou G, Ferreres G (2009) A method for flexible aircraft LFT modelling. In: Proceedings of the European control conference
84. Torralba J, Puyou G, Demourant F (2009) Self-scheduling multiobjective control law design for a flexible aircraft. In: AIAA guidance, navidation, and control conference, Chicago
85. Vanek B (2008) Control methods for high-speed supercavitating vehicles. PhD thesis, Graduate School of the University of Minnesota
86. Vidyasagar M (1988) Control system synthesis: a coprime factorization approach. MIT, Cambridge
87. Wang FC, Chen HT (2009) Design and implementation of fixed-order robust controllers for a proton exchange membrane fuel cell system. Int J Hydrogen Energy 34:2705–2717
88. Westermayer C (2011) 2DOF parameter-dependent longitudinal control of a blended wing body flexible aircraft. PhD thesis, Vienna University of Technology
89. Westermayer C, Schirrer A, Hemedi M, Kozek M (2010) Linear parameter-varying control of a large blended wing body flexible aircraft. In: 18th IFAC symposium on automatic control in aerospace, Nara
90. Westermayer C, Schirrer A, Hemedi M, Kozek M, Wildschek A, Robust $\mathscr{H}_\infty$ flight and load control of a flexible aircraft using a 2DOF multi-objective design. In: Proceedings of 2009 CACS international automatic control conference, Taipei
91. Whorton M, Buschek H, Calise AJ (1996) Homotopy algorithm for fixed order mixed $\mathscr{H}_2/\mathscr{H}_\infty$ design. J Guidance Control Dyn 19:1262–1269
92. Wildschek A, Maier R, Hromčík M, Haniš T, Schirrer A, Kozek M, Westermayer C, Hemedi M (2009) Hybrid controller for gust load alleviation and ride comfort improvement using direct lift control flaps. In: Proceedings of the 3rd EuCASS
93. Wu F (1995) Control of linear parameter varying systems. PhD thesis, University of California, Berkeley
94. Youla DC, Jabr HA, Bongiorno JJ (1976) Modern Wiener-Hopf design of optimal controllers. II. The multivariable case. IEEE Trans Autom Control 21(3):319–338
95. Zhou K, Doyle JC, Glover K (1996) Robust and optimal control. Prentice Hall, Upper Saddle River

Chapter 7
Feed-Forward Control Designs

T. Haniš, M. Hromčík, A. Schirrer, M. Kozek and C. Westermayer

7.1 Gust Loads Alleviation System Via Convex Optimization

T. Haniš and M. Hromčík

The potential advantages of blended wing body (BWB) aircrafts in terms of fuel efficiency are opposed by technical challenges such as the alleviation of gust loads. Due to low wing loading, gusts generally have a more severe impact on BWB aircraft than on conventional aircraft wing tube aircraft. This section presents the design and optimization of a gust load alleviation system (GLAS) for a large BWB airliner. Numerical simulations are performed with an aeroelastic model of the initial aircraft model created within the NACRE project including GLAS in order to compute time series of modal displacements for deriving equivalent static load cases which are used for resizing of the aircraft structure. This design is carried out in this section is carried out for the 750-passenger NACRE BWB aircraft predesign model. The same methodology has been shown and carried out on the ACFA BWB configuration in [22].

Remark: Note that the scope of the $\mathscr{L}_\infty$-optimization of gust load alleviation in this context can only be utilized to verify feasibility of a GLAS for the given aircraft. The resulting controller is not directly applicable for implementation on an aircraft—this requires certification criteria such as the CS-25 "continuous turbulence design criteria" to be carefully addressed which is out of scope in this design and in the context of the ACFA 2020 project in general.

T. Haniš · M. Hromčík
Czech Technical University, Prague, Czech Republic

A. Schirrer (✉) · M. Kozek · C. Westermayer
Vienna University of Technology, Vienna, Austria
e-mail: alexander.schirrer@tuwien.ac.at

M. Kozek and A. Schirrer (eds.), *Modeling and Control for a Blended Wing Body Aircraft*,
Advances in Industrial Control, DOI 10.1007/978-3-319-10792-9_7

7.1.1 Introduction

The coupled aeroelastic/flight mechanic BWB model used for this investigation is parameterized in Mach, dynamic pressure, fuel mass, and center of gravity (CG) position. The CG variation is achieved by fuel redistribution which is important on a BWB airplane for trim without too large control surface deflections in order to achieve optimum cruise performance. For some fuel configurations the BWB airliner is statically unstable, thus requiring artificial stabilization. The BWB airliner is controlled/stabilized by an underlying feedback control system using trailing edge flaps (see Chap. 6 for details on feedback control laws design). The elevators and spoilers on the upper side of the wings are used for feed-forward control. On each wing, the three inner spoilers are actuated simultaneously, and the three outer spoilers are actuated simultaneously as well. The control commands by the feed-forward GLAS are added to the commands computed by feedback flight control laws. Taking into account maneuver load alleviation, gust loads become the dominant sizing factor. For efficient gust load alleviation, the weighted $\mathscr{L}_\infty$ norm of the responses of wing bending and torsion moment need to be minimized for gusts of different scale lengths throughout the whole flight envelope while not exceeding maximum and minimum load factors. The worst-case gust length of a particular flight condition will be taken into account, but augmentation of the optimization for more gust lengths and operating points is straightforward.

7.1.2 Gust Load Alleviation System Design

The GLAS (see Fig. 7.1) is based on a triggered feed-forward control system for attenuation of aircraft excitation $\mathbf{d}(t)$ by exogenous disturbance signal $w(t)$, in our case wind gust of $1 - \cos$ shape. Design of the wind gust detection system itself, the trigger, is not treated here. It is assumed that it is possible to estimate an upcoming wind gust and its direction with a certain time delay needed for estimation. The

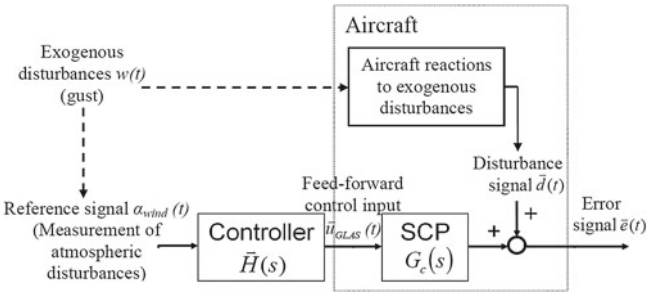

Fig. 7.1 GLAS setup

reference signal α_{wind} is then the triggering signal used as input for the GLAS feed-forward controller $H(s)$ and it is considered as a unit step signal. The GLAS $H(s)$ can be realized as a FIR shaping input (step) command α_{wind} and producing control signals $\mathbf{u}_{\text{GLAS}}$, or as a memory storing device containing the control signals sequences $\mathbf{u}_{\text{GLAS}}$ and putting them out once triggered by α_{wind}. The effect of $\mathbf{u}_{\text{GLAS}}$ on $\mathbf{e}(t)$ is expressed as a response of the transfer function $G_{\text{c}}(s)$, the so-called Secondary Control Path (SCP). Considering a model of the aircraft linearized in a certain trim point, the error signal $\mathbf{e}(t)$ is just the sum of aircraft response $\mathbf{d}(t)$ to wind gust disturbance $w(t)$ and response of the aircraft to the GLAS control command $\mathbf{u}_{\text{GLAS}}$. The error signal $\mathbf{e}(t)$ contains the wing bending and torsion moments and shear forces at wing cuts, as well as the incremental load factor $\Delta n_z(t)$. The design objective is to choose $H(s)$ in order to minimize the $\mathscr{L}_\infty$ norm of a criterion based on forces and moments as will be explained later, keep $\Delta n_z(t)$ within certain limits (for passenger safety), and at the same time remain within various limits for the $\mathscr{L}_\infty$ norm of $\mathbf{u}_{\text{GLAS}}(t)$, that is, considering the saturation of control surfaces. The control surfaces used for the GLAS are the elevator u_{Elevator} and the spoilers u_{Spoiler}. The vector of control commands $\mathbf{u}_{\text{GLAS}}(t)$ thus can be written as:

$$\mathbf{u}_{\text{GLAS}}(t) = \left[u_{\text{Elevator}}(t),\ u_{\text{Spoiler}}(t)\right]^{\text{T}} \tag{7.1}$$

where u_{Elevator} is elevator control command and u_{Spoiler} denotes spoilers command.

7.1.3 Convex Synthesis

The convex synthesis approach is exploited to design the control law. This methodology described by [2, 4], can easily address both time- and frequency-domain criterions and constraints. A nice overview and aircraft control specific designs can be found in [7].

The generalized plant in Fig. 7.2 is considered. Therein, system P represents the controlled plant, K is the feedback control law and H is the feed-forward control system. The signals w and z are exogenous input signals and controlled (criterion) output signals, respectively. Signals u_{FF} and u_{FB} are input signals actuated by feed-forward and feedback control systems. The signals y and u_{ref} are the measurable output signals and the reference signal for the feed-forward control system, respectively.

The convex synthesis methodology can be applied for both feedback and feed-forward control system design. Nevertheless, only the feed-forward control system design will be addressed in this section. The feedback control law K in Fig. 7.2 is considered as a fixed control law. The parameterization of the discrete-time feed-forward controller $H(z)$ is affine in the weights θ_i,

$$H(z) = \sum_{i=1}^{n} \theta_i \cdot H_i(z), \tag{7.2}$$

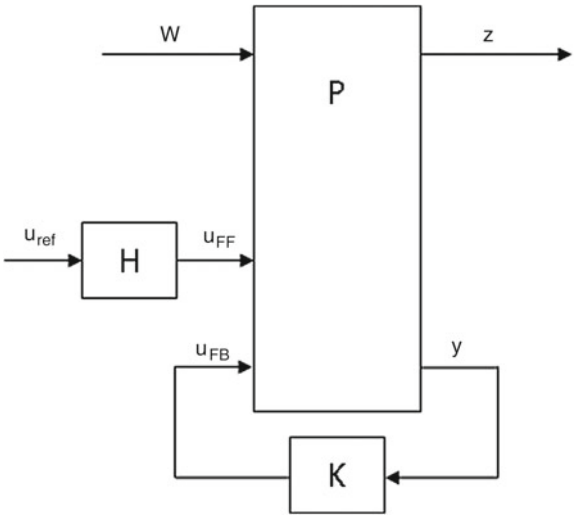

Fig. 7.2 Convex synthesis design plant

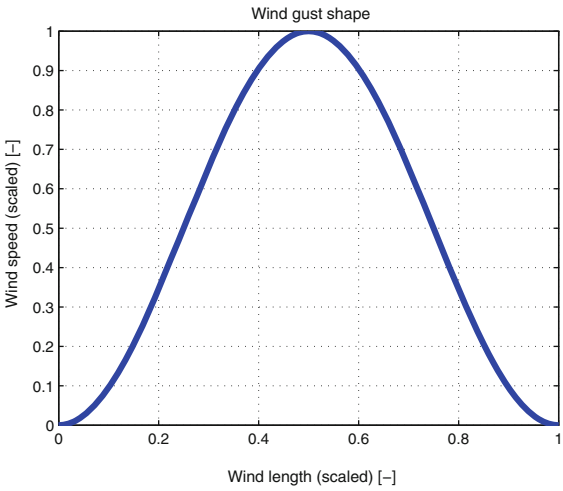

Fig. 7.3 Considered wind gust profile

where the transfer functions $H_i(z)$ are a priori fixed basis functions and scalars, θ_i for $i \geq 1$ are the decision variables of the optimization problem. The exogenous input signal $w(t)$ is considered as one case of a $1 - \cos$-shaped gust (plotted in Fig. 7.3). The result of the optimization will be the FIR filter $H(z)$ (decision variables θ_i define the coefficients of such FIR filter), therefore the reference input signal u_{ref} is considered as a discrete unit pulse at time $t = 0$ as plotted in Fig. 7.4. The time-domain response of the feed-forward-controlled closed-loop system can be expressed by (7.3) in an affine form,

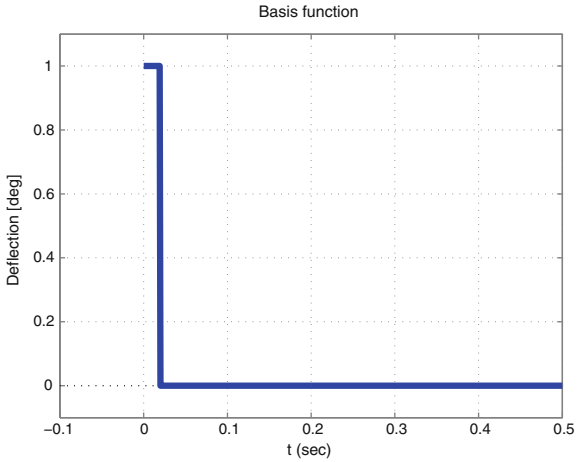

Fig. 7.4 Reference input signal

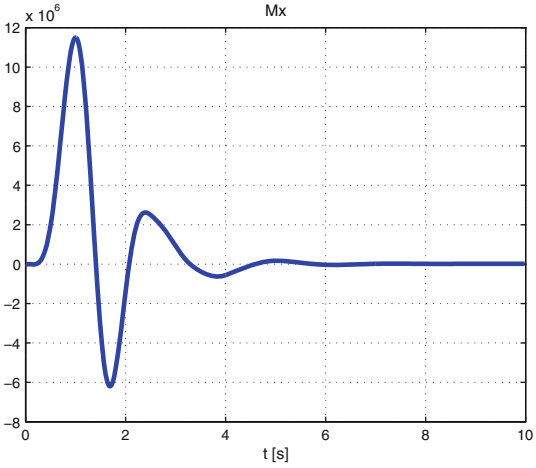

Fig. 7.5 Mx response to wind gust input

$$z(t) = \theta_0 \cdot z_0(t) + \sum_{i=1}^{n} \theta_i \cdot z_i(t), \tag{7.3}$$

where $z_0(t)$ is the response of the feed-forward-controlled closed-loop system for disturbance signal $w(t)$ (according to (7.4), plotted in Fig. 7.5). In this case the coefficient θ_0 is equal to one. The second term corresponds to the response of closed-loop system (defined by (7.5), plotted in Figs. 7.6 and 7.7) for reference signal u_{ref} (in this case a discrete unit pulse) shaped by particular basis function $H_i(z)$ which are chosen to be unit delays so that $H(z)$ becomes a FIR filter by design.

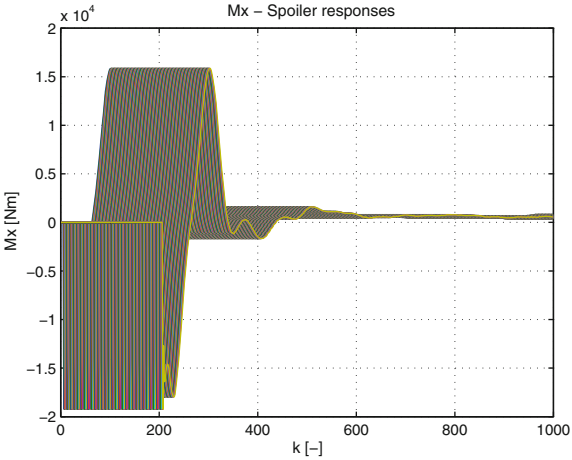

Fig. 7.6 Mx responses to the Spoiler input

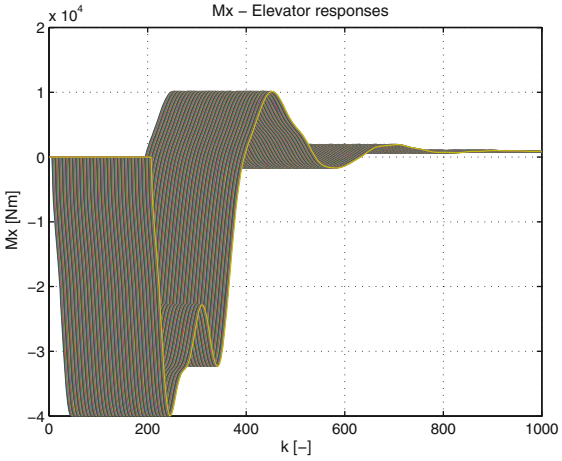

Fig. 7.7 Mx responses to the Elevator input

$$Z_0(z) = P(z)W(z) \tag{7.4}$$

$$Z_i(s) = P(z)H_i(z)U(z). \tag{7.5}$$

The correspondence between the time-domain and the z-domain is defined by

$$z_i(t) = Z^{-1}\{Z_i(z)\}. \tag{7.6}$$

Finally, the convex optimization task can be defined as a linear program with criteria expressed as:

$$\min_{\theta} c^{\mathrm{T}}\theta, \tag{7.7}$$

and constraints:

$$A\theta \leq b \tag{7.8}$$

The criterion as well as constraints will be explained in detail in Sect. 7.1.4.

7.1.4 Formulation of the Optimization Problem

With sizing gusts of different lengths from 30 ft (9.14 m) to 500 ft (152.4 m) starting at time $t = 0$ it was sufficient to fulfill the following constraints within a time interval $[0; t_{\mathrm{end}}\,10\,\mathrm{s}]$ since oscillations excited by gusts sufficiently diminish after that amount of time. First, only one length of a sizing wind gust case is considered to keep the definition simple and clear. The maximum and minimum control surface deflections need to be bounded by:

$$u_{\mathrm{Elevator}}(n) \leq u_{\mathrm{ElevatorMax}}, \quad \forall n \in [0; t_{\mathrm{end}} F_{\mathrm{s}}] \tag{7.9}$$

$$u_{\mathrm{Elevator}}(n) \geq u_{\mathrm{ElevatorMin}}, \quad \forall n \in [0; t_{\mathrm{end}} F_{\mathrm{s}}] \tag{7.10}$$

$$u_{\mathrm{Spoiler}}(n) \leq u_{\mathrm{SpoilerMax}}, \quad \forall n \in [0; t_{\mathrm{end}} F_{\mathrm{s}}] \tag{7.11}$$

$$u_{\mathrm{Spoiler}}(n) \geq u_{\mathrm{SpoilerMin}}, \quad \forall n \in [0; t_{\mathrm{end}} F_{\mathrm{s}}]\,. \tag{7.12}$$

With subscript Max denoting maximum allowed deflection of the respective control surface, and subscript Min denoting prescribed minimum allowed deflection of the respective control surface (maximal negative deflection). Control surface deflection rate $\mathrm{d}u/\mathrm{d}t$ needs to be limited because the available actuators' energy is finite. Thereby, F_{s} is the sampling frequency, and $T_{\mathrm{s}} = 1/F_{\mathrm{s}}$ denotes the sampling time of the discrete-time controller. Then rate limits of control surfaces are defined by:

$$\frac{u_{\mathrm{Elevator}}(n) - u_{\mathrm{Elevator}}(n-1)}{T_{\mathrm{s}}} \leq \frac{\mathrm{d}u}{\mathrm{d}t}_{\mathrm{ElevatorMax}}, \quad \forall n \in [1; t_{\mathrm{end}} F_{\mathrm{s}}] \tag{7.13}$$

$$\frac{u_{\mathrm{Elevator}}(n) - u_{\mathrm{Elevator}}(n-1)}{T_{\mathrm{s}}} \geq \frac{\mathrm{d}u}{\mathrm{d}t}_{\mathrm{ElevatorMin}}, \quad \forall n \in [1; t_{\mathrm{end}} F_{\mathrm{s}}] \tag{7.14}$$

$$\frac{u_{\text{Spoiler}}(n) - u_{\text{Spoiler}}(n-1)}{T_\text{s}} \;\leq\; \frac{\text{d}u}{\text{d}t}_{\text{SpoilerMax}}, \quad \forall n \in [1; t_\text{end} F_\text{s}] \tag{7.15}$$

$$\frac{u_{\text{Spoiler}}(n) - u_{\text{Spoiler}}(n-1)}{T_\text{s}} \;\geq\; \frac{\text{d}u}{\text{d}t}_{\text{SpoilerMin}}, \quad \forall n \in [1; t_\text{end} F_\text{s}] \tag{7.16}$$

For passenger safety, the maximum and the minimum load factors need to be bounded as well.

$$n_z(n) \;\leq\; 2.5, \quad \forall n \in [0; t_\text{end} F_\text{s}] \tag{7.17}$$

$$n_z(n) \;\geq\; 1, \quad \forall n \in [0; t_\text{end} F_\text{s}]\,. \tag{7.18}$$

The cost function J is defined as a function of the vector of control commands $\mathbf{u}_{\text{GLAS}}(n)$ with tuning parameters a_1, a_2, a_3 and b_1, b_2, b_3. Considering that positive as well as negative peak forces and moments need to be reduced in magnitude, the cost function J can by divided into two parts:

$$\begin{aligned} J_\text{max} = \max_{n \in [0,\ t_\text{end} F_\text{s}]} \Bigg[& a_1 \cdot \Bigg(\sum_{i=0}^{n} f_z^{\text{Gust}}(i) \cdot w(n-i) + \sum_{i=0}^{n} f_z^{\text{Elevator}}(i) \cdot u_{\text{Elevator}}(n-i) \\ & \qquad + \sum_{i=0}^{n} f_z^{\text{Spoiler}}(i) \cdot u_{\text{Spoiler}}(n-i) \Bigg) \\ & + a_2 \cdot \Bigg(\sum_{i=0}^{n} m_x^{\text{Gust}}(i) \cdot w(n-i) + \sum_{i=0}^{n} m_x^{\text{Elevator}}(i) \cdot u_{\text{Elevator}}(n-i) \\ & \qquad + \sum_{i=0}^{n} m_x^{\text{Spoiler}}(i) \cdot u_{\text{Spoiler}}(n-i) \Bigg) \\ & + a_3 \cdot \Bigg(\sum_{i=0}^{n} m_y^{\text{Gust}}(i) \cdot w(n-i) + \sum_{i=0}^{n} m_y^{\text{Elevator}}(i) \cdot u_{\text{Elevator}}(n-i) \\ & \qquad + \sum_{i=0}^{n} m_y^{\text{Spoiler}}(i) \cdot u_{\text{Spoiler}}(n-i) \Bigg) \Bigg] \end{aligned} \tag{7.19}$$

$$
\begin{aligned}
J_{\min} = \min_{n\in[0,\ t_{\text{end}}F_s]} \Bigg[& b_1 \cdot \Bigg(\sum_{i=0}^{n} f_z^{\text{Gust}}(i) \cdot w(n-i) + \sum_{i=0}^{n} f_z^{\text{Elevator}}(i) \cdot u_{\text{Elevator}}(n-i) \\
& + \sum_{i=0}^{n} f_z^{\text{Spoiler}}(i) \cdot u_{\text{Spoiler}}(n-i) \Bigg) \\
& + b_2 \cdot \Bigg(\sum_{i=0}^{n} m_x^{\text{Gust}}(i) \cdot w(n-i) + \sum_{i=0}^{n} m_x^{\text{Elevator}}(i) \cdot u_{\text{Elevator}}(n-i) \\
& + \sum_{i=0}^{n} m_x^{\text{Spoiler}}(i) \cdot u_{\text{Spoiler}}(n-i) \Bigg) \\
& + b_3 \cdot \Bigg(\sum_{i=0}^{n} m_y^{\text{Gust}}(i) \cdot w(n-i) + \sum_{i=0}^{n} m_y^{\text{Elevator}}(i) \cdot u_{\text{Elevator}}(n-i) \\
& + \sum_{i=0}^{n} m_y^{\text{Spoiler}}(i) \cdot u_{\text{Spoiler}}(n-i) \Bigg) \Bigg] . \qquad (7.20)
\end{aligned}
$$

Finally an overall criterion is defined as:

$$J = J_{\max} - J_{\min}. \qquad (7.21)$$

Thereby, $w(n)$ is the discrete-time gust excitation and $f_z^{\text{Gust}}(i)$, $f_z^{\text{Elevator}}(i)$, $f_z^{\text{Spoiler}}(i)$ denote the ith sample of impulse responses of the linearized aircraft model to gust excitation, elevators inputs, and spoilers inputs, respectively. At selected wing cut, the respective ith sample of pulse responses for torsion moment are $m_y^{\text{Gust}}(i)$, $m_y^{\text{Elevator}}(i)$, $m_y^{\text{Spoiler}}(i)$, and for bending moment $m_x^{\text{Gust}}(i)$, $m_x^{\text{Elevator}}(i)$, $m_x^{\text{Spoiler}}(i)$. The static shear force, torsion moment, and bending moment for 1 g level flight are not considered in this design.

The optimization problem can thus be formulated as:

$$\min_{u_{\text{Elevator}},\ u_{\text{Spoiler}}} J \qquad (7.22)$$

with constraints expressed by (7.9)–(7.18).

7.1.5 Gust Load Alleviation System: Results

Simulations of the resulting feed-forward control system are presented in this section. The deflections of spoilers and elevator commanded by the triggered GLAS are plotted in Figs. 7.8 and 7.9. One can see that maximal and minimal deflection constraints of each control surface are fulfilled.

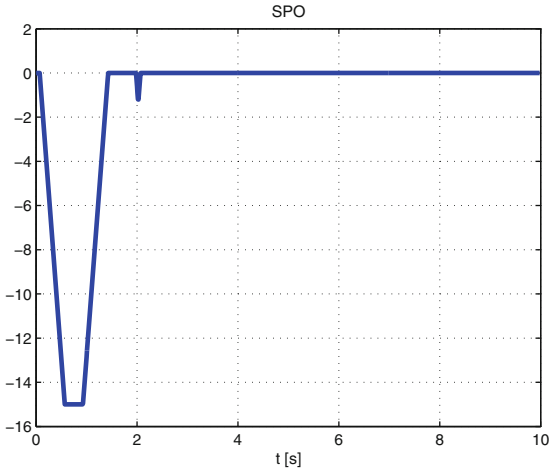

Fig. 7.8 Spoiler deflection signal

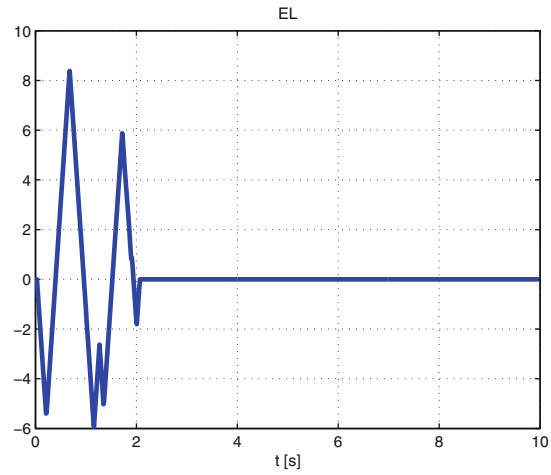

Fig. 7.9 Elevator deflection signal

Similarly, requirements for deflection rates of spoilers as well as elevators (plotted in Figs. 7.10 and 7.11) are taken into account during the optimization and fulfilled by the resulting control law. One can see that the deflection rate constraints are the limiting factor of the resulting control law and limit achievable control performance. The dynamic aircraft wing bending moment was reduced by more than 50 % in the sense of the $\mathscr{L}_\infty$ norm. The resulting structural load alleviation performance in wing bending is plotted in Fig. 7.12.

Similarly, the dynamic wing torsion moment was reduced by more than 60 % in the $\mathscr{L}_\infty$ norm sense. The resulting structural load alleviation performance in wing torsion is plotted in Fig. 7.13. Eventually the vertical acceleration response is presented in Fig. 7.14. One can see that also the constraints for vertical acceleration are fulfilled.

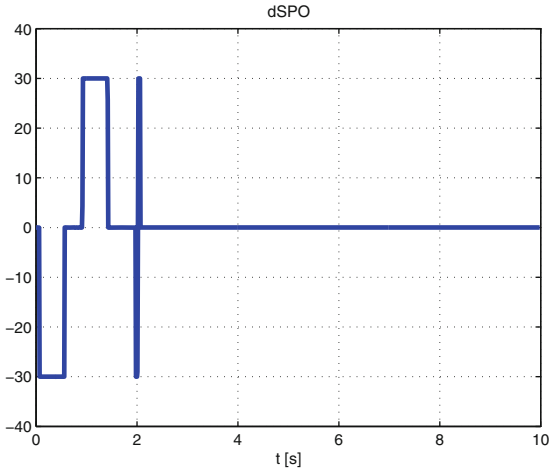

Fig. 7.10 Spoiler deflection signal rate

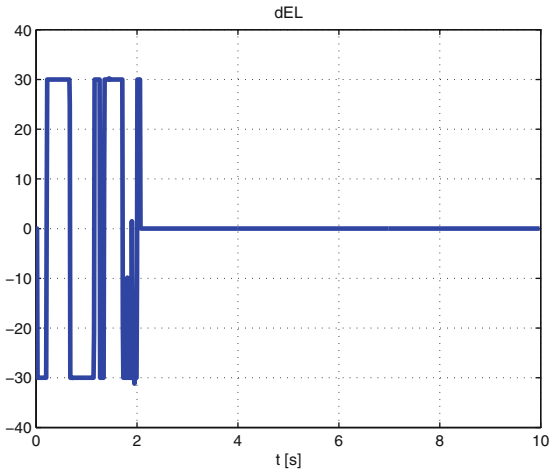

Fig. 7.11 Elevator deflection rate

7.2 Lateral Maneuver Loads Alleviation System Via Convex Optimization

A. Schirrer and M. Kozek

In this section, a maneuver load alleviation system is designed for the ACFA BWB configuration by a convex synthesis approach. The feed-forward design can directly be cast into a convex optimization problem and is thus efficiently solvable. Its development is based on the multi-model feed-forward design developed for the NACRE BWB 750-passenger aircraft model, published in [16].

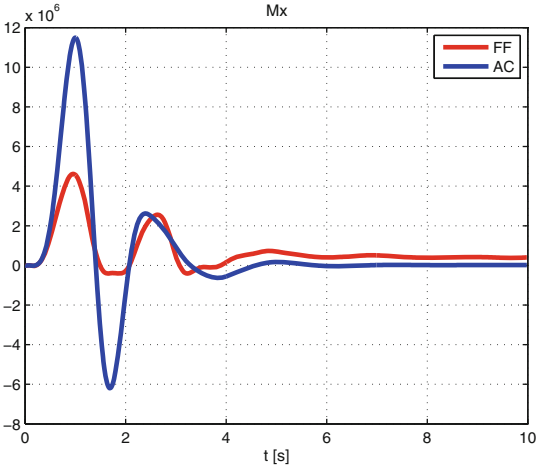

Fig. 7.12 Wing bending moment attenuation

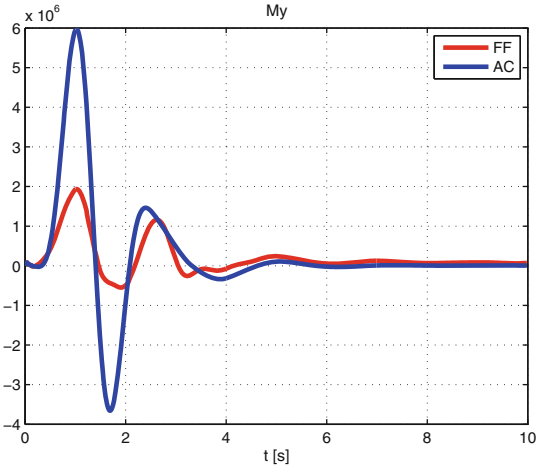

Fig. 7.13 Wing torsional moment attenuation

7.2.1 Design Goals and Problem Definition

The control goals related to Maneuver loads alleviation are most effectively addressed via a dynamic pilot command preshaper (feed-forward control law) once the closed-loop system is designed and conditioned (robustified) sufficiently well. The closed-loop plants obtained by earlier control designs are then utilized as design plants for the feed-forward design. This control design stage has the following goals:

- Given a step input roll angle reference signal, drive the system such that a decoupled roll maneuver with the given end angle is flown.
- Mach and dynamic pressure are assumed measurable and available for controller scheduling. The design task will be reduced to designs for fixed values of the

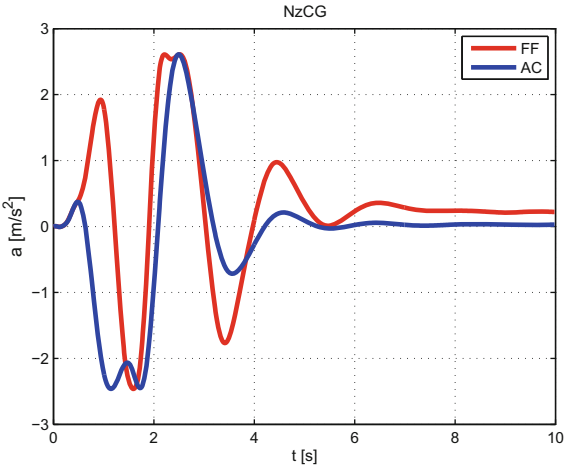

Fig. 7.14 Vertical acceleration at the center of gravity

Mach and dynamic pressure parameters and the same set of basis functions will be used across all designs so that only numerator coefficients need to be scheduled/interpolated a posteriori.

- The CG and Fuel parameters are considered unknown during operation and thus the controller should yield satisfactory responses for all CG/Fuel cases.
- The following requirements on the response shape must be fulfilled robustly:
  - Average static gain (DC gain) from roll reference to roll angle equal to 1 over all CG/Fuel cases.
  - Fulfill roll rise time requirement to 95 % rise level in 7 s.
  - No or minimal overshoot (less than 1 %) in the roll reference response.
  - Decoupling: restrict side-slip response β to ± 10 mrad for a 1 rad roll step.
  - For a 60° roll step, all rate and deflection bounds of the control surfaces have to hold. The deflection bounds for Flap 5 (outer aileron) are reduced to 50 % in order to retain controllability for the One-Engine-Inoperable case.
- The sizing loads with respect to the roll maneuver (that is, the maximum total loads occurring in a shaped 60° roll maneuver over all parameter cases) should be minimized.

7.2.2 Methodology

7.2.2.1 Linear Matrix Inequalities (LMIs)

An Linear Matrix Inequality (LMI) problem is a convex optimization problem commonly used in control design (see [3]) as:

$$\inf_{\mathbf{x}} \left(\mathbf{c}^{\mathrm{T}} \mathbf{x} \right) \tag{7.23}$$

$$\text{s.t. } \mathbf{F}(\mathbf{x}) = \mathbf{F}_0 + \sum_{i=1}^{n} x_i \mathbf{F}_i \succeq 0. \tag{7.24}$$

The matrices $\mathbf{F}_i = \mathbf{F}_i^{\mathrm{T}} \in \mathbb{R}^{n \times n}$ are symmetric and fixed, $\mathbf{x} = [x_1, \ldots, x_n]^{\mathrm{T}}$ are the decision variables, and $\mathbf{c}^{\mathrm{T}}$ is the cost vector. The constraint $\mathbf{F}(\mathbf{x}) \succeq 0$ means that the matrix $\mathbf{F}(\mathbf{x})$ be positive-semidefinite, that is, that it possesses only non-negative eigenvalues.

7.2.2.2 Convex Control Design

With a plant transfer function (or, time-domain response signals) parameterized in affine form,

$$\mathbf{G}(s) = \mathbf{G}_0(s) + \sum_{i} \mathbf{G}_i(s)\theta_i, \tag{7.25}$$

as in the case of a feed-forward design or the Youla-parameterized convex feedback control design, important time- and frequency-domain requirements can be stated as linear programing (LP), quadratic programing (QP), or Linear Matrix Inequality (LMI) constraints (convex in the parameters $\boldsymbol{\theta}$), see [6]. Similarly, by bounding a constraint by an additional free variable instead of a constant, any such constraint can be turned into an objective. Then, the bounding variable itself is considered as the minimizing objective.

Time-Domain: Single-Input Single-Output (SISO) $\mathscr{L}_\infty$ Bounds

A central benefit of convex synthesis methods is the direct incorporation of time-domain constraints and objectives, which enables template-based step-response shaping. Closed-loop time-domain responses are affine in $\boldsymbol{\theta}$:

$$z(t) = \mathscr{L}^{-1}\{\mathbf{Z}(s)\} = z_0(t) + \sum_{i=1}^{n} z_i(t)\theta_i. \tag{7.26}$$

To constrain a time-domain response $z(t)$ by given lower and upper time-domain bounds $z_{\mathrm{L}}(t_k) < z(t_k) < z_{\mathrm{U}}(t_k)$, $t_k \in \{t_1, \ldots, t_N\}$, the expansion into the affine form yields two linear programing (LP)-type constraints for each t_k:

$$\left[-z_1(t_k),\ \ldots,\ -z_n(t_k)\right]\boldsymbol{\theta} < z_0(t_k) - z_{\mathrm{L}}(t_k), \tag{7.27}$$

$$\left[\ z_1(t_k),\ \ldots,\ \ z_n(t_k)\right]\boldsymbol{\theta} < z_{\mathrm{U}}(t_k) - z_0(t_k). \tag{7.28}$$

Note that (7.27)–(7.28) also represent two (scalar) LMI constraints and can directly be included in an LMI problem.

Frequency-Domain: Multi-input Multi-output (MIMO) $\mathscr{H}_\infty$ Bound

The constraint $\|\mathbf{G}\|_\infty < x$ can be discretized *for a stable* $\mathbf{G}(j\omega)$ at a frequency grid $\omega_k \in \{\omega_1, \ldots, \omega_N\}$ via N constraints $\bar{\sigma}(\mathbf{G}(j\omega_k)) < x$. These can be translated into (real-valued) LMI constraints:

$$\left.\begin{bmatrix} x\mathrm{I} & \mathrm{Re}(\mathbf{G}) & \mathbf{0} & \mathrm{Im}(\mathbf{G}) \\ & x\mathrm{I} & \mathrm{Im}(\mathbf{G}^{\mathrm{H}}) & \mathbf{0} \\ & & x\mathrm{I} & \mathrm{Re}(\mathbf{G}) \\ \mathrm{sym.} & & & x\mathrm{I} \end{bmatrix}\right|_{j\omega_k} \succ 0, \tag{7.29}$$

where $\mathrm{Re}(\cdot)$, $\mathrm{Im}(\cdot)$, and $(\cdot)^{\mathrm{H}}$ indicate the real part, imaginary part, and the Hermitian transpose, respectively. This LMI is affine in the parameters (see [6, 15]). Note that this constraint asserts $\mathbf{G}$ stable a priori and is thus not applicable to enforce stability of $\mathbf{G}$.

Frequency-Domain: MIMO $\mathscr{H}_2$ Bound

The $\mathscr{H}_2$ norm of a stable, strictly proper linear dynamic system $\mathbf{G}(j\omega)$ is

$$\|\mathbf{G}(j\omega)\|_2 = h = \sqrt{\frac{1}{2\,\pi}\int_{-\infty}^{\infty} \mathrm{tr}\left[(\mathbf{G}(j\omega))^{\mathrm{H}}\,(\mathbf{G}(j\omega))\right]\mathrm{d}\omega}. \tag{7.30}$$

For a sufficiently fine and broad finite frequency gridding, (7.30) can be approximated by the Riemann sum

$$h \cong \widetilde{h} = \sqrt{\frac{1}{\pi}\sum_{k=1}^{N} \mathrm{tr}\left[(\mathbf{G}(j\omega_k))^{\mathrm{H}}\,(\mathbf{G}(j\omega_k))\right](\omega_{k+1} - \omega_k)}. \tag{7.31}$$

This $\mathscr{H}_2$ norm approximation can be expanded to a (convex) quadratic form for $\mathbf{G}$ affine in $\boldsymbol{\theta}$ ($\beta \in \mathbb{R}$, $\boldsymbol{\gamma} = [\gamma_1, \ldots, \gamma_n]^{\mathrm{T}} \in \mathbb{R}^n$, $\boldsymbol{\Gamma} = [\Gamma_{i,j}] \in \mathbb{R}^{n\times n}$):

$$\mathbf{G}(j\omega_k) = \mathbf{G}_k = \widetilde{\boldsymbol{G}}_k + \sum_{i=1}^{n} \mathbf{G}_{ki}\theta_i, \tag{7.32}$$

$$\widetilde{h}^2 = \frac{1}{\pi}\left(\beta + \boldsymbol{\gamma}^{\mathrm{T}}\boldsymbol{\theta} + \boldsymbol{\theta}^{\mathrm{T}}\boldsymbol{\Gamma}\boldsymbol{\theta}\right), \tag{7.33}$$

$$\beta = \sum_{k=1}^{N} \mathrm{tr}\left[\widetilde{\mathbf{G}}_k^{\mathrm{H}}\widetilde{\mathbf{G}}_k\right], \quad \gamma_i = \sum_{k=1}^{N} 2\,\mathrm{Re}\left\{\mathrm{tr}\left[\widetilde{\mathbf{G}}_k^{\mathrm{H}}\mathbf{G}_{ki}\right]\right\},$$

$$\Gamma_{i,j} = \sum_{k=1}^{N} \mathrm{Re}\left\{\mathrm{tr}\left[\mathbf{G}_{ki}{}^{\mathrm{H}}\mathbf{G}_{kj}\right]\right\}.$$

Note that only real terms remain due to the properties of the trace and the Hermitian transpose. The matrix $\boldsymbol{\Gamma}$ is positive (semi-)definite, making the function $\widetilde{h}^2(\boldsymbol{\theta})$ convex, and $\boldsymbol{\Gamma}$ can be decomposed into its Cholesky factors $\boldsymbol{\Gamma} = \mathbf{L}^{\mathrm{T}}\mathbf{L}$. Then, an LMI constraint equivalent to $\tilde{h}^2 < x$ ($x \in \mathbb{R}^+$) is given as (see [17])

$$\left[\begin{array}{c|c} \mathrm{I}_n & \mathbf{L}\boldsymbol{\theta} \\ \hline \boldsymbol{\theta}^{\mathrm{T}}\mathbf{L}^{\mathrm{T}} & x - \beta - \boldsymbol{\gamma}^{\mathrm{T}}\boldsymbol{\theta} \end{array}\right] \succ 0. \tag{7.34}$$

Note that this constraint is of fixed size ($(n+1) \times (n+1)$) with respect to the frequency grid size N, which allows to use high approximation precision by a fine grid in the precalculation of β, $\boldsymbol{\gamma}$, and $\boldsymbol{\Gamma}$.

Adaptive Constraint Refinement

The optimization problem size is primarily determined by the number of basis functions (and thereby weighting parameters) and by the number of gridpoints in time or frequency at which point-wise constraints (or objectives) are defined. An adaptive grid refinement procedure has thus been implemented for high computational efficiency:

1. Start with coarse design grids.
2. Formulate and solve optimization problem (7.23)–(7.24) for the current design grids.
3. Validate the solution on fine validation grids.
4. Pick, per violated objective/constraint, at most n_{add} points that are most violated (and mutually sufficiently spaced) and add them to the design grids.
5. If no violations: done. Else: return to step (2).

7.2.3 Control Design

7.2.3.1 Reference Control Law Design

To formulate the load minimization criterion, a reference control law is necessary to obtain an initial feed-forward law that shapes the response to approximately fulfill the posed requirements. This task has been helped by the sensible shaping of the closed loop in the initial control design (by partial eigenstructure assignment, see Sect. 6.2). The dominant rigid-body (RB) poles already partially fulfill the response shape requirements.

Figure 7.15 depicts a simple interconnection of the feed-forward controller $\mathbf{K}_{\mathrm{ff}}$ and the closed-loop plant. Thereby $\mathbf{r} = \begin{bmatrix} r_\phi \\ r_\beta \end{bmatrix}$ is the (2×1) reference signal vector. A simple choice of reference control law is obtained as follows:

- Compute the optimal (2×2) static decoupling coefficient matrix $\widetilde{\mathbf{K}}_{\mathrm{ff}} = \begin{bmatrix} k_{11} & k_{12} \\ k_{21} & k_{22} \end{bmatrix}$ that minimizes the following objective function:

$$J = \sum_{j_{\mathrm{CG}}, j_{\mathrm{Fuel}}} \left\| \mathbf{I} - \mathbf{G}_{\mathrm{cl}, j_{\mathrm{CG}}, j_{\mathrm{Fuel}}}(j0)\widetilde{\mathbf{K}_{\mathrm{ff}}} \right\|, \tag{7.35}$$

  where $\mathbf{G}_{\mathrm{cl}, j_{\mathrm{CG}}, j_{\mathrm{Fuel}}}$ is the closed-loop transfer function of the aircraft for the parameter cases j_{CG} and j_{Fuel} (j_{Mach} and $j_{\mathrm{Dyn.Pressure}}$ are fixed for the studied design) from $\mathbf{u} = \begin{bmatrix} \delta_{\mathrm{Fl34}} \\ \delta_{\mathrm{Ru}} \end{bmatrix}$ to $\mathbf{z} = \begin{bmatrix} \phi \\ \beta \end{bmatrix}$ (see Fig. 7.15). The reference feed-forward law acts only on $\mathbf{u}$, so $\mathbf{Q}_{\mathrm{ref}} = \begin{bmatrix} \mathbf{Q}_{\mathrm{ref},1} \\ \mathbf{Q}_{\mathrm{ref},1} \end{bmatrix} = \begin{bmatrix} \mathbf{Q}_{\mathrm{ref},1} \\ \mathbf{0} \end{bmatrix}$.
- Add PT1 filters to fulfill control command rate limits in the 60° roll maneuver:

$$\mathbf{Q}_{\mathrm{ref},1} = \widetilde{\mathbf{K}_{\mathrm{ff}}} \begin{bmatrix} \frac{1}{Ts+1} & 0 \\ 0 & \frac{1}{Ts+1} \end{bmatrix} \tag{7.36}$$

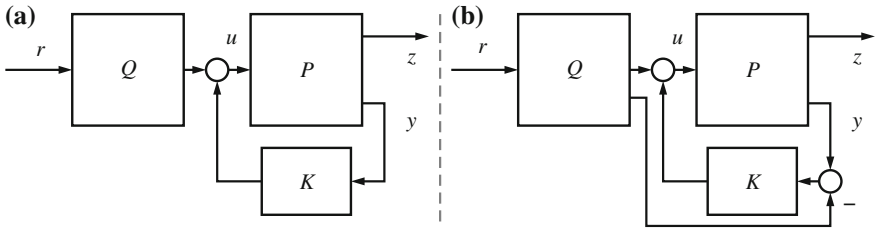

Fig. 7.15 Two interconnection architectures of a (possibly scheduled) feed-forward controller **Q** with feedback-controlled plant **P**, **a** only directly affects the control input u, whereas **b** also modifies the measured signals fed to the feedback controller K

The time constant was chosen $T = 1$ s which does not violate the rate limits and leads to a rise level of 90 . . . 95 % in 7 s in the roll reference–roll transfer function.

This reference law is used to compute the preliminary sizing total loads and parameter cases for the roll maneuver.

7.2.3.2 Feed-Forward Design by Convex Optimization

The optimization problem is formulated and solved by the LP/LMI control design optimization framework developed in [15].

The structure depicted in Fig. 7.15 has been utilized to design the feed-forward controller $\mathbf{Q}(s)$ by convex optimization. The closed-loop is comprised of the aircraft model (plant $\mathbf{P}$) and the combined control law $\mathbf{K}$ of stage 1 (initial feedback-controlled plant via partial eigenstructure assignment, see Sect. 6.2) and stage 2 (robust controller obtained by DGK-iteration, see Sect. 6.3).

The feed-forward law has one input (the roll reference ϕ_{ref}) and access to an extended set of nine separate outputs

$$\mathbf{u}_{\text{ext}} = \left[\Delta\delta_{\text{Fl3}},\ \Delta\delta_{\text{Fl4}},\ \Delta\delta_{\text{Fl5}},\ \Delta\delta_{\text{Ru}},\ \Delta\beta,\ \Delta\phi,\ \Delta p,\ \Delta r,\ \Delta Nz_{\text{lat.law}}\right]^{\text{T}}. \tag{7.37}$$

The control law $\mathbf{Q}$ is obtained as weighted sum of basis functions $\mathbf{Q}_i(s)$:

$$\mathbf{Q}(s) = \sum_{i=1}^{n_Q} \mathbf{Q}_i(s)\theta_i \tag{7.38}$$

This basis is composed of 20 basis functions per SISO channel which were chosen ad hoc as PT1 and PT2 dynamics with their poles evenly distributed in the dynamic range of interest. Note that the same basis is utilized for all feed-forward designs across the parameter range to facilitate a posteriori scheduling on the flight parameters.

The current optimization problem can then be formulated as an LP problem as follows:

$$\text{minimize}\ \ \mathbf{c}^{\text{T}}\mathbf{x} \tag{7.39}$$

$$\text{subject to}\ \ \mathbf{A}\mathbf{x} \leq \mathbf{b} \tag{7.40}$$

where the cost vector $\mathbf{c}$ and the constraints are obtained automatically by the optimization framework, based on an adaptive invocation of time-domain constraints and objectives on the closed loop. The vector of decision variables $\mathbf{x}$ contains the feed-forward control law weights θ_i as well as bound variables to formulate signal or system norm objectives (see Sect. 7.2.2.2).

Table 7.1 Defined objectives and constraints for feed-forward design

Objective set 1	Minimize $\phi_{\text{ref}} \rightarrow Fz_k$ peaks, $k = 1, \ldots, 14$ with respect to sizing loads
Objective set 2	Minimize $\phi_{\text{ref}} \rightarrow Mx_k$ peaks, $k = 1, \ldots, 14$ with respect to sizing loads
Objective set 3	Minimize $\phi_{\text{ref}} \rightarrow My_k$ peaks, $k = 1, \ldots, 14$ with respect to sizing loads
Constraint set 1	Constrain roll time-domain response $\phi_{\text{ref}} \rightarrow \phi$ in time-domain template (tracking, rise-time, overshoot, and undershoot goals)
Constraint set 2	Constrain coupling of roll reference to side-slip time-domain response $\phi_{\text{ref}} \rightarrow \beta$ (decoupling, coordinated turn)
Constraint set 3	Constrain control surface deflections and rates in roll maneuver $\phi_{\text{ref}} \rightarrow \delta_{\text{Fl3}}, \delta_{\text{Fl4}}, \delta_{\text{Fl5}}, \delta_{\text{Ru}}, \dot{\delta}_{\text{Fl3}}, \dot{\delta}_{\text{Fl4}}, \dot{\delta}_{\text{Fl5}}, \dot{\delta}_{\text{Ru}}$

These objectives and constraints are listed in Table 7.1 and closely related to those listed in Chap. 5. They are defined for each fuel and each CG case (31 cases) in the optimization framework and iteratively added to the actual LP formulation until the full validation on all parameter cases and on a fine time gridding ($T_{\text{s}} = 0.05\,\text{s}$) is successful for all constraints and objectives. This method has shown to be highly efficient and enables a computationally feasible design for very large constraint sets (of which most constraints are inactive at the optimal solution, but have to be tested).

The objective formulations are normalized with respect to the initial sizing loads (as obtained from the initial control law) in the following way:

Let $\overline{z}_{jk}$ be the preliminary sizing total load of load j ($j \in \{Fz, Mx, My\}$) at cut k ($k = 1, \ldots, 14$). Also, let $z_{0,jk,\text{cfmq}}$ be the corresponding trim (static/1 g) load at CG case c, fuel case f, Mach case m, and dynamic pressure case q. Then, the allowed lateral dynamic load in this parameter case until sizing is

$$z_{\text{dyn,max},jk,\text{cfmq}} = \left|\overline{z}_{jk}\right| - \left|z_{0,jk,\text{cfmq}}\right|. \tag{7.41}$$

This quantity is utilized to scale the objective such that an objective value of 1 means that the load becomes globally sizing and thus this normalization introduces global information into the local optimization problem. The actual optimization objective is the maximum of all scaled control objectives, so an objective function value of less than 1 means that the linear validation of the roll maneuver generates total loads which are less than the sizing loads.

7.2.3.3 Obtaining a Scheduled Control Law Using the Multi-stage Design Procedure

The multi-staged control law design allows one to employ direct a posteriori interpolation methods, specifically tailored to the partial control law at each stage.

In the scope of the lateral ACFA control design, the following interpolation onsets are utilized:

- The 1st-order "stage 1" control law (partial eigenstructure assignment, see Sect. 6.2) is parameterized in Mach number and dynamic pressure. Because of its low dynamic complexity, it can be transformed to a unique controllability companion form and a well-defined element-wise interpolation of the state-space system in this representation can be performed.
- The 30th-order "stage 2" control law (DGK-iteration, see Sect. 6.3) is of low authority and robust against considerable plant dynamics variations. Validation of the fixed control law with plants and the scheduled stage 1 control law across the entire flight envelope shows Robust Stability (RS). However, the added performance in terms of vibration attenuation at the design case at cruise flight conditions becomes marginal or lost as the plant parameters differ too much. This could be repaired by redesigns of the "stage 2" control law in other flight parameter points, but due to the associated effort this is out of scope here. For a posteriori scheduling onsets refer to [14, 15].
- The feed-forward control law developed in this section is robustly designed for a particular Mach and Dynamic Pressure parameter case to provide Robust Performance (RP) for all fuel and CG cases. It turned out that it is necessary to parameterize the feed-forward control law by the Mach and Dynamic Pressure parameters to achieve the demanded high performance. This interpolation can also be done in an a posteriori manner and it is simplified by utilizing the same set of basis functions for all designs. Then, only the optimization variables (the weightings θ_i) need to be interpolated. The optimization problem can directly be extended to consider multiple models with perturbed Mach and Dynamic Pressure parameters, however, increasing the size of the problem. Note also that the feed-forward law cannot destabilize the (linear) aircraft model.

7.2.4 Validation

The optimization is carried out and yields a dynamic controller $\mathbf{Q}(s)$ which satisfies all constraints and minimizes the roll maneuver-induced total loads with respect to sizing load levels. As a result, a typical optimization result for loads alleviation is shown in Fig. 7.16 for a representative case in cruise flight conditions and cut moment My_{13}. In this maneuver, all constraints (tracking, rise time, settling, undershoot) on the roll response, side-slip decoupling and input magnitudes and rates are satisfied. As an example, the roll response and the demanded template are shown in Fig. 7.17 for the same parameter case.

Note that this specific formulation of the objective allows uncritical loads to increase in favor of further reduction in the critical load levels, which is correct for the considered global optimization goal.

The final validation over the entire relevant parameter space is shown in Sect. 8.1.4.

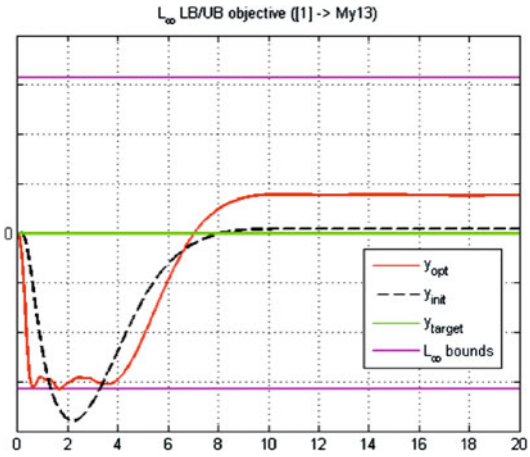

Fig. 7.16 Typical loads reduction result (selected parameter case at cruise flight conditions at cut My_{13}) for an optimal feed-forward controller satisfying all roll maneuver requirements robustly

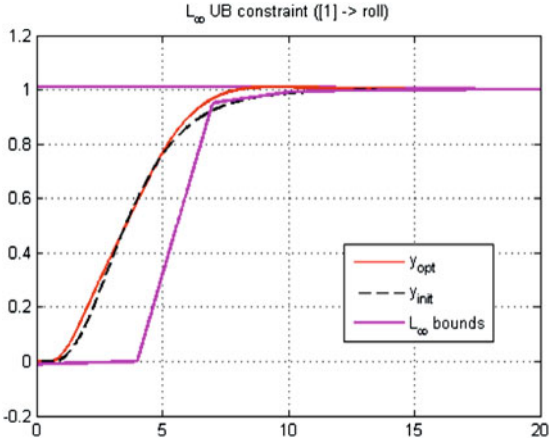

Fig. 7.17 Typical roll tracking performance for an optimal feed-forward controller (selected parameter case at cruise flight conditions)

7.3 Maneuver Loads Alleviation System Via $\mathscr{H}_\infty$ Full-Information Feed-Forward Design

C. Westermayer, A. Schirrer and M. Kozek

The design methodology for the feed-forward controller presented in the following is based on the so-called two degree of freedom (2DOF) concept. The fundamentals of this concept can be found in [18, 23], where the separation of feedback and feed-forward controllers is introduced by the use of two stable Youla parameters. While in the literature various approaches based on the 2DOF concept are reported [5, 8, 10, 13], the feed-forward control design approach shown here is based on the findings in [11, 12]. Therein, an $\mathscr{H}_\infty$ full-information approach is presented for both,

reference signal tracking and measurable disturbance rejection. The optimization problem is formulated as an LMI optimization problem and its applicability for the linear parameter varying (LPV) case is discussed. This design is carried out for the ACFA BWB configuration for the longitudinal dynamics. It has been developed in detail in [19] and published in [21].

7.3.1 Methodology

7.3.1.1 2DOF Concept and Feed-Forward Design

Starting point of the presented design methodology is based on the fact that the design of feedback and feed-forward controller can be decoupled. This is demonstrated in [9, 12] for the general 2DOF control architecture as shown in Fig. 7.18 (left). Therein, the decoupling is revealed by splitting up the control signal into $\mathbf{u} = \mathbf{K}_{\mathrm{ff}}\mathbf{r} + \mathbf{K}_{\mathrm{fb}}\mathbf{y}$ and rewriting it in terms of two stable Youla parameters for parametrization and a right fractional coprime factorization of the system plant $\mathbf{G}$.

As indicated in the right diagram of Fig. 7.18, the input to the feedback controller $\mathbf{K}_{\mathrm{fb}}$ is the difference between the ideal system response provided by the prefilter or feed-forward controller $\mathbf{K}_{\mathrm{ff}}$ and the real measurements. The only input to $\mathbf{K}_{\mathrm{ff}}$ is the reference command, while its generated control signal is acting directly on the system $\mathbf{G}$. The independence of $\mathbf{K}_{\mathrm{ff}}$ from $\mathbf{K}_{\mathrm{fb}}$ enables self-contained focusing on design specifications most relevant for feed-forward control, which in terms of $\mathscr{H}_\infty$ design and according to the Bounded Real Lemma is expressed by a performance path, where $\|\mathbf{T}\|_\infty \leq \gamma$ is to be minimized. This is indicated in Fig. 7.19 where $\mathbf{T}_{zr}$ is obtained by a lower Linear Fractional Transformation (LFT) of the augmented plant $\mathbf{P}$ and the state feedback matrix $\mathbf{F}$.

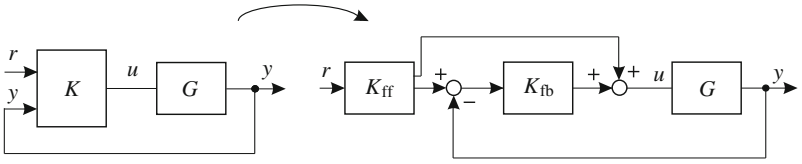

Fig. 7.18 General 2DOF architecture

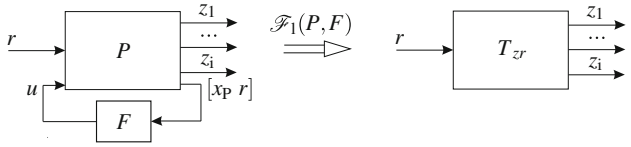

Fig. 7.19 Generalized closed loop and optimization transfer function matrix $\mathbf{T}_{zr}$ obtained by a lower LFT

Thereby, the augmented plant $\mathbf{P}$ has to be built such that the particular design specifications are met. $\mathbf{P}$ is again an interconnection of the system plant $\mathbf{G}$, frequency weightings $\mathbf{W}_i$ and additionally a reference model $\mathbf{T}_{\text{ref}}$ to be tracked. Details on their formulation for the given problem will be presented in Sect. 7.3.3. It is important to note that according to Fig. 7.19 the feedback vector is composed of the state vector $\mathbf{x}_\text{P}$ and the reference input vector $\mathbf{r}$. Both are assumed to be known which reasons the name full-information design.

7.3.1.2 Full-Information LMI Optimization Problem

Before the LMI optimization problem can be formulated, the closed-loop system has to be derived. Therefore, the open-loop representation

$$\begin{bmatrix} \dot{\mathbf{x}}_\text{P} \\ \mathbf{z} \\ \mathbf{x}_\text{P} \\ \mathbf{r} \end{bmatrix} = \underbrace{\begin{bmatrix} \mathbf{A}_\text{P} & \mathbf{B}_{\text{P}_1} & \mathbf{B}_{\text{P}_2} \\ \mathbf{C}_{\text{P}_1} & \mathbf{D}_{\text{P}_{11}} & \mathbf{D}_{\text{P}_{12}} \\ \mathbf{I} & \mathbf{0} & \mathbf{0} \\ \mathbf{0} & \mathbf{I} & \mathbf{0} \end{bmatrix}}_{\mathbf{P}} \begin{bmatrix} \mathbf{x}_\text{P} \\ \mathbf{r} \\ \mathbf{u} \end{bmatrix} \tag{7.42}$$

and the full-information control law $\mathbf{u} = \mathbf{F}_1\mathbf{x} + \mathbf{F}_2\mathbf{r}$ have to be connected, yielding

$$\begin{bmatrix} \dot{\boldsymbol{x}}_\text{P} \\ \mathbf{z} \end{bmatrix} = \underbrace{\begin{bmatrix} \mathbf{A}_\text{P} + \mathbf{B}_{\text{P}_2}\mathbf{F}_1 & \mathbf{B}_{\text{P}_1} + \mathbf{B}_{\text{P}_2}\mathbf{F}_2 \\ \mathbf{C}_{\text{P}_1} + \mathbf{D}_{\text{P}_{12}}\mathbf{F}_1 & \mathbf{D}_{\text{P}_{11}} + \mathbf{D}_{\text{P}_{12}}\mathbf{F}_2 \end{bmatrix}}_{\mathbf{T}} \begin{bmatrix} \mathbf{x}_\text{P} \\ \mathbf{r} \end{bmatrix}, \tag{7.43}$$

where the static feedback matrix $\mathbf{F} = [\mathbf{F}_1, \mathbf{F}_2]$ was appropriately partitioned. With the closed-loop system defined, the procedure to derive the full-information optimization LMI is equivalent to a pure state feedback design. The finally obtained results are given by the following proposition.

Proposition 7.1 [12] *Consider the system* (7.43)*. If there exist matrices* $\boldsymbol{F}_2$, $\bar{\boldsymbol{Y}}$ *and* $\bar{\boldsymbol{Q}} = \bar{\boldsymbol{Q}}^\text{T}$*, such that* $\bar{\boldsymbol{Q}} > 0$ *and*

$$\begin{bmatrix} \boldsymbol{A}_\text{P}\bar{\boldsymbol{Q}} + \bar{\boldsymbol{Q}}\boldsymbol{A}_\text{P}^\text{T} + \boldsymbol{B}_{\text{P}_2}\bar{\boldsymbol{Y}} + \bar{\boldsymbol{Y}}^\text{T}\boldsymbol{B}_{\text{P}_2}^\text{T} & \boldsymbol{B}_{\text{P}_1} + \boldsymbol{B}_{\text{P}_2}\boldsymbol{F}_2 & (\boldsymbol{C}_{\text{P}_1}\bar{\boldsymbol{Q}} + \boldsymbol{D}_{\text{P}_{12}}\bar{\boldsymbol{Y}})^\text{T} \\ (\boldsymbol{B}_{\text{P}_1} + \boldsymbol{B}_{\text{P}_2}\boldsymbol{F}_2)^\text{T} & -\gamma\boldsymbol{I} & (\boldsymbol{D}_{\text{P}_{11}} + \boldsymbol{D}_{\text{P}_{12}}\boldsymbol{F}_2)^\text{T} \\ \boldsymbol{C}_{\text{P}_1}\bar{\boldsymbol{Q}} + \boldsymbol{D}_{\text{P}_{12}}\bar{\boldsymbol{Y}} & \boldsymbol{D}_{\text{P}_{11}} + \boldsymbol{D}_{\text{P}_{12}}\boldsymbol{F}_2 & -\gamma\boldsymbol{I} \end{bmatrix} < 0 \tag{7.44}$$

hold, then

1. *the matrix* $\boldsymbol{A}_\text{P}$ *is exponentially stable and*
2. *there exists a scalar* $\gamma > 0$ *such that* $||T_{zr}||_\infty < \gamma$ *holds.*

If a feasible solution is obtained, the optimal $\mathscr{H}_\infty$ static full-information feedback matrix is given by:

$$\mathbf{F}_\text{opt} = [\mathbf{Y}\mathbf{Q}^{-1}, \mathbf{F}_2]. \tag{7.45}$$

An important fact is that the full-information LMI formulation of Proposition 7.1 can be extended to linear parameter varying systems $\mathbf{G}(\boldsymbol{\rho})$ with system matrices $\mathbf{A}_\mathrm{G}(\boldsymbol{\rho})$, $\mathbf{B}_\mathrm{G}(\boldsymbol{\rho})$, $\mathbf{C}_\mathrm{G}(\boldsymbol{\rho})$, $\mathbf{D}_\mathrm{G}(\boldsymbol{\rho})$ depending affinely on the parameter vector $\boldsymbol{\rho}(t)$. However, for the given model of the BWB aircraft, a polytopic representation is not directly available, that is, the system matrices are not described as affine functions of the parameter vector from the outset.

7.3.1.3 Deriving the Final Feed-Forward Controller $\mathbf{K_{ff}}$

The result of the LMI optimization according to Proposition 7.1 is the optimal feedback matrix $\mathbf{F}_\mathrm{opt}$. In order to obtain the final feed-forward controller $\mathbf{K}_\mathrm{ff}$, the output and feed-through matrices $\mathbf{C}_{\mathrm{P}_1}$ and $\mathbf{D}_{\mathrm{P}_{11}}$, $\mathbf{D}_{\mathrm{P}_{12}}$ of the augmented plant $\mathbf{P}$ have to be replaced by [12]

$$\mathbf{C}_{\mathrm{P}_{\mathrm{ff},1}} = \begin{bmatrix} \mathbf{E}\mathbf{C}_\mathrm{G} & \mathbf{0}\ \mathbf{0}\ \mathbf{0}\ \mathbf{0} \\ \mathbf{0} & \mathbf{0}\ \mathbf{0}\ \mathbf{0}\ \mathbf{0} \end{bmatrix}, \quad \mathbf{D}_{\mathrm{P}_{\mathrm{ff},11}} = \begin{bmatrix} \mathbf{0} \\ \mathbf{0} \end{bmatrix}, \quad \mathbf{D}_{\mathrm{P}_{\mathrm{ff},12}} = \begin{bmatrix} \mathbf{E}\mathbf{D}_\mathrm{G} \\ \mathbf{I} \end{bmatrix} \tag{7.46}$$

yielding

$$\mathbf{P}_\mathrm{ff} = \begin{bmatrix} \mathbf{A}_\mathrm{P} & \mathbf{B}_{\mathrm{P}_1} & \mathbf{B}_{\mathrm{P}_2} \\ \mathbf{C}_{\mathrm{P}_{\mathrm{ff},1}} & \mathbf{D}_{\mathrm{P}_{\mathrm{ff},11}} & \mathbf{D}_{\mathrm{P}_{\mathrm{ff},12}} \\ \mathbf{I} & \mathbf{0} & \mathbf{0} \\ \mathbf{0} & \mathbf{I} & \mathbf{0} \end{bmatrix}. \tag{7.47}$$

The index $\mathbf{G}$ refers to the system plant and the selector matrix $\mathbf{E}$ is used to select all outputs $\mathbf{y}$ used by the feedback controller $\mathbf{K}_\mathrm{fb}$. As evident from Fig. 7.20 the feed-forward controller is the result of the lower LFT

$$\mathbf{K}_\mathrm{ff} = \mathscr{F}_\mathrm{l}(\mathbf{P}_\mathrm{ff}, \mathbf{F}_\mathrm{opt}). \tag{7.48}$$

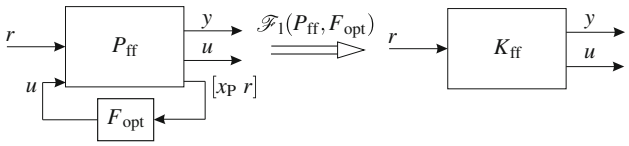

Fig. 7.20 Modified generalized closed-loop including the optimal solution $\mathbf{F}_\mathrm{opt}$ (*left*) and final feed-forward controller $\mathbf{K}_\mathrm{ff}$ obtained by a lower LFT (*right*)

7.3.2 Design Goals and Problem Definition

The design specifications (as listed in Chap. 5) to be addressed in the feed-forward controller design process are given as follows:

1. Track the reference command input given by the vertical acceleration at the CG position Nz_{CG}. The rise time of Nz_{CG} to a unit step command input must be between 3–5 s and no overshoot is tolerated.
2. Overshoot of accompanying pitch rate response at the CG position, q_{CG}, must be lower than 30 %.
3. Constrain the demanded control signals by maximum deflection and deflection rate limits according to Table 5.1.
4. Minimize maximum structural loads caused by maneuver tracking. As reference maneuvers serve $+1.5$ and -1.0 g Nz_{CG} reference steps, where $g = 9.81\ m/s^2$.

All these specifications have to be fulfilled over the considered flight envelope. The performance of the designed controllers has to be demonstrated together with the feedback control law. Here, the LPV feedback control law from Sect. 6.5 is utilized.

7.3.3 Control Design

7.3.3.1 Design Architecture

The first step of the $\mathscr{H}_\infty$ full-information feed-forward design process is to define an appropriate design architecture representing a standard problem formulation in the $\mathscr{H}_\infty$ framework which addresses the essential design specifications. The augmented plant used in this work is shown in Fig. 7.21.

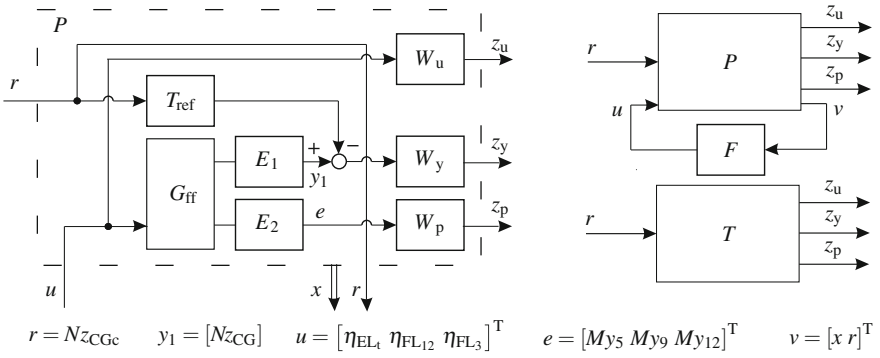

Fig. 7.21 *Left* augmented plant for feed-forward full-information control design; *Right* generalized closed loop

The performance weights $\mathbf{W}_u$, $\mathbf{W}_y$, and $\mathbf{W}_\mathrm{p}$ have to be appropriately chosen in order to enforce the desired performance during optimization. Details on these choices are given in Sect. 7.3.3.2. The systems $\mathbf{G}_\mathrm{ff}$, $\mathbf{T}_\mathrm{ref}$, $\mathbf{W}_u$, $\mathbf{W}_y$, and $\mathbf{W}_\mathrm{p}$ are given in state-space representation $(\mathbf{A}_i, \mathbf{B}_i, \mathbf{C}_i, \mathbf{D}_i)$, where the index i is used as placeholder for the aforementioned system names. Interconnecting these systems according to Fig. 7.21 leads to the augmented system $\mathbf{P}$ in state-space form

$$\begin{bmatrix} \dot{\boldsymbol{x}}(t) \\ \mathbf{z}(t) \\ \mathbf{x}(t) \\ r(t) \end{bmatrix} = \underbrace{\left[\begin{array}{c|cc} \mathbf{A}_\mathrm{P} & \mathbf{B}_{\mathrm{P}_1} & \mathbf{B}_{\mathrm{P}_2} \\ \hline \mathbf{C}_{\mathrm{P}_1} & \mathbf{D}_{\mathrm{P}_{11}} & \mathbf{D}_{\mathrm{P}_{12}} \\ \mathbf{I} & \mathbf{0} & \mathbf{0} \\ \mathbf{0} & \mathbf{I} & \mathbf{0} \end{array}\right]}_{\mathbf{P}} \begin{bmatrix} \mathbf{x}(t) \\ r(t) \\ \mathbf{u}(t) \end{bmatrix}, \tag{7.49}$$

where

$$\mathbf{A}_\mathrm{P} = \begin{bmatrix} \mathbf{A}_{\mathrm{G}_\mathrm{ff}} & \mathbf{0} & \mathbf{0} & \mathbf{0} & \mathbf{0} \\ \mathbf{B}_{\mathrm{W}_\mathrm{y}}\mathbf{E}_1\mathbf{C}_{\mathrm{G}_\mathrm{ff}} & \mathbf{A}_{\mathrm{W}_\mathrm{y}} & \mathbf{0} & \mathbf{0} & -\mathbf{B}_{\mathrm{W}_\mathrm{y}}\mathbf{C}_{\mathrm{T}_\mathrm{ref}} \\ \mathbf{0} & \mathbf{0} & \mathbf{A}_{\mathrm{W}_\mathrm{u}} & \mathbf{0} & \mathbf{0} \\ \mathbf{B}_{\mathrm{W}_\mathrm{p}}\mathbf{E}_2\mathbf{C}_{\mathrm{G}_\mathrm{ff}} & \mathbf{0} & \mathbf{0} & \mathbf{A}_{\mathrm{W}_\mathrm{p}} & \mathbf{0} \\ \mathbf{0} & \mathbf{0} & \mathbf{0} & \mathbf{0} & \mathbf{A}_{\mathrm{T}_\mathrm{ref}} \end{bmatrix}, \tag{7.50}$$

$$\mathbf{B}_{\mathrm{P}_1} = \begin{bmatrix} \mathbf{0} \\ -\mathbf{B}_{\mathrm{W}_\mathrm{y}}\mathbf{D}_{\mathrm{T}_\mathrm{ref}} \\ \mathbf{0} \\ \mathbf{0} \\ \mathbf{B}_{\mathrm{T}_\mathrm{ref}} \end{bmatrix}, \quad \mathbf{B}_{\mathrm{P}_2} = \begin{bmatrix} \mathbf{B}_{\mathrm{G}_\mathrm{ff}} \\ \mathbf{B}_{\mathrm{W}_\mathrm{y}}\mathbf{E}_1\mathbf{D}_{\mathrm{G}_\mathrm{ff}} \\ \mathbf{B}_{\mathrm{W}_\mathrm{u}} \\ \mathbf{B}_{\mathrm{W}_\mathrm{p}}\mathbf{E}_2\mathbf{D}_{\mathrm{G}_\mathrm{ff}} \\ \mathbf{0} \end{bmatrix}, \tag{7.51}$$

$$\mathbf{C}_{\mathrm{P}_1} = \begin{bmatrix} \mathbf{D}_{\mathrm{W}_\mathrm{y}}\mathbf{E}_1\mathbf{C}_{\mathrm{G}_\mathrm{ff}} & \mathbf{C}_{\mathrm{W}_\mathrm{y}} & \mathbf{0} & \mathbf{0} & -\mathbf{D}_{\mathrm{W}_\mathrm{y}}\mathbf{C}_{\mathrm{T}_\mathrm{ref}} \\ \mathbf{0} & \mathbf{0} & \mathbf{C}_{\mathrm{W}_\mathrm{u}} & \mathbf{0} & \mathbf{0} \\ \mathbf{D}_{\mathrm{W}_\mathrm{p}}\mathbf{E}_2\mathbf{C}_{\mathrm{G}_\mathrm{ff}} & \mathbf{0} & \mathbf{0} & \mathbf{C}_{\mathrm{W}_\mathrm{p}} & \mathbf{0} \end{bmatrix}, \tag{7.52}$$

$$\mathbf{D}_{\mathrm{P}_{11}} = \begin{bmatrix} -\mathbf{D}_{\mathrm{W}_\mathrm{y}}\mathbf{D}_{\mathrm{T}_\mathrm{ref}} \\ \mathbf{0} \\ \mathbf{0} \end{bmatrix}, \quad \mathbf{D}_{\mathrm{P}_{12}} = \begin{bmatrix} \mathbf{D}_{\mathrm{W}_\mathrm{y}}\mathbf{E}_1\mathbf{D}_{\mathrm{G}_\mathrm{ff}} \\ \mathbf{D}_{\mathrm{W}_\mathrm{u}} \\ \mathbf{D}_{\mathrm{W}_\mathrm{p}}\mathbf{E}_2\mathbf{D}_{\mathrm{G}_\mathrm{ff}} \end{bmatrix}. \tag{7.53}$$

Both, the state vector of the augmented plant $\mathbf{x}$ and the reference input vector $\mathbf{r}$ are known, forming together the full-information feedback vector. Therefore, the feedback law can be written as $\mathbf{u} = \mathbf{F}\mathbf{v} = \mathbf{F}_1\mathbf{x} + \mathbf{F}_2\mathbf{r}$, with $\mathbf{F}$ as the static feedback matrix. The generalized closed-loop is shown in the right drawing of Fig. 7.21. Using a lower LFT $\mathbf{T} = \mathscr{F}_\mathrm{l}(\mathbf{P}, \mathbf{F})$ leads to the performance transfer paths from r to z_y, $\mathbf{z}_\mathrm{u}$ and $\mathbf{z}_\mathrm{p}$ to be minimized:

$$\left\| \begin{matrix} \mathbf{T}_{z_u,r} \\ \mathbf{T}_{z_y,r} \\ \mathbf{T}_{z_p,r} \end{matrix} \right\|_\infty < \gamma. \tag{7.54}$$

Due to the resulting complexity originating from the state feedback law, a more detailed decomposition of the single performance transfer paths $\mathbf{T}_i$ is not considered at this point. Three possible approaches for solving the $\mathscr{H}_\infty$ optimization problem of (7.54) in MATLAB® are:

1. Building the interconnected structure according to Fig. 7.21 and using the function `hinfsyn` with the method setting `ric`. Using this setting, the full-information gain matrix is included in the output argument `info`.
2. Instead of the `hinfsyn` also the function `msfsyn` can be used. The advantage of this function is that it can be applied to linear parameter varying systems with its parameters varying in a polytope.
3. Formulating the appropriate LMIs according to Proposition 7.1 and introducing the system matrices (7.50)–(7.53). The LMIs can be solved using for example the LMI solver `mincx` of the Robust Control Toolbox of MATLAB® [1].

The third option has been shown to be more efficient and can also be extended to the LPV design case. With the optimal feedback gain matrix $\mathbf{F}_{\text{opt}}$ as the primary optimization result of (7.54), the feed-forward controller $\mathbf{K}_{\text{ff}}$ is obtained as outlined in Sect. 7.3.1.3 by the lower LFT $\mathbf{K}_{\text{ff}} = \mathscr{F}_l(\mathbf{P}_{\text{ff}}, \mathbf{F}_{\text{opt}})$, where $\mathbf{P}_{\text{ff}}$ is the modified augmented plant.

7.3.3.2 Reference Model and Performance Weighting Function Definition

To fulfill the required design specifications, an appropriate reference model as well as a correct shape for the performance weighting functions have to be selected:

Reference model T_{ref}: The reference model selected for the model matching problem must first of all fulfill the requirements concerning rise time, overshoot, and settling time of the controlled variable Nz_{CG} to be tracked. Moreover, it is advantageous to incorporate existing actuator dynamics G_{act} and sensor delays G_{sen} in the reference model since these dynamics represent hard constraints for the attainable tracking response which cannot be ignored in the design. Therefore, the reference model T_{ref} consists of three components

$$T_{\text{ref}} = G_{\text{sen}} G_{\text{ref}} G_{\text{act}}, \tag{7.55}$$

where G_{sen} is a first-order Padé approximation with 160 ms delay and G_{act} is the linearized model of the slowest actuator, the combined elevator EL_{t}:

$$G_{\text{sen}} = \frac{(s - 12.5)}{(s + 12.5)}, \quad G_{\text{act}} = \frac{7.5}{s^2 + 3.9s + 7.5}. \tag{7.56}$$

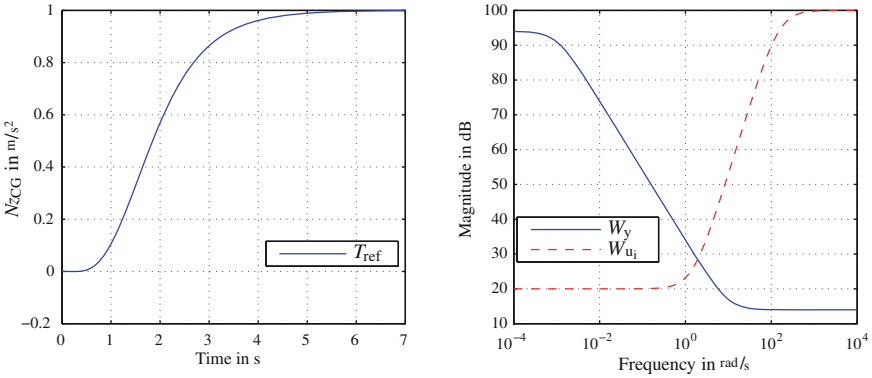

Fig. 7.22 *Left* T_{ref} time response representing an ideal Nz_{CG} command response; *Right* frequency response plot of weighting functions $\mathbf{W}_y$ and $\mathbf{W}_{\text{u}_\text{i}}$

The reference transfer function is given by a second-order system

$$G_{\text{ref}} = \frac{\omega^2}{s^2 + 2\zeta\omega s + \omega^2} \tag{7.57}$$

with its parameters set to $\omega = 1.5\,\text{rad/s}$ and $\zeta = 1$. The corresponding time response of the reference model T_{ref} is shown in Fig. 7.22 (left).

Command tracking $\mathbf{W}_y$: For command tracking, the difference between the reference model T_{ref} and the system output to be tracked must be minimized. This can be achieved by a low-pass filter of the form

$$\mathbf{W}_y = t_{\text{y1}} \frac{s + t_{\text{y2}} \cdot 10}{s + t_{\text{y2}} \cdot 0.001}, \tag{7.58}$$

as shown in Fig. 7.22 (right), with the corresponding tuning parameters t_{y1} and t_{y2} appropriately set (see also Sect. 7.3.3.3).

Control energy $\mathbf{W}_u$: The control energy demanded by the feed-forward controller for reference model tracking can be adjusted by high-pass filters of the form

$$\mathbf{W}_u = \begin{bmatrix} t_{\text{u11}} \frac{(s+t_{\text{u21}}\cdot 1)^2}{(s+t_{\text{u21}}\cdot 100)^2} & 0 & 0 \\ 0 & t_{\text{u12}} \frac{(s+t_{\text{u22}}\cdot 1)^2}{(s+t_{\text{u22}}\cdot 100)^2} & 0 \\ 0 & 0 & t_{\text{u13}} \frac{(s+t_{\text{u23}}\cdot 1)^2}{(s+t_{\text{u23}}\cdot 100)^2} \end{bmatrix}, \tag{7.59}$$

with their general shape shown in Fig. 7.22 (right). The tuning factor t_{u1i} serves to limit the absolute deflections, while t_{u2i} is used to constrain the deflection rates. According to the actuator properties, the tuning factor t_{u2i} is highest for the outmost flap FL_3. Second-order filters are utilized to ensure a sufficiently steep roll-off and

thereby minimize excitation of the aeroelastic modes by the maneuver. This is most important, according to the open-loop analysis in Sect. 5.1.3.2, for the control surfaces at the wing, FL_{12} and FL_3.

Maneuver loads $\mathbf{W}_p$: The maximum Maneuver loads primarily originate from the static content and the first wing bending mode as will be shown below. Therefore, static weighting has shown to be sufficient for the performance outputs:

$$\mathbf{W}_p = \begin{bmatrix} t_{p1} & 0 & 0 \\ 0 & t_{p2} & 0 \\ 0 & 0 & t_{p3} \end{bmatrix}. \tag{7.60}$$

7.3.3.3 Controller Tuning

With the design architecture according to Sect. 7.3.3.1 and the general shape of corresponding weighting functions as defined in Sect. 7.3.3.2, the subsequent design step is the selection of the tuning factors. This can be carried out either manually or in an automated way as will be presented in the following.

Manual Tuning

Manually adjusting the factors of the performance weighting functions (7.58)–(7.60) is not a trivial task when several design specifications have to be considered simultaneously. However, a basic understanding of the tuning possibilities, is similar to the feedback design case, crucial for a successful control design. Exemplarily, t_{y1} is varied to show the effect on tracking performance and t_{p1} is varied to evaluate the effect on Maneuver loads control. In Fig. 7.23, the unit step time response of $\mathbf{K}_{ff}$ from r to Nz_{CG}, q_{CG}, and η_{EL_t} is shown. Therefore, t_{y1} was increased stepwise from $t_{y1} = 0.01$, where $t_{y1} = 1$ represents an optimized setting. In spite of the large tuning parameter variation, the effect on the tracking performance is moderate. Increasing t_{y1} improves tracking performance and also requires faster control inputs. The effect of increased t_{p1} is presented in Fig. 7.24. There, Maneuver loads at the wing root $My5$ and at the outer wing My_{12} are compared. Increasing the weighting on one load output typically leads to reduced Maneuver loads at this and adjacent cut positions, however, this can also cause increased loads at more distant load outputs (waterbed effect). Basically it has been shown that including the wing bending load outputs My also positively affects the vertical force load outputs Fz. In general, a strong relation between load outputs and control energy outputs is evident.

Automated Tuning

In order to accelerate the aforementioned tuning parameter selection, an automated approach similar as mentioned in Sect. 6.5.3.3 for feedback control design

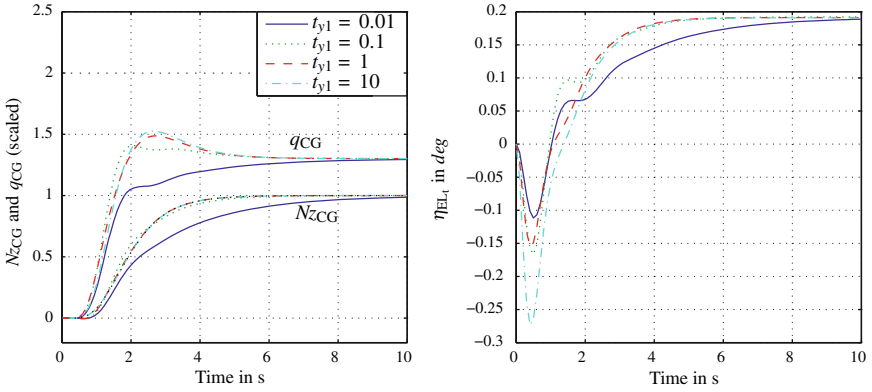

Fig. 7.23 *Left* unit step time response of $\mathbf{K}_{\mathrm{ff}}$ from r to Nz_{CG} and q_{CG} for increasing tuning factor t_{y1}; *Right* corresponding $\eta_{\mathrm{EL_t}}$ time response

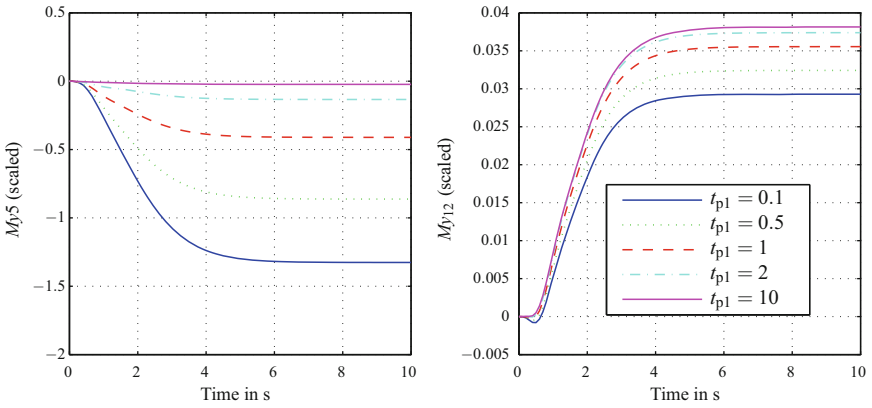

Fig. 7.24 *Left* unit step time response of $\mathbf{K}_{\mathrm{ff}}$ from r to $My5$ for increasing tuning factor t_{p1}; *Right* corresponding My_{12} time response

is described in this section. Therefore, several optimization criteria c_i must be formulated for the design specifications listed in Sect. 7.3.2 mathematically. The following criteria are based on a reference command step $r = 1.5$ g, which is a typical validation step to investigate maximum control deflections and rates. For the sake of brevity $y_1(t) = y_{\mathrm{Nz_{CG}}}(t)$ and $y_2(t) = y_{\mathrm{q_{CG}}}(t)$ are introduced and the reference response for Nz_{CG} is denoted by y_{ref}:

1. Minimization of the deviation from the Nz_{CG} reference model time response:

$$c_1 = \sum_{t_i=1}^{5} (y_1(t_i) - y_{\mathrm{ref}}(t_i))^2 \tag{7.61}$$

2. Limitation of the q_{CG} overshoot:

$$c_2 = \begin{cases} (\frac{\hat{y}_2}{\bar{y}_2})^2 - 1.3^2, & \text{if } \frac{\hat{y}_2}{\bar{y}_2} > 1.3 \\ 0, & \text{otherwise,} \end{cases} \tag{7.62}$$

where

$$\hat{y}_2 = \max_{t<10} y_2(t), \ \bar{y}_2 = y_2(t = 10) \tag{7.63}$$

is the maximum and the stationary value of $y_2(t)$, respectively.

3. Limitation of the control energy:

$$c_3 = \begin{cases} (\frac{\hat{\eta}_i}{\eta_{\mathrm{i,max}}})^2, & \text{if } \frac{\hat{\eta}_i}{\eta_{\mathrm{i,max}}} > 0.95 \\ 0, & \text{otherwise,} \end{cases} \tag{7.64}$$

$$c_4 = \begin{cases} (\frac{\hat{\dot{\eta}}_i}{\dot{\eta}_{\mathrm{i,max}}})^2, & \text{if } \frac{\hat{\dot{\eta}}_i}{\dot{\eta}_{\mathrm{i,max}}} > 0.95 \\ 0, & \text{otherwise,} \end{cases} \tag{7.65}$$

where

$$\hat{\eta}_i = \max_{t<10} |\eta_i(t)|, \ \hat{\dot{\eta}}_i = \max_{t<10} |\dot{\eta}_i(t)| \tag{7.66}$$

is the maximum deflection and deflection rate of the demanded control signal, respectively, while $\eta_{\mathrm{i,max}}$, $\dot{\eta}_{\mathrm{i,max}}$ are specified actuator properties.

4. Minimization of Maneuver loads: for maneuver load reduction, a comparative value is necessary. Here, it is obvious to use Maneuver loads obtained with the LPV feedback controller $\hat{M}_{yi,\mathrm{fb}}$ according to Sect. 6.5 for comparison:

$$c_5 = \left(\frac{h_i \cdot \hat{M}_{yi,\mathrm{ff}}}{\hat{M}_{yi,\mathrm{fb}}} \right)^2, \tag{7.67}$$

where

$$\hat{M}_{yi,\mathrm{ff}} = \max_{t<10} M_{yi,\mathrm{ff}}(t), \quad \hat{M}_{yi,\mathrm{fb}} = \max_{t<10} M_{yi,\mathrm{fb}}(t). \tag{7.68}$$

The factor h_i is a weighting factor indicating the impact of the load output in the optimization. Typically, this factor is set to the value $1 \leq h_5 \leq 2$ for the load output at the wing root My_5 and to the value $0.95 \leq h_{9,12} \leq 1.2$ for the outer positions My_9, My_{12}. The primary goal of the optimization is to reduce loads at the inner wing (cut position 3–7) without increasing the loads at the outer wing.

All these criteria are summed up and form the final cost function to minimize:

$$\min_{t_{y1},t_{u11},t_{u12},t_{u13},t_{p1},t_{p2},t_{p3}} \left\{ \sum_{i=1}^{5} c_i \right\} \tag{7.69}$$

The tuning parameters t_{y2}, t_{u21}, t_{u22}, t_{u23} are not included in the optimization. These are determined a priori and kept constant during the optimization. In order to solve the optimization problem (7.69), again different optimization tools can be applied at this stage. Similar to the feedback design case, a genetic algorithm is utilized (see Sect. 6.5.3.3).

7.3.3.4 A Posteriori Scheduling

Up to now, only the nominal design case was considered for the feed-forward controller. Now, also the parameter varying case will be investigated. Then, the dynamics of the linear design plant is parameter dependent $\mathbf{G}_{\mathrm{ff}} = \mathbf{G}_{\mathrm{ff}}(\boldsymbol{\rho}(t))$, where $\boldsymbol{\rho}(t)$ represents the flight parameters θ_q and θ_{Ma} as well as the fuel-mass parameter θ_{fuel}. The fuel-mass parameter is also taken into consideration since the obtained RP over its parameter range was not satisfactory. The parameter dependency of the plant implies that the augmented plant according to (7.49)–(7.53) is parameter dependent $\mathbf{P} = \mathbf{P}(\boldsymbol{\rho}(t))$, with weighting functions $\mathbf{W}_u$, $\mathbf{W}_y$ and $\mathbf{W}_{\mathrm{p}}$ determined as shown in Sect. 7.3.3.3. In order to account for the parameter dependency, an a posteriori scheduling approach due to linear interpolation was considered.

This approach is composed of the following design steps:

1. Perform an automated weighting factor optimization according to Sect. 7.3.3.3 on a rough gridding comprising the flight envelope of interest.
2. Validate the obtained grid point controllers.
3. Design intermediate grid point controllers using weighting functions obtained by linear interpolation of the weighting functions from the rough gridding.
4. Perform element-wise linear interpolation of the system matrices $\mathbf{A}, \mathbf{B}, \mathbf{C}, \mathbf{D}$ from the finely gridded $\mathbf{K}_{\mathrm{ff,i}}$.

In Fig. 7.25 the Nz_{CG} and q_{CG} responses of the linearly interpolated controllers $\mathbf{K}_{\mathrm{ff,i}}$ to a unit reference step are shown exemplarily for the parameters $\theta_q = 9{,}000$, $\theta_{\mathrm{fuel}} = 91\,\%$ and $0.82 \leq \theta_{\mathrm{Ma}} \leq 0.835$. The response hardly changes with varying θ_{Ma} number. In the right plot, the corresponding $\eta_{\mathrm{EL_t}}$ time response is plotted. Strong variations of the control signal for only moderate changes in θ_{Ma} number become evident.

In [19] also an LPV design scheduling approach including the vertex plants in the LMI optimization was applied and verified. Comparing the results of both approaches has shown that a better performance is obtained with the a posteriori scheduling approach for the given application. For that reason this approach was chosen to design the parameter-dependent feed-forward controller over the entire considered operating range. The finally obtained results are presented in the next chapter.

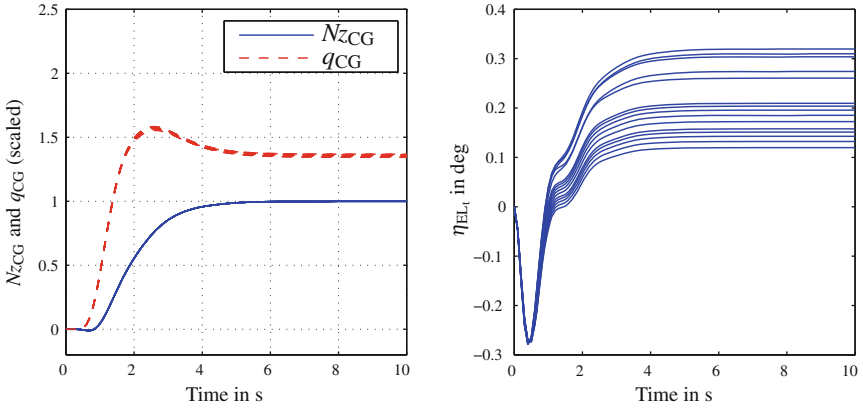

Fig. 7.25 *Left* unit step response of a posteriori scheduled $\mathbf{K}_{\mathrm{ff}}i$ from r to Nz_{CG} and q_{CG} for $0.82 \leq \theta_{\mathrm{Ma}} \leq 0.835$ and $\theta_q = 9{,}000$; *Right* corresponding $\eta_{\mathrm{EL_t}}$ time response

7.3.4 Validation

This section reports on the validation of the obtained parameter-dependent feed-forward controller $\mathbf{K}_{\mathrm{ff}}(\theta_{\mathrm{Ma}}, \theta_q, \theta_{\mathrm{fuel}})$ in order to assess the performance improvement obtained by this prefilter. These results were already presented in [20]. Before considering the obtained results, however, it is important to note that $\mathbf{K}_{\mathrm{ff}}$ is validated together with the LPV feedback controller $\mathbf{K}_{\mathrm{fb}}$, forming together a 2DOF control architecture according to Fig. 7.18. In order to directly express the obtained performance improvements given by $\mathbf{K}_{\mathrm{ff}}$, again the validation plots show the system response to an $r = 1.5$ g reference step command. Moreover, such reference step size also enables to evaluate maximum Maneuver loads as will be shown in the following.

7.3.4.1 Command Response Behavior and Maneuver Load Reduction

For evaluation of the command response, again essential flight mechanic data Nz_{CG}, q_{CG}, Nz_{f}, and C^* are provided in Fig. 7.26 for a representative set of validation models. The Nz_{CG} response has similar characteristics independent of the parameter case and fulfills the requirements concerning rise time and overshoot. A slightly rippled response after $t = 3.5$ s can be observed for some of the validation models. This can be explained by a higher deviation of the linearized actuator model used for design from the nonlinear model. This deviation is only moderately compensated by the feedback controller and therefore visible in the time response. The q_{CG} response is not as pure as the Nz_{CG} response, however, also in this case a significant improvement in comparison to feedback control only appears. The maximum overshoot can be reduced significantly and the maximum overshoot requirement of 30 % is exceeded

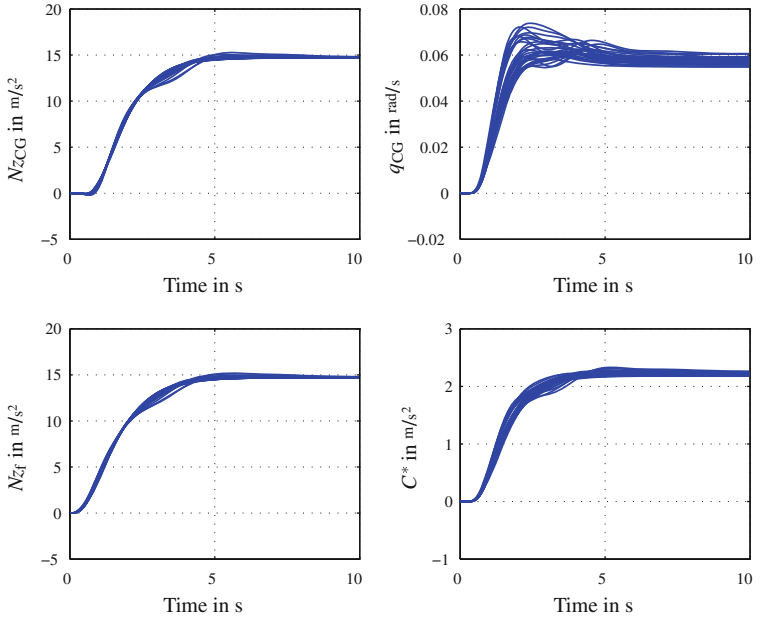

Fig. 7.26 2DOF flight mechanic data time response to $r = 1.5\,\mathrm{g}$ reference step command for representative validation models chosen from the parameter envelope

for a few cases only. The Nz_f response is hardly different from the Nz_{CG} response, while for C^* the spreading effect of q_{CG} is visible.

In Fig. 7.27 the demanded control surface deflections η_i and deflection rates $\dot{\eta}_i$ of $\mathbf{K}_{ff}$ are shown for the combined elevator EL_t, the combined inner flap FL_{12}, and the outer flap FL_3. While the deflection rate signals $\dot{\eta}_i$ are rather similar for the various parameter cases, in the deflection signals η_i a broad spreading is visible, indicating the strong variations in low-frequency system dynamics. Both, maximum deflections and deflection rates are well below the given limits for the respective actuators. During design, special attention was paid to keep the necessary deflections for FL_{12} comparatively low, since this flap is mainly used for the roll maneuvers in lateral control. However, only additional tests can ensure that this actuator does not exceed the deflection limits in extremal coordinated turn maneuvers. The deflection of FL_3 is slightly higher but still below the maximum deflection limits.

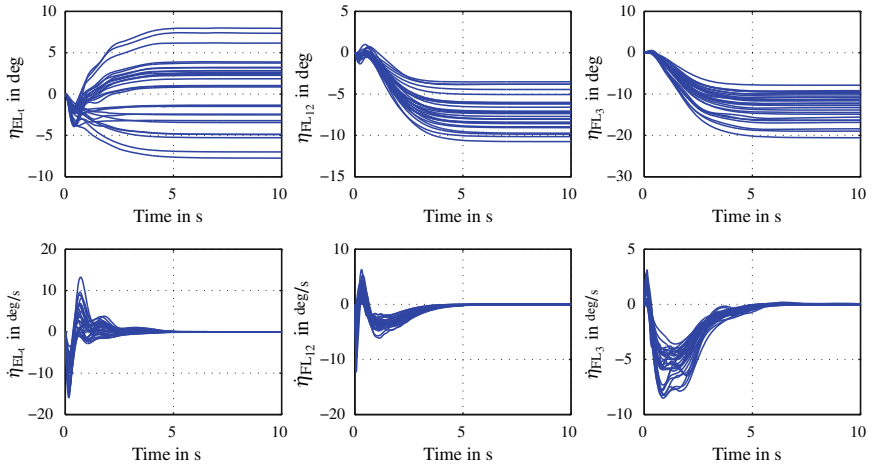

Fig. 7.27 $\mathbf{K}_{\mathrm{ff}}$ control input deflection and deflection rate time responses to $r = 1.5\,\mathrm{g}$ reference command step for representative validation models chosen from the parameter envelope

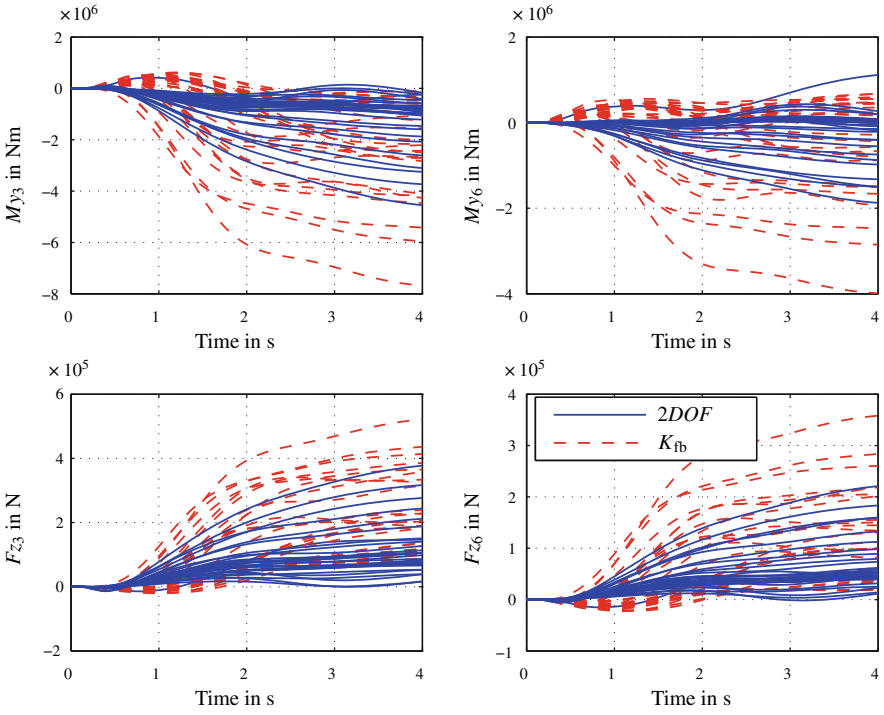

Fig. 7.28 Load output time response comparison of $\mathbf{K}_{\mathrm{fb}}$ and 2DOF for an $r = 1.5\,\mathrm{g}$ reference step command and representative validation models chosen from the parameter envelope

Finally, in Fig. 7.28 a comparison of the Maneuver loads time response obtained for $\mathbf{K}_{\text{fb}}$ only (solid) and for the 2DOF concept (dashed) based on representative load outputs is provided. Thereby, a significant reduction of incremental loads is visible for all outputs, which emphasizes the effectiveness of the chosen control design approach.

References

1. Balas G, Chiang R, Packard A, Safonov M (2010) MATLAB robust control toolbox 3, user's guide. MathWorks
2. Boyd S, Barratt C, Norman S (1990) Linear controller design: limits of performance via convex optimization. Proc IEEE 78:529–574
3. Boyd S, El Ghaoui L, Feron E, Balakrishnan V (1994) Linear matrix inequalities in system and control theory. vol 15 SIAM
4. Boyd S, Vandenberghe L (2004) Convex optimization. Cambridge University Press, Cambridge
5. Cerone V, Milanese M, Regruto D (2007) Robust feedforward design for a two-degrees of freedom controller. Syst Control Lett 56:736–741
6. Dardenne I (1999) Développement de méthodologies pour la synthèse de lois de commande d'un avion de transport souple. PhD thesis, Ecole Natrionale Supérieure de l'Aéronautique et de l'Espace (SUPAERO), France, 1999. (English: Development of methodologies for control law synthesis for a flexible transport aircraft)
7. Ferreres G, Roos C (2005) Efficient convex design of robust feedforward controllers. In: Proceedings 44th IEEE conference on decision and control and European control conference, pp 6460–6465
8. Hoyle DJ, Hyde RA, Limebeer DJN (1991) An $\mathscr{H}_\infty$ approach to two degree of freedom design. In: Proceedings of the 30th conference on decision and control, Brighton, England
9. Limebeer DJN, Kasenally EM, Perkins JD (1993) On the design of robust two degree of freedom controllers. Automatica 29(1):157–168
10. Prempain E, Bergeon B (1998) A multivariable two-degree-of-freedom control methodology. Automatica 34(12):1601–1606
11. Prempain E, Postlethwaite I (2000) A new two-degree-of-freedom gain scheduling method applied to the Lynx MK7. J Syst Control Eng 214(1):299–311
12. Prempain E, Postlethwaite I (2001) Feedforward control: a full-information approach. Automatica 37:17–28
13. Prempain E, Postlethwaite I (2008) A feedforward control synthesis approach for LPV systems. In: Proceedings of the American control conference, pp 3589–3594
14. Rugh WJ, Shamma JS (2000) Survey paper: research on gain scheduling. Automatica 36:1401–1425
15. Schirrer A (2011) Efficient robust control design and optimization methods for flight control. PhD thesis, Vienna University of Technology
16. Schirrer A, Westermayer C, Hemedi M, Kozek M (2011) Multi-model convex design of a scheduled lateral feedforward control law for a large flexible BWB aircraft. In: Preprints of the 18th IFAC world congress, Milano, Italy, pp 2126–2131
17. Sima D (2001) LMI optimization in connection with quadratic and nonlinear functions. In: Proceedings of the 3rd Niconet workshop on numerical software in control and engineering, Belgium, pp 91–96
18. Vidyasagar M (1987) Control system synthesis: a factorization approach. MIT Press, Cambridge
19. Westermayer C (2011) 2DOF parameter-dependent longitudinal control of a blended wing body flexible aircraft. PhD thesis, Vienna University of Technology

20. Westermayer C, Schirrer A, Hemedi M, Kozek M (2011) An $\mathscr{H}_\infty$ full information appoach for the feedforward controller design of a large BWB flexible aircraft. In: Proceedings of the 4th EuCASS, St. Peterburg, Russia
21. Westermayer C, Schirrer A, Hemedi M, Kozek M (2013) An $\mathscr{H}_\infty$ full information approach for the feedforward controller design of a large blended wing body flexible aircraft. In: Progress in flight dynamics, guidance, navigation, control, fault detection, and avionics, vol 6, EDP Sciences, pp 685–706
22. Wildschek A, Haniš T, Stroscher F (2013) $\mathscr{L}_\infty$-optimal feedforward gust load alleviation design for a large blended wing body airliner. In: Progress in flight dynamics, guidance, navigation, control, fault detection, and avionics, vol 6, EDP Sciences, pp 707–728
23. Youla D, Bongiorno J (1985) A feedback theory of two-degree-of-freedom optimal wiener-hopf design. IEEE Trans Autom Control 30:652–665

Part III
Validation and Discussion

Chapter 8
Validation, Discussion and Outlook

M. Kozek, A. Schirrer, F. Stroscher, M. Valášek, Z. Šika, T. Vampola, T. Belschner and A. Wildschek

8.1 Main Results and Validation

M. Kozek, A. Schirrer, F. Stroscher, M. Valášek, Z. Šika, T. Vampola and T. Belschner

8.1.1 Aircraft Design

Conceptual designs for two configurations, a 450-passenger blended wing body (BWB) and an ultra-wide-body aircraft with carry-through wing box (CWB), were performed by Technical University of Munich and AIRBUS. Both aircraft were designed for the same mission roughly defined by the following parameters:

- Long-Range Cruise Mach number: 0.85
- Maximum range at Max Pax Payload: 7,200 nm
- Approach speed should be <150 kt
- Maximum operating Mach number MMO: 0.89
- Maximum operating speed VMO: 340 kt CAS
- Max cruise altitude: 43,100 ft

M. Kozek (✉) · A. Schirrer
Vienna University of Technology, Vienna, Austria
e-mail: martin.kozek@tuwien.ac.at

F. Stroscher
Technische Universität München, Munich, Germany

M. Valášek · Z. Šika · T. Vampola
Czech Technical University in Prague, Prague, Czech Republic

T. Belschner
University of Stuttgart, Stuttgart, Germany

A. Wildschek
Airbus Group Innovation (formerly EADS Innovation Works), Munich, Germany

M. Kozek and A. Schirrer (eds.), *Modeling and Control for a Blended Wing Body Aircraft*,
Advances in Industrial Control, DOI 10.1007/978-3-319-10792-9_8

The concurrent design was mainly done to compare the BWB configuration to a more conventional design in particular with respect to fuel efficiency. It turned out that the BWB aircraft shows about 13 % better fuel efficiency compared to the CWB aircraft which is mainly due to lower weight of the BWB and better aerodynamic performance. Therefore, the BWB configuration was retained for further work on active control concepts.

The final BWB configuration has a very blended shape between the center body and the outer wing in order to get a smooth load and lift distribution along the blended wing span. A quite high sweep and aft position of the wing is important to make the aircraft stable. The BWB provides a lot of space underneath the cabin for the center tank and so it can be efficiently used to trim the aircraft during cruise. However, this makes the fuel system safety critical because it must be operational to keep the aircraft center of gravity within an acceptable range. More details about fuel management concepts can be found in [13]. The longitudinal control is done by rear elevons located both on the center body and on the wing (except aft of the engine pylons). The area dedicated to those movables is rather high in order to provide sufficient control authority. The lateral control is critical on this aircraft, especially in the one engine out case, and is achieved by split ailerons and rather high winglets equipped with a rudder. A detailed description of the design can be found in [13].

Two engines are located on the upper side of the center body so it is expected to provide efficient shielding for the fan noise. Unfortunately in the frame of the ACFA 2020 project, it was not possible to assess the exterior noise benefit of this configuration versus a classic aircraft of the same size. However, a small study on interior noise comfort was performed with respect to turbulent boundary layer noise, which is the major noise source in cruise condition. Statistical energy analysis was applied for a portion of the cargo/cabin area, whereby some optimization of the cabin treatment was performed. The BWB shows significant lower noise levels than the CWB and both aircraft are quieter than a generic conventional single aisle aircraft configuration which was used as an additional reference. With respect to cabin noise one can conclude that the BWB configuration is quite favorable.

8.1.2 Dynamic Modeling

The generation of aeroelastic parameterized reduced-order models (ROMs) for the NACRE and ACFA 2020 BWB was a joint effort of numerous partners (DLR, FOI, ONERA, HAI, NTUA, TUM). In order to consider several fuel/payload cases, a set of structural models representing the various mass configurations were developed for both aircraft. A structural model was provided by the NACRE consortium but was significantly refined to make it applicable for structural dynamics investigations. The steady and unsteady aerodynamics for the NACRE and the ACFA 2020 BWB have been calculated for a variety of flight conditions, that is, Mach numbers, dynamic pressure, center of gravity positions and mass cases. In order to be able to use spoiler

devices for the controller design, aerodynamic loads (lift, drag, pitching moment) were calculated by using an unsteady vertex blob code.

For the control system design low-order models have been used which comprise only 2–6 flexible modes and use simplified linear actuator and sensor models. By application of adequate order reduction methods (balanced truncation, singular perturbation approximation (SPA)) it is assured that the input/output (I/O) behavior is preserved in an optimal way. During the control design process higher order models comprising around 12 modes and also more detailed nonlinear actuator and sensor models have been used to validate the robustness of the controller designs. Finally, full order models (80 modes for the ACFA 2020 BWB) are used to evaluate the loads for the structural resizing.

Model inputs are the control surface deflections and engine thrust as well as gusts. For the modeling of the gust response a set of gust inputs have been considered whereby as inputs 2D von-Kármán turbulence models are used. Model outputs are the rigid-body (RB) motion, accelerations at preselected positions for vibration damping [8] as well as cut forces and moments for estimation of control performance and critical cases with respect to loads. Regarding the comfort criteria, CTU developed filters (for example, sea sickness) delivering comfort outputs based on the states of the aeroelastic models [26].

8.1.3 Control Concepts

Control design for a large flexible aircraft and in particular the BWB configuration is a quite challenging task due to numerous objectives and severe constraints which have to be taken simultaneously into account. Major goal of the ACFA 2020 project was to investigate and to combine various modern robust control and linear parameter varying (LPV) design techniques as well as adaptive control concepts. Basic feedback control is augmented by an additional feed-forward control path to alleviate the effect of turbulence and gusts. To achieve the desired handling qualities and to alleviate maneuver loads also a feed-forward control path for pilot commands is used.

A large variety of design methods ($\mathscr{H}_\infty$-, $\mathscr{H}_2$-optimal control design, $\mathscr{H}_\infty$ fixed-order optimization methods) and robust and scheduled extensions of these methods have been applied. Furthermore, modern convex synthesis design techniques have been investigated. An adaptive multi-input multi-output (MIMO) feed-forward control concept has been investigated to mitigate turbulence induced vibrations and related loads. To validate the real-time behavior of the adaptation a flight test with the DLR Advanced Technologies Testing Aircraft (ATTAS) has been performed [24]. This aircraft is already equipped with sensors and actuators to flight test active feed-forward gust and vibration control concepts [5, 7]. The signal power of the lateral engine acceleration was reduced by 40 % by the converged feed-forward controller. In principle, the converged controller can be always active which provides Robust Performance (RP) of the feed-forward loop also in case of plant uncertainties

or plant variations with time. Alternatively, adaptation could be just used during flight testing and transformed into a fixed or scheduled controller for regular operation.

The adaptive feed-forward control concept has been also successfully applied to the NACRE BWB to control the first wing bending mode. This significantly improves the ride comfort but the effects on loads (wing root moments) were partially detrimental in particular for discrete gusts which are typically most important for the structural sizing. The basic concept and main results can be found in [24]. It is beneficial to add active damping to the structure by feedback control and to combine this with a feed-forward gust load alleviation system (GLAS) deploying the spoilers when entering a gust. For the ACFA 2020 BWB an even more advanced gust loads alleviation system using optimization techniques to determine the best sequence of control surface deployments has been developed.

The comprehensive work on control design for the ACFA 2020 BWB has been presented in several papers at the EUCASS conference 2011. Robust and LPV control techniques [3, 16, 19], low-complexity control system design [6] as well as adaptive Neural-Network-based control design have been investigated. Each of the investigated control concepts delivered promising results with respect to the main goals and most of the methods are complementary. For example, a feed-forward GLAS was combined with an LPV controller [21]. It is important to mention that the flight mechanics of the ACFA 2020 BWB is quite challenging for control design mainly due to two facts:

- Actuator dynamics was chosen rather slow; for example, elevator bandwidth is 0.5 Hz due to the large size and weight of the large control surface.
- The aerodynamics of the ACFA 2020 BWB is in a predesign stage. In the transonic region strong nonlinear effects are present due to a complex shock system which results in strong fluctuations also in the flight dynamic properties with variation of dynamic pressure and angle of attack.

Summarizing, the control design task was much more challenging as it would be for a more optimized aircraft design. Nevertheless, the controlled ACFA 2020 BWB configuration fulfills handling quality requirements while showing significantly reduced loads and reasonable ride comfort. This illustrates the power of the applied modern control design techniques.

8.1.4 Sizing Loads Alleviation

A comparison of maneuver loads and loads caused by turbulence gusts is essential in order to detect the source and magnitude of maximum dynamical structural loads. For a subsequent structural resizing process, the maximum total loads, which are the sum of the static trim loads and the dynamic loads from maneuvers and gusts, have to be determined. For longitudinal control, the maximum structural loads of the controlled aircraft under the multistage control concept comprised of the LPV feedback controller (Sect. 6.5) and the $\mathscr{H}_\infty$ full-information feed-forward controller (Sect. 7.3) have been evaluated. For lateral control, the multistage concept consisting of the

robust eigen structure assignment initial controller (Sect. 6.2), the DGK-iteration feedback controller (Sect. 6.3) and the multimodel feed-forward Maneuver loads alleviation controller (Sect. 7.2) has been utilized.

8.1.4.1 Extremal Structural Loads in Longitudinal Maneuvers and Gusts

Figures 8.1 and 8.2 show a comparison of maximum positive and negative total loads (sum of static and dynamic loads) over all cut positions along the wing and over the flight envelope for three longitudinal simulation test cases:

1. Updraft and downdraft gusts (Gu and Gd) (blue), where the response to all defined $1 - \cos$ gusts is evaluated
2. $+1.5$ and $-1.0\,$g maneuver (Mp and Mn) using $\mathbf{K}_{\text{fb}}$ controller only (red)
3. $+1.5$ and $-1.0\,$g maneuver using 2DOF controller (magenta-dotted).

The worst-case structural gust load at each cut position is then compared to the worst-case structural maneuver loads, as presented in Figs. 8.1 and 8.2. When considering Fig. 8.1 it turns out that the absolute maximum bending moments My_{i} are caused by maneuvers using feedback controller $\mathbf{K}_{\text{fb}}$ only. The absolute maximum gust loads are approximately 20 % lower than the arising Maneuver loads. Due to feed-forward maneuver load control, the maximum Maneuver loads can be reduced up to 35 % and render the gust loads the new sizing loads. This result holds over the entire wing span as can be seen also in the right plot. A similar characteristics is given for the vertical force load outputs Fz_i in Fig. 8.2. Again, the 2DOF controller reduces the cut forces significantly, which renders the gust loads sizing.

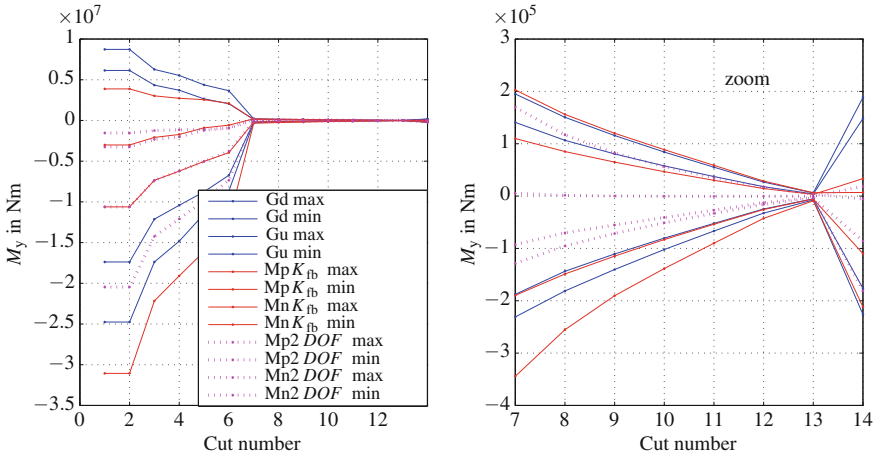

Fig. 8.1 Comparison of maximum and minimum total cut moments My_i over all cut positions i along the wing and over the flight envelope for various validation cases

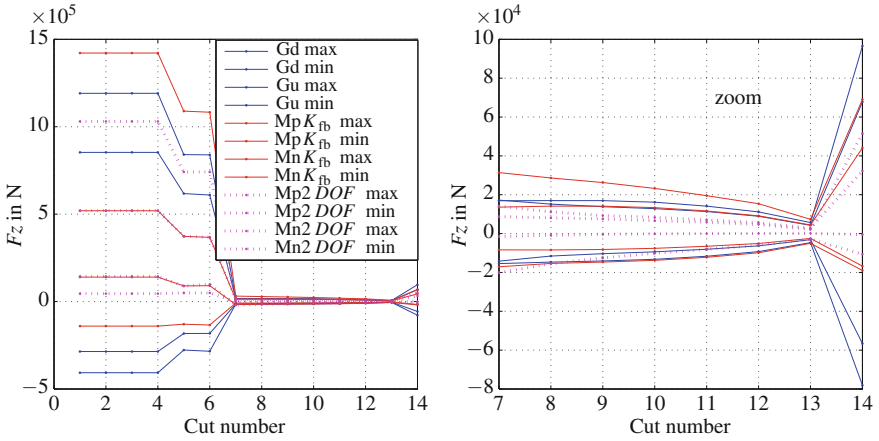

Fig. 8.2 Comparison of maximum and minimum total cut forces Fz_i over all cut positions along the wing and over the flight envelope for various validation cases

8.1.4.2 Extremal Structural Loads in Lateral Maneuvers and Gusts

The extremal loads in lateral maneuvers (60° roll maneuver) and for lateral gusts have been evaluated over the given validation set. Figure 8.3 shows the extremal absolute cut moments. The maximum and minimum values both for longitudinal and lateral cases form the basis for the subsequent resizing task.

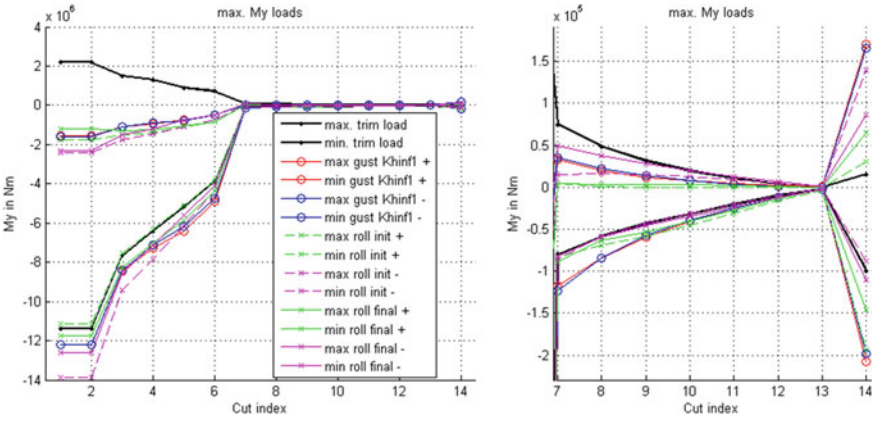

Fig. 8.3 Extremal total cut moments for lateral (60° roll) maneuver and gusts

8.1.5 Resizing and Mass Reduction

In a final step, the wing of the ACFA 2020 BWB was resized taking into account the loads reduction achieved by active loads alleviation. The resizing was formulated as a structural optimization problem for the wing area of the ACFA 2020 BWB. MSC Nastran SOL200 was used to solve the optimization problem. The considered region for sizing is the upper and lower panels of the wing box, ranging from wing root to the tip of the winglet. The only objective is minimization of total mass whereby several constraints are considered, namely strain constraints depending on material strength, static stability (buckling) and flutter constraints. The flutter speed is assessed by the MSC Nastran dynamic aeroelastic analysis, SOL145. The maneuver case is sizing without loads alleviation, whereas with loads alleviation gust and maneuver loads become equally important. In total, a structural weight saving of about 4 t, out of 19 t mass of a single wing box has been achieved. About 25 % of this weight saving is due to active loads alleviation. The flutter constraint was quite important and formed the main limitation for the possible weight saving. The separation of loads analysis and structural design limited the effectiveness and flexibility of the resizing process. The results collected in this section are partly adopted from [22].

8.1.5.1 Strategy for the Assessment of Structural Weight Saving by Load Alleviation

It was demonstrated before that the active load alleviation techniques are able to reduce the structural loading in terms of wing bending. Therefore, a structural sizing task has been performed where flight loads derived from the transient simulations are employed. Two structural redesigns in terms of wall thickness were derived, one without and one with using load alleviation. The difference in total mass of these serves as measure for weight saving by load alleviation.

A numerical optimization problem is formulated as structural sizing approach. A gradient-based design optimization task is set up with the MSC Nastran design optimization tool (SOL200), which is an established and efficient tool for sizing optimization. For the computation of design responses and sensitivities, linear static analysis of the BWB finite element (FE) model is applied. The solver uses equivalent static load cases, derived from simulation results from the time-domain simulation model of the BWB aircraft. A single objective, minimization of total mass, is applied. Structural strain constraints are considered, depending on material strength and static stability (buckling). The considered region for sizing is the upper and lower panels of the wing box, ranging from wing root to the tip of the winglet.

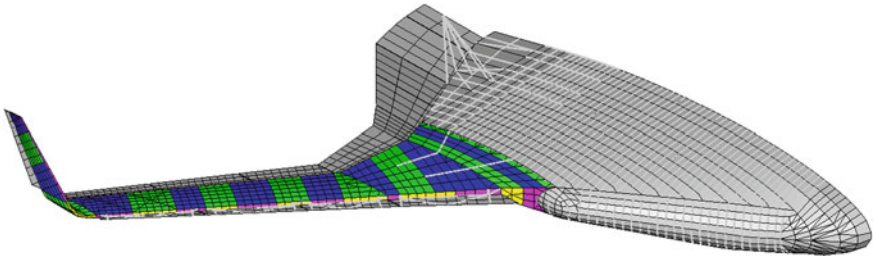

Fig. 8.4 FE model with design zones of the wingbox

8.1.5.2 Setup of the Design Optimization Model

The FE model of the BWB aircraft configuration is used as baseline model for structural optimization. For the whole wing box primary structure, the finite element properties are modified and reorganized. The wing box is subdivided into 18 design zones, as shown in Fig. 8.4. Within each of these, the shell properties of skin panels, spars and ribs remain constant. A common quasi-orthotropic laminate is chosen for stringers and skin, whose principle stiffness axis is oriented span wise. The design variables are stringer thickness and skin thickness of the individual wing box design zones. In total 36 design variables are employed.

The objective of the optimization problem is minimization of the total mass of the half-span FE model. The initial configuration was designed with 10 mm skin and stringer thickness for all design zones. The mass of the initial configuration at MTOW configuration is 190.0 t. This configuration is used as starting point in optimization.

As constraints, the extreme values of composite strain are employed. First, a strength criterion is used, which is based on the first-ply-failure theory. The allowable strains are directly taken from the worst cases for the ply failure strains, which normally are below 1 % for carbon fiber composite materials. Second, panel buckling of the wing box skin is considered via additional strain constraints. The maximum allowable in-plane strains for structural stability are computed individually for each design zone within the optimization procedure.

Another constraint in optimization is the flutter speed, which is assessed by the MSC Nastran dynamic aeroelastic analysis (SOL145). From the experiences in flutter analysis of the BWB aircraft, the lowest flutter speed occurred at maximum weight configuration. Thus, the flutter check of the optimized configurations is performed for symmetric boundary conditions at maximum weight configuration. From the flight envelope of the BWB aircraft the critical target flutter point is at 225 m/s equivalent air speed at sea level and Mach number 0.65. In optimization a structural layout is found that fulfills this requirement by constraining the damping value above the flutter speed to negative numbers, which corresponds to positive physical damping and thus dynamic stability.

The considered flight load cases for the resizing activity are provided in terms of time histories of all relevant states during maneuver or gust loads simulation.

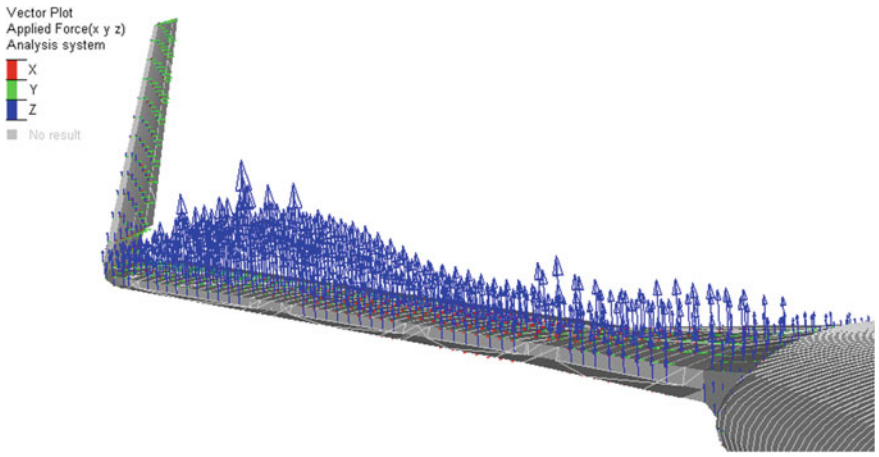

Fig. 8.5 Force distribution (X, Y, Z-direction) of an equivalent static load case of a maneuver simulation

The so-called mode displacement method was found to be an appropriate way to derive static FE load vectors from simulation results, which recover the same deflections as appear in time domain simulation. With modal displacement histories η_e given, as well as the eigenvectors Φ_{ge} and stiffness matrix in physical coordinates $\mathbf{K}_{gg}$ of the FE model, an equivalent static load vector can be derived, as denoted in (8.1).

$$\begin{Bmatrix} F_i \\ M_i \end{Bmatrix} = \mathbf{K}_{gg} \Phi_{ge} \eta_e \tag{8.1}$$

The resulting equivalent forces F_i and moments M_i at all degrees of freedom are now applied to the FE model, see Fig. 8.5. Static analysis results into a displacement situation at a specific point in time, during the underlying transient simulation.

8.1.5.3 Results of the Optimization Process

The optimization converges in about 20 design iterations, with comparatively low computational effort, due to the efficient derivation of analytical sensitivities. As mentioned before, two sizing tasks are performed, one without and one with load alleviation. A total structural mass of 256 t is achieved without using load alleviation and 254 t, thus 2 t or 1 % less, when using load alleviation. Compared to the total structural mass, this is not an impressive number, but in relation to the wing structure only ($\approx$15 t each) it becomes more significant. Finally it is worth mentioning that the outer wing thickness remains relatively high, even when applying load alleviation, as shown in Fig. 8.6. This is due to a minimum required torsional stiffness of the outer wing, in order to fulfill the flutter constraint. It can be concluded that flutter prevents a minimum weight design, fully taking advantage of active load alleviation.

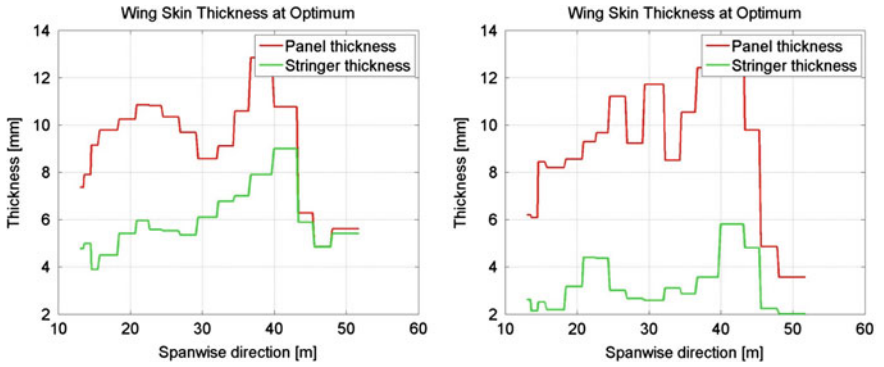

Fig. 8.6 Thickness distribution of wingbox panels and stringers at optimized configuration (*left* without, *right* with load alleviation)

8.1.6 Comfort Evaluation

8.1.6.1 Vibration Comfort Criteria

The comfort assessment of the examined aircraft was developed by setting up the selected comfort criteria and by their connection to the structural model of the examined aircraft of the type of flying wing. The comfort is a peculiar phenomenon where the fully objective processes as the vibrations meet with the fully subjective processes of human perception of vibration comfort. Moreover, the vibration comfort must be decomposed into two distinct human phenomena—the proper vibration comfort and the sea sickness. Both of them are relevant to the aircraft design. This chapter summarizes the evaluation of the ride comfort assessment of the developed aircraft concept ACFA 2020.

The vibration comfort criteria both for the proper vibration comfort and the sea sickness are used the implementation of the British Standard BS 6841:1987 [2]. It is similar but more operationally described than the equivalent standards ISO 2631-1:1997/VDI 2057 [9]. The implementation was done in Simulink and connected to the ROM with control of ACFA 2020. This describes the whole-body vibration influence on a human being and his/her feeling. The investigated person is a sitting person on a vibrating seat. The translational vibration modes in x (longitudinal), y (lateral), z (vertical) directions at the seat, at the back and at the feet and the rotational modes around the x, y, z directions at the seat of the sitting person are considered. The different vibration excitation (in different places, in different axes) are measured, processed by RMS, then frequency weighted by filtering, then weighted by their importance, and finally added as vector components (Fig. 8.7). The evaluation process from Fig. 8.7 is formulated within BS 6841 [2] in the following form

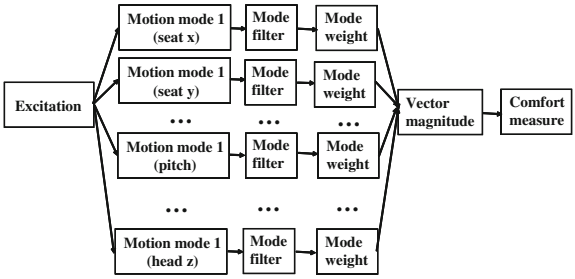

Fig. 8.7 The evaluation process of vibration comfort

$$a = \Big(k_x W_d a_x^2 + k_y W_d a_y^2 + k_z W_k a_z^2 + k_r W_e r_x^2 + k_r W_e r_y^2 + k_r W_e r_z^2 + k_x W_c a_{bx}^2 + k_y W_d a_{by}^2 + k_z W_k a_{bz}^2 + k_x W_k a_{fx}^2 + k_y W_k a_{fy}^2 + k_z W_k a_{fz}^2\Big)^{1/2} \tag{8.2}$$

where W_x are frequency weights and k_x are weights of vibration mode importance described in the standard [2]. The filters are described by the transfer functions in the Laplace domain.

$$H_b(s) = \frac{4\pi^2 f_2^2 s^2}{(s^2 + 2\pi f_1/Q_1 s + 4\pi^2 f_1^2)(s^2 + 2\pi f_2/Q_1 s + 4\pi^2 f_2^2)} \tag{8.3}$$

$$H_w(s) = \frac{s + 2\pi f_3}{s^2 + 2\pi f_4/Q_2 s + 4\pi^2 f_4^2} \frac{2\pi K f_4^2}{f_3} \tag{8.4}$$

and also

$$H_w(s) = \frac{(s + 2\pi f_3)(s^2 + 2\pi f_5/Q_3 s + 4\pi^2 f_5^2)}{(s^2 + 2\pi f_4/Q_2 s + 4\pi^2 f_4^2)(s^2 + 2\pi f_6/Q_4 s + 4\pi^2 f_6^2)} \frac{2\pi K f_4^2 f_6^2}{f_3 f_5^2} \tag{8.5}$$

The complete frequency weights are then computed as

$$\begin{aligned} W_c &= H_b(s) H_w(s), \quad W_d = H_b(s) H_w(s), \\ W_e &= H_b(s) H_w(s), \quad W_g = H_b(s) H_w(s) \end{aligned} \tag{8.6}$$

Based on the filter coefficients in [2] the filters were implemented in MATLAB/Simulink® for the further connection with the aircraft model and the amplitude characteristics of filters are depicted in Fig. 8.8. These evaluation criteria cover the influence on one person. They have been combined for different positions of seats

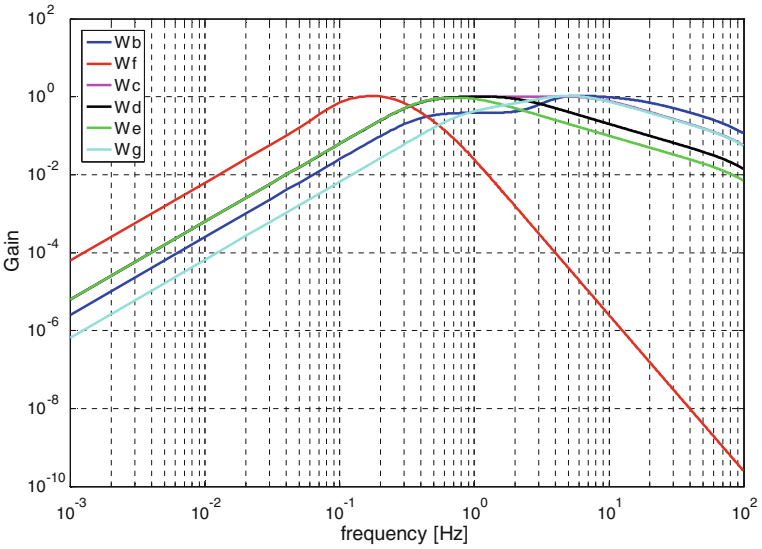

Fig. 8.8 Amplitude characteristics of transfer functions of comfort filters based on BS 6841

and their attachment to the aircraft structure. Two types of vibration phenomena are considered: the proper vibration comfort and the sea sickness.

8.1.6.2 ACFA 2020 Model Extension for Vibration Comfort Assessment

The vibration comfort criteria described in this section are valid for the impression of one person and has to be applied for the whole aircraft. According to the investigation there are two main problems. The first problem is the influence of the interaction of the human body with the passenger seat. The human body is an active member in the influence of vibrational excitation on the human body that modifies the influence described in the previous chapter. The passenger seat is a vibrational filter between the external excitation and the human body. The direct implementation of the active human body and the passenger seat is difficult because the parameters are missing or difficult to be identified. The other problem is the resulting computational complexity. Because of the lack of design parameters of details of passenger seats for ACFA 2020 and the computational complexity it was decided to replace the model of the interaction of active human body with the passenger seat by the integrated passenger-seat model (Fig. 8.9) based on the experiments and identification carried out by project partners CTU, FME, and DLR [17]. The second problem is the influence of the aircraft cabin floor on which the passenger seats are mounted. The problem is that the cabin floor is generally a complicated structural element the influence of which must be somehow integrated into the ROMs used for control design and testing. Consequently, the control design naturally leads to a design iteration. The initial

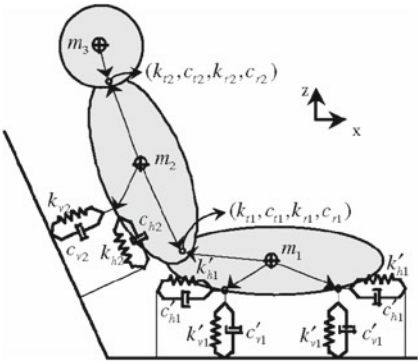

Fig. 8.9 Concept of integrated model of a sitting passenger with the seat

cabin floor design was integrated into the ROM of ACFA 2020 and used for control design. Subsequently, the influence of the improved cabin floor model on the resulting vibration comfort has been investigated. The consequence of this investigation is that the new improved cabin floor model is working like a low-pass filter with the cut off frequency at 5 Hz. The solution to both of these problems has required the following ACFA model extensions for the vibrational comfort assessment.

8.1.6.3 Experiments with Aircraft Seat and Its Identification

The experimental investigations of the dynamic characteristics of the seats are required for performing the correct comfort modeling [17]. Therefore the goal is the experimental identification of the transmissibility functions from the floor of an aircraft cabin through a typical passenger seat to the sitting person. For this purpose, a multiaxial vibration simulator MAVIS has been utilized (Fig. 8.10). A typical passenger seat with the test dummies is mounted on the vibrating table. All experiments were performed at the test laboratory of the Institute of Aeroelasticity of DLR in Göttingen. The measurement of transmissibility functions was performed with two different tests signals. First, a sine sweep signal was used. The sine sweep signal was applied at three different levels. In addition to the translational axes x, y, z, also the rotational motions φ_x, φ_y, φ_z were excited. The level for the rotational axes was selected in that way that the vibration severity was comparable to the translational axes. Table 8.1 lists the characteristics of the sine sweep excitation for the three levels and the different excitation axes. Second, a broadband random signal was applied at one level. Once the response at the cabin floor is available, the transmissibility functions identified here can be used for evaluation of vibration levels that the passengers are exposed to. To investigate the influence of possible nonlinearities in more detail the transmissibility functions of the different levels of sine sweep excitation were compared to each other. The structural behavior at the low level is reasonably linear. The verification of computational models should therefore be mainly accomplished with data of the low level, if the models are assumed to be linear.

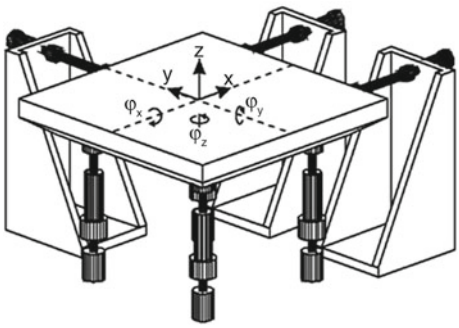

Fig. 8.10 Scheme of structure of multiaxial vibration simulator MAVIS

Table 8.1 Characteristics of applied sine sweep excitations

Level	Axis	Frequency		Velocity (oct/min)
		1–2 Hz	10–40 Hz	
Low	x, y, z	2.5 mm	0.125 g	2
Medium	x, y, z	5.0 mm	0.250 g	2
High	x, y, z	10.0 mm	0.500 g	2
Low	$\varphi_x, \varphi_y, \varphi_z$	0.025 rad	1.25 rad/s^2	2
Medium	$\varphi_x, \varphi_y, \varphi_z$	0.050 rad	2.50 rad/s^2	2
High	$\varphi_x, \varphi_y, \varphi_z$	0.100 rad	5.00 rad/s^2	2

The identification of seat model parameters were carried out based on experimental results. The measured frequency response data (transmissibility functions) between 6 components (x, y, z, φ_x, φ_y, φ_z) of acceleration of the vibration simulator table (Fig. 8.10) and accelerations on the several points on the dummy (Fig. 8.11) are the base for the seat dynamic model creation and identification. Even though within the MATLAB® environment the frequency response data can be partly used directly for the control design, the complete incorporation of the seat dynamics needs creation and identification of the state-space model. The aircraft model ACFA 2020 intended for the control design has been formulated as linear, therefore the requested seat model should be also linear.

There are several possible ways how to propose the dynamic model structure, principally on the scale from fully black box models to the detailed physical models. The several different types of models have been tested for the identification target. The best one seems to be relatively simple 3D mechanical model of 12° of freedom with clear physical interpretation of the model parameters (Fig. 8.12). Such type of model can naturally includes mechanical relations between acceleration outputs in several points (Fig. 8.11) of the dummy. Consequently, also the total number of identification parameters is relatively low with respect to other model forms. It has totally 23 mass, stiffness, damping and length parameters. Different optimization methods can be used for the finding of model parameters in order to find solution close to the experimental frequency response for different I/O channels. The global optimization

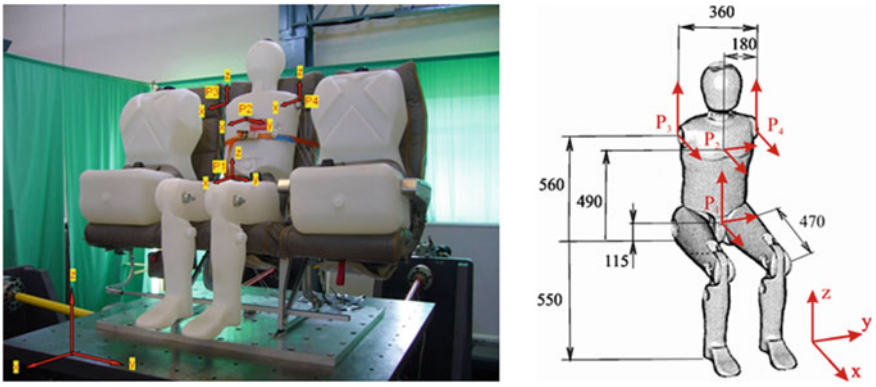

Fig. 8.11 Test dummy with dimensions, sensor positions and measurement directions

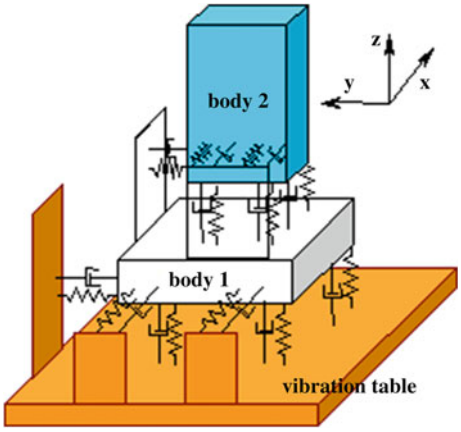

Fig. 8.12 Structure of considered 12 DOF mechanical model of seat for identification

methods have been used for the finding of the initial guess of the local parameter search [17]. The example of identification results is in Fig. 8.13 for transmissibility from *y* acceleration of table to *y* acceleration in dummy point P1. The accuracy of identification is always trade-off between fulfilments for different I/O channels and model complexity. The influence of the improved cabin floor on the resulting vibration comfort is very important. The consequence of this investigation is that the new improved cabin floor is working qualitatively like a low-pass filter with the cut off frequency at 5 Hz. The influence of the improved floor model has been included by its simplified (reduced) model with the property of the low-pass filter with the cutoff frequency near 5 Hz.

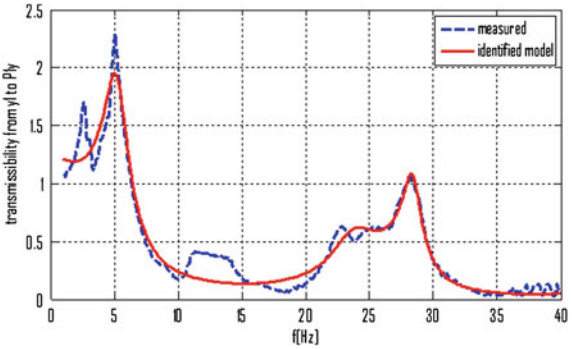

Fig. 8.13 Transmissibility from *y* acceleration of table to *y* acceleration in dummy point P1

8.1.6.4 Vibration Comfort Assessment Approach

The overall assessment of the vibration comfort of ACFA 2020 is following. The vibration comfort is evaluated at the selected positions of the passenger seats (Fig. 8.14). The accelerations in the translational and rotational directions are processed by the filters corresponding the influence of the floor and then the influence of the seats and consequently processed by the filters of the standard BS 6841. The overall assessment is carried out by the evaluation of the vibration comfort for the following loading cases, both for proper vibration comfort and for sea sickness:

- Longitudinal maneuver
- Longitudinal wind disturbance
- Longitudinal gust disturbance
- Lateral wind disturbance
- Lateral maneuver.

8.1.6.5 Conclusion to Comfort Evaluation

The evaluation during the project has been devoted to the comparison of the achieved absolute values of the vibration comfort to the values described in the standard [2]. The examples of some of the evaluation results obtained from the complete simulation for the testing passenger seats (Fig. 8.14) are in Figs. 8.15, 8.16 and 8.17.

The results for the longitudinal maneuver vibration comfort have been deeply below the approximate maximum limit of "not uncomfortable" level according to [2]. The values of the sea sickness corresponds to the values that are "a little uncomfortable" according to [2] despite the comparison of sea sickness is even more specific to particular environment—application. This value is understandable during the maneuver.

The results for the longitudinal wind disturbance excitation vibration comfort is achieving the level that is at the boundary between the level "not uncomfortable"

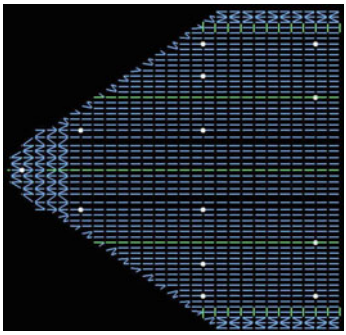

Fig. 8.14 The positions of evaluated passenger seats for vibration comfort evaluation

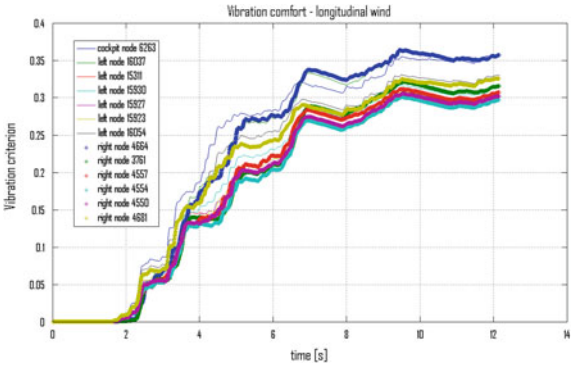

Fig. 8.15 Vibrational comfort during the simulation of longitudinal wind disturbance

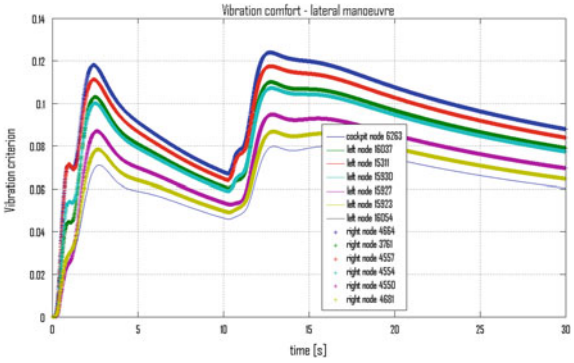

Fig. 8.16 Vibrational comfort evaluation during the simulation of lateral maneuver

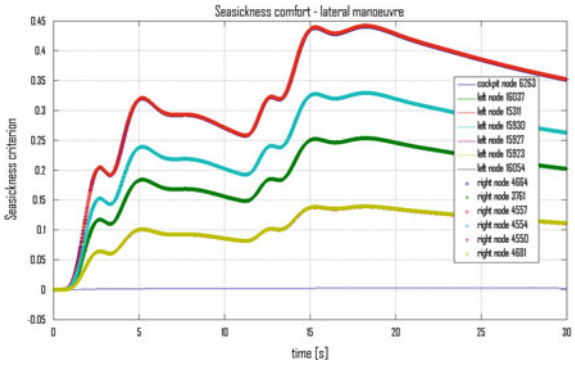

Fig. 8.17 Sea sickness evaluation during the simulation of lateral maneuver

and the level that is "a little uncomfortable" according to [2]. The value for the sea sickness evaluation corresponds again to the level that is "a little uncomfortable" according to [2].

The vibration comfort excitation for the longitudinal gust disturbance is achieving the level that is "uncomfortable" according to norm. This value is understandable during the short event of gust excitation. Similar situation has been identified for the sea sickness evaluation during the longitudinal gust disturbance.

The vibration comfort excitation for the lateral maneuver is achieving the level that deeply below the maximum limit of the level "not uncomfortable". The value of sea sickness is in the range "a little uncomfortable".

8.1.7 High-Fidelity Validation

High-fidelity validations have been defined within the scope of the ACFA 2020 project as the combined simulation of load control algorithms developed in Sects. 6 and 7 with high-fidelity models presented in Sect. 3. The ROMs developed in Sect. 4 have been based on methods of variable accuracy because the aim was to obtain an efficient representation of the aircraft's aeroelastic behavior across a large range of speed, altitudes and reduced frequencies. These ROMs constitute the models for controller design, but they can only give an approximate aerodynamic response of the aircraft. Especially, during transient maneuvers that involve flight dynamics, elastic deformations and strong actuation of the control surfaces, nonlinear effects not covered by the ROMs may be of considerable magnitude. Therefore, the aerodynamic response of the simulations was not generated by the ROMs themselves, but by the high-fidelity simulation tools for nonstationary compressible flows. Consequently, the forces, moments and modal forces have been computed by time-accurate simulations of the inviscid three-dimensional compressible flow equations around the

aircraft (the Euler equations of fluid dynamics) also referred to as computational fluid dynamics (CFD) solvers.

A pull-up maneuver case was defined as test case for comparison of the predicted loads, carried out in parallel by two partners using different CFD solvers, one developed by FOI (code "Edge") and one developed by NTUA (code "PUMA"). The latter was also used by HAI. These aeroservoelastic simulations showed a very close agreement between the results obtained by separate partners with different high-fidelity software for the common test case. Two other load cases have been investigated afterwards, the first being a coordinated turn analyzed by NTUA-HAI, and the second being a gust load investigated by FOI. The gust has been simulated using CFD methods, and revealed much larger differences than in the pull-up test case with respect to the ROM simulations. The results of some simulations indicated that the differences could arise from the ROM gust models used for controller design.

It is important to mention that only open-loop simulations have been carried out in the ACFA 2020 project. Although closed-loop simulations have been planned (in a cosimulation between MATLAB/Simulink® solvers and the CFD solvers plus flexible aircraft models) considerable numerical and interface problems prevented a successful implementation. Efficient closed-loop simulations would require some adaption of the simulation environment that is used in both ROM simulations and high-fidelity simulations for coupling the flight dynamics, the modal equations of elasticity, the control algorithm and the aerodynamics. A suitable planning of interfaces, data-exchange, and time-step coordination will, however, consume a significant amount of resources and calls for dedicated consideration in any research project.

8.1.8 System Design

The bulk of the work done within the ACFA 2020 project focused on the key issues of aerodynamics, structures and controllers for the BWB concept. However, investigations were carried out to assess the aircraft's stability and the controllers' efficiency in the case of failures. Based on these, a basic flight control, fuel and power supply system was designed.

The models and performed investigations for the ACFA 2020 BWB are based on the assumption of a fully operational aircraft. Since this does not reflect the reality, faulty components and partly functional systems have to be considered as well. In particular the probability of a catastrophic event has to be below the limits stated in the certification specifications issued by the regulatory authorities. Another important aspect is the availability of the maneuver and gust load alleviation functions, because the allowed reduction of safety margins and therefore structural weight relies on it (see CS-25).

The first step in the design process for the flight control system was the determination of a basic architecture with which the different failure cases could be investigated. For the system design only the criterion of stability has been used. Furthermore, redundancy strategies were analyzed for their applicability. In addition

the growing trend towards a more-electric aircraft was taken into account by using electromechanical actuators (EMAs) for the control surface actuation.

The initial control surface configuration was used as the starting point for a functional hazard assessment at the aircraft level. As a first step, the ACFA 2020 ROMs were tested for stability under positive and negative g-loads as well as updraft and downdraft gusts. Since the controllers were verified for normal operation within the cruise part of the flight envelope, failure case simulations could be conducted. The initial control surface configuration did not provide an adequate failure tolerance. In particular, a jammed EMA respectively a jammed flap in deflected position significantly affects the aircraft's attitude and control authority which results in a catastrophic event due to instability of the aircraft. A segmentation of the control surfaces was identified as the most promising approach to make actuation failures tolerable. After several iterations with the above mentioned functional hazard assessment followed by an associated fault tree analysis a trade-off was found between the reduction of control authority of a single flap by segmentation (see Fig. 8.18) and the rising overall probability for a jam. Overall, the jamming issue of the EMAs which is not definitely solved yet and the low failure tolerance compared to conventional aircraft configurations remains challenging for the system design.

In the next step, a basic flight control and power supply system was designed on the basis of the obtained results and allocated safety margins. In addition, several EMAs architectures were proposed for the primary control surfaces as well as the spoilers and the slat system of the BWB aircraft. The above mentioned low failure tolerance causes the need for a dual data and power bus connection of EMAs actuating flaps for the pitch, roll, yaw and spoiler control. A survey on the power bus mapping to the electric loads resulted in an implementation of four high- and low-voltage power buses. Under the aspect of a gentle degradation of the flight control system and the prevention of single point failures, this was considered as the most promising approach.

The usage of fuel transfer within the fuel system is a common approach to adjust the center of gravity and therefore avoid high trim deflections during cruise. For the ACFA 2020 BWB, studies showed that an aerodynamically favorable approach with an active stabilization for unstable center of gravity (CG) positions is only possible to a certain extent. In particular, a landing with a CG adjusted for cruise performance is impossible with the bandwidth of currently available actuators. In a classic aircraft design, the trim tanks are located in an elevated position of the aircraft's tail. Therefore, adjusting the CG back to a landing configuration in case of failed pumps can be simply done by opening a valve, allowing the fuel to flow back to the main tanks by gravity. The BWB concept as well as the location of the rear trim tanks in the lower part of the fuselage causes comparatively more effort for the design of a fuel system. After considering all aspects, a safety critical fuel system was designed to allow the readjustment of the stability reserve in any flight condition (see Fig. 8.19). In detail, these are the subsystems engine feed, fuel transfer and trim, fuel jettison, tank venting as well as the fuel management.

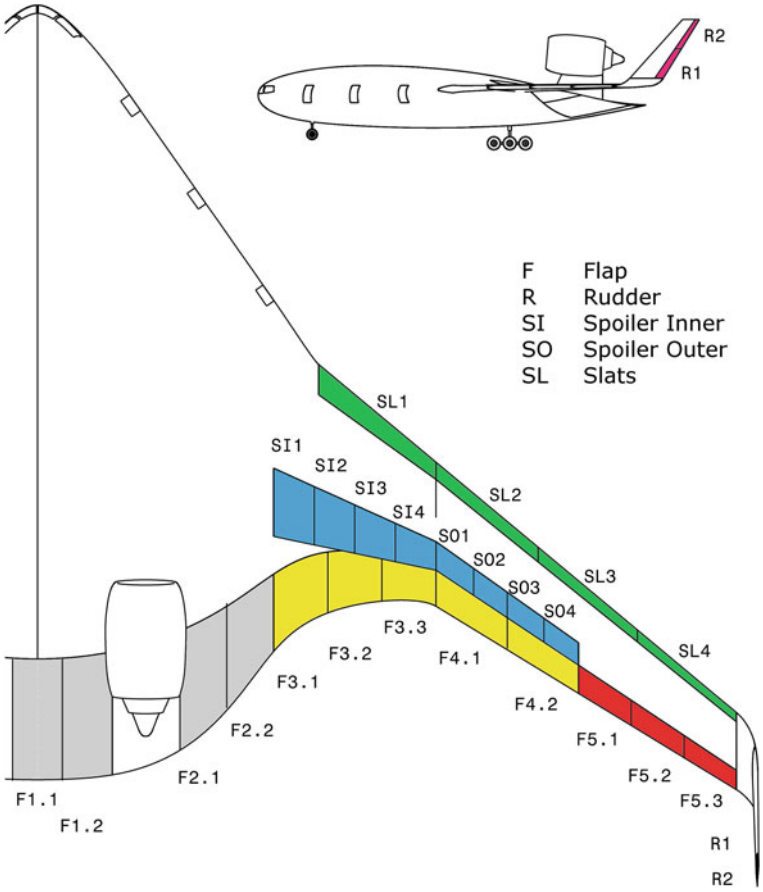

Fig. 8.18 ACFA 2020 BWB, final control surface layout from the system design perspective

8.1.9 Summary

The BWB concept proved to be very efficient with respect to fuel burn also for medium-sized transport aircraft (450PAX). Compared to a more conventional configuration by application of same engine technology more than 13 % less fuel burn has been estimated for the BWB aircraft. The major part of the project dealt with the development of advanced active control concepts in particular to achieve a significant loads reduction and high ride comfort. Major results are published in [6, 10, 16, 19, 21]. It was shown that the ride comfort can be largely improved by a combined feedback and adaptive feed-forward control concept. Nevertheless, the achieved values for ride comfort are at the lower levels of discomfort and particular attention should be paid to this area also in future studies on BWB type aircraft. The adaptive feed-forward control concept to reduce turbulence induced vibrations was

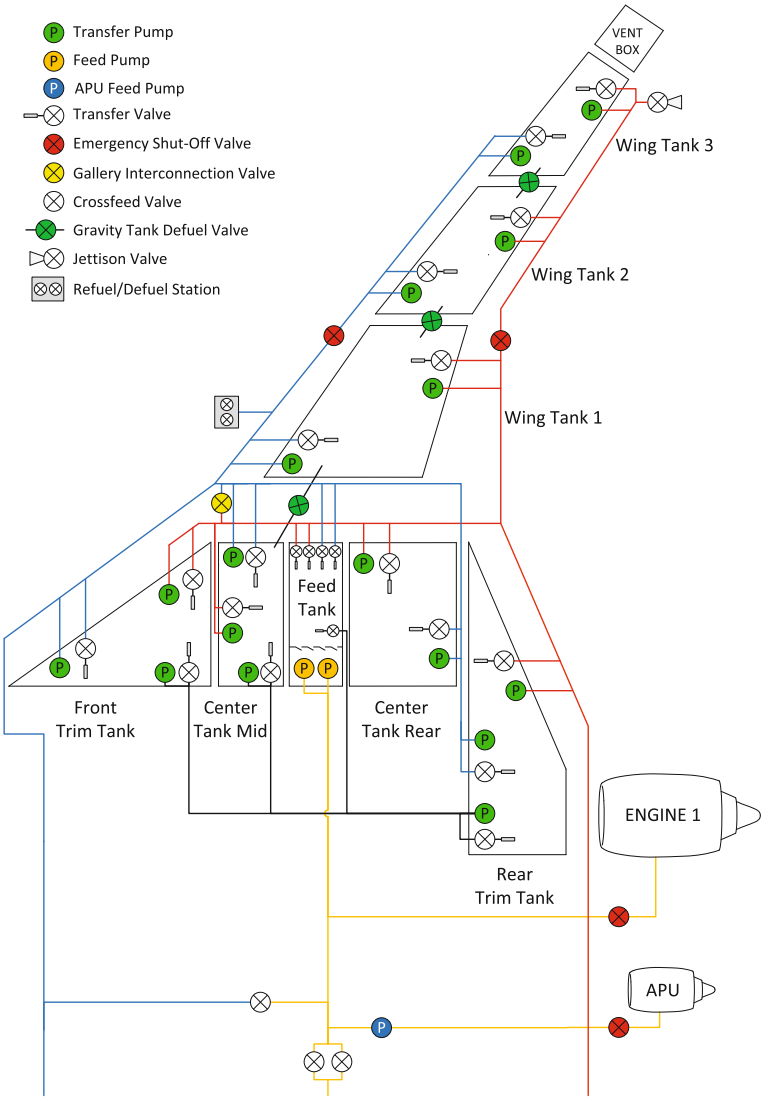

Fig. 8.19 Fuel system, *central* and *right* part

in addition validated by flight tests with the ATTAS aircraft. Loads due to discrete gusts can be also significantly alleviated by combined feedback and feed-forward concepts. In a final step the ACFA 2020 BWB has been resized according to the loads achieved with active loads alleviation resulting in additional weight savings. The ACFA 2020 project showed that the BWB concept is quite attractive mainly with respect to fuel burn and that it can be further improved by enhanced active control. Nevertheless there is still a long way to go to bring such an unconventional

configuration to reality. From an aeromechanics point of view, the next most interesting topics to investigate after the ACFA 2020 project are the low-speed handling qualities. Also BWB sensitivity against gust and best suited control surface layout for gust load alleviation would be important topics not sufficiently addressed in ACFA 2020. In order to get a coordinated progress in the BWB knowledge the next step should be also in another direction, for example, pressurized center body structural design and integrated approaches to optimize loads control and structure in a single step.

8.2 Discussion

M. Kozek and A. Schirrer

Although the ACFA 2020 project was designed to cover the main design aspects of a future BWB passenger aircraft several topics must be treated in more depth. Some of those topics are discussed in the following section.

8.2.1 Structural Model of Aircraft Body

In order to have maximum design freedom for the interior volume, the strength of the pressurized aircraft body has been modeled without any interior structures, compare Sect. 3.3. This enables the engineers to freely assign the interior space to cockpit, passenger area, main fuel tank, and housing for the landing gear. Due to the large dimensions and the comparatively small curvature of the outer skin, however, considerable material and construction effort is necessary to achieve an acceptably stiff wall.

By connecting the upper and lower skins either by simple struts or complete stringers a considerable weight reduction can be expected (see for example, Fig. 3.3 in Sect. 3.2.1 for the NACRE model). Struts designed for pure tension load could be very small, easy to place in the interior volume, and still provide an effective means to counteract the cabin pressure effect. One or more stringers placed in longitudinal and/or lateral direction would require a more integrated design approach, but also considerably add to the overall stiffness of the aircraft body.

A beneficial effect of such reinforcements would be given by the additional support of the passenger floor. The dimensions of the maximum span would be reduced, thus also reducing the need for structural stiffness. Both strength and dynamical behavior of the floor construction could be improved. Note that for the integration of stringers in the passenger area several additional criteria apply. Issues such as passenger comfort, safe emergency evacuation, but also ease of modular production need to be considered when such an integral design approach is intended.

A general remark is in order on the design stage of the overall structure. As in any conceptual design, the optimization of the structure would require an iterative approach. Recent publications on BWB design mainly follow that line, although aerodynamic design is the main focus of these approaches [1, 12]. In [4] a tool for such a design process is presented for an open rotor BWB concept, and in [11] a multidisciplinary design optimization (MDO) for a BWB with distributed propulsion is demonstrated. However, an integral approach that explicitly considers the control concept during that early stage is still missing.

A representative detail with potential for optimization in ACFA 2020 is flutter analysis: In order to achieve acceptable stability margins against flutter with a simple remedy the skin thickness on the outer wing portions was increased. This can only be a first step, leading to a redesign of the complete outer wing which also considers weight issues. As mentioned before, such iterative optimizations could not be performed within the ACFA 2020 project.

8.2.2 Actuator Models

The control surfaces of the ACFA 2020 BWB design are partly unusual. Split ailerons, rather high winglets with rudders, but mostly large rear elevons constitute control surfaces which cannot be modeled by existing standard equipment. The rear elevons proposed in the project are rather large in order to provide sufficient control authority; however, in order to limit weight, size, and power consumption the maximum bandwidth was limited to 0.5 Hz. This conservative approach to model the actuation of the elevons naturally leads to a small bandwidth of the control surface. It should be noted that a trade-off between bandwidth (and thus power consumption) and control authority exists: Large and efficient elevons will be slow in actuation and vice versa [20]. The optimum balance in that choice is not easy to see; only when the closed-loop performance is assessed the quality of the actuator design can be evaluated. It would therefore require an iterative design loop, where after a redesign of the actuators the controllers also have to be optimized again. It should be mentioned here that alternative technologies for actuation have been developed specifically for BWB configurations [23], where an all-electric morphing trailing edge device is presented. Another interesting approach is the use of canards (for example [14]) to stabilize the BWB for large angles of attack and possibly improve control bandwidth. Results for detailed modeling of BWB control surfaces are presented in [18], where nonlinear effects were modeled using 3D-CFD methods and wind tunnel experiments.

In the ACFA 2020 project the elevons have been modeled with a comparatively low bandwidth (see Sect. 5.1), thus effectively limiting the achievable bandwidth of the overall closed-loop behavior. The reason for this fact is that available state-of-the-art technology was assumed for actuation, and no specific optimization of the underlying technologies has been performed. With this approach the predicted actuator performance could be guaranteed, however, it is desirable that a higher bandwidth can be achieved by a dedicated optimization.

Note that in the control designs the aforementioned limitations showed up specifically in the mode damping capabilities of the closed-loop dynamics. While handling qualities could be guaranteed within the given margins, higher elastic modes could not be effectively damped due to the limited actuator bandwidth.

8.2.3 Flight Envelope and Control Design

One of the main challenges in designing control algorithms for aircraft is the strong variation in flight envelope parameters (see Sect. 5.1.1 and also [20]). Although important design cases have been investigated by the project team (for example, one engine out capabilities) the flight envelope considered by control design has been considerably clipped to a set of cruise conditions. Even within this envelope only a rough grid of design and validation points has been selected. This choice is necessary due to the limitations of a publicly funded research project; nevertheless, in the ACFA project the fundamental functionality of the control for a large BWB design has been successfully demonstrated.

The obtained results would still need to be extended to the complete flight envelope, which is a considerable effort but without the need for new control developments. A more critical issue is the control development for important standard maneuvers like take-off, approach, and landing. Due to the low air speeds extremal weights, and dynamic pressure in these cases dedicated control strategies have to be developed. Additionally, the transition between those dedicated control strategies and the control for cruise condition must be optimized for stability, bumpless transfer, and performance. These parts of the control design have not been covered by the ACFA 2020 project and would constitute a considerable additional effort. Control design for BWB in general is far from being concluded. In [20], an active control design for pitch stabilization of a BWB aircraft is presented, and control challenges with respect to take-off and landing are discussed. An adaptive L_1 state feedback controller is designed for BWB in [25], considering low-speed and large angle of attack during landing.

8.2.4 High-Fidelity Simulations

Within the ACFA 2020 project high-fidelity simulations involving the coupling between fluid dynamics, structural elasticity, flight dynamics and control have been realized in open-loop (see Sect. 8.1.7). Such simulations require a closed-simulation loop between the MATLAB/Simulink® models and the CFD models, respectively. One of the main problems encountered was the different implementation of timescales and integration algorithms. The combined effect required a much too fine time interval for the Euler algorithm utilized in the CFD part of the simulation thus generating very large simulation times.

Aeroservoelastic simulations where the equations of fluid dynamics are solved by high-fidelity tools is not common practice on full aircraft configurations (for control surfaces such investigations exist, see for example, [18]). An additional challenge was that the flow regime was transonic, thus involving flow discontinuities (shocks). This work should thus be regarded as innovative in the field of multidisciplinary simulations. One of the outcome of the simulations is that the ROM may not be accurate outside of its validation interval, for example, the interval of angles of attack, side-slip angle, roll angle, and control surfaces deflection angles where CFD was carried out.

A possible discrepancy between the high-fidelity gust and the ROM gust may have also been identified. As the prediction of gust loads at transonic speeds requires high-fidelity tools it would be recommendable, in future projects, to investigate further the accuracy of ROMs of gust loads.

The combination of critical physical phenomena and a problematic parametrization of the individual simulation tools led to numerical problems for simulations of closed-loop control. In order to avoid this type of limitations in future projects, it would be appropriate that the implementation of a simulation interface, between different software from different disciplines, has its own dedicated task and that the product of this work be a deliverable of the project.

8.2.5 System Design

Systems architecture is an important step towards implementation of the control system. Based on the existing design of the ACFA 2020 BWB, investigations were carried out to assess the safety in the case of failures (see Sect. 8.1.8). First tests led to redundancy strategies in combination with the implementation of EMAs. A segmentation of the control surfaces was identified as the most promising approach.

EMA architectures were investigated and adapted to the specific needs of the ACFA 2020 BWB configuration. Since landing with a CG adjusted for cruise performance is impossible, a safety-critical fuel system was designed to allow the readjustment of the stability reserve. The criticality and the location of the trim tanks within the lower part of the fuselage resulted in an exceptionally high complexity of the automatic fuel functions; an implementation of four power buses seemed to be necessary. Together with a duplex power supply of the primary control surface actuators, an adequate system configuration was devised.

Due to the fact that this work is placed in a predesign phase, additional investigations and design steps would have to follow. In context of the conducted analysis and designed systems there are diverse possibilities for improvements. The applied approaches are mostly conservative, leaving potential for optimization in following design and review phases. In particular, a further improvement of the EMA technology is regarded as the part having an immediate positive effect on the complexity of the flight control system.

8.3 Outlook

A. Wildschek

This book summarizes the results of the very ambitious European research project ACFA 2020. With a budget of less than 5 Million Euros, methods and tools ranging from aircraft predesign, flexible aircraft modeling and control design, to the investigation of details such as gust loads and control system architecture were studied. The aircraft configuration chosen for application of developed tools and methods is the BWB aircraft; a tailless aircraft configuration widely promoted in the literature of the past decades for its potential for significant fuel efficiency improvement. The beginning of the ACFA 2020 project revealed the shortcomings of state-of-the-art aircraft predesign tools, as aircraft trim and controllability cannot be decoupled from the lift distribution, as it is the case for aircraft with tails. Since the main focus of the ACFA 2020 project was the development of methods and tools for flexible aircraft modeling and control, only a limited budget was available for aircraft predesign. The resulting crude BWB design unfortunately does not give a solid answer to how useful such a tailless aircraft design is for a civil transport application, but reveals several interesting problems related to performance and control of this configuration.

A large variety of promising control synthesis methods for flexible aircraft control are discussed, ranging from LPV control design techniques to adaptive and robust feed-forward maneuver and gust loads alleviation concepts. Most of these methods provide a feasibility check for aircraft control rather than control laws ready to be implemented on a flying aircraft. For predesign of novel aircraft configurations, however, such control feasibility checks are an important first step and the developed control synthesis methods can be transferred to any other aircraft configuration. In order to minimize trim drag, and exploit the full fuel efficiency improvement achievable on the ACFA 2020 BWB, a significant relaxation of pitch stability margin would be beneficial. Such high pitch unstable aircraft configurations, however, are impractical for civil transport for several reasons. First, the control system for highly unstable aircraft is very expensive in terms of development and certification. Second, the fail-safe behavior required for civil aircraft can only be reached with rather moderate pitch instabilities [20]. Lastly, the fast actuation of the BWB's large pitch control surfaces necessary for active stabilization requires very powerful, and thus heavy and energy consuming actuators, jeopardizing the efficiency improvement aspired with this tailless configuration. In addition, the short maintenance intervals required for actuators running at a high number of load cycles every flight which are well known from high-agility fighter aircraft are impractical for civil applications. As relaxed static pitch stability which is seen as an important enabler for minimizing trim drag, and thus realizing a fuel-efficient BWB configuration, increases cost for design, certification, and maintenance, it can already be seen how economically risky the development of such a civil BWB transport aircraft is.

One solution to overcome these problems is to go for a slightly stable aircraft, and redesign the configuration for minimum trim drag throughout the mission con-

sidering also aircraft flexibility, and sacrificing some of the aspired fuel efficiency improvement for the sake of incalculable cost and risk. It is concluded that a higher level interdisciplinary benefit versus risk assessment would be required in order to comprehensively evaluate the BWB aircraft. That would take into account the consideration that a successful civil transport aircraft configuration not only must fulfill the requirement for low fuel consumption, but also for high aircraft availability and reliability, low operating costs (including maintenance costs), as well as economically justifiable cost for design, manufacturing, and certification. In that context it is to note that despite some uncertainties in the gust response modeling, a trend toward severe vertical acceleration during discrete sizing gust encounter due to the inherently low wing loading of such configurations was identified, thus raising questions with respect to passenger safety on such BWB configurations. The investigations show that active gust load alleviation can offer some remedy to this problem, but cannot solve it completely unless much more powerful actuators are used adding the drawbacks already described above.

Finally, due to budget constraints, the low-speed flight behavior of the BWB was only limitedly investigated in the presented project although most handling quality issues are related to this flight regime. The integration of a high-lift system required for achieving take-off and landing distances comparable to the ones of conventional tailed aircraft, for example, proves to be difficult due to the inability to adequately counterbalance the resulting nose-down moment [15]. In addition, the detrimental effect of rear CG position on stall and spin characteristics of a BWB configuration must be thoroughly investigated in the future. In the end it remains questionable if a tailless configuration really provides the best trade-off between the various requirements for a civil transport aircraft.

References

1. Brenner MW, Trépanier J-Y, Tribes C, Petro E (2012) Conceptual design framework for blended wing body aircraft. In: Proceedings of 12th AIAA aviation technology, integration, and operations conferencee and 14th AIAA/ISSM, Indianapolis, Indiana
2. British standard BS (1987) 6841:1987
3. Demourant F, Ferreres G (2011) An LPV multiobjective control law design based on Youla parametrization for a flexible BWB aircraft. In: 4th European conference for aerospace sciences (EUCASS 2011), St. Petersburg, Russia
4. Gern FH (2013) Conceptual design and structural analysis of an open rotor hybrid wing body aircraft. In: 54th AIAA/ASME/ASCE/AHS/ASC structures, structural dynamics, and materials conference, Boston, Massachusetts
5. Hahn K-U, Koenig R (1992) ATTAS flight test and simulation results of the advanced gust management system LARS. In: AIAA atmospheric flight mechanics conference, Hilton Head Island
6. Haniš T, Kučera V, Hromcík M (2011) Low order H_∞ optimal control for ACFA blended wing body. In: 4th European conference for aerospace sciences (EUCASS 2011), St. Petersburg, Russia
7. Hecker RS, Hahn K-U (2007) Advanced gust load alleviation system for large flexible aircraft. In: CEAS European air & space conference, Berlin, Germany

8. Hemedi M, Schirrer A, Westermayer C, Kozek M (2010) Integrated input-output selection strategy for robust control of complex parameter varying systems. In: 10th international conference on motion and vibration (MOVIC 2010), Tokyo, Japan
9. ISO 2631-1:1997 / vdi 2057 (1997)
10. Kučera V, Hromčík M (2011) Delay-based signal shapers and ACFA 2020 BWB aircraft FCS. In: Proceedings of the 4th EuCASS
11. Leifsson L, Ko A, Mason WH, Schetz JA, Grossman B, Haftka RT (2013) Multidisciplinary design optimization of blended-wing-body transport aircraft with distributed propulsion. Aerosp Sci Technol 25:16–28
12. Lyu Z, Martins JRRA (2014) Aerodynamic design optimization studies of a blended-wing-body aircraft. J Aircr 7:1–14
13. Meyer M, Breitsamter C (2011) Influencing the aerodynamics of the ACFA2020 aircraft with flap and trailing edge device oscillations. In: Proceedings of the 4th EuCASS
14. Nasir REM, Kuntjoro W, Wisnoe W (2012) Longitudinal static stability of a blended wing-body unmanned aircraft with canard as longitudcinal control surface. J Mech Eng 9:99–121
15. Paulus D, Binder S, Petterson Ö, Baier H, Hornung M (2012) The integration of an efficient high lift system in the design process of a blended wing body aircraft. In: 12th AIAA aviation technology, integration, and operations (ATIO) conference and 14th AIAA/ISSM, Indianapolis, Indiana
16. Schirrer A, Westermayer C, Hemedi M, Kozek M (2011) Robust feedback lateral control using a parameterized LFR model and DGK-iteration. In: 4th European conference for aerospace sciences (EUCASS 2011), St. Petersburg, Russia
17. Šika Z, Valášek M, Vampola T, Fullekrug U, Klimmek T (2011) Dynamic model of passenger seats for vibration comfort evaluation and control. In: Proceedings of ICOVP, Prague
18. Waters MW, Voskuijl LLM, Geuskens FJJMM (2013) Control allocation performance for blended wing body aircraft and its impact on control surface design. Aerosp Sci Technol 29:18–27
19. Westermayer C, Schirrer A, Hemedi M, Kozek M (2011) An H_∞ full information approach for the feedforward controller design of a large BWB flexible aircraft. In 4th European conference for aerospace sciences (EUCASS 2011), St. Petersburg, Russia
20. Wildschek A (2014) Flight dynamics and control related challenges for design of a commercial blended wing body aircraft. In: AIAA guidance, navigation, and control conference, National Harbor, Maryland
21. Wildschek A, Haniš T (2011) $mathscr L_\infty$-optimal feed-forward gust load alleviation for a large blended wing body airliner. In: 4th European conference for aerospace sciences (EUCASS 2011), St. Petersburg, Russia
22. Wildschek A, Haniš T, Stroscher F (2013) $\mathscr{L}_\infty$-optimal feedforward gust load alleviation design for a large blended wing body airliner. In: Progress in flight dynamics, guidance, navigation, control, fault detection, and avionics, vol 6. EDP Sciences, pp 707–728
23. Wildschek A, Havar T, Plötner K (2010) An all-composite, all-electric, morphing trailing edge device for flight control on a blended-wing-body airline. J Aerosp Eng 224:1–9
24. Wildschek A, Maier R, Hahn K-U, Leißling D, Preß M, Zach A (2009) Flight test with an adaptive feed-forward controller for alleviation of turbulence excited structural vibrations. In: AIAA guidance, navigation, and control conference, Chicago
25. Zheng FL, Xu J (2013) Angle of attack control of a blended wing body aircraft using state feedback L1 adaptive controller. In: Chinese automation congress (CAC), Changsha, China
26. Zuziak P, Šika Z, Valášek M, Vampola T, Klimmek T (2010) Vibration control of flexible aircraft with respect to passengers comfort. In: ISMA 2010, Leuven, Belgium

Index

M. Kozek and A. Schirrer (eds.), *Modeling and Control for a Blended Wing Body Aircraft*, Advances in Industrial Control, DOI 10.1007/978-3-319-10792-9